THE UNIVERSITY of ADELAIDE

Mesoporous Silica Nanocomposites for Drug and Gene Delivery

Lin Xiong

A thesis submitted for the degree of Doctor of Philosophy

School of Chemical Engineering

Faculty of Engineering, Computer and Mathematic Sciences

The University of Adelaide

December 2016

Table of Contents

Thesis Declaration Statement by Author

I certify that this work contains no material which has been accepted for the award of any other degree or diploma in my name, in any university or other tertiary institution and, to the best of my knowledge and belief, contains no material previously published or written by another person, except where due reference has been made in the text. In addition, I certify that no part of this work will, in the future, be used in a submission in my name, for any other degree or diploma in any university or other tertiary institution without the prior approval of the University of Adelaide and where applicable, any partner institution responsible for the joint-award of this degree.

I give consent to this copy of my thesis when deposited in the University Library, being made available for loan and photocopying, subject to the provisions of the Copyright Act 1968.

The author acknowledges that copyright of published works contained within this thesis resides with the copyright holder(s) of those works.

I also give permission for the digital version of my thesis to be made available on the web, via the University's digital research repository, the Library Search and also through web search engines, unless permission has been granted by the University to restrict access for a period of time.

Name of Candidate: Lin Xiong

Signature:

Date: 11/26/2016

Acknowledgement

First and foremost, I would like to express my most sincere gratitude to my principle supervisor Prof. Shizhang Qiao, for his invaluable and continuous guidance, support and encouragement throughout my Ph.D research and study, without which it would be impossible for me to have this wonderful opportunity of study in a vibrant group and made some achievements during my Ph.D period. During the past four years, I have benefited a lot from his guidance on forming innovative research ideas, making effective research plan and composing high quality research papers.

Also, I would like to give my great thankfulness to my co-supervisor A/Prof. Jingxiu Bi. Without her guidance and support on biological experiment, I would not have been able to conduct my Ph.D research on bioactive nanomaterials.

Besides, I am grateful to A/Prof. Sheng Dai, who gave me some very helpful advice for my Ph.D research. My gratitude should also go to Dr. Xin Du and Dr. Bingyang Shi, who provided the important chemical and biological training in the beginning of my Ph.D project.

In addition, I would like to give my thanks to Dr. Qiuhong Hu in school analytical lab for her important training and support on various characterization instruments. I want to express my gratitude to Ms. Lyn Waterhouse, Dr Agatha Labrinidis, and other relevant staff in Adelaide Microscopy for their technique support on microscopies.

Moreover, I would like to thank Prof. Freddy Kleitz in Université Laval for his valuable advices and comments on my several research papers. I also owe my great thanks to Dr. Youhong Tang in Flinders University and Professor Xiaolin Wang in University of Wollongong for their kind helps with my sample characterization. My research project could not have proceeded smoothly without their support.

Furthermore, I want to thank my colleagues in pharmaceutical lab, including Ms. Lei Liu, Mr. Bingyang Zhang and Mr. Xiaolin Cui. It is the corporation with these colleagues that made my research much easier. I also want to thank other members in Prof. Qiao's research group for their help in my life and research, including Dr. Ji

Liang, Dr. Yao Zheng, Dr. Ruifeng Zhou, Dr. Yan Jiao, Dr. Sheng Chen, Dr. Jingjing Duan, Dr. Lei Zhang, Dr. Tianyi Ma, Mr. Jingrun Ran, Mr. Jinglong Liu, Mr. Dongdong Zhu, Mr. Fangxi Xie, Ms. Xuesi Wang, Mr. Mohammad Ziaur Rahman and Ms. Bita Bayatsarmadi.

Especially, I need to express my earnest appreciation to Australia Research Council Discovery Project which has financially supported my Ph.D project, and The University of Adelaide who offered me the postgraduate scholarship and covered my living costs during this period.

Last but not least, I want to thank my beloved parents. Words cannot express my gratefulness for their sacrifice, firm support and sustained encouragements during my Ph.D period. This thesis would not be possible without the support and love from them.

Abstract

A drug delivery system is an essential tool for improving drug therapies by overcoming the limitations of 'free' drug delivery including low solubility in water, poor stability in biological systems, short residence time, unspecific toxicity and side effects. Nowadays, nanomaterials have become ideal vehicles for drug delivery owing to their very small size and high surface-to-volume ratio. Their small size ensures access to different biological tissues, efficient cellular uptake and facilitates intracellular delivery of therapeutics. Their high surface area allows for high drug loading and the attachment of various functional groups. Among various nanomaterials, mesoporous silica nanoparticles show great potential for delivery application due to their good biocompatibility, well-developed mesoporosity, and versatile surface functionalization. However, to construct an efficient delivery system, the primary silica nanoparticles still need to be optimized in structure to load large biomolecules and modified in surface chemistry to achieve efficient targeting and release control.

With this aim, this Ph.D thesis has demonstrated the design and fabrication of a serial of novel mesoporous silica based nanocomposites as drug and gene delivery carriers. These researches include:

(1) We firstly studied the controllable synthesis of stellate mesoporous silica nanoparticles with radial pore morphology. By using triethanolamine as the base catalyst and adjusting the surfactant composition, reaction temperature and time, and reagent ratio, we demonstrated that the particle size of these nanomaterials could be tailored continuously from 50 to 140 nm and the pore size could be tuned from 2 to 20 nm, respectively. After further functionalization with low molecular weight poly(ethyleneimine), these nanocomposites demonstrated good capability for intracellular delivery of the anticancer drug doxorubicin.

(2) Then, we developed a cancer cell-specific nuclear-targeted delivery system based on mesoporous silica nanoparticles. Mesoporous silica nanoparticles with 40 nm particle size were modified with dual targeting ligands, i.e., folic acid for cancer

cell targeting and dexamethasone for nuclear targeting. The resulting nanocarriers could not only enhance the inhibition efficacy of doxorubicin on cancerous Hela cells through active nucleus accumulation but also reduce toxic side effects on normal cells though receptor-mediated selective cellular uptake.

(3) Next, we studied magnetic core–shell silica nanoparticles with large radial mesopores for small interfering RNA (siRNA) delivery. These nanoparticles possess both high loading capacity of siRNA and strong magnetic response under an external magnetic field. Furthermore, an acid-liable coating composed of tannic acid was applied to further protect the siRNA loaded in the large pores. The coating also increased the dispersion stability of the siRNA-loaded carrier and served as a pH-responsive releasing switch. Using these nanocarriers, enhanced delivery of functional siRNA into human osteosarcoma cancer cells was achieved with the aid of the external magnetic field.

(4) Finally, we prepared bowl-like mesoporous organosilica nanoparticles for DNA delivery. The nanoparticles were prepared by a simple “hard templating followed by hydrothermal etching” method. After amine functionalization, these nano-bowls showed significantly higher loading capacity for plasmid DNA than traditional structured (hollow, dendric, MCM41 type) silica-based nanocarriers thanks to their large accessible center cavity. Furthermore, after co-loading with an endosomolytic reagent in the mesopores, enhanced transfection efficiency comparable to the polymer standard was achieved for in vitro plasmid DNA transfection.

In summary, these findings have demonstrated the design and fabrication of several novel silica nanocomposties for drug and gene delivery, provided a deeper understanding of the relationship between the physicochemical properties of silica nanocomposties and their bioactivity, and may pave a way of the further development of silica-based delivery system.

Chapter 1 Introduction

1.1 Background and significance

Nowadays, the rapid advancement of nanotechnology and nanomaterial science are revolutionizing the world of medical therapy.[1] For example, the size- and shape-dependent optical and electronic properties of gold nanoparticles have led to their wide applications in biological diagnosis and photothermal therapy.[2, 3] Magnetic nanoparticles have been extensively investigated for magnetic resonance imaging (MRI), hyperthermia, magnetic field-targeted delivery, and protein separation.[4, 5] These applications of nanotechnology and nanomaterials for treatment, diagnosis, monitoring, and control of biological systems have been named as “nanomedicine” by the National Institutes of Health.[6]

In nanomedicine, drug delivery applications plays a dominate role, accounting for about three-quarters of the research activity and of the nanomedicine market.[1] An important reason for this is the great potential of nanosized drug carriers to address one of the most pressing threats for current human society - cancer.[7] These nanocarriers are expected to overcome limitations associated with conventional chemotherapy drug formulations, surmount various biological barriers and deliver drugs precisely to the cancer sites.[8] A typical successful example is the liposomal doxorubicin (Doxil), which was approved by the US Food and Drug Administration for the treatment of Kaposi's sarcoma.[9] In contrast to the free doxorubicin drug which has dangerous dose-dependent cardiotoxicity, the liposome encapsulated drug shows an equivalent efficacy and improved safety profile. Thus, these nanomaterial-based delivery systems could provide new application opportunities for traditional drugs to reduce the side effects.[10] Meanwhile, with the development of biotechnology, there is also considerable interest in exploiting the nanocarriers for delivery of new drugs including therapeutic proteins and genes.[11, 12] As the origins of many diseases including cancer are related to genetic defection and mutation, gene therapy has been considered as a promising therapeutic method by delivering

foreign nucleic acids (DNA, RNA, and oligonucleotides) into living cells.[13] Because gene molecules are much larger in size and less stable than common small molecule drugs, nanocarriers with special particle structure and surface chemistry need to be developed for their delivery.

So far, different formulations of nanomaterials have been explored for drug delivery purpose. These include liposomes, polymer micelles, emulsions, polymer nanogels and inorganic particles (gold, carbon, iron oxide, silica, etc.). The unique advantages of mesoporous silica nanocomposites are highly developed porosity, well-defined morphology, versatile functionalization and good biocompatibility.[14-18]

1.2 Objective and thesis outline

The objective of this project is to design and fabricate a serial of novel mesoporous silica nanocomposites with favorable structure and surface functionalization as drug and gene delivery nanocarriers. The main achievements obtained in this thesis are presented in the form of four published papers in peer-reviewed journals. The following chapters in this thesis are organized according to the sequence below:

In chapter 2, a literature review on the synthesis, functionalization and delivery application of mesoporous silica nanocomposites is given.

In chapter 3, tunable stellate mesoporous silica nanoparticles with radial pore morphology were synthesized using triethanolamine as the base catalyst. By adjusting the surfactant composition, reaction temperature and time, and reagent ratio, the particle size of the material could be tailored continuously ranging from 50 to 140 nm and the pore size from 2 to 20 nm. After functionalization with low molecular weight poly(ethyleneimine), these nanocomposites demonstrated good potential for intracellular delivery of the anticancer drug doxorubicin. This investigation has been published in *J. Mater. Chem. B*, **2015**, 3, 1712.

In chapter 4, mesoporous silica nanoparticles with 40 nm particle size were modified with dual targeting ligands, i.e., folic acid and dexamethasone, to construct a cancer-cell-specific nuclear-targeted delivery system. The resulting nanocarriers not only enhanced the inhibition efficacy of doxorubicin on cancerous Hela cells

through active nucleus accumulation but also reduced toxic side effects on normal cells though receptor mediated selective cellular uptake. This investigation has been published in *Small*, **2015**, 11, 5919.

In chapter 5, magnetic core–shell silica nanoparticles were developed for small interfering RNA (siRNA) delivery. These nanoparticles were fabricated by coating super-paramagnetic magnetite nanocrystal clusters with radial large-pore mesoporous silica. These nanoparticles possess both high loading capacity of siRNA and strong magnetic response under an external magnetic field. An acid-liable coating composed of tannic acid further protected the siRNA loaded in these nanoparticles. The coating also increased the dispersion stability of the siRNA-loaded carrier and served as a pH-responsive releasing switch. Using the magnetic silica nanoparticles with tannic acid coating as carriers, enhanced delivery of functional siRNA into human osteosarcoma cancer cells was achieved with the aid of the external magnetic field. This investigation has been published in *Small*, **2016**, 12, 4735.

In chapter 6, bowl-like mesoporous organosilica nanoparticles were prepared for the first time by a simple “hard templating followed by hydrothermal etching” method. After amine functionalization, these nano-bowls showed significantly higher loading capability for plasmid DNA than traditional (hollow, dendric, MCM41 type) silica-based nanocarriers thanks to their large accessible center cavity. Furthermore, after co-loading with an endosomolytic reagent in the mesopores, enhanced transfection efficiency comparable to the polymer standard was achieved for in vitro plasmid DNA transfection. This investigation has been published in *Nanoscale*, **2016**, 8, 17446.

In chapter 7, a general summary of the results in this thesis and a brief discussion on future directions of the work are presented.

1.3 References

[1] V. Wagner, A. Dullaart, A.-K. Bock, A. Zweck, *Nat. Biotechnol.* **2006,** *24*, 1211.

[2] X. Yang, M. Yang, B. Pang, M. Vara, Y. Xia, *Chem. Rev.* **2015,** *115*, 10410.

[3] E. C. Dreaden, A. M. Alkilany, X. Huang, C. J. Murphy, M. A. El-Sayed, *Chem. Soc. Rev.* **2012,** *41*, 2740.

[4] N. Lee, T. Hyeon, *Chem. Soc. Rev.* **2012,** *41*, 2575.

[5] Y. Pan, X. Du, F. Zhao, B. Xu, *Chem. Soc. Rev.* **2012,** *41*, 2912.

[6] S. M. Moghimi, *The FASEB Journal* **2005,** *19*, 311.

[7] D. Peer, J. M. Karp, S. Hong, O. C. Farokhzad, R. Margalit, R. Langer, *Nat. Nanotechnol.* **2007,** *2*, 751.

[8] J. A. Hubbell, A. Chilkoti, *Science* **2012,** *337*, 303.

[9] Y. Barenholz, *J. Controlled Release* **2012,** *160*, 117.

[10] K. Bourzac, *Nature* **2012,** *491*, S58.

[11] T. M. Allen, *Science* **2004,** *303*, 1818.

[12] J. A. Hubbell, *Nature* **2010,** *467*, 1051.

[13] M. A. Mintzer, E. E. Simanek, *Chem. Rev.* **2009,** *109*, 259.

[14] I. Slowing, J. Viveroescoto, C. Wu, V. Lin, *Adv. Drug Delivery Rev.* **2008,** *60*, 1278.

[15] D. J. Irvine, *Nat. Mater.* **2011,** *10*, 342.

[16] Z. Li, J. C. Barnes, A. Bosoy, J. F. Stoddart, J. I. Zink, *Chem. Soc. Rev.* **2012,** *41*, 2590.

[17] Y. Chen, H. Chen, J. Shi, *Expert Opin. Drug Deliv.* **2014,** 1.

[18] C. Argyo, V. Weiss, C. Brauchle, T. Bein, *Chem. Mater.* **2014,** *26*, 435.

Chapter 2 Literature Review

2.1 Introduction

2.1.1 Drug delivery system

Nowadays, the development of medical treatments is driving the evolution of therapeutic agents and also the delivery method. Many drugs can not be administered directly due to their low solubility in water, poor stability in biological systems, short residence time, unspecific toxicity and side effects.[1] A drug delivery system (DDS) is expected to overcome the limitations of 'free' drugs and can be described as a formulation that controls the release rate and period of drug to specific parts in the body. A well-designed DDS is an essential tool for improving current therapies by manipulating the biological profiles of therapeutics, such as pharmacokinetics, biodistribution, tissue uptake, and so on. To this end, the ideal DDS should meet several strict requirements simultaneously: 1) biocompatibility, 2) high loading and protection of the therapeutics, 3) efficient targeting, 4) no premature release, 5) efficient cellular uptake, and 6) controllable release.[2, 3] Therefore, the construct of an effective DDS is one of the major challenges of medicine today.

With the development of nanomaterials and nanotechnology, nanoparticulate drug carriers may provide a solution to the above challenge. Due to the small size of nanoparticles, they can penetrate various physiological barriers and access different tissues, cells and even sub-cellular compartments.[4, 5] Meanwhile, the small size of nanoparticles also lead to a high surface-to-mass ratio, which means they have a large surface area to bind, adsorb and carry drugs, or to conjugate with various functional moieties such as targeting ligands.[6] Furthermore, distinct from most of the molecular delivery system, nanoparticulate carriers can be constructed into a multifunctional platform which can not only co-deliver multiple therapeutic agents but also provide additional theranostic functions, such as diagnostic imaging,

photothermal therapy, and photodynamic therapy. Until now, various types of nanoparticles, such as lipid, polymer, carbon, gold, iron oxide, metal–organic framework, quantum dot, upconversion nanocrystal and silica, have been investigated for drug delivery applications (**Fig. 1**).[7]

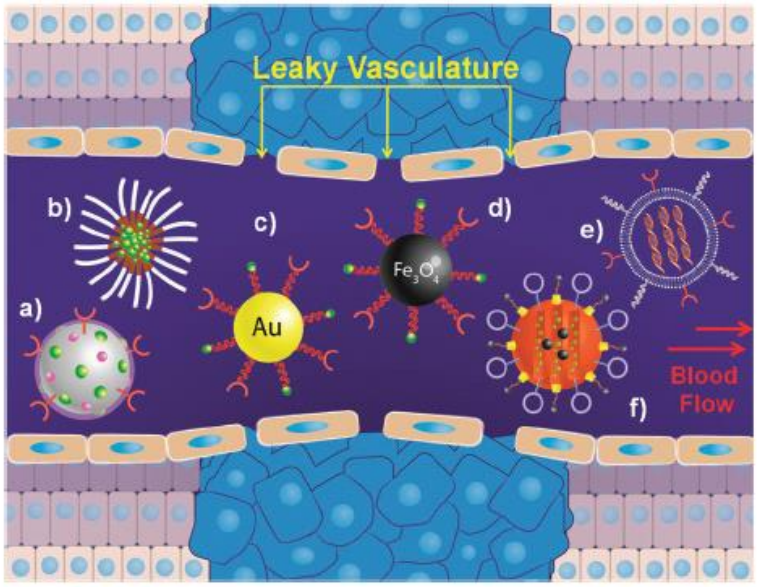

Fig. 1 Various nanoparticulate carriers: (a) polymeric nanogel, (b) polymeric micelle, (c) gold nanoparticle, (d) iron oxide nanoparticle, (e) siRNA in a liposome delivery vector, and (f) a stimuli-responsive capped mesoporous silica nanoparticles. Reproduced from Ref. [7] with permission. Copyright (2012) The Royal Society of Chemistry.

2.1.2 Mesoporous silica nanoparticles

In the last decade, mesoporous silica nanoparticles (MSNs) (**Fig. 2**) have emerged as one of the most promising nanomaterials for drug delivery.[8-11] This is due to their unique flexibility, versatility and stability compared with other platforms. Firstly, the flexible and relatively low-cost fabrication of MSNs is highly suitable for scalable production and clinical translation. Secondly, the structural parameters of MSNs can be tailored in a wide range, such as particle morphologies (sphere, rod, hollow, rattle-type, etc.), particle sizes (20-250 nm), pore structure and pore sizes (2-40 nm). Thirdly, the surface of MSNs can be facilely modified by various organic moieties or conjugated with other nanostructures to satisfy the particular requirements of a specific application. Finally, silica materials are generally biocompatible and could be degraded or excreted from human body eventually.

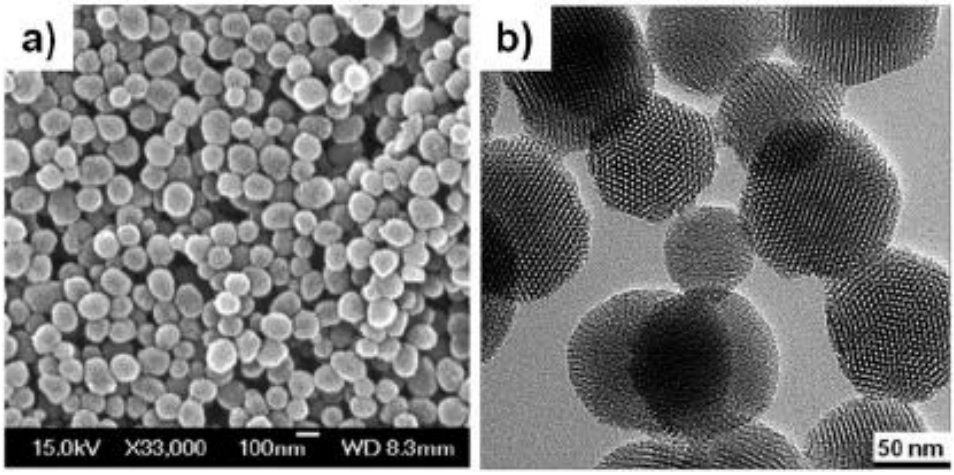

Fig. 2 Typical scanning electron microscopy (SEM) (a) and transmission electron microscopy (TEM) (b) images of MCM-41 mesoporous silica nanoparticles. Reproduced from Ref. [7] with permission. Copyright (2012) The Royal Society of Chemistry.

2.2 Particle synthesis

2.2.1 Synthesis mechanism

Mesoporous materials are classified as having a pore diameter between 2 and 50 nm following the recommendation by International Union of Pure and Applied Chemistry (IUPAC). The first reported and most common class of mesoporous silica materials is Mobil composite material number 41 (MCM-41) developed by the Mobil Oil Company in 1992, which is characterized by a hexagonal array of uniformly sized one-dimensional mesopores.[12] The formation of mesoporous silica materials involves hydrolysis and condensation of silica precursors (e.g., silicic acid, $Si(OH)_4$, or polysilicic acids) in the presence of structure directing agents (SDA), commonly amphiphilic surfactants. In a typical synthesis, the amphiphilic surfactant molecules assemble into complex liquid crystal structures above the critical micelle concentration or through interaction with silica species.[13] Then the silica species concentrate at the hydrophilic interface of SDA through electrostatic attraction or hydrogen bonding and condense to form an amorphous silica framework. The final mesoporous silica product is obtained after the removal of surfactant template by extraction or calcination. **Fig. 3** shows the formation pathways for MCM-41.

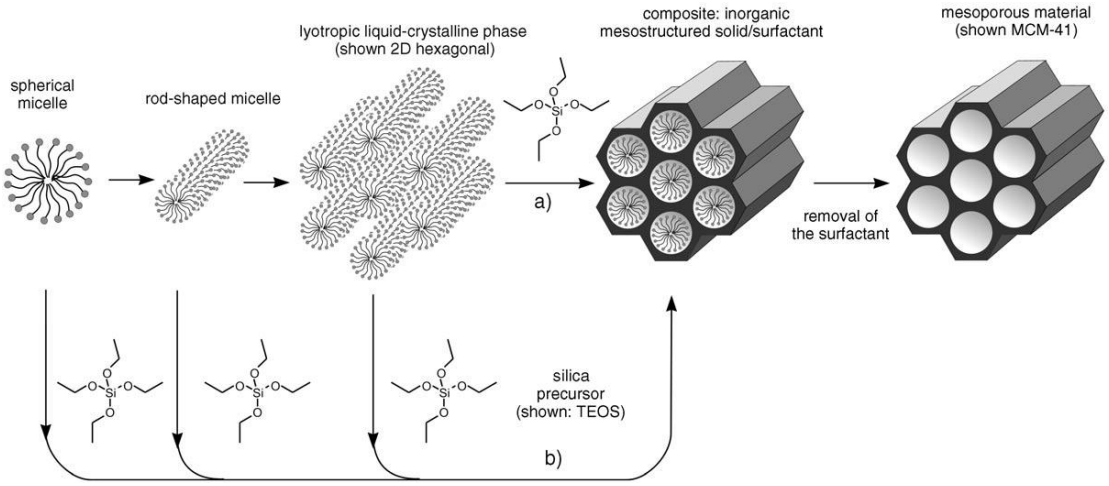

Fig. 3 Formation of mesoporous materials by structure-directing agents: a) true liquid crystal template mechanism, b) cooperative liquid crystal template mechanism. Reproduced from Ref. [13] with permission. Copyright (2006) John Wiley and Sons.

2.2.2 Particle size

In its first introduction, MCM-41 appeared as micrometer-sized, amorphous aggregates. Till now, the modified procedure has enabled the synthesis of MSNs with monodisperse particle size as small as 25 nm.[14] For instance, **Fig. 4** shows that the particle size of mesoporous silica could be adjusted from 30 to 280 nm by controlling the synthesis pH. The drastic reduction in particle size and improvement in size polydispersity facilitate the application of these nanoparticles for biological purposes.[11] The prerequisite for size control of MSNs involves controlling the hydrolysis and condensation rates of the silica sources, which are highly associated with several factors such as reaction pH, silica source, solvent, additives, and temperature.[15] Among various factors, Chiang et al. demonstrated that pH has the largest influence rather than the amount of silica source and reaction time on the control of particle sizes of MSNs.[16]

For drug delivery application, a control over the particle size is important because the size has an influence on the biodistribution,[17] cellular uptake,[18] nucleus entering[19] and biocompatibility[14] of MSNs. For example, in order to achieve passive accumulation of the drug carriers inside tumor tissues via the enhanced permeation and retention (EPR) effect,[20] a particle diameter between 30 nm and 150 nm is desired. It is also found that the uptake of MSNs by HeLa cells is

particle-size-dependent from 30 to 280 nm, and the maximum uptake occurred at the nanoparticle size of 50 nm.[18]

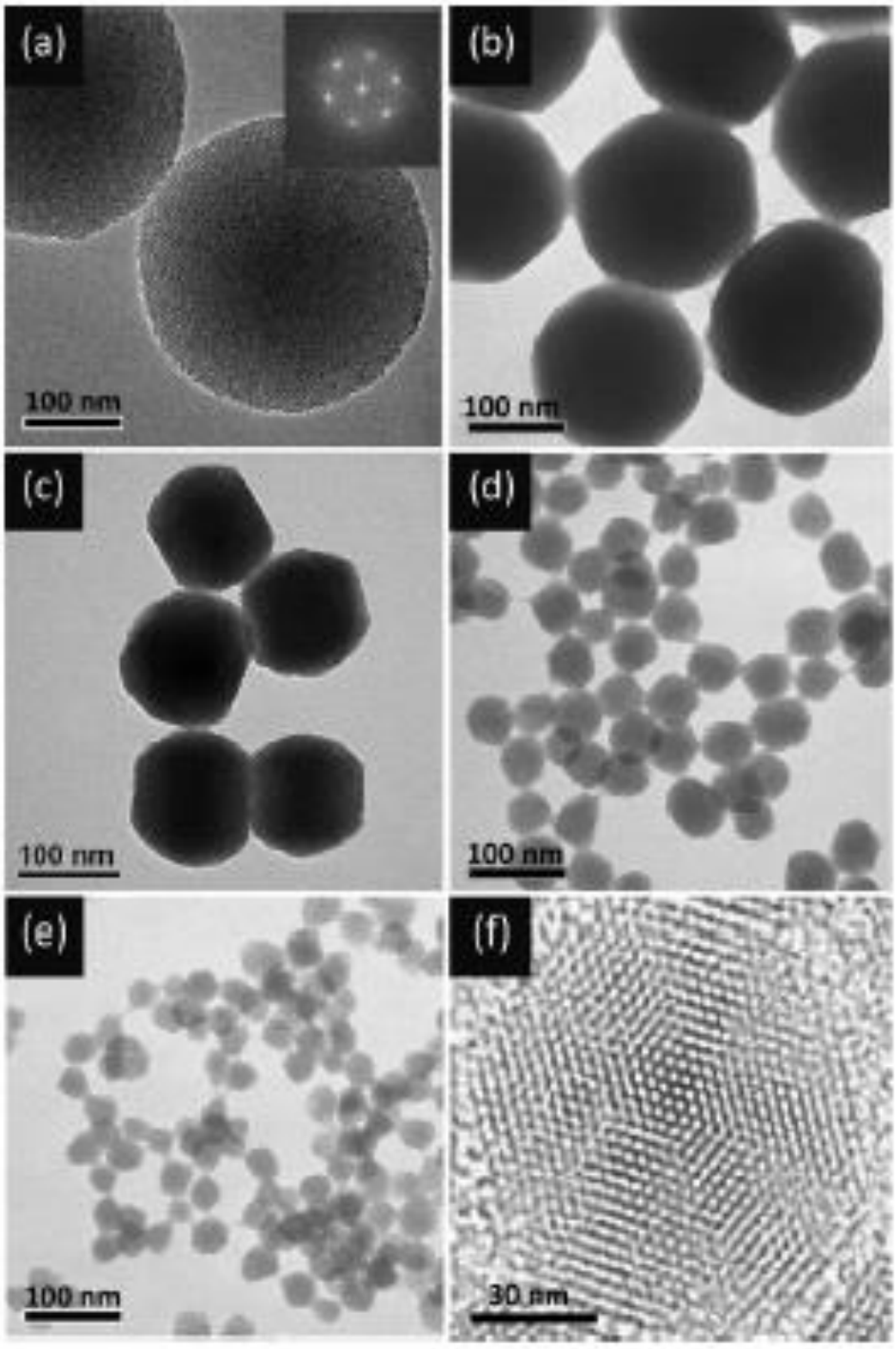

Fig. 4 TEM images of mesoporous silica with different average sizes: a) 280 nm; inset: FFT analysis of the TEM image; b) 170 nm, c) 110 nm, d) 50 nm, e) 30 nm. f) High-resolution TEM image of a single particle in (c). Reproduced from Ref. [18] with permission. Copyright (2009) John Wiley and Sons.

2.2.3 Particle morphology

By tailoring the molar ratio between silica precursors and surfactants, pH control, addition of co-solvents or organic swelling agents, and introduction of organoalkoxysilane precursors during the co-condensation reaction, the particle morphology of MSNs can be varied from sphere, rod, to wormlike structures.[10] Cai and co-workers studied factors affecting the morphology of MCM-41 type MSNs and concluded that the morphology of the particle is determined by the type of catalyst used.[21] More specifically, NH_4OH leads to a rod-like morphology, while NaOH forms short and smaller size micelles, making the particles spherical. Furthermore, hollow MSNs can be fabricated by various templating methods, such as hard-templating,[22] vesicle-templating,[23] microemulsion-templating,[24] and selective etching[25-27]. Recently, more complex structures such as multi-shelled hollow nanospheres,[28] yolk-shell nanoparticles[29], dendric nanoparticles,[30] and Janus-type nanoparticles[31] have also been reported. **Fig. 5** shows the structural development of spherical silica nanoparticles.[32]

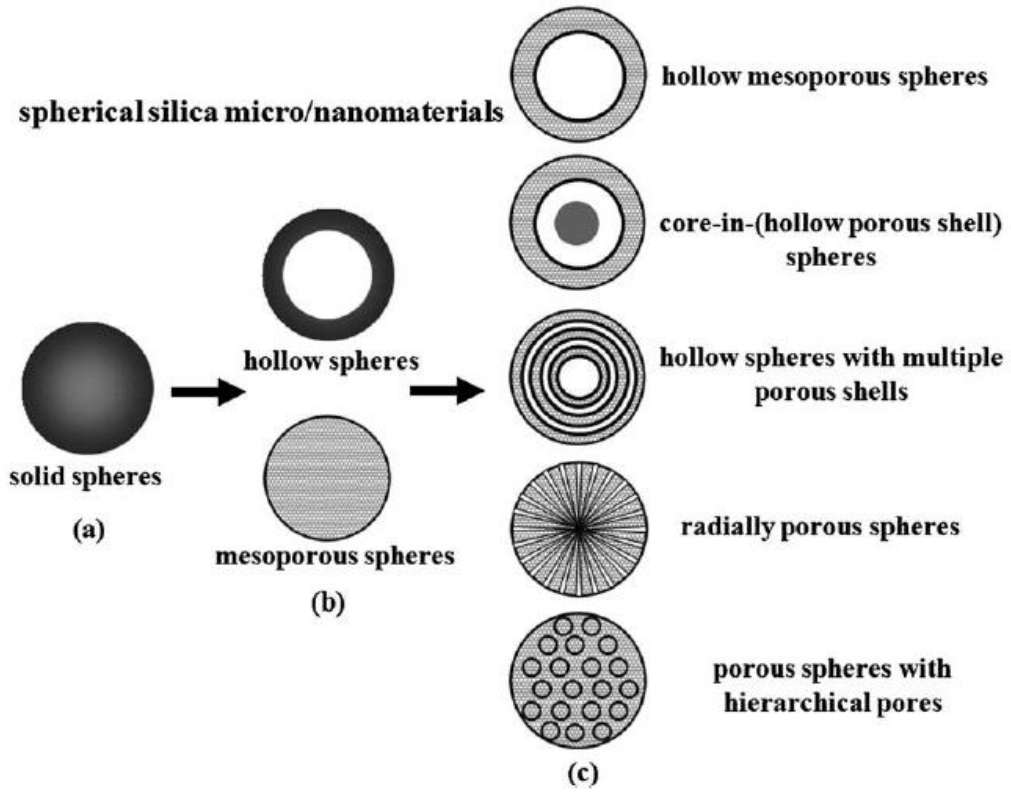

Fig. 5 Structural evolution of spherical silica micro/nanomaterials. Reproduced from Ref. [32] with permission from The Royal Society of Chemistry.

Particle morphology has a great influence on the loading capability of MSNs. Hollow MSNs have been reported to show high loading capacity of anti-cancer drugs and therapeutical proteins.[27, 33] The morphology also affects the cellular uptake and biodistribution of MSNs.[34-36] Tang and co-workers studied the biodistibutions of rod-shaped MSNs with different aspect ratios. They found that short-rod MSNs are easily trapped in the liver, while long-rod MSNs accumulate in the spleen.[36]

2.2.4 Pore size and structure

Pore size is an important factor that affects adsorption and release of guest molecules in porous materials. For instance, it has been reported that increasing the pore diameter of SBA-15 type mesoporous silica from 8.2 to 11.4 nm resulted in the increase of bovine serum albumin loading from 15% to 27%.[37] In other reports, the decreases in pore diameter of MCM-41 or MCM-48 type mesoporous silica led to lower release rates of ibuprofen, erythromycin and other drugs.[38, 39] The commonly used pore template of cetyltrimethylammonium bromide (CTAB) can only produce pore dimensions in the range of 3–4 nm,[6] which could be further reduced after pore surface modification. Although the pore size of bulk mesoporous materials can be readily enlarged by using micelle swelling agent such as trimethylbenzene (TMB), pore size-expansion in nanoparticles is more challenging, as the dilute synthetic conditions often make the swelling agent preferentially dissolved in the solvent rather than in the surfactant micelles. Some researchers have tried to enlarge the pore size of CTAB templated MSNs by adding an excess amount of TMB as compared to CTAB,[40] or by hydrothermal treatment of the dried silica/surfactant composite in the presence of either TMB[41] or surfactants with longer alkyl chains.[42, 43]

Pore structure types, in terms of pore connectivity and geometry, also have an influence on the loading and release properties. To date, different geometrical arrangements (2D-hexagonal, 3D-hexagonal, and cubic,[44] as shown in **Fig. 6**) of pore arrays in MSNs have been obtained by the use of structure-directing agents that self-assemble with silica precursors.[45] It is reported that the interconnected pore

systems provide easier and faster diffusion process than unconnected pore systems.[46]

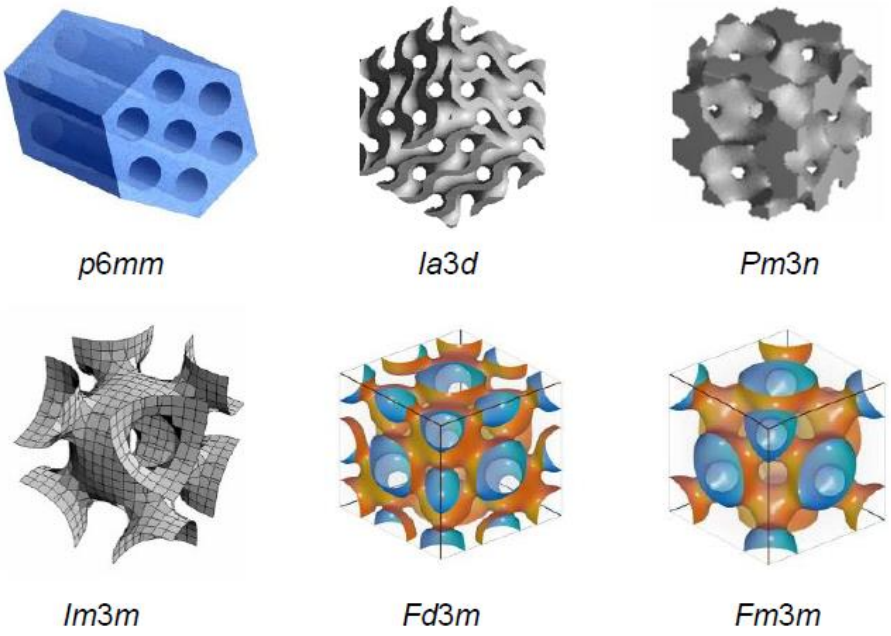

Fig. 6 Pore geometry in mesoporous silica nanoparticles.

2.3 Surface functionalization

Surface functionalization is usually necessary for MSNs because it can endow the nanoparticles with desirable characteristics for delivery application such as improved biocompatibility, dispersibility, targeting specificity, and control of release. [47] Besides, the cellular uptake efficiency and uptake mechanism of the MSNs are also determined by the surface functional groups.[48-50] Till now, the MSNs have been functionalized with various reactive organic groups, such as amine, thiol, vinyl, azide, alkyne and maleimide, which means infinite possibilities for further modification.[51-55]

Depending on the morphology and structure, the MSNs have at least three distinct domains which can be independently functionalized: the particle framework, the external surface of nanoparticles and the surface in the mesopore channels. In general, there are two routes for surface functionalization of MSNs: co-condensation and post-grafting.

2.3.1 Co-condensation

In co-condensation method, the functionalization is carried out during the nanoparticle synthesis. It involves co-condensation of hydrolyzed alkoxysilanes with organoalkoxysilanes in the presence of structure-directing agents and results in functionalized nanoparticles in one pot. Since the organic groups are direct components of the sliane precursor, they are generally more homogeneously distributed in the pore channels and pore blocking is not a problem. However, it is important to note that the organosilane present in the reaction media can disturb the assembly between the surfactant and the hydrolyzed silane, and lead to disordered mesostructure or reduction of pore size in the product. Therefore, the degree of functionalization by co-condensation is affected by the molecular size and the hydrophilic/hydrophobic nature of the organosilane.[51, 56] In addition, the SDA in the as-prepared product has to be removed by extraction, because calcination would remove the organic functional groups as well. Nevertheless, the co-condensation method can also be intentionally used to tune the morphology of MSNs.[57] For instance, a hydrophilic co-condensing agent leads to the formation of small and round particles while hydrophobic one gives rod shape particles.[56] More importantly, condensation reactions with bridged organosilica precursors of the type $(R'O)_3Si\text{-}R\text{-}Si(OR')_3$ can produce the so-called periodic mesoporous organosilica (PMO) materials, which has organic units incorporated in the three-dimensional framework of the silica matrix.[13]

2.3.2 Post-grafting

In post-grafting method, the organic groups are introduced to the surfaces of mesostructured silica matrix after its formation. This process occurs typically by the reaction of free silanol groups on the silica surfaces with organosilanes such as $(R'O)_3SiR$, although other reagents such as chlorosilanes, disilazanes, organolithium and Grignard reagents have also been reported.[58] The functionalization can be carried out either by solution-based reactions or by deposition from the vapor phase. In contrast to co-condensation, the mesostructure and morphology of MSNs can

usually be maintained using this functionalization. On the other side, because the silanols on the external particle surface and at the pore openings are more readily accessible than those inside the pores, post grafting can lead to a non-homogeneous distribution of the organic groups due to the limited diffusion of organosilanes. This preferential functionalization of external surface by post-grafting has been supported by X-ray photoelectron spectroscopy (XPS) results and affects the reaction and adsorption behavior of modified MSNs.[59, 60] The degree of inhomogeneity depends on both the reaction media/solvent and the type of grafting reagent. For example, in the case of grafting with 3-aminopropyltriethoxysilane (APTES), an anhydrous solvent like toluene is usually used because the silanes form clustering in the presence of water and lead to non-uniform distribution.[61] In addition, it was found that grafting silanes of larger size are more likely to be grafted onto external surface sites than smaller ones.[62]

2.3.3 Site-selective functionalization

Functional groups located at different parts of MSNs can affect the delivery performance in different aspects. The functional groups on the external particle surface can influence the biocompatibility, dispersibility and cellular uptake of MSNs, while the functional groups inside the mesopores can tune the loading and releasing of different drugs. Therefore, a site-selective functionalization for different domains of MSNs surface is highly desirable for delivery applications. Selective functionalization can be realized by making variations to the two basic aforementioned methods

A common method for selective functionalization is though post-grafting of organosilanes on mesoporous silica still containing the SDA. Because the pore channels of the as-prepared mesoporous silica are filled with SDA template, the functionalization should occur preferentially on the external surface due to the diffusion limit. Then, after extraction of the SDA, the inner surface can be functionalized separately. However, it should be noted that although this method are usually applicable for micrometer sized mesoporous silica, it is not always

successful for nanometer-sized MSNs. It has been reported that grafting reagents can still diffuse into the inner pores of MSNs even with the presence of SDA as a result of the reduced diffusion barrier of shorter channels.[62, 63]

Selective functionalization was also achieved by a sequential co-condensation approach.[64] In this method, different functionalized triethoxysilanes are added into the particle formation media at specific times of the particle growth. In this way, functional groups can be chosen to be completely dispersed inside the channels, concentrated in parts of the mesopores, or exclusively placed on the external surface as shown in **Fig. 7**. Furthermore, the functional group density can be adjusted by variation of the organosilane-to-silane ratio.

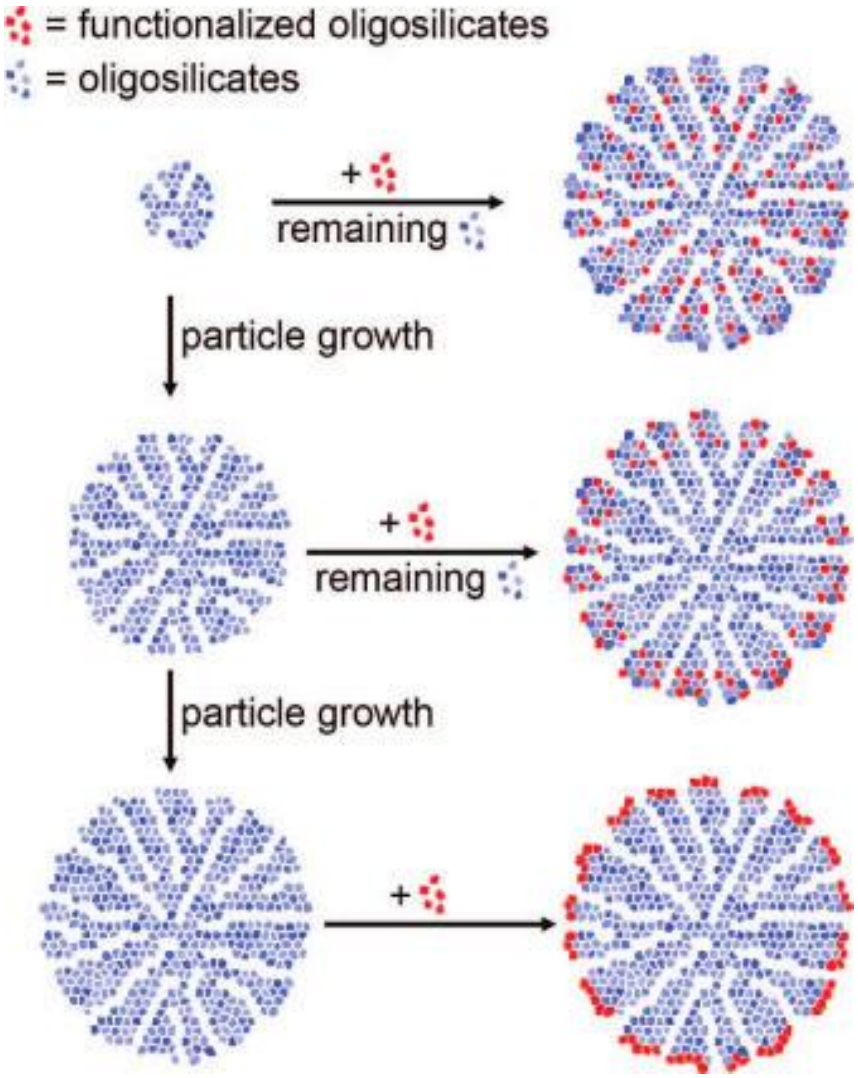

Fig. 7 Site-selective functionalization by sequential co-condensation. Reproduced from Ref. [64] with permission. Copyright (2008) American Chemical Society.

2.4 Drug and gene delivery

Since the first introduction of mesoporous silica materials to drug delivery in the early 2000s,[65] various types of mesoporous silica based delivery systems have been developed so far in order to achieve efficient drug loading, targeted drug delivery, controllable drug release and multi-functional theranostic purpose. **Fig. 8** shows the structure of a typical MSNs-based multifunctional delivery platform. Some important achievements of MSN-based carrier over the last decade are summarized in this section.

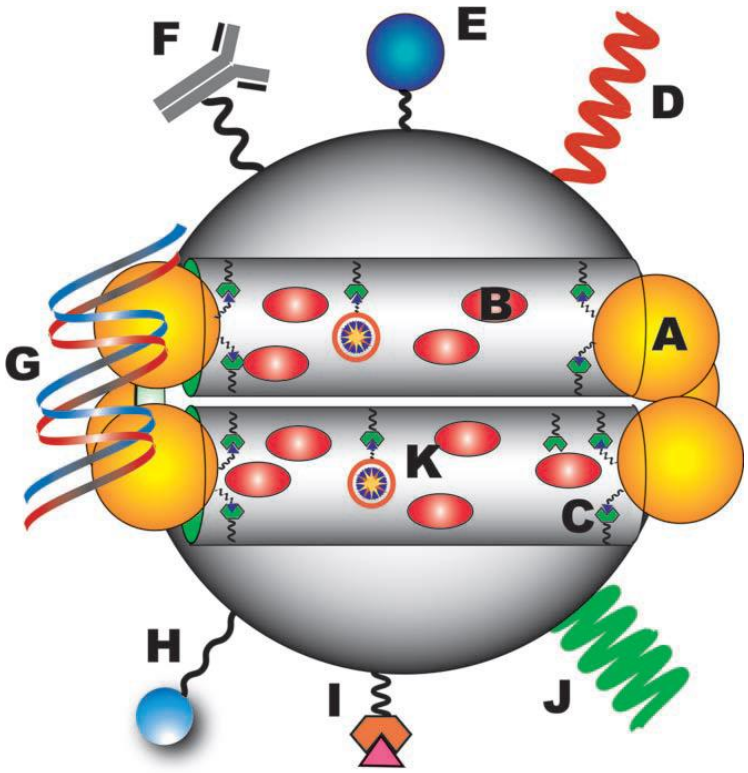

Fig. 8 MSNs as a platform for drug delivery. A) Nanoparticles attached to MSNs as functional gatekeepers. B) Hydrophobic/hydrophilic guest molecules entrapped in the interior of the nanochannels. C) Stimuli-responsive linkers, which chemically attach MSNs and gatekeepers. D) Grafting with a protecting polymer, such as PEG, shields the MSN surface from interacting with opsonizing proteins. E) Bioimaging agents such as magnetic nanoparticles, quantum dots, or fluorophores. F) Targeting ligands such as antibodies. G) Complexation with plasmid DNA. H) Additional ligands such as cell- penetrating peptides. I) Incorporation of a diagnostic label. J) Stimuli-responsive polymers. K) Attachment of functional groups that could modify the metabolism of cells. Reproduced from Ref. [3] with permission. Copyright (2010) John Wiley and Sons.

2.4.1 Drug loading

One of the main advantages of MSNs in delivery application is their capability to carry various therapeutic reagents in large amounts due to their high specific surface areas and pore volumes. The loading cargo can be hydrophilic or hydrophobic in nature and their molecular weight can range from hundreds for small molecular drugs to hundreds of thousands for double-stranded DNA. The loading of therapeutics in MSNs can be can be generally divided into two categories according to the interaction mechanism: non-covalent and covalent.

Non-covalent loading is the most common method to construct a MSN-based delivery system. The cargos are absorbed on the outer surface or into the porous structure of MSNs through Van der Waals forces, hydrogen bonds, or electrostatic attraction. For hydrophilic drugs, the loading is commonly proceeded though adsorption from aqueous solution. In this case, the surface charge of MSNs need to be considered. The point of zero charge for primary silica, i.e. the pH at which the net-surface charge is zero, is about 2-3, due to the presence of surface silanol groups. Thus, primary MSNs are negatively charged under biologically relevant conditions and positively charged drugs such as doxorubicin can be readily absorbed. For negatively charged drugs, a surface modification of MSNs can be carried out to facilitate electrostatic attraction. For example, high amounts of salicylic acid have been absorbed by amine modified mesoporous silica while the primary material show negligible absorption.[66] Due to their structural integrity in organic solvents, the MSNs are especially suitable for loading hydrophobic drugs from nonaqueous media. For the loading process, the solvent can be chosen in a wide range according to the hydrophobic drug, which is usually difficult for organic or polymer carriers.

The other loading mechanism is covalently linking the drug to functional groups present on the MSNs. The unique advantage of covalent loading is that premature drug release can be effectively avoided. However, it is necessary to retain the drug activity after the chemical linkage is cleaved. Furthermore, this loading method is difficult for drugs without linkable groups in their molecular structure.

2.4.2 Targeted delivery

To reduce unspecific toxicity and side effects, great efforts have been made to deliver drugs to the specific abnormal cells. The mesoporous silica based DDS are expected to achieve this goal through the following two methods:

1) Passive targeting. In chemotherapy of cancer, the passive targeting is based on tumor features including leaky blood vessels and poor lymphatic drainage. In contrast to free drugs which diffuse nonspecifically, a nano-sized drug carrier like MSNs can accumulate in the tumor tissues vessels by the enhanced permeability and retention (EPR) effect.[67] The passive targeting ability of MSNs is strongly related to their structural parameters including size and surface chemistry. It is reported that the nanoparticle sizes should be below 400 nm to escape from the leaky vasculature of tumors. Meanwhile, it is also necessary to prevent none-specific protein adsorption to the particles, which would cause rapid clearance of particles by the mononuclear phagocytic system.[68] This means providing MSNs with "stealth" properties need to be achieved by functionalizing the surface with biocompatible polymers, such as polyethylene glycol.[69] Although passive targeting can be achieved to a certain extent, there are limitations to this strategy. For example, some diseases such as blood cancer do not exhibit the EPR effect. Thus, other targeting methods should be developed.

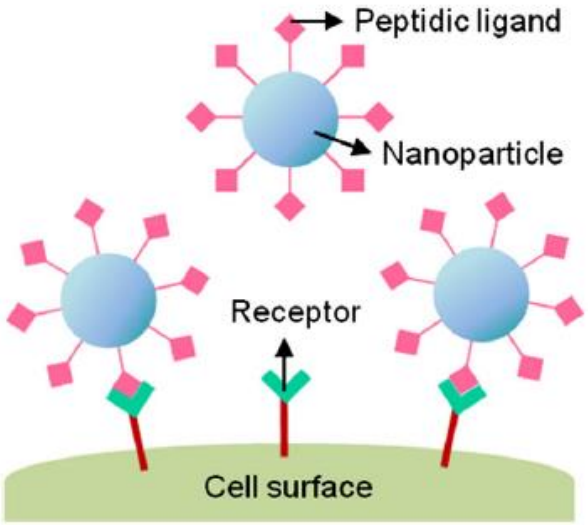

Fig. 9 Schematic illustration of targeted nanoparticles with peptide ligands. Reproduced from Ref. [70] with permission. Copyright (2013) Elsevier.

2) Active targeting. The active targeting strategy is based on the fact that there is distinct differences between defect cells and normal ones. For example, it has been found that some receptors and antigens are over-expressed on the membrane of cancer cells, such as folate receptor, transferrin receptor, and human epidermal growth factor receptors. Therefore, the surface of MSNs can be modified with corresponding ligands that interact with these receptors of particular cells. These targeting ligands promote nanocarrier binding and cell internalization as illustrated in **Fig. 9**. The ligands can be antibodies,[71] aptamers,[72] peptides,[73] or small molecules.[48] It is worthy noting that the targeting objects are not limited to specific cells, but can also be sub-cellular organelles or particular tissue. For example, nuclear-targeting MSNs have been developed by conjugating MSNs with transactivator of transcription (TAT) peptide. The resulted carriers can facilitate the nuclear internalization of loaded anti-cancer drugs through the importin-mediated cytoplasm-nuclear transport and lead to a significant enhanced anticancer activity.[19] More recently, mitochondrial and tumor vascular targeting MSNs were also reported.[74, 75]

2.4.3 Stimuli-responsive delivery

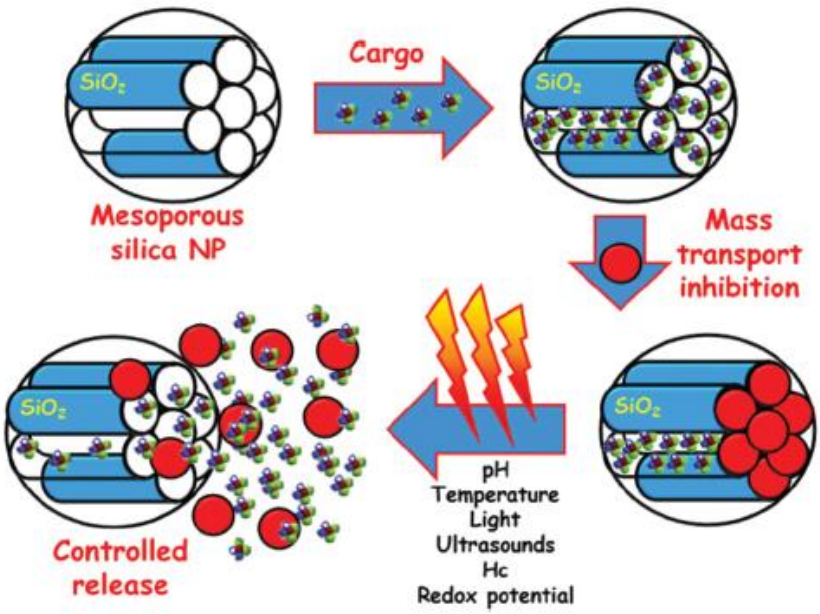

Fig. 10 Schemes of MSNs as stimuli-responsive drug delivery devices. Reproduced from Ref. [69] with permission. Copyright (2013) The Royal Society of Chemistry.

As shown by **Fig. 10**, MSNs can be functionalized with various stimuli-responsive nanovalves or gateskeepers so that the drug release is precisely controlled via different internal and/or external stimuli, such as pH,[76] redox potential,[77] enzyme,[78],metal ion,[79] light,[80] and temperature.[81]

Responsive release based on pH variations has received the greatest attention because pH in the human body varies not only between different organs and tissues but also between normal and defected cells. For example, cancerous and inflammatory tissues (pH $\approx$ 6.8), as well as endosomal and lysosomal cell compartments (pH $\approx$ 5.5), have a more acidic pH than blood or healthy tissues (pH $\approx$ 7.4).[82] As shown in **Fig. 11**, cyclodextrin (CD) and Low-molecular-weight linear polyetherimide (PEI) complexes were utilized by Kim and co-workers to achieve controlled release in an acidic environment. Guest molecules were first loaded into pores and then CD/PEI inclusion complexes were attached onto the surface of MSNs. Due to the bulkiness of these compounds the cargo is protected until polypseudorotaxane is ruptured. Under acidic conditions, the CD complex can be broken and hence release of cargo.[83]

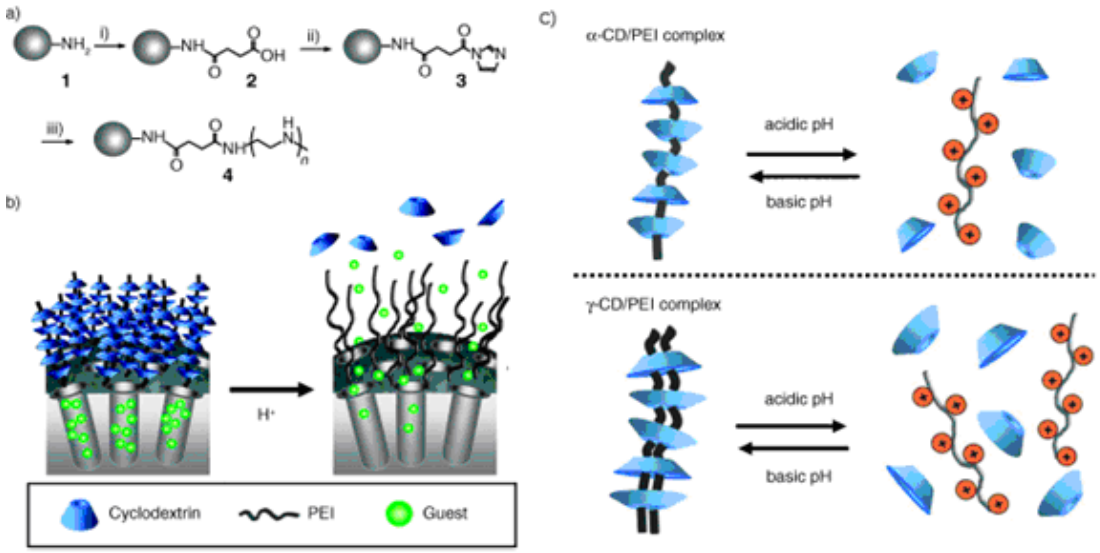

Fig. 11 a) Synthetic route to PEI-functionalized silica particles. b) Schematic of pH-responsive release of guest molecules from mesoporous silica. i) succinic anhydride, triethylamine; ii) 1,1'-carbonyldiimidazole; iii) PEI. c) Schematic illustration of the pH dependence of polypseudorotaxane formation from PEI and CDs. Adapted from Ref. [83] with permission. Copyright (2007) John Wiley and Sons.

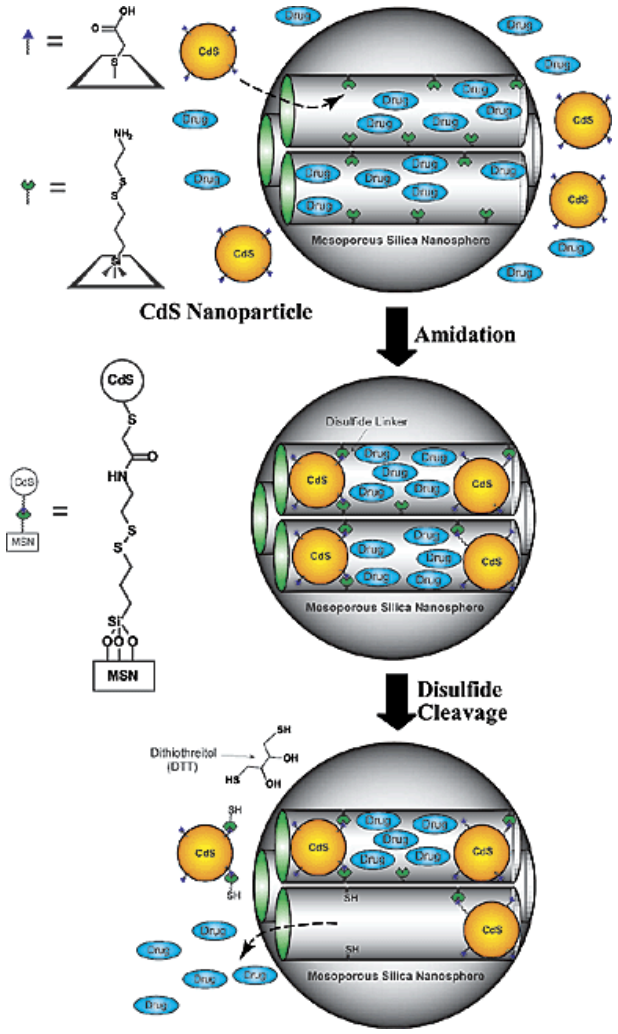

Fig. 12 Schematic representation of the CdS nanoparticle-capped MSN-based drug/neurotransmitter delivery system. Reproduced from Ref. [77] with permission. Copyright (2003) American Chemical Society.

The application of MSNs as redox-responsive DDS was demonstrated on the release of neurotransmitters by using CdS nanoparticles as the chemically removable caps (**Fig. 12**).[77] In this system, the CdS caps were conjugated to MSNs through the disulfide bond and the release of cargo was triggered by reducing agents such as dithiothreitol (DTT) and mercaptoethanol (ME). Because the intracellular glutathione (GSH) levels in most cancer cells are 100–1000-fold higher than the extracellular levels, the naturally occurring redox potentials between the extracellular and the intracellular space can be utilized as an internal stimulus to trigger the cargo release from MSNs.[84] Based on the same strategy, a series of redox-responsive MSN systems were developed by using different gatekeepers, such as Fe_3O_4[85] and Au nanoparticles.[86]

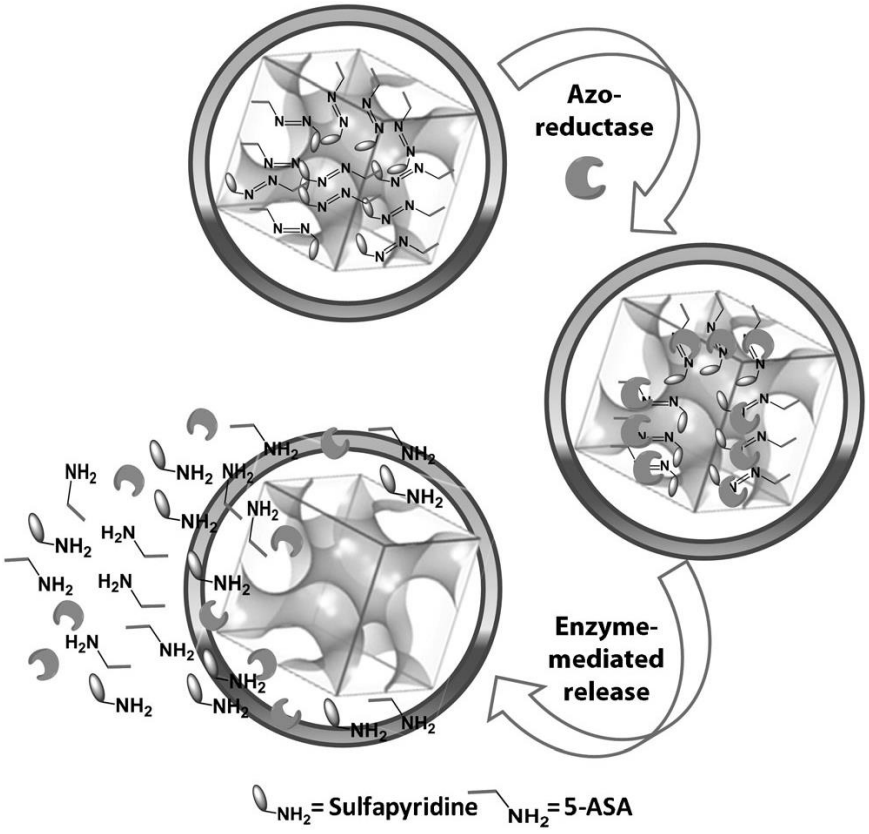

Fig. 13 Enzymatic release of 5-aminosalicylic acid and sulfapyridine from MSNs in the presence of azoreductase. Reproduced from Ref. [78] with permission. Copyright (2012) John Wiley and Sons.

Enzyme responsive nanogating is a very interesting strategy due to the anomalous increase of enzymatic presence or activity in some specific tissues. In a proof-of-concept design as shown by **Fig. 13**, an azo-reductase-responsive delivery system was constructed by covalently bind sulfasalazine, a prodrug for inflammatory bowel disease, to MSNs. The drug was released only inside the colon through interaction with azo-reductase.[78] Other enzyme-responsive examples include biotin-avidin capped MSNs as a protease responsive system[87] and β-D-galactosidase responsive lactose coated MSNs.[88] In addition, Park et al. prepared alpha-amylase and lipase responsive MSNs using β-CD capping enzyme responsive system.[89]

Light responsive drug release also exhibits great potentials because it can be controlled both spatially and temporally. Fujiwara and co-workers reported the first light responsive mesoporous silica material for reversible photo-controlled release.[90] The pore walls of MCM-41 silica was grafted with coumarin, which goes

through reversible intermolecular dimerization under UV light. The dimerization of coumarin under UV light with wavelengths longer than 310 nm yields a cyclobutane product that blocks the mesopores. The exposure to 250 nm UV light cleaves the cyclobutane ring of the coumarin dimer and lead to cargo release. Zink et al. employed photoisomerization of azobenzene to expel luminescent molecules from the nanopores of MSNs by tethering azobenzene molecules to the interior walls of the mesopores.[80] As illustrated by **Fig. 14**, the azobenzene molecules are exited at wavelength around their isosbestic point (400–450 nm). Both the trans-to-cis and cis-to-trans isomerization can be activated, driving the wagging motions of untethered portion of azobenzene molecules. This sweeping motion physically expels the cargo from the confined nanopores of the nanoparticles, thereby acting as sort of a nanoimpeller.

Temperature is another stimulus that can be used to trigger the delivery from MSNs. The conjugation of various thermo-sensitive polymers, such as poly(N-isopropylacrylamide) (PNIPAM) and its derivatives, onto the surface of MSNs have been used for the construction of a thermo-responsive release system.[91] These temperature-sensitive polymers are able to swell or shrink in response to temperature changes, which lead to the open or close of the nanogates.

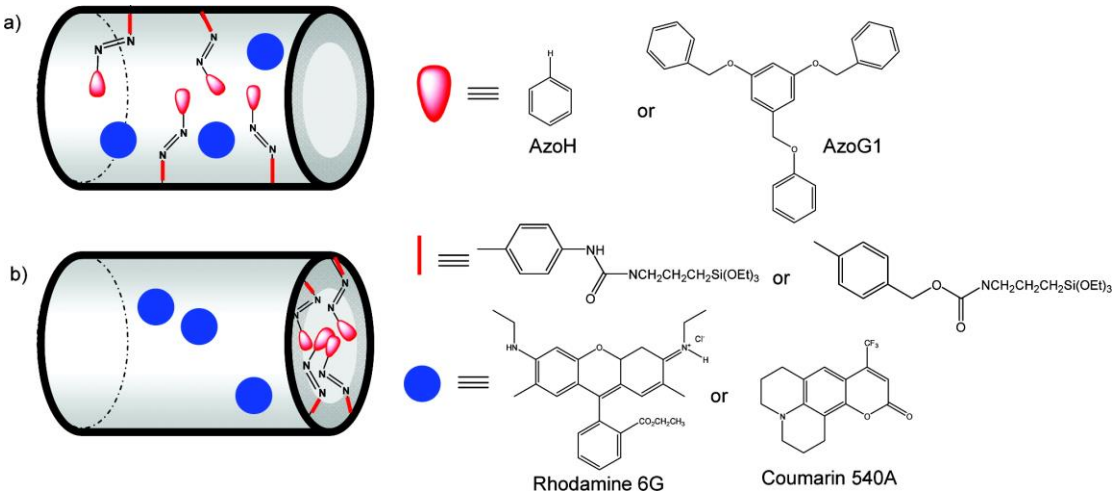

Fig. 14 photo-responsive azobenzene-functionalized silica particles. Reproduced from Ref. [80] with permission. Copyright (2007) American Chemical Society.

2.4.4 Gene delivery

Gene therapy holds promise for the treatment of both acquired and inherited diseases like Alzheimer's disease, cancer, cardiovascular, inflammatory, adenosine deaminase deficiency, and cystic fibrosis. In gene therapy, foreign nucleic acids are delivered into living cells where they can alter gene expression at the transcriptional or post-transcriptional level. Many forms of nucleic acids exist as current and potential therapeutics, such as plasmids, antisense oligonucleotides, ribozymes, DNAzymes, aptamers, and small interfering RNA (siRNA). However, these nucleic acids are large, negatively charged molecules that cannot cross a negatively charged plasma membrane by passive diffusion. Furthermore, they are highly susceptible to enzymatic degradation by serum nuclease. Therefore, the successful gene therapy strongly relies on efficient delivery vehicles.[92, 93] Current gene delivery systems are divided into two major categories: viral and non-viral. Although viral carriers generally exhibit higher efficiency than non-viral ones, they also raise potential risk such as excessive immune response and mutagenesis. On the other hand, non-viral systems have drawn great research interest in recent years due to the ease of preparation and reduced safety concern.[94, 95]

Among various non-viral carriers, silica-based nanocomposites have unique advantages such as well-defined morphology, size, versatile surface functionalization and good biocompatibility.[96-98] Previous researches on silica-based gene delivery carrier fall into two general aspects: surface chemistry and particle structure. For surface chemistry, because the primary silica surface is negatively charged under biologically relevant conditions, the loading of nucleic acids are usually carried out on silica surface modified by various species such as metal ions,[99] amine silane,[95] cationic polymers,[100, 101] and peptides.[102] For particle structure, the silica based gene carriers have evolved from solid spheres to mesoporous nanoparticles, and hierarchical structure like hollow or dendric particles.[41, 100, 103-107] It has been proven that porous silica with large mesopore sizes (>10 nm) are more favourable for loading nucleic acids than those with small pores (<5 nm).[41, 99, 104, 105, 107]

2.4.5 Co-delivery of multiple cargos

For the treatment of many diseases (in particular cancer, cardiovascular diseases, neurological disorders, malaria, and acquired immune deficiency syndrome), it is desirable to deliver a combination of different drugs to maximize therapeutic effect and reduce drug resistance.[108] The structure and surface chemistry of MSNs can be optimized for co-delivery of various new drugs with diverse physicochemical properties.

For diabetic treatment, Lin and co-workers developed boronic acid-functionalized MSNs for controlled release of both insulin and cyclic adenosine monophosphate (cAMP). Gluconic acid-modified insulin proteins (G-Ins) were immobilized on the exterior surface of MSN through glucose-responsive boronic ester bond and also served as caps to encapsulate cAMP molecules inside the mesopores of MSNs. The introduction of saccharides triggered the release of both G-Ins and cAMP. The system is superior than the conventional glucose-responsive insulin delivery systems in that the decrease of insulin release with cycles can be balanced by the release of cAMP from the mesopores.[109]

Co-delivery by MSNs has also been explored for cancer therapy. He and co-workers encapsulated an anticancer drug doxorubicin (Dox) inside the mesopores of MSNs and modified the MSNs with polyamidoamine (PAMAM) dendrimers. The dendrimers further complexed with siRNAs targeted against mRNA encoding Bcl-2 protein, which is the main player for nonpump resistance. The anticancer efficacy of Dox co-delivered with siRNA increased 132 times compared to free Dox, mainly because the simultaneously delivered siRNA significantly suppressed the Bcl-2 mRNA, and efficiently overcome the nonpump resistance.[110]

2.4.6 Multi-functional delivery system

Instead of just being a drug/gene carrier, mesoporous silica nanoparticles can be combined with other functional species to form multi-functional nanocomposites for diagnosis and therapy purpose. For example, mesoporous silica nanocomposites with magnetic and/or luminescent components represent the most widely reported

multifunctional theranostic agents. Luminescent materials (such as organic dyes, quantum dots, and rare-earth nanophosphors) or magnetic nanoparticles have been successfully combined with the mesoporous silica in the form of covalent linkage, core–shell, embedded or rattle-type structures as shown in **Fig. 15**.[111] These strategies to fuse luminescence and magnetism into one mesoporous silica matrix enable a multifunctional carrier by which therapeutic and diagnostic capabilities are achieved at the same time.

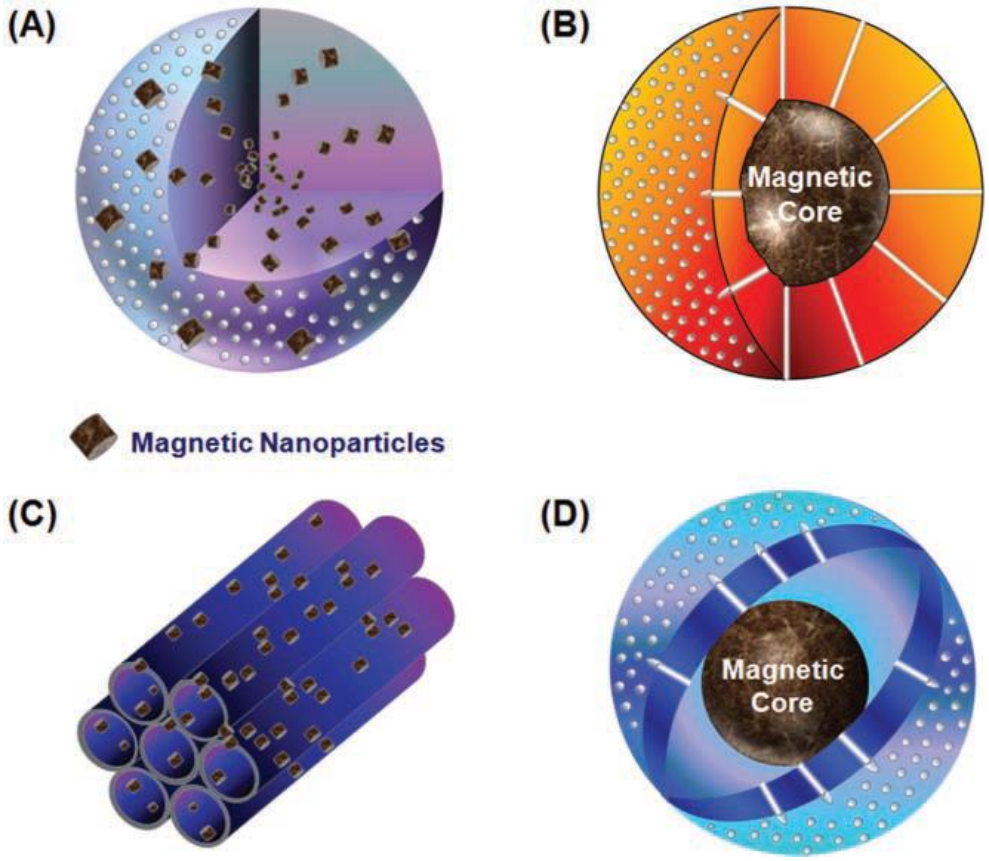

Fig. 15 Magnetic nanoparticle/ mesoporous silica nanocomposites: A) mesoporous silica spheres embedding monodisperese magnetic nanocrystals, B) microspheres encapsulating magnetic cores into perpendicularly aligned mesoporous shells, C) ordered mesoporous materials loaded with magnetic nanoparticles inside the porous channels or cages, and D) rattle-type magnetic nanocomposites. Reproduced from Ref. [112] with permission. Copyright (2011) John Wiley and Sons.

2.4.7 Biocompatibility

A critical issue for any drug delivery system is its biocompatibility. Silica is viewed as low toxicity and has been classified as a generally recognized as safe material (GRAS)

by the U.S. Food and Drug Administration (FDA).[113] However, the potential toxicity and hazardous effects of nanosized MSNs still need more detailed investigation, especially the long term fate in vivo. Several reports have proven the degradation of mesoporous silica materials in vitro.[114] Furthermore, the excretion of silica species via urinary and hepatobiliary system has been observed in vivo after intravenous injection.[17, 36] However, due to the varied structure of mesoporous silica materials and the different synthesis processes, there is still no consensus in the toxicity of MSNs.[11] The toxicity of MSNs can be influenced by various factors including particle size,[115] surface modification,[114] porous structure,[14] dosage,[116] cell types,[117] injection methods[118] *etc*.. A viewpoint is that toxicity is related partly to surface silanol groups,[119] which can interact with membrane components by hydrogen bond or with the positively charged tetraalkylammonium-containing phospholipids by electrostatic force.

2.5 Summary

Mesoporous silica nanoparticles have risen as a potential multifunctional drug/gene delivery platform to enhance therapeutic efficacy and reduce side effects. However, as a new application in nanomedicine, the MSN-based delivery systems still face two major challenges at the present stage:

1) Loading and delivery of large biomolecules. With the fast development of biomedicine, proteins (enzymes, antibodies) and genes (DNA, RNA) have emerged as new therapeutic agents and required effective delivery vehicle.[120, 121] These biomolecules are much larger in size than common small molecule drugs. However, in most previously reported MSNs, the pore sizes are usually too small (< 5 nm) to encapsulate large biomolecules. Meanwhile, most of the studied MSNs for delivery application are of the MCM41-type with hexagonal pore array, which lacks structure flexibility to simultaneously accommodate multiple different cargos. Thus, the particle and pore structure of MSNs need to be further optimized for loading and delivery of large therapeutic agents.

2) Targeted delivery and controlled release. Although intensive research efforts have been made to achieve targeted delivery and controlled release by surface functionalization of MSNs, the reported functionalization strategies often suffer form different drawbacks. A prominent issue is the cost of functionalization over the benefits.[122] Many functionalization methods involve the usage of expensive biomolecules and complex synthesis procedure, which not only increase the fabrication cost of the whole delivery system but also bring in additional toxicity/biocompatibility concern and regulatory hurdles. Besides, in many earlier designs, the controlled release usually lies at a conceptual level. For instance, some stimuli-responsive systems have gating features in non-aqueous solvents, or employ external stimuli such as UV light that is not suitable for physiological environment.[88] Therefore, the surface functionalization of MSNs still need to be explored to achieve targeted delivery and controlled release in an economic, safe and realistic way.

To meet the above the above challenges, the researches in this thesis have been focused on the following two aspects:

1) Novel silica nanostructure for gene delivery. In chapter 3, we systematically investigated the synthesis of stellate mesoporous silica nanoparticles, which have radial pore sizes up to 20 nm. In chapter 5, we further incorporated this radial pore structure into magnetic core-shell nanoparticles and applied them for siRNA delivery. In chapter 6, we developed bowl-like mesoporous organosilica nanoparticles with large central cavities for DNA delivery.

2) Simple and effective silica functionalization for delivery purpose. In chapter 3, we functionalized the silica nanoparticles with low molecular weight poly(ethyleneimine) and studied its effect on drug delivery. In chapter 4, we fabricated a cancer-cell-specific nuclear-targeted nanocarrier by modifying the silica nanoparticles simultaneously with two targeting ligands, folic acid and dexamethasone, both of which are FDA approved molecules. In chapter 5, we developed a pH-responsive capping for magnetic silica nanoparticles. The capping was prepared by a facile one-pot coating of tannic acid, which is a natural polymer and generally recognized as safe by FDA.

2.6 References

[1] C. E. Ashley, E. C. Carnes, G. K. Phillips, D. Padilla, P. N. Durfee, P. A. Brown, T. N. Hanna, J. Liu, B. Phillips, M. B. Carter, N. J. Carroll, X. Jiang, D. R. Dunphy, C. L. Willman, D. N. Petsev, D. G. Evans, A. N. Parikh, B. Chackerian, W. Wharton, D. S. Peabody, C. J. Brinker, *Nat Mater* **2011,** *10*, 389.

[2] D. J. Irvine, *Nat. Mater.* **2011,** *10*, 342.

[3] J. L. Vivero-Escoto, I. I. Slowing, B. G. Trewyn, V. S. Y. Lin, *Small* **2010,** *6*, 1952.

[4] W. H. De Jong, P. J. Borm, *Int. J. Nanomedicine* **2008,** *3*, 133.

[5] J. A. Hubbell, A. Chilkoti, *Science* **2012,** *337*, 303.

[6] J. M. Rosenholm, C. Sahlgren, M. Lindén, *Nanoscale* **2010,** *2*, 1870.

[7] Z. Li, J. C. Barnes, A. Bosoy, J. F. Stoddart, J. I. Zink, *Chem. Soc. Rev.* **2012,** *41*, 2590.

[8] I. I. Slowing, B. G. Trewyn, S. Giri, V. S. Y. Lin, *Adv. Funct. Mater.* **2007,** *17*, 1225.

[9] Q. He, J. Shi, *J. Mater. Chem.* **2011,** *21*, 5845.

[10] F. Tang, L. Li, D. Chen, *Adv. Mater.* **2012,** *24*, 1504.

[11] D. Tarn, C. E. Ashley, M. Xue, E. C. Carnes, J. I. Zink, C. J. Brinker, *Acc. Chem. Res.* **2013,** *46*, 792.

[12] C. T. Kresge, M. E. Leonowicz, W. J. Roth, J. C. Vartuli, J. S. Beck, *Nature* **1992,** *359*, 710.

[13] F. Hoffmann, M. Cornelius, J. Morell, M. Fröba, *Angew. Chem., Int. Ed.* **2006,** *45*, 3216.

[14] Y.-S. Lin, C. L. Haynes, *J. Am. Chem. Soc.* **2010,** *132*, 4834.

[15] K. C. W. Wu, Y. Yamauchi, *J. Mater. Chem.* **2012,** *22*, 1251.

[16] Y.-D. Chiang, H.-Y. Lian, S.-Y. Leo, S.-G. Wang, Y. Yamauchi, K. C. W. Wu, *The Journal of Physical Chemistry C* **2011,** *115*, 13158.

[17] Q. He, Z. Zhang, F. Gao, Y. Li, J. Shi, *Small* **2011,** *7*, 271.

[18] F. Lu, S.-H. Wu, Y. Hung, C.-Y. Mou, *Small* **2009,** *5*, 1408.

[19] L. Pan, Q. He, J. Liu, Y. Chen, M. Ma, L. Zhang, J. L. Shi, *J. Am. Chem. Soc.* **2012,** *134*, 5722.

[20] Q. He, J. L. Shi, *Adv. Mater.* **2014,** *26*, 391.

[21] Q. Cai, Z.-S. Luo, W.-Q. Pang, Y.-W. Fan, X.-H. Chen, F.-Z. Cui, *Chem. Mater.* **2001,** *13*, 258.

[22] W. Zhao, M. Lang, Y. Li, L. Li, J. Shi, *J. Mater. Chem.* **2009,** *19*, 2778.

[23] H. Djojoputro, X. F. Zhou, S. Z. Qiao, L. Z. Wang, C. Z. Yu, G. Q. Lu, *J. Am. Chem. Soc.* **2006,** *128*, 6320.

[24] Y.-S. Lin, S.-H. Wu, C.-T. Tseng, Y. Hung, C. Chang, C.-Y. Mou, *Chem. Commun.* **2009,** 3542.

[25] T. Zhang, J. Ge, Y. Hu, Q. Zhang, S. Aloni, Y. Yin, *Angew. Chem., Int. Ed.* **2008,** *47*, 5806.

[26] A. Yildirim, M. Bayindir, *J. Mater. Chem. A* **2015,** *3*, 3839.

[27] Y. Chen, H. Chen, L. Guo, Q. He, F. Chen, J. Zhou, J. Feng, J. Shi, *ACS Nano* **2010,** *4*, 529.

[28] J. Liu, S. B. Hartono, Y. G. Jin, Z. Li, G. Q. Lu, S. Z. Qiao, *J. Mater. Chem.* **2010,** *20*, 4595.

[29] J. Liu, H. Q. Yang, F. Kleitz, Z. G. Chen, T. Yang, E. Strounina, G. Q. M. Lu, S. Z. Qiao, *Adv. Funct. Mater.* **2012,** *22*, 591.

[30] X. Du, S. Z. Qiao, *Small* **2015,** *11*, 392.

[31] X. Li, L. Zhou, Y. Wei, A. M. El-Toni, F. Zhang, D. Y. Zhao, *J. Am. Chem. Soc.* **2014,** *136*, 15086.

[32] X. Du, J. He, *Nanoscale* **2011,** *3*, 3984.

[33] J. Zhang, S. Karmakar, M. Yu, N. Mitter, J. Zou, C. Z. Yu, *Small* **2014,** *10*, 5068.

[34] X. Huang, X. Teng, D. Chen, F. Tang, J. He, *Biomaterials* **2010,** *31*, 438.

[35] B. G. Trewyn, J. A. Nieweg, Y. Zhao, V. S. Y. Lin, *Chem. Eng. J. (Lausanne)* **2008,** *137*, 23.

[36] X. Huang, L. Li, T. Liu, N. Hao, H. Liu, D. Chen, F. Tang, *ACS Nano* **2011,** *5*, 5390.

[37] M. Vallet-Reg ί, F. Balas, M. Colilla, M. Manzano, *Prog. Solid State Chem.* **2008,**

36, 163.

[38] P. Horcajada, A. Rámila, J. Pérez-Pariente, M. Vallet-Regí, *Microporous Mesoporous Mater.* **2004,** *68*, 105.

[39] I. Izquierdo-Barba, Á. Martinez, A. L. Doadrio, J. Pérez-Pariente, M. Vallet-Regí, *Eur. J. Pharm. Sci.* **2005,** *26*, 365.

[40] I. I. Slowing, B. G. Trewyn, V. S. Y. Lin, *J. Am. Chem. Soc.* **2007,** *129*, 8845.

[41] M.-H. Kim, H.-K. Na, Y.-K. Kim, S.-R. Ryoo, H. S. Cho, K. E. Lee, H. Jeon, R. Ryoo, D.-H. Min, *ACS Nano* **2011,** *5*, 3568.

[42] M. Mizutani, Y. Yamada, K. Yano, *Chem. Commun.* **2007,** 1172.

[43] M. Mizutani, Y. Yamada, T. Nakamura, K. Yano, *Chem. Mater.* **2008,** *20*, 4777.

[44] N. Lai, C. Lin, P. Ku, L. Chang, K. Liao, W. Lin, C. Yang, *Nano Research* **2014,** *7*, 1439.

[45] N. Z. Knezevic, E. Ruiz-Hernandez, W. E. Hennink, M. Vallet-Regi, *RSC Advances* **2013,** *3*, 9584.

[46] A. Popat, J. Liu, Q. Hu, M. Kennedy, B. Peters, G. Q. Lu, S. Z. Qiao, *Nanoscale* **2012,** *4*, 970.

[47] J. Lu, M. Liong, J. I. Zink, F. Tamanoi, *Small* **2007,** *3*, 1341.

[48] I. Slowing, B. G. Trewyn, V. S. Lin, *J. Am. Chem. Soc.* **2006,** *128*, 14792.

[49] R. Guillet-Nicolas, A. Popat, J. L. Bridot, G. Monteith, S. Z. Qiao, F. Kleitz, *Angew Chem Int Ed Engl* **2013,** *52*, 2318.

[50] C. E. Ashley, E. C. Carnes, G. K. Phillips, D. Padilla, P. N. Durfee, P. A. Brown, T. N. Hanna, J. Liu, B. Phillips, M. B. Carter, N. J. Carroll, X. Jiang, D. R. Dunphy, C. L. Willman, D. N. Petsev, D. G. Evans, A. N. Parikh, B. Chackerian, W. Wharton, D. S. Peabody, C. J. Brinker, *Nat. Mater.* **2011,** *10*, 389.

[51] T. Suteewong, H. Sai, R. Cohen, S. Wang, M. Bradbury, B. Baird, S. M. Gruner, U. Wiesner, *J. Am. Chem. Soc.* **2011,** *133*, 172.

[52] A. Maria Chong, X. Zhao, A. T. Kustedjo, S. Qiao, *Microporous Mesoporous Mater.* **2004,** *72*, 33.

[53] Q. Yang, S. Wang, P. Fan, L. Wang, Y. Di, K. Lin, F.-S. Xiao, *Chem. Mater.* **2005,** *17*, 5999.

[54] R. Vathyam, E. Wondimu, S. Das, C. Zhang, S. Hayes, Z. Tao, T. Asefa, *The Journal of Physical Chemistry C* **2011,** *115*, 13135.

[55] H. Meng, W. X. Mai, H. Zhang, M. Xue, T. Xia, S. Lin, X. Wang, Y. Zhao, Z. Ji, J. I. Zink, A. E. Nel, *ACS Nano* **2013,** *7*, 994.

[56] A. Popat, S. B. Hartono, F. Stahr, J. Liu, S. Z. Qiao, G. Qing Max Lu, *Nanoscale* **2011,** *3*, 2801.

[57] S. Huh, J. W. Wiench, J.-C. Yoo, M. Pruski, V. S. Y. Lin, *Chem. Mater.* **2003,** *15*, 4247.

[58] D. Bruhwiler, *Nanoscale* **2010,** *2*, 887.

[59] M. H. Lim, A. Stein, *Chem. Mater.* **1999,** *11*, 3285.

[60] T. Yokoi, H. Yoshitake, T. Tatsumi, *J. Mater. Chem.* **2004,** *14*, 951.

[61] Y. Inaki, Y. Kajita, H. Yoshida, K. Ito, T. Hattori, *Chem. Commun.* **2001,** 2358.

[62] N. Gartmann, D. Brühwiler, *Angew. Chem., Int. Ed.* **2009,** *48*, 6354.

[63] A. B. Bourlinos, T. Karakostas, D. Petridis, *The Journal of Physical Chemistry B* **2003,** *107*, 920.

[64] J. Kecht, A. Schlossbauer, T. Bein, *Chem. Mater.* **2008,** *20*, 7207.

[65] M. Vallet-Regi, A. Ramila, R. P. del Real, J. Pérez-Pariente, *Chem. Mater.* **2001,** *13*, 308.

[66] J. M. Rosenholm, M. Lindén, *J. Controlled Release* **2008,** *128*, 157.

[67] D. Peer, J. M. Karp, S. Hong, O. C. Farokhzad, R. Margalit, R. Langer, *Nat. Nanotechnol.* **2007,** *2*, 751.

[68] M. Ferrari, *Nat. Nanotechnol.* **2008,** *3*, 131.

[69] M. Colilla, B. Gonzalez, M. Vallet-Regi, *Biomaterials Science* **2013,** *1*, 114.

[70] Y. Yun, Y. W. Cho, K. Park, *Adv. Drug Delivery Rev.* **2013,** *65*, 822.

[71] C.-P. Tsai, C.-Y. Chen, Y. Hung, F.-H. Chang, C.-Y. Mou, *J. Mater. Chem.* **2009,** *19*, 5737.

[72] X. He, Y. Zhao, D. He, K. Wang, F. Xu, J. Tang, *Langmuir* **2012,** *28*, 12909.

[73] L. Pan, J. Liu, Q. He, J. L. Shi, *Adv. Mater.* **2014,** *26*, 6742.

[74] Y. Zhang, Z. Hu, G. Xu, C. Gao, R. a. Wu, H. Zou, *Nano Research* **2014,** *7*, 1103.

[75] Y. Chen, P. Xu, H. Chen, Y. Li, W. Bu, Z. Shu, Y. Li, J. Zhang, L. Zhang, L. Pan, X. Cui, Z. Hua, J. Wang, L. Zhang, J. L. Shi, *Adv. Mater.* **2013,** *25*, 3100.

[76] A. Popat, J. Liu, G. Q. Lu, S. Z. Qiao, *J. Mater. Chem.* **2012,** *22*, 11173.

[77] C.-Y. Lai, B. G. Trewyn, D. M. Jeftinija, K. Jeftinija, S. Xu, S. Jeftinija, V. S. Y. Lin, *J. Am. Chem. Soc.* **2003,** *125*, 4451.

[78] A. Popat, B. P. Ross, J. Liu, S. Jambhrunkar, F. Kleitz, S. Z. Qiao, *Angew. Chem., Int. Ed.* **2012,** *51*, 12486.

[79] Z. Zhang, D. Balogh, F. Wang, I. Willner, *J. Am. Chem. Soc.* **2013,** *135*, 1934.

[80] S. Angelos, E. Choi, F. Vögtle, L. De Cola, J. I. Zink, *The Journal of Physical Chemistry C* **2007,** *111*, 6589.

[81] Z. Y. Zhou, S. M. Zhu, D. Zhang, *J. Mater. Chem.* **2007,** *17*, 2428.

[82] L. E. Gerweck, K. Seetharaman, *Cancer Res.* **1996,** *56*, 1194.

[83] C. Park, K. Oh, S. C. Lee, C. Kim, *Angew. Chem., Int. Ed.* **2007,** *46*, 1455.

[84] G. Saito, J. A. Swanson, K.-D. Lee, *Adv. Drug Delivery Rev.* **2003,** *55*, 199.

[85] S. Giri, B. G. Trewyn, M. P. Stellmaker, V. S. Y. Lin, *Angew. Chem., Int. Ed.* **2005,** *44*, 5038.

[86] F. Torney, B. G. Trewyn, V. S. Y. Lin, K. Wang, *Nat. Nanotechnol.* **2007,** *2*, 295.

[87] A. Schlossbauer, J. Kecht, T. Bein, *Angew. Chem., Int. Ed.* **2009,** *48*, 3092.

[88] A. Bernardos, E. Aznar, M. D. Marcos, R. Martínez-Máñez, F. Sancenón, J. Soto, J. M. Barat, P. Amorós, *Angew. Chem., Int. Ed.* **2009,** *48*, 5884.

[89] C. Park, H. Kim, S. Kim, C. Kim, *J. Am. Chem. Soc.* **2009,** *131*, 16614.

[90] N. K. Mal, M. Fujiwara, Y. Tanaka, *Nature* **2003,** *421*, 350.

[91] Y. Zhu, S. Kaskel, T. Ikoma, N. Hanagata, *Microporous Mesoporous Mater.* **2009,** *123*, 107.

[92] M. A. Mintzer, E. E. Simanek, *Chem. Rev.* **2009,** *109*, 259.

[93] V. Sokolova, M. Epple, *Angew. Chem., Int. Ed.* **2008,** *47*, 1382.

[94] C. Kneuer, M. Sameti, U. Bakowsky, T. Schiestel, H. Schirra, H. Schmidt, C.-M. Lehr, *Bioconjugate Chem.* **2000,** *11*, 926.

[95] D. J. Bharali, I. Klejbor, E. K. Stachowiak, P. Dutta, I. Roy, N. Kaur, E. J. Bergey, P. N. Prasad, M. K. Stachowiak, *Proc. Natl. Acad. Sci. U. S. A.* **2005,**

102, 11539.

[96] D. Luo, W. M. Saltzman, *Gene Ther.* **2005,** *13*, 585.

[97] I. Slowing, J. Viveroescoto, C. Wu, V. Lin, *Adv. Drug Delivery Rev.* **2008,** *60*, 1278.

[98] C. Hom, J. Lu, F. Tamanoi, *J. Mater. Chem.* **2009,** *19*, 6308.

[99] S. M. Solberg, C. C. Landry, *J. Phys. Chem. B* **2006,** *110*, 15261.

[100] D. R. Radu, C.-Y. Lai, K. Jeftinija, E. W. Rowe, S. Jeftinija, V. S. Y. Lin, *J. Am. Chem. Soc.* **2004,** *126*, 13216.

[101] T. Xia, M. Kovochich, M. Liong, H. Meng, S. Kabehie, S. George, J. I. Zink, A. E. Nel, *ACS Nano* **2009,** *3*, 3273.

[102] D. Brevet, O. Hocine, A. Delalande, L. Raehm, C. Charnay, P. Midoux, J.-O. Durand, C. Pichon, *Int. J. Pharm.* **2014,** *471*, 197.

[103] X.-x. He, K. Wang, W. Tan, B. Liu, X. Lin, C. He, D. Li, S. Huang, J. Li, *J. Am. Chem. Soc.* **2003,** *125*, 7168.

[104] F. Gao, P. Botella, A. Corma, J. Blesa, L. Dong, *J. Phys. Chem. B* **2009,** *113*, 1796.

[105] X. Du, B. Shi, J. Liang, J. Bi, S. Dai, S. Z. Qiao, *Adv. Mater.* **2013,** *25*, 5981.

[106] Y. Fatieiev, J. G. Croissant, S. Alsaiari, B. A. Moosa, D. H. Anjum, N. M. Khashab, *ACS Appl. Mater. Interfaces* **2015,** *7*, 24993.

[107] K. Zhu, M. Wu, H. Lai, C. Guo, J. Li, Y. Wang, Y. Chen, C. Wang, J. L. Shi, *Biomaterials* **2016,** *74*, 188.

[108] S.-H. Hu, S.-Y. Chen, X. Gao, *ACS Nano* **2012,** *6*, 2558.

[109] Y. Zhao, B. G. Trewyn, I. I. Slowing, V. S. Y. Lin, *J. Am. Chem. Soc.* **2009,** *131*, 8398.

[110] A. M. Chen, M. Zhang, D. Wei, D. Stueber, O. Taratula, T. Minko, H. He, *Small* **2009,** *5*, 2673.

[111] P. Yang, S. Gai, J. Lin, *Chem. Soc. Rev.* **2012,** *41*, 3679.

[112] J. Liu, S. Z. Qiao, Q. H. Hu, G. Q. Lu, *Small* **2011,** *7*, 425.

[113] J. Zhang, J. M. Rosenholm, *Ther. Delivery* **2015,** *6*, 891.

[114] V. Cauda, A. Schlossbauer, T. Bein, *Microporous Mesoporous Mater.* **2010,** *132*,

60.

[115] H. Vallhov, S. Gabrielsson, M. Strømme, A. Scheynius, A. E. Garcia-Bennett, *Nano Lett.* **2007,** *7*, 3576.

[116] Q. J. He, J. L. Shi, F. Chen, M. Zhu, L. X. Zhang, *Biomaterials* **2010,** *31*, 3335.

[117] K. Kang, J.-S. Lim, *Immune Network* **2012,** *12*, 104.

[118] S. P. Hudson, R. F. Padera, R. Langer, D. S. Kohane, *Biomaterials* **2008,** *29*, 4045.

[119] I. I. Slowing, C.-W. Wu, J. L. Vivero-Escoto, V. S. Y. Lin, *Small* **2009,** *5*, 57.

[120]M. Amidi, E. Mastrobattista, W. Jiskoot, W. E. Hennink, *Adv. Drug Delivery Rev.* **2010,** *62*, 59.

[121] M. E. Davis, J. E. Zuckerman, C. H. J. Choi, D. Seligson, A. Tolcher, C. A. Alabi, Y. Yen, J. D. Heidel, A. Ribas, *Nature* **2010,** *464*, 1067.

[122] Z. Cheng, A. Al Zaki, J. Z. Hui, V. R. Muzykantov, A. Tsourkas, *Science* **2012,** *338*, 903.

Chapter 3 Tunable Stellate Mesoporous Silica Nanoparticles for Intracellular Drug Delivery

3.1 Introduction, Significance and Commentary

Mesoporous silica nanoparticles have attracted great research interests for their potential as drug delivery carriers. To achieve highly efficient delivery, the nanoparticle properties such as size, morphology, pore structure and surface functionalization need to be tightly controlled. In this work, we first demonstrated the controllable synthesis of uniform mesoporous silica nanoparticles with special stellate pore structure. Then, surface functionalization of these particles was carried out to construct a label-free anticancer drug carrier with enhanced intracellular delivery capability. The highlights and novelty of this work include:

1. Controllable synthesis with clarified mechanism.

Systematic study was conducted to elucidate the effects of synthesis conditions (including reaction temperature and time, and reagent ratio) on the structure of stellate mesoporous silica nanoparticles. The particle size of these nanoparticles can be tailored continuously ranging from 50 to 140 nm and the pore size from 2 to 20 nm. Based on experimental results, a consistent two-phase reaction mechanism is proposed for the particle formation process.

2. Label-free drug carrier with enhanced intracellular delivery capability.

After modification of the stellate mesoporous silica nanoparticles with low molecular weight polyethyleneimine though a glutaraldehyde linker, the resulting nanocomposites not only possess auto-fluorescence allowing for convenient particle tracking, but also show enhanced intracellular delivery efficacy compared with both unmodified and amine modified counterparts when used as an anticancer drug carrier.

3.2 Tunable Stellate Mesoporous Silica Nanoparticles for Intracellular Drug Delivery

This section is included in the thesis as it appears as a paper published by L. Xiong, X. Du, B. Shi, J. Bi, F. Kleitz and S. Z. Qiao. Tunable stellate mesoporous silica nanoparticles for intracellular drug delivery, *J. Mater. Chem. B*, **2015**, 3, 1712.

Statement of Authorship

Title of Paper	Tunable stellate mesoporous silica nanoparticles for intracellular drug delivery
Publication Status	☑ Published ☐ Accepted for Publication ☐ Submitted for Publication ☐ Unpublished and Unsubmitted w ork w ritten in manuscript style
Publication Details	First published online 08 Dec 2014 DOI: 10.1039/C4TB01601G

Principal Author

Name of Principal Author (Candidate)	Lin Xiong (First Author)		
Contribution to the Paper	Research plan, material synthesis, material characterization, material performance assessment, manuscript drafting		
Overall percentage (%)	80 %		
Certification:	This paper reports on original research I conducted during the period of my Higher Degree by Research candidature and is not subject to any obligations or contractual agreements with a third party that would constrain its inclusion in this thesis. I am the primary author of this paper.		
Signature		Date	2016/11/22

Co-Author Contributions

By signing the Statement of Authorship, each author certifies that:

i. the candidate's stated contribution to the publication is accurate (as detailed above);
ii. permission is granted for the candidate in include the publication in the thesis; and
iii. the sum of all co-author contributions is equal to 100% less the candidate's stated contribution.

Name of Co-Author	Dr. Xin Du		
Contribution to the Paper	Assistance with research plan, material synthesis		
Signature		Date	16-Nov-2016

Name of Co-Author	Bingyang Shi		
Contribution to the Paper	Assistance with material performance assessment		
Signature		Date	17-Nov-2016

Name of Co-Author	A/Prof Jingxiu Bi		
Contribution to the Paper	Assistance with research organization		
Signature		Date	24/11/2016

Name of Co-Author	Prof Freddy Kleitz		
Contribution to the Paper	Assistance with manuscript revision		
Signature		Date	19-Nov-2016

Name of Co-Author	Prof Shi Zhang Qiao (Corresponding Author)		
Contribution to the Paper	Design of the project, organization of the research and supervision, manuscript revision		
Signature		Date	24/11/2016

Please cut and paste additional co-author panels here as required.

Journal of Materials Chemistry B

PAPER

View Article Online
View Journal | View Issue

Cite this: J. Mater. Chem. B, 2015, 3, 1712

Tunable stellate mesoporous silica nanoparticles for intracellular drug delivery†

Lin Xiong,[a] Xin Du,[a] Bingyang Shi,[a] Jingxiu Bi,[a] Freddy Kleitz[b] and Shi Zhang Qiao*[a]

Received 26th September 2014
Accepted 5th December 2014

DOI: 10.1039/c4tb01601g

www.rsc.org/MaterialsB

Stellate mesoporous silica nanoparticles with special radial pore morphology were easily synthesized using triethanolamine as the base catalyst in a wide range of synthesis conditions. By adjusting the surfactant composition, reaction temperature and time, and reagent ratio, the particle size of the material could be tailored continuously ranging from 50 to 140 nm and the pore size from 2 to 20 nm. By analyzing the effects of different synthesis parameters, it is concluded that the particles are formed following a nucleation-growth mechanism and the reaction kinetics play an important role in determining the particle size and pore structure. These stellate MSNs can be conveniently functionalized with a nontoxic low molecular weight poly(ethylene imine) (PEI, 800 Da) by a delayed condensation method. The resulting nanocomposites not only possess auto-fluorescence for suitable particle tracking but also demonstrate good potential for intracellular delivery of the anticancer doxorubicin drug.

1. Introduction

Mesoporous silica nanoparticles (MSNs) have attracted great research interest because of their potential usage as drug delivery carriers.[1,2] For these sophisticated applications, a tight control over the particle size and the pore structure of the material is highly desirable. For example, the particle size of MSNs was reported to have an influence on the biodistribution,[3] cellular uptake,[4] nucleus entry[5] and biocompatibility[6] while the pore structure is related to the drug release profile[7] and loading capability[8,9] of MSNs. Therefore, a considerable amount of effort has been made towards a precise control over the size and pore structure of MSNs.

To achieve passive accumulation of the drug carriers inside tumor tissues *via* the enhanced permeation and retention (EPR) effect,[1] a particle diameter between 30 nm and 150 nm is desired. Although nano-sized silica nanoparticles can be readily prepared following the Stöber method,[10] nano-sized MSNs were not successfully synthesized until about a decade ago, by controlling the reactant concentration[11,12] or by adopting a dilution and quenching method.[13] Later, other studies showed that the particle size can be controlled by introducing a second surfactant[14,15] and/or co-solvent in the synthesis mixture.[16] More recently, particle size control through reaction pH adjustment was also demonstrated.[4,17] However, the preparation methods in these previous reports usually involved highly diluted solutions, which led to difficulties in scale-up and isolation of the products. By employing triethanolamine (TEA) as the base catalyst, Bein and coworkers succeeded in synthesizing MSNs with the particle diameter below 100 nm and narrow particle size distributions, this time from concentrated solutions.[18]

On the other hand, a large mesopore structure (pores >5 nm) possesses several advantages such as high drug loading[19] and capability of loading large biomolecules,[20] *e.g.*, proteins[21] or nucleic acids.[22,23] However, most of the reported pore sizes of MSNs are limited to 3–4 nm because of the commonly used surfactant template, cetyltrimethylammonium bromide (CTAB). Although using pore swelling agents[21] or dual surfactants[24] can enlarge mesopores, these methods generally cannot guarantee the maintenance of uniform particles below 200 nm or require specific treatments such as a prolonged hydrothermal process.[25–27] Therefore, it is still a challenge to combine the features of small particle size, narrow particle size distribution and large mesopores within one MSN system.

Very recently, Zhang *et al.* reported a facile procedure for synthesizing MSNs with size below 200 nm and mesopores up to 17 nm.[28] Furthermore, these MSNs possess a special radial pore morphology, the so-called stellate pore morphology, and this kind of structure was reported to facilitate mass transport inside the pores.[29,30] From the view point of synthesis, this work can be seen as a derivatization of the previous synthesis method of Bein[18] in that not only the base catalyst was exchanged from triethanolamine to several kinds of other small organic amines but also the standard CTAB surfactant was replaced by cetyltrimethylammonium tosylate (CTAT). Although the feasibility of

[a]School of Chemical Engineering, The University of Adelaide, Adelaide, SA 5005, Australia. E-mail: s.qiao@adelaide.edu.au; Fax: +61 8 8303 4373; Tel: +61 8 8313 6443

[b]Department of Chemistry and Centre de Recherche sur les Matériaux Avancés (CERMA), Université Laval, Quebec City, QC G1V 0A6, Canada

† Electronic supplementary information (ESI) available: Surface reaction, TGA curve, TEM and SEM images, nitrogen adsorption–desorption, calibration curve, drug release profile and confocal microscopy images. See DOI: 10.1039/c4tb01601g

using different catalysts and surfactants to control the morphology and porous structure of the final particles has been explored, quantitative aspects of the synthesis protocol, such as the effects of using mixed surfactants, the ratio between reactants, reaction temperature and reaction time, must still be thoroughly substantiated and clarified. In this work, a significant influence of these factors on the final MSN products is demonstrated in a TEOS/CTAT/TEA/H_2O system. We evidence that by tuning these parameters, it is possible to easily adjust the pore structure and particle size of stellate MSNs over a wide range. Furthermore, the particle formation mechanism is studied by analyzing the products obtained under different synthesis conditions. Finally, the stellate MSNs are functionalized with low molecular weight poly(ethylene imine) (PEI), and the resulting nanocomposites demonstrate excellent potential for intracellular delivery of anticancer drug doxorubicin (DOX).

2. Materials and methods

2.1 Materials

Tetraethyl orthosilicate (TEOS), (3-aminopropyl)-triethoxysilane (APTES), triethanolamine (TEA), cetyltrimethylammonium bromide, cetyltrimethylammonium tosylate, branched polyethylenimine (PEI, MW: 800 Da), glutaraldehyde (GA, 50 wt%), ethanol, dimethylsulfoxide (DMSO), 3-[4,5-dimethylthialzol-2-yl]-2,5-diphenyltetrazolium bromide (MTT), and trypsin (0.25%) were purchased from Sigma Aldrich. Doxorubicin hydrochloride (DOX) was purchased from Bejing Huafeng United Technology Co., Ltd Dulbecco's Modified Eagle's Medium (DMEM), fetal bovine serum (FBS), trypsin–EDTA, penicillin–streptomycin (PS) mixture, and phosphate buffered saline (PBS) were purchased from Gibco-BRL (Grand Island, USA). All chemicals were used as received without further purification.

2.2 Synthesis of MSNs

MSNs were synthesized using TEOS as the silica source, triethanolamine as the base catalyst, CTAT and/or CTAB as the structure-directing agent. According to the literature,[28] MSNs with stellate morphology were synthesized at 80 °C with a molar ratio of 1.0TEOS : 0.06CTAT : 0.026TEA : 80.0H_2O. Using that formula as a starting point, the variations in this study are summarized in Table 1 with the respective denotation and physical parameters of samples.

In a typical synthesis, a given amount of CTAT/CTAB and TEA was first dissolved in 25 mL DI water to form a clear solution at a pre-set reaction temperature. Then, 3.9 mL of TEOS was quickly added to the solution and after a selected period of time the mixture was centrifuged at 16 000 rpm for 15 min. The white precipitate was copiously washed with DI water, collected, and dried in an oven at 60 °C for 24 h. After the particle synthesis, the surfactant template was removed by calcination at 550 °C for 6 h with a ramp rate of 0.5 °C min^{-1} in air, unless otherwise specified.

2.3 Functionalization of MSNs

The functionalization process is presented in Scheme 1 and Fig. S1.† Firstly, the delayed co-condensation method[31] was adapted to synthesize amine-modified MSNs (amine–MSN). The synthesis procedure is similar to the T10 sample except that a 200 μL mixture of TEOS and APTES (volume ratio 1 : 1) was added at 1 h after the reaction began at 80 °C. After washing the amine-functionalized particles with ethanol and water, the CTAT surfactant was extracted two times in a refluxing solution of hydrochloric acid (HCl) in ethanol (10% v/v) at 78 °C for 24 h. For glutaraldehyde (GA) conjugation, 50 mg of extracted particles were dispersed in 10 mL of sodium phosphate buffer (pH 7.4). Then 100 μL of glutaraldehyde (50 wt%) was added, and

Table 1 Synthesis conditions and structural parameters[a]

Sample	Reactant ratio (TEOS/surfactant/TEA/H_2O mole ratio)	Temperature (°C)	Time (h)	Surfactant composition (CTAT/CTAB mole ratio)	Particle size (nm)	S_{BET} (m^2 g^{-1})	V_t (cm^3 g^{-1})	V_f (cm^3 g^{-1})
B10	1 : 0.06 : 0.026 : 80	80	2	0 : 10	45 ± 5	689	1.14	0.47
T3B7				3 : 7	50 ± 5	762	1.57	0.59
T5B5				5 : 5	60 ± 5	717	1.46	0.62
T7B3				7 : 3	70 ± 7	615	1.35	0.56
T9B1				9 : 1	95 ± 9	602	1.37	0.57
T10(T80)				10 : 0	110 ± 12	581	1.36	0.51
TC/2	1 : 0.06 : 0.013 : 80				130 ± 9	375	1.00	0.37
TC/4	1 : 0.06 : 0.0065 : 80				140 ± 13	424	0.88	0.38
TC/8	1 : 0.06 : 0.00325 : 80				—	427	1.32	0.44
TN	1 : 0.06 : 0 : 80				—	245	0.84	0.25
T95	1 : 0.06 : 0.026 : 80	95			108 ± 10	454	0.77	0.43
T65		65			110 ± 11	708	1.82	0.61
T50		50			80 ± 7	788	1.71	0.69
T50-24h			24		100 ± 6	531	1.14	0.46
TSi/3	0.33 : 0.06 : 0.026 : 80	80	2		70 ± 8	885	2.16	0.97

[a] Particle sizes were estimated by averaging 50 particles from the SEM images. Total pore volumes (V_t) and framework pore volumes (V_f) were determined from N_2 adsorbed at $P/P_0 = 0.99$ and $P/P_0 = 0.8$, respectively.

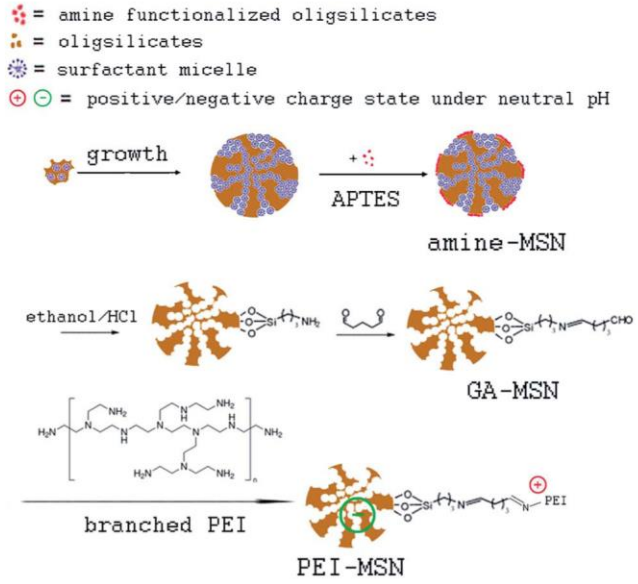

Scheme 1 Synthesis scheme of amine and PEI functionalized MSNs.

stirred at room temperature for 6 h. The glutaraldehyde modified MSNs (GA–MSN) were collected by centrifugation and washed intensively with ethanol several times to remove excess glutaraldehyde. Afterwards, the particles were dispersed in 10 mL of PEI aqueous solution (0.5 mg mL^{-1}) and stirred at room temperature for 6 h. Finally, the suspension was centrifuged and the precipitate was washed with ethanol and dried to obtain PEI-modified MSNs (PEI–MSN). For comparison, unmodified MSNs (ex-MSN) were also prepared according to the synthesis procedure of T10, except that the CTAT surfactant was removed by extraction rather than calcination.

2.4 DOX loading and release

For doxorubicin loading, 5 mg of MSNs were mixed with 5 mL of DOX solution in PBS (0.5 mg mL^{-1}) and stirred for 24 h under a dark environment. Then, the nanoparticles were collected by centrifugation at 13 500 rpm for 10 min. The precipitate was washed gently with PBS three times and dried at 60 °C. To evaluate the DOX loading efficiency, the supernatant and all the washing liquid fractions were collected, and the residual DOX content was determined using a standard curve by UV-vis adsorption at 480 nm. The release profile of DOX from MSNs was investigated at 37 °C in two different release media: (a) acetate buffer, pH 5.0; and (b) PBS, pH 7.4, using a dialysis bag diffusion technique. The DOX loaded particles (5 mg) were suspended in 5 mL release media in the dialysis membrane bag (MWCO 1/4 3500) and the bag was immersed in 15 mL release media and shaken at a speed of 100 rpm at 37 °C. The amount of DOX released at different time intervals was determined by UV-vis measurements at 480 nm.

2.5 Cell culture and cell viability

HeLa cells were grown in DMEM culture medium supplemented with 10% (v/v) FBS and penicillin–streptomycin (100 U mL^{-1} and 100 μg mL^{-1}, respectively) in a humidified 5% CO_2 atmosphere at 37 °C. For all experiments, cells were harvested by using 0.25% trypsin and resuspended in fresh medium before plating.

The viability of cells in the presence of MSNs was investigated using MTT assay. HeLa cells were seeded into 96-well plates at a density of 1×10^4 per well in 100 μL of media and grown for 24 h. Then, the growth medium was replaced with 100 μL of cell culture medium containing different concentrations of MSNs with or without DOX loading. After incubation for 24 h, the medium was removed. Then 100 μL fresh medium and 10 μL MTT (5.0 mg mL^{-1} in PBS) were added to each well and the cells were further incubated for 4 h. After that, the growth medium was removed and 150 μL of DMSO was added to each well to ensure complete solubilization of formazan crystals. Finally, the absorbance was determined using a Biotek Microplate Reader (Biotek, USA) at a wavelength of 570 nm. Data were expressed as mean ± standard deviation (SD) of four independent experiments. The viability of untreated cells was assumed to be 100%.

2.6 Confocal laser scanning microscopy (CLSM)

To check cellular uptake and auto-fluorescence of PEI–MSN, HeLa cells were seeded at a concentration of 2×10^5 cells per well in a 6-well plate with one piece of cover glass at the bottom of each well and cultured for 24 h. PEI–MSN with or without DOX loading was then added to the incubation medium at a concentration of 50 μg mL^{-1}. After a desired period of time, the medium was removed. The cells were washed twice with PBS and fixed with 4 wt% formaldehyde. The cell nucleus was stained with Hoechst 33258 (2 μM) for 10 min at room temperature. After incubation, the cells were softly washed twice to remove excessive Hoechst 33258. At last, 2 mL of PBS was added and the cover glass was visualized under a confocal laser scanning microscope (Leica Confocal 1P/FCS). Optical sections were averaged 4 times to reduce noise. Images were processed using Leica confocal software.

2.7 Characterization of materials

Scanning electron microscopy (SEM) images were taken on a Quanta 450 scanning electron microscope. TEM observations were carried out on a Tecnai G2 Spirit transmission electron microscope at an acceleration voltage of 120 kV. Nitrogen adsorption–desorption isotherms were measured at −196 °C on a TriStar II surface area and porosity analyzer. The samples were degassed at 110 °C for 12 h before measurements. The Brunauer–Emmett–Teller (BET) specific surface areas (SBET) and the Barrett–Joyner–Halenda (BJH) pore-size distributions were derived from the adsorption branch of the isotherms. Thermogravimetric analysis of samples was performed on an S60/51920 TGA/DSC thermogravimetric analyzer using an oxygen flow of 30 mL min^{-1} and a heating ramp of 10 °C min^{-1}. Fluorescence emission and excitation spectra were recorded on a RF-5301PC spectrofluorophotometer (Shimadzu Scientific Instruments). Fourier transform infrared (FTIR) spectra of samples were recorded on a Thermo Scientific NICOLET 6700

spectrometer at room temperature. The dynamic light scattering (DLS) particle size distribution and zeta-potential of MSNs dispersed in H_2O were measured using a Malvern Zetasizer Nano ZS (Malvern Inst. Ltd, U.K.) at room temperature. The pH of the suspension was adjusted with 0.1 M HCl or NaOH when necessary and monitored using a pH meter (EL20, METTLER TOLEDO).

3. Results and discussion

In this study, we first investigated separately the effects of using mixed surfactants, varying the reaction temperature and reaction time, silica precursor quantity, and the catalyst concentration. Then, by analyzing the above results, summarized in Table 1, a mechanism for the particle formation is proposed. Finally, surface-functionalization of the stellate MSNs is demonstrated and the resulting composite nanoparticles are tested as intracellular drug delivery carriers.

3.1 Effects of mixed surfactants

From the SEM and TEM images in Fig. 1, it is clear that uniform nanoparticles can be synthesized using a mixture of surfactants, CTAT and CTAB. Note that, for all the samples shown in the images, the total mole ratio of surfactant/TEOS is kept constant at 0.06. As the CTAT composition in the surfactant mixture increases from 0 (sample B10) to 100% (sample T10), the particle size increases gradually from about 50 to 110 nm. This effect on particle size will be discussed in more detail after explaining the particle formation mechanism (Section 3.6). Meanwhile, the appearance of the particle surface in the SEM images changes from a smooth to a wrinkled surface with large pores, which appears on the particles synthesized at high CTAT content. The TEM images further confirm these particle structures after calcination, being discrete with little inter-particle aggregation.

The nitrogen physisorption isotherms and the corresponding pore size distributions for these samples, shown in Fig. 2, demonstrate more clearly the evolution of the mesoporous structure with varying surfactant compositions. For B10, the narrow peak centered at 2 nm in the pore size distribution (PSD) curve originates from the cetyltrimethylammonium template and the broad peak around 40 nm is believed to be caused by the inter-particle textural porosity. For T3B7 and T5B5, the PSD curves show peaks around 3 nm and this peak becomes broader with increasing CTAT content in the synthesis mixture. For T7B3, the peak around 3 nm remains, but another broad one centered around 10 nm also appears, suggesting the presence of a hierarchical porous structure. Although MSNs with hierarchical porous structures have been synthesized by using a co-surfactant,[32] co-solvent[33] and/or organosilica precursors,[34] it is interesting to note that it occurs in our case with two surfactants, CTAT and CTAB, consisting of the same cetyltrimethylammonium cation (CTA^+). In other words, this implies that a hierarchical structure could be achieved by adjusting solely the anionic nature of the surfactant. A further increase of the CTAT component leads to the presence of larger mesopores. T9B1 and T10 show pore sizes around 14 nm and 20 nm, respectively. The gradual enlargement of the mesopores with increasing CTAT content may be explained by an anion competition mechanism, as discussed before,[28] where the tosylate anions compete with silicate oligomers during the particle formation. One may speculate that, with increasing CTAT, more tosylate anions become incorporated into the as-prepared particles and larger mesopores are obtained after calcination. This hypothesis is supported partially by the thermogravimetry results for the surfactants (Fig. S2†) and the as-prepared samples (Fig. S3†). It is observed that as the CTAT increases in the synthesis mixture, the weight loss between 300 °C and 350 °C increases accordingly for the as-prepared

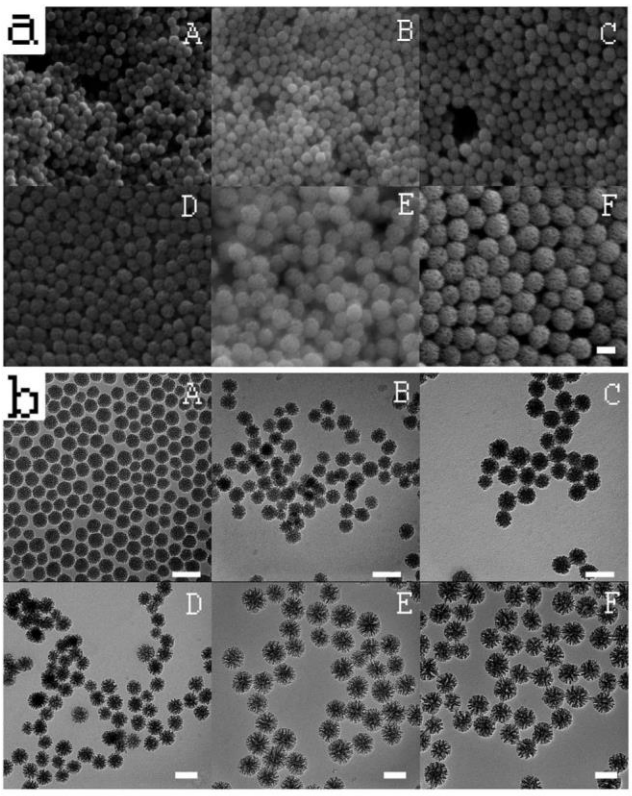

Fig. 1 SEM (a) and TEM (b) images of MSN particles synthesized with mixed surfactants: (A) B10, (B) T3B7, (C) T5B5, (D) T7B3, (E) T9B1, and (F) T10. Scale bars are 100 nm.

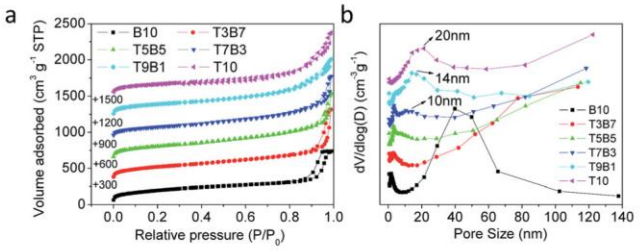

Fig. 2 Nitrogen adsorption–desorption isotherms (a) and respective pore size distributions (b) of the various MSN particles synthesized with mixed surfactants.

samples. Although the decomposition of the surfactant in mesoporous silica is a complex process involving multiple reactions and steps, the weight loss below 300 °C could mainly be attributed to the Hofmann degradation and fragmentation of CTA^+ binding to silica (SiO^-).[35] On the other hand, the presence of CTA^+ in interactions with tosylate anions, that is, CTAT molecules, incorporated into the as prepared samples might contribute to the weight loss between 300 °C and 350 °C, which corresponds to the organic components removed by oxidation.[35]

3.2 Effects of the reaction temperature

Fig. 3 shows SEM and TEM images of particles synthesized at various temperatures. Both the morphology viewed in SEM and the image contrast in TEM suggest an increase in the particle porosity as the reaction temperature decreases from 95 °C to 50 °C. In terms of morphology, the particle sizes for T95, T80, and T65 are all around 110 nm, except for T50 which shows a smaller particle size of about 80 nm.

The nitrogen sorption results of these samples are shown in Fig. 4. All of the isotherms show a hysteresis loop at a high relative pressure ($P/P_0 > 0.9$), suggesting the existence of textural interparticle mesopores. The adsorbed volume measured below the relative pressure of 0.8, which can be attributed to the framework porosity, progressively increases with decreasing synthesis temperature. The most probable pore sizes of samples T95 and T80 are 8 nm and 20 nm, respectively, determined from the peak maximum of the PSD curves. For samples T65 and T50, although the most probable pore sizes are clearly above 20 nm, the exact values are difficult to ascertain because of the very broad distributions, which could be explained by the size overlap between the framework pores and the textural pores. Besides, T65 and T50 show a significantly higher framework pore volume than that of T80 and T95. These results are in good agreement with the observation from SEM and TEM analyses.

The influence of the reaction temperature can be explained in terms of the reaction kinetics. A lower temperature leads to a lower reaction rate, which is also reflected by the product yield. The final yields of the collected silica synthesized at 95 °C, 80 °C, 65 °C and 50 °C are 96%, 85%, 37% and 16%, respectively. This drastic decrease in the reaction rate with a decreasing temperature may lead to slower particle growth, and therefore, the particle size obtained at 50 °C would be significantly smaller than the other ones. On the other hand, a similar particle size but with a gradual decrease in pore volume in the order of T65, T80 and T95 indicates that a pore filling or contraction process may occur after the particle size reaches a critical value. These results suggest that reaction kinetics also play an important role in influencing the formation of large mesopores, in addition to the anion competition mechanism.

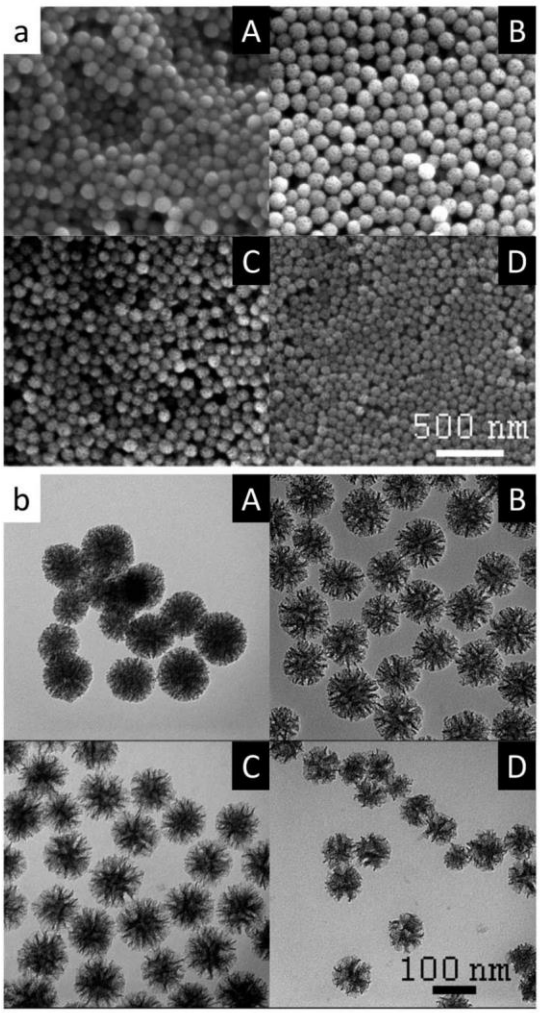

Fig. 3 SEM (a) and TEM (b) images of particles synthesized at various temperatures: (A) T95, (B) T80, (C) T65, and (D) T50.

3.3 Effect of the reaction time

To clarify the influence of the reaction kinetics, samples were prepared at the same reaction temperature but subjected to different reaction times in order to analyze the particle evolution as a function of time.[36,37] The reaction temperature is set at 35 °C for a slow reaction and thus the ease of observation of different reaction stages.

SEM images of the products from 0.5 h to 24 h of the reaction are shown in Fig. 5. No discrete particles could be identified in the 0.5 h and 1 h products, and only some wrinkled structures appeared in the 2 h product. It should be noted that after 2 h of reaction, the two immiscible phases of H_2O/TEOS can still be distinguished if stirring was stopped. This suggests that the

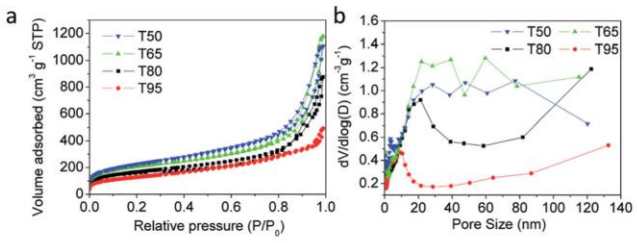

Fig. 4 Nitrogen adsorption–desorption isotherms (a) and respective pore size distributions (b) of particles synthesized at various temperatures.

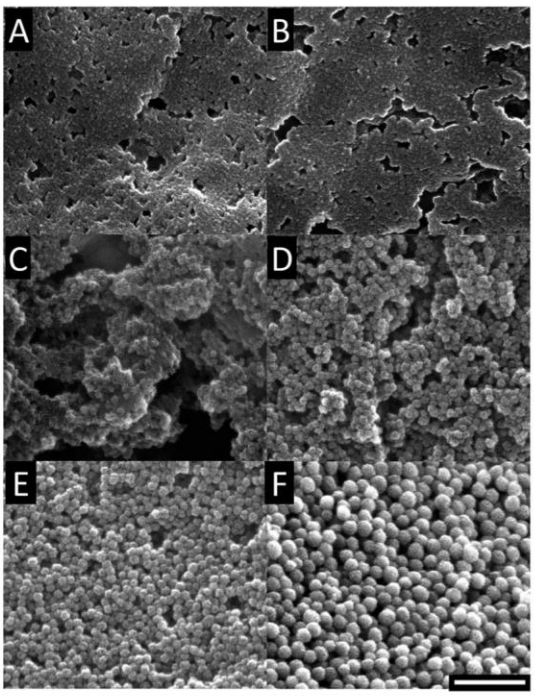

Fig. 5 SEM images of particles synthesized at 35 °C after (A) 0.5 h, (B) 1 h, (C) 2 h, (D) 4 h, (E) 6 h and (F) 24 h. Scale bar is 500 nm.

particles are not formed in a homogeneous system but in a system more similar to that used to prepare silica nanoparticles from basic amino acids.[37,38] This kind of two-phase synthesis was reported to contribute to the monodispersity of the final particles.[39] After 4 h of the reaction, uniform particles of 50 nm become identifiable and their size increases slightly up to about 60 nm after 6 h. Finally, spherical particles of 100 nm with large pores on their surface are obtained after 24 h. Meanwhile, the particles obtained after different reaction periods at 35 °C were analyzed by nitrogen sorption to monitor the pore size evolution (Fig. S4†). While the sample obtained at 6 h shows a pore size around 20 nm, the samples obtained beyond 12 h show almost a constant pore size of about 12 nm. Because uniform-sized silica particles are obtained regardless of the reaction time from 4 h to 24 h, it can be inferred that only particle growth occurs at this stage without new particle nucleation/formation. The particle growth period was also observed for reactions at other temperatures. From 2 h to 24 h at 50 °C, the particle size increases from 80 nm for the T50 sample to 100 nm for the T50-24h sample (Fig. S5†). Thus, we assume that the reaction follows a nucleation-growth mechanism. Besides, it is interesting to note that the prolonged reaction time at 50 °C also leads to a reduced framework pore volume and pore size (Fig. S5†), which is consistent with the particle evolution at 35 °C and corresponds well to the kinetic effect of different reaction temperatures.

3.4 Effect of the silica precursor quantity

If a nucleation-growth process accurately describes the particle formation mechanism, it should be reasonable that the particle size can be directly controlled by changing the quantity of the silica precursor. To verify this hypothesis, the sample TSi/3 was synthesized using 1/3 TEOS amount of the formula for T10. Here, it was expected that the usage of the reduced silica precursor should lead to a decreased particle size, because fewer silicate species would participate in the particle growth process.

The characterization results of TSi/3 in Fig. 6 are consistent with our expectation. This sample is also constituted of relatively uniform nanoparticles. However, the particle size of TSi/3 is around 70 nm and significantly smaller than that of T10, which shows a particle size around 110 nm (see Fig. 1). Besides, large mesopores around 10 nm are also observed on the particle surface from the SEM investigations. Furthermore, the PSD clearly indicates that, in addition to the large mesopores represented by the peak at 12 nm, a significant amount of 3 nm mesopores also exist in this sample. From the SEM and TEM observations, these 3 nm mesopores are more likely to be located in the inner part of the particles, indicating that they are essentially formed at an early stage of the particle formation. It is documented that the pH in the MSN synthesis mixture declines as the silica condensation proceeds.[17,38] Therefore, this hierarchical structure may be justified by the pH variation and anion competition during the reaction process. At the beginning of the reaction, the pH of the system is high (above 11) so that the tosylate anion dissociates easily from the CTA^+ cation. Under these conditions, normal 3 nm CTA^+/silicate micelles are formed and aggregate into a mesophase to form the primary particles. As the reaction proceeds and the pH drops to near neutral, binding of tosylate to CTA^+ will eventually become strong enough to compete with silicate species, and from this time larger mesopores will begin to develop due to the incorporation of the tosylate anions.

3.5 Effect of the catalyst concentration

The catalyst amount is an important factor in determining both the particle size and the pore structure of TEA-derived silica.[18]

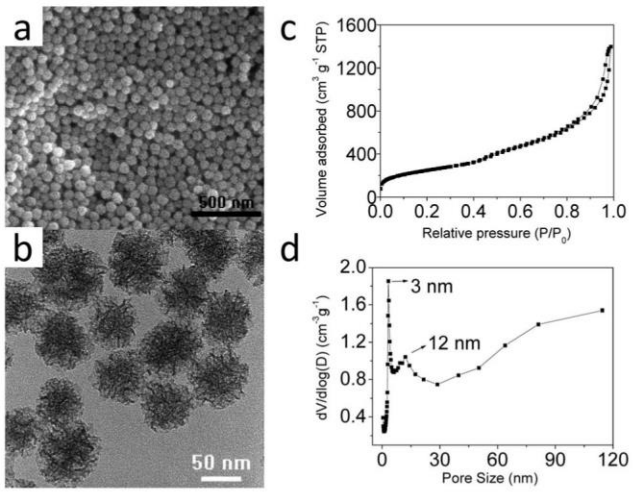

Fig. 6 SEM (a) and TEM (b) images, nitrogen adsorption–desorption isotherm (c) and pore size distribution curve (d) of TSi/3.

Although the effect of TEA/TEOS ratios (from 8 to 0.026) has been studied,[28] this work emphasizes that 0.026 is not the lowest limit. Stellate nanoparticles with large surface pores can still be successfully synthesized at much lower TEA/TEOS ratios of 0.013 and 0.0065, but the particle size increases slightly to 130–150 nm (Fig. S6†). Interestingly, another study also reported that a lower TEA catalyst quantity could result in larger MSNs when CTAB is used as the surfactant.[5] Based on a nucleation-growth model, it can be suggested that at low TEA concentration, the hydrolysis rate of TEOS is limited, leading to fewer primary particles formed in the initial period, which then further grow into larger particles. Meanwhile, owing to the very low base concentration used, the pH of the reaction mixture may decrease so quickly that particle nucleation can only occur in the short initial period. Afterwards, during the prolonged growth stage, the particles gradually grow in size and become spherical in shape, as demonstrated in Fig. 5. However, when we try to further increase the particle size by reducing the TEA/TEOS ratio to 0.00325, some smaller particles of several tens of nanometers are present accompanied by large pore spheres above 100 nm. When no TEA was added at all, only aggregated irregular particles that are smaller than 40 nm were obtained. These irregular particles present low surface area and almost only textural porosity (Fig. S7†), which could be attributed to the weak interactions between silicate species and the surfactant template. Therefore, it can be concluded that there is a very low, but critical, base concentration, below which stellate MSNs cannot be obtained.

3.6 Proposed mechanism for particle formation

Based on the above analysis of the effects of different synthesis parameters, a possible formation mechanism for the stellate MSNs is proposed in Scheme 2. The whole process can be divided into 4 stages: (1) TEOS molecules diffuse into the water phase and become hydrolyzed into silicate species. Following condensation processes, the oligomeric silicate species assemble with CTA^+ cations, through adsorption, to form hybrid micelles *via* the S^+I^- (S: surfactant; I: inorganic species) pathway; (2) several hybrid micelles aggregate and form primary particles; (3) due to the decrease of pH, partly silicated micelles begin to form, as tosylate anions compete with silicate for CTA^+. These partly silicated micelles add to the primary particles and result in particle growth and the formation of large mesopores. (4) With the further decrease of pH, the interactions between silicate species and CTA^+ become even weaker. The continuous deposition of silicate species into the large mesopores should lead then to a decrease in particle porosity. In this nucleation-growth model, the final particle size is greatly influenced by the number of nuclei/primary particles formed at the initial reaction period. When CTAB is replaced by CTAT in the mixed surfactant system, the amount of free CTA^+ cations in the reaction medium could become lower due to the stronger binding of tosylate over bromide towards CTA^+. Because the nucleation is promoted by forming hybrid micelles between CTA^+ and silicate species, fewer free CTA^+ cations may lead to fewer nuclei and thus larger final particle sizes, as demonstrated in Fig. 1.

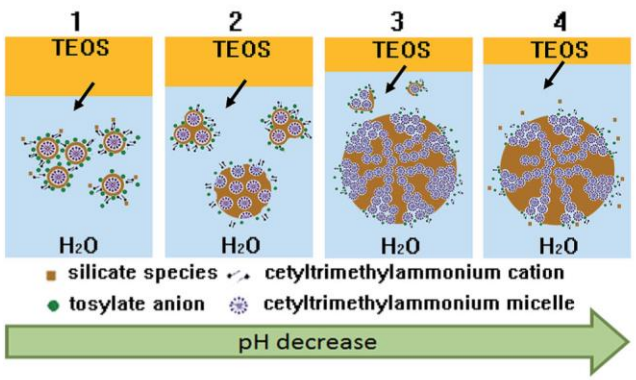

Scheme 2 Scheme for the proposed formation process of stellate MSNs.

3.7 Surface functionalization and delivery application

An important advantage of MSNs as a drug delivery platform is their tunable surface chemistry and the ease of conjugation with various functional groups.[40] In this study, a nontoxic low molecular weight branched PEI (800 Da) was conjugated to the above large pore stellate MSNs to form an intracellular DOX-delivery system, because PEI has been proven to enhance cellular uptake,[41] dispersion at physiologic pH,[42] and endosome escape[43] of MSNs. Although the functionalization with large organic groups often leads to pore blocking/saturation,[9] a large mesopore structure was reported to alleviate this problem.[44,45] Furthermore, by taking advantage of the particle growth process, a delayed condensation method[31] can readily be applied to selectively functionalize the external part of the particles, while leaving the inner part mostly unmodified to interact with the DOX molecules.

Fig. 7a and b show the SEM and TEM images of amine- and PEI-modified particles. By comparing amine–MSNs with the previous T10 sample, it can be concluded that the delayed co-condensation with APTES does not change the particle size and morphology significantly. After further PEI modification, there

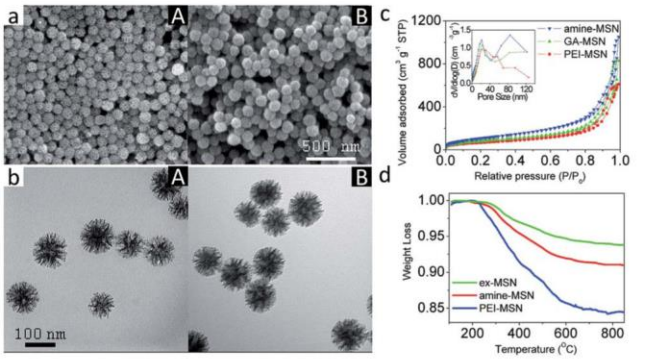

Fig. 7 SEM (a) and TEM (b) images of (A) amine–MSN and (B) PEI–MSN. Nitrogen adsorption–desorption isotherms with respective pore size distributions inserted (c) and thermogravimetric curves (d) of the functionalized MSNs.

is a visible reduction of surface porosity due to the PEI coating, which was confirmed by nitrogen sorption measurements (Fig. 7c). The increased organic content of functionalized particles is also reflected in TGA measurements, as shown in Fig. 7d. The weight loss from 110 °C to 850 °C for ex-MSN, amine–MSN and PEI–MSN is 6%, 9% and 15%, respectively.

The successful surface functionalization was further confirmed by surface zeta potential measurements and FTIR. In Fig. 8a, while unmodified ex-MSNs show an isoelectrical point (IEP) around 3, amine–MSNs and PEI–MSNs show IEP of nearly 7 and 9, respectively. The increase in IEP reflects the increase of surface amine groups. Besides, a slight increase in the particle size after functionalization can be identified from the DLS size distributions shown in Fig. 8b. The average particle sizes determined by DLS for ex-MSNs, amine–MSNs and PEI–MSNs are 154 nm, 168 nm and 202 nm, respectively. These sizes are larger than those observed in TEM, which could be due to the surface hydration layer and/or slight aggregation in solution. This kind of deviation was also observed in several other studies.[4,18] In the FTIR spectra shown in Fig. 8c, all of the particles show typical peaks corresponding to silica around 789 cm^{-1}, 960 cm^{-1} and 1040 cm^{-1}, which are attributed to the symmetric Si–O, Si–OH and asymmetric Si–O–Si vibrations, respectively. The peak around 1630 cm^{-1} is due to physisorbed water.[30] However, in the range of 1400–1600 cm^{-1} shown in Fig. 8d, the unmodified ex-MSNs show no peak while amine–MSNs show a peak around 1520 cm^{-1} which is assigned to N–H bending.[30] After conjugation of the amine–MSN with the glutaraldehyde linker, two peaks around 1540 cm^{-1} and 1710 cm^{-1} appear, which can be attributed to C=C and C=O in glutaraldehyde and its oligomer.[46] Note that the characteristic band of C=N occurs around 1640 cm^{-1} and may be masked by the 1630 cm^{-1} band of water. However, the change of the powder color from white to yellow (Fig. S8†) suggests the formation of a Schiff bond.[47] After the reaction with PEI, a peak around 1465 cm^{-1} corresponding to C–H bending appears, which is accompanied by an increase of the C–H stretching band in 2800–3000 cm^{-1}.

Interestingly, the PEI–MSN particles show auto-fluorescence without additional fluorescent label, as shown by the emission and excitation spectra in Fig. 9. Similar auto-fluorescence has previously been reported[46,48] using aldehyde as a crosslinker between amine groups, and it was attributed to the n–π* transition of the C=N bonds in the Schiff's base. In addition, to test the possibility of using this auto-fluorescence for tracking particles in intracellular delivery, the fluorescence stability of PEI–MSN in an aqueous solution of pH = 5 was checked because both the extracellular tumor microenvironment and the endosome/lysosome organelles exhibit a mild acidic pH.[49] Although Schiff bases are usually unstable under acidic conditions, the fluorescence intensity of PEI–MSN remained stable up to 24 h as shown in Fig. 9a (inset), which could be attributed to the exceptional stability of the cross-linking formed by glutaraldehyde.[50] Confocal microscopy images (Fig. 9b) confirm the green fluorescence of PEI–MSNs in the cell culture.

Following this, DOX was loaded into PEI–MSN, amine–MSN and ex-MSN, and the loading efficiencies determined by UV-vis adsorption using a standard curve (Fig. S9†) were 21%, 26%, and 30%, respectively, which is consistent with the increasing order of the pore volume. The resulting DOX-loaded particles exhibited sustained and pH-dependent release behavior owing to the increased solubility of DOX at low pH (Fig. S10†). In the MTT tests shown in Fig. 10, all the three types of particles showed good biocompatibility below a particle concentration of 100 μg mL^{-1} with the cell viability above 80%. On the other hand, PEI–MSN showed higher inhibition efficacy towards HeLa cells than amine–MSN and ex-MSN after DOX loading, which could be attributed to the enhanced cell uptake of the nanoparticles with the surface PEI modification.[41] The successful delivery of DOX by PEI–MSN was verified by confocal microscopy (Fig. S11†) and the delivery process was monitored up to 24 h (Fig. S12†). It is observed that there is already significant DOX accumulation in the HeLa cell cytoplasm after 1

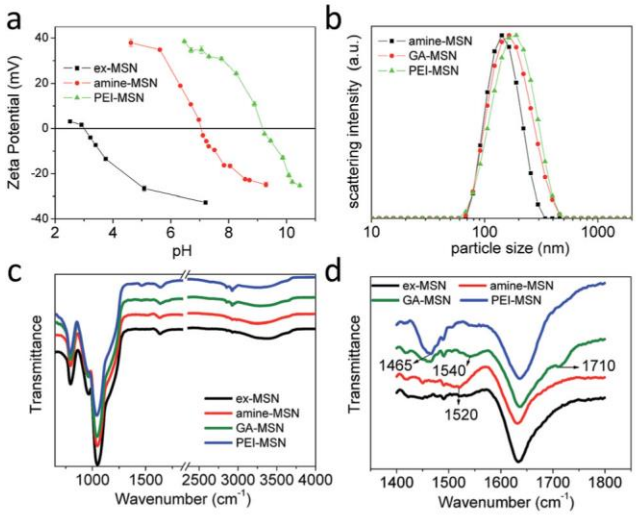

Fig. 8 Zeta potential (a), DLS size distributions (b) and FTIR spectra (c) of functionalized MSNs. The spectra in (d) are the enlarged part of (c).

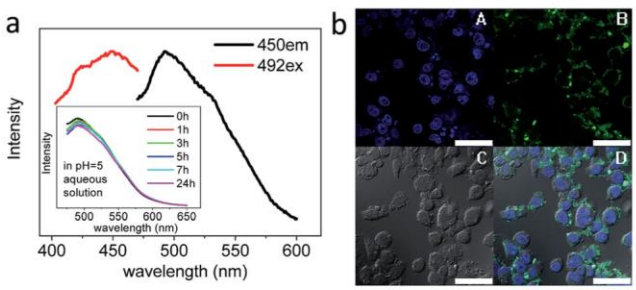

Fig. 9 (a) Emission and excitation fluorescence spectra of PEI–MSN. "em450" indicates an emission at 450 nm excitation. Similarly, "ex492" stands for an excitation spectrum at 492 nm detection. The inset is the emission spectra at 450 nm excitation obtained after incubation in pH = 5 aqueous solution for various times. (b) CLSM images of HeLa cells after incubation with 50 μg mL^{-1} PEI–MSN for 3 h. Image (D) is the merged picture of the blue channel from Hoechst (A), green channel from PEI–MSN (B), and the differential interference contrast channel (C). Scale bars are 50 μm.

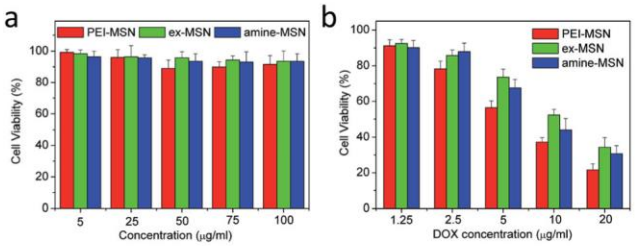

Fig. 10 HeLa cell viabilities after 24 h of incubation with MSNs (a) and DOX-loaded MSNs (b).

h of incubation with PEI–MSN, suggesting efficient cell uptake. The DOX-loaded particles are mainly located at the periphery of cell nuclei. After 4 h, the DOX concentration in the cytoplasm increases further. After 12 h, DOX diffusion into the cell nucleus can be observed. After 24 h, almost all DOX has been translocated to the cell nucleus, where it plays its anticancer role. These results demonstrate that PEI–MSN has excellent potential as an intracellular drug delivery system.

4. Conclusions

In summary, stellate MSNs with a particle size of 50–140 nm and a pore size of 2–20 nm are obtained easily by choosing suitable synthesis parameters. The particle formation follows a nucleation-growth process, in which the reaction kinetics greatly influences the particle size and mesoporous structure of the final products. Taking into account that parameters, such as the surfactant composition, reaction temperature and time, and reactant ratio, can be adjusted continuously, it is reasonable to deduce that both the particle size and the pore structure can be tailored accordingly. Moreover, these MSNs can be suitably modified with biofunctional groups/molecules, *e.g.* nontoxic low molecular weight PEI, and have demonstrated good intracellular delivery capability. Therefore, the excellent flexibility of the structure and surface chemistry endow these stellate MSNs with great prospects in drug delivery applications and will also facilitate further studies on various size/structure-dependent nanoparticle–cell interactions.

Acknowledgements

This work was financially supported by the Australian Research Council (ARC) through the Discovery Project program (DP130104459 and DP140104062). Lin Xiong acknowledges a scholarship from The University of Adelaide.

Notes and references

1 Q. He and J. L. Shi, *Adv. Mater.*, 2014, **26**, 391–411.
2 C. Argyo, V. Weiss, C. Bräuchle and T. Bein, *Chem. Mater.*, 2014, **26**, 435–451.
3 Q. He, Z. Zhang, F. Gao, Y. Li and J. L. Shi, *Small*, 2011, **7**, 271–280.
4 F. Lu, S.-H. Wu, Y. Hung and C.-Y. Mou, *Small*, 2009, **5**, 1408–1413.
5 L. Pan, Q. He, J. Liu, Y. Chen, M. Ma, L. Zhang and J. L. Shi, *J. Am. Chem. Soc.*, 2012, **134**, 5722–5725.
6 Y.-S. Lin and C. L. Haynes, *J. Am. Chem. Soc.*, 2010, **132**, 4834–4842.
7 Y. Gao, Y. Chen, X. Ji, X. He, Q. Yin, Z. Zhang, J. L. Shi and Y. Li, *ACS Nano*, 2011, **5**, 9788–9798.
8 A. Popat, J. Liu, Q. Hu, M. Kennedy, B. Peters, G. Q. Lu and S. Z. Qiao, *Nanoscale*, 2012, **4**, 970–975.
9 M. Bouchoucha, R. C. -Gaudreault, M.-A. Fortin and F. Kleitz, *Adv. Funct. Mater.*, 2014, **24**, 5911–5923.
10 W. Stöber, A. Fink and E. Bohn, *J. Colloid Interface Sci.*, 1968, **26**, 62–69.
11 Q. Cai, Z.-S. Luo, W.-Q. Pang, Y.-W. Fan, X.-H. Chen and F.-Z. Cui, *Chem. Mater.*, 2001, **13**, 258–263.
12 R. I. Nooney, D. Thirunavukkarasu, Y. Chen, R. Josephs and A. E. Ostafin, *Chem. Mater.*, 2002, **14**, 4721–4728.
13 C. E. Fowler, D. Khushalani, B. Lebeau and S. Mann, *Adv. Mater.*, 2001, **13**, 649–652.
14 Y. Han and J. Y. Ying, *Angew. Chem., Int. Ed.*, 2005, **44**, 288–292.
15 K. Suzuki, K. Ikari and H. Imai, *J. Am. Chem. Soc.*, 2004, **126**, 462–463.
16 J. Gu, W. Fan, A. Shimojima and T. Okubo, *Small*, 2007, **3**, 1740–1744.
17 Z.-A. Qiao, L. Zhang, M. Guo, Y. Liu and Q. Huo, *Chem. Mater.*, 2009, **21**, 3823–3829.
18 K. Möller, J. Kobler and T. Bein, *Adv. Funct. Mater.*, 2007, **17**, 605–612.
19 L. Jia, J. Shen, Z. Li, D. Zhang, Q. Zhang, C. Duan, G. Liu, D. Zheng, Y. Liu and X. Tian, *Int. J. Pharm.*, 2012, **439**, 81–91.
20 H. S. Shin, Y. K. Hwang and S. Huh, *ACS Appl. Mater. Interfaces*, 2014, **6**, 1740–1746.
21 I. I. Slowing, B. G. Trewyn and V. S. Y. Lin, *J. Am. Chem. Soc.*, 2007, **129**, 8845–8849.
22 S. B. Hartono, W. Gu, F. Kleitz, J. Liu, L. He, A. P. Middelberg, C. Yu, G. Q. Lu and S. Z. Qiao, *ACS Nano*, 2012, **6**, 2104–2117.
23 Y. Chen, C. Chu, Y. Zhou, Y. Ru, H. Chen, F. Chen, Q. He, Y. Zhang, L. Zhang and J. L. Shi, *Small*, 2011, **7**, 2935–2944.
24 D. Niu, Z. Ma, Y. Li and J. L. Shi, *J. Am. Chem. Soc.*, 2010, **132**, 15144–15147.
25 M. Mizutani, Y. Yamada, T. Nakamura and K. Yano, *Chem. Mater.*, 2008, **20**, 4777–4782.
26 F. Gao, P. Botella, A. Corma, J. Blesa and L. Dong, *J. Phys. Chem. B*, 2009, **113**, 1796–1804.
27 M.-H. Kim, H.-K. Na, Y.-K. Kim, S.-R. Ryoo, H. S. Cho, K. E. Lee, H. Jeon, R. Ryoo and D.-H. Min, *ACS Nano*, 2011, **5**, 3568–3576.
28 K. Zhang, L.-L. Xu, J.-G. Jiang, N. Calin, K.-F. Lam, S.-J. Zhang, H.-H. Wu, G.-D. Wu, B. Albela, L. Bonneviot and P. Wu, *J. Am. Chem. Soc.*, 2013, **135**, 2427–2430.
29 V. Polshettiwar, D. Cha, X. Zhang and J. M. Basset, *Angew. Chem., Int. Ed.*, 2010, **49**, 9652–9656.
30 X. Du and J. He, *Nanoscale*, 2012, **4**, 852–859.
31 J. Kecht, A. Schlossbauer and T. Bein, *Chem. Mater.*, 2008, **20**, 7207–7214.
32 H. Djojoputro, X. F. Zhou, S. Z. Qiao, L. Z. Wang, C. Z. Yu and G. Q. Lu, *J. Am. Chem. Soc.*, 2006, **128**, 6320–6321.

33 X. Du and J. He, *Langmuir*, 2011, **27**, 2972–2979.
34 Y. Chen, H. Chen, M. Ma, F. Chen, L. Guo, L. Zhang and J. L. Shi, *J. Mater. Chem.*, 2011, **21**, 5290.
35 F. Kleitz, W. Schmidt and F. Schüth, *Microporous Mesoporous Mater.*, 2001, **44–45**, 95–109.
36 T. Suteewong, H. Sai, M. Bradbury, L. A. Estroff, S. M. Gruner and U. Wiesner, *Chem. Mater.*, 2012, **24**, 3895–3905.
37 T. Yokoi, J. Wakabayashi, Y. Otsuka, W. Fan, M. Iwama, R. Watanabe, K. Aramaki, A. Shimojima, T. Tatsumi and T. Okubo, *Chem. Mater.*, 2009, **21**, 3719–3729.
38 T. Yokoi, T. Karouji, S. Ohta, J. N. Kondo and T. Tatsumi, *Chem. Mater.*, 2010, **22**, 3900–3908.
39 J. Wang, A. Sugawara-Narutaki, M. Fukao, T. Yokoi, A. Shimojima and T. Okubo, *ACS Appl. Mater. Interfaces*, 2011, **3**, 1538–1544.
40 J. L. Vivero-Escoto, I. I. Slowing, B. G. Trewyn and V. S. Y. Lin, *Small*, 2010, **6**, 1952–1967.
41 T. Xia, M. Kovochich, M. Liong, H. Meng, S. Kabehie, S. George, J. I. Zink and A. E. Nel, *ACS Nano*, 2009, **3**, 3273–3286.
42 J. M. Rosenholm, A. Meinander, E. Peuhu, R. Niemi, J. E. Eriksson, C. Sahlgren and M. Lindén, *ACS Nano*, 2009, **3**, 197–206.
43 C. Hom, J. Lu, M. Liong, H. Luo, Z. Li, J. I. Zink and F. Tamanoi, *Small*, 2010, **6**, 1185–1190.
44 A. Martin, G. Morales, F. Martinez, R. van Grieken, L. Cao and M. Kruk, *J. Mater. Chem.*, 2010, **20**, 8026–8035.
45 A. Martín, R. A. García, D. S. Karaman and J. M. Rosenholm, *J. Mater. Sci.*, 2013, **49**, 1437–1447.
46 W. Wei, L. Y. Wang, L. Yuan, Q. Wei, X. D. Yang, Z. G. Su and G. H. Ma, *Adv. Funct. Mater.*, 2007, **17**, 3153–3158.
47 T. G. Waddell, D. E. Leyden and M. T. DeBello, *J. Am. Chem. Soc.*, 1981, **103**, 5303–5307.
48 Z. Wang, H. Zhu, D. Li and X. Yang, *Colloids Surf., A*, 2008, **329**, 58–66.
49 E. S. Lee, Z. Gao and Y. H. Bae, *J. Controlled Release*, 2008, **132**, 164–170.
50 I. Migneault, C. Dartiguenave, M. J. Bertrand and K. C. Waldron, *BioTechniques*, 2004, **37**, 790–806.

3.3 Supplementary Information

This section is included in the thesis as supplementary information to section 3.2. It includes additional information which is not put in the main text of the published paper, but as electronic supplementary information freely accessible online.

Tunable Stellate Mesoporous Silica Nanoparticles for Intracellular Drug Delivery

Lin Xiong,[a] *Xin Du,*[a] *Bingyang Shi,*[a] *Jingxiu Bi,*[a] *Freddy Kleitz,*[b]

*and Shi Zhang Qiao**[a]

[a] School of Chemical Engineering, The University of Adelaide, Adelaide, SA 5005, Australia

[b] Department of Chemistry and Centre de Recherche sur les Matériaux Avancés (CERMA), Université Laval, Quebec City, QC G1V 0A6, Canada.

* Address correspondence to: s.qiao@adelaide.edu.au

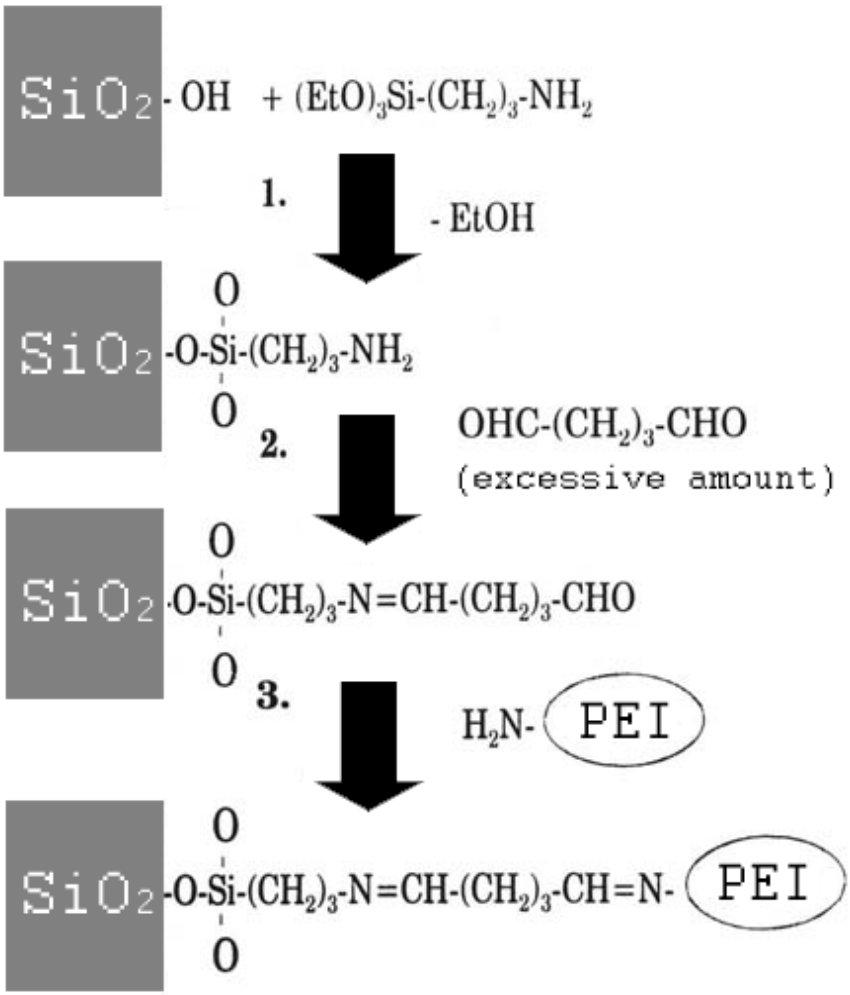

Fig. S1 Surface functionalization reactions of mesoporous silica nanoparticles.

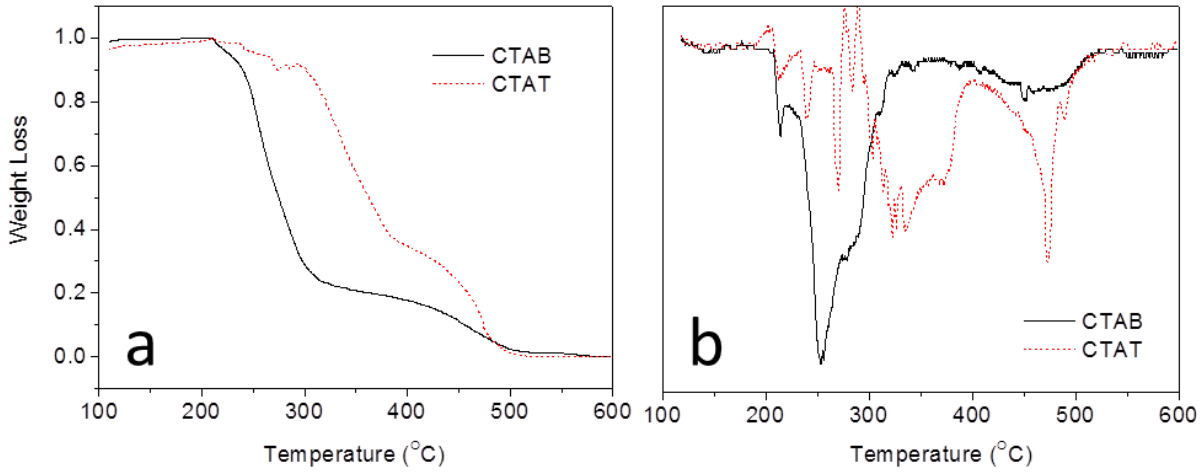

Fig. S2 TGA (a) and DTG (b) curves of CTAB and CTAT surfactants.

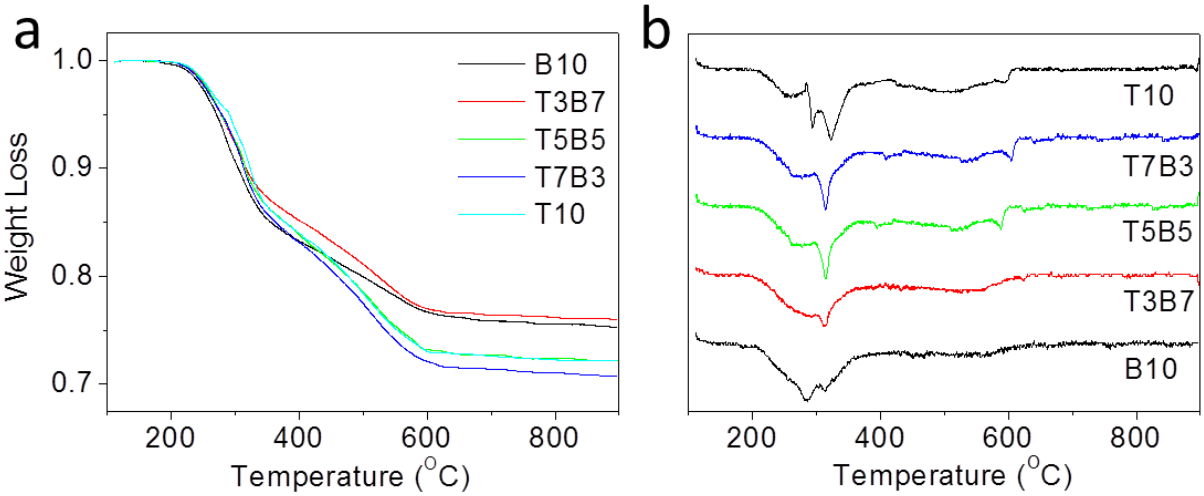

Fig. S3 TGA (a) and DTG (b) curves of as-prepared samples synthesized with mixed surfactants.

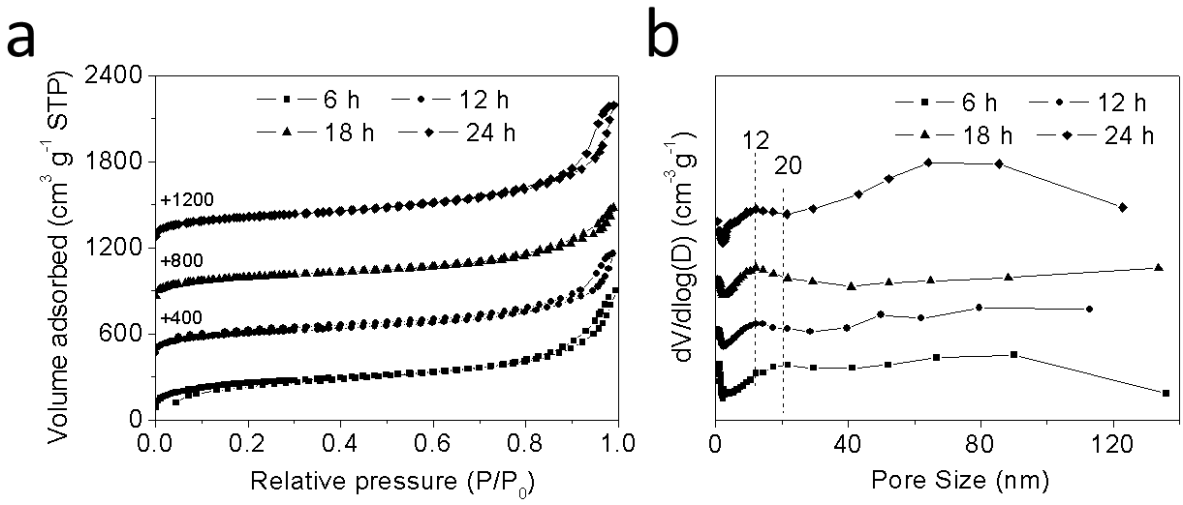

Fig. S4 Nitrogen adsorption-desorption isotherms (a) and respective pore size distribution curves (b) of stellate particles after various reaction times (6 h, 12 h, 18 h and 24 h) at 35 °C.

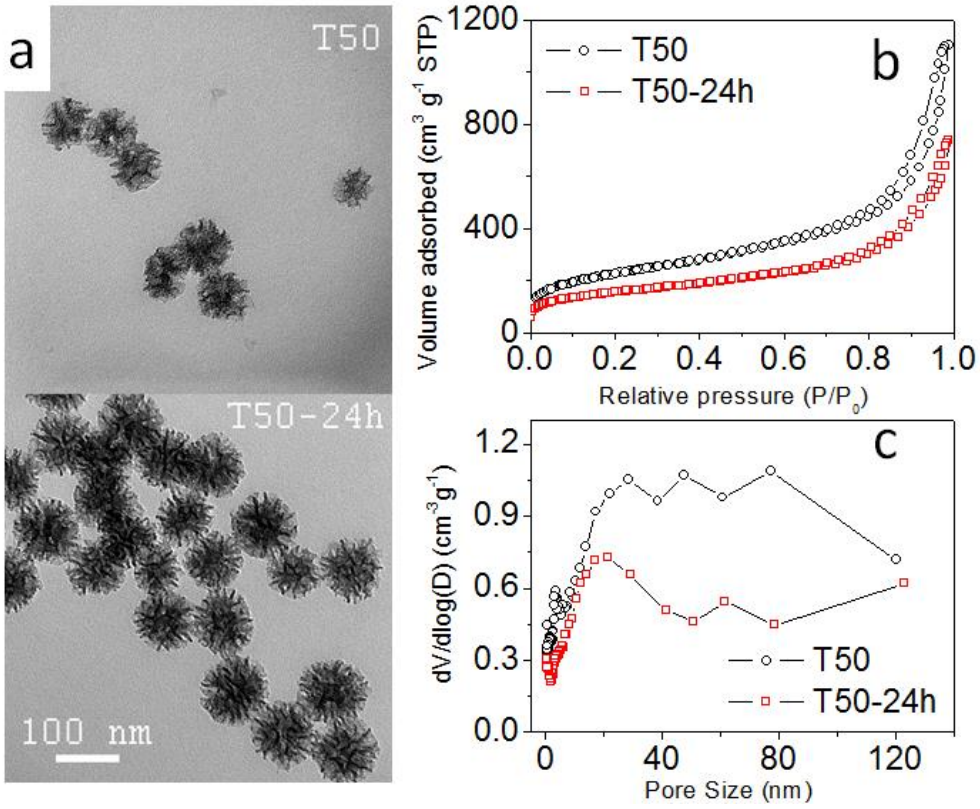

Fig. S5 TEM images (a), nitrogen adsorption-desorption isotherms (b) and respective BJH pore size distribution curves (c) of T50 and T50-24h.

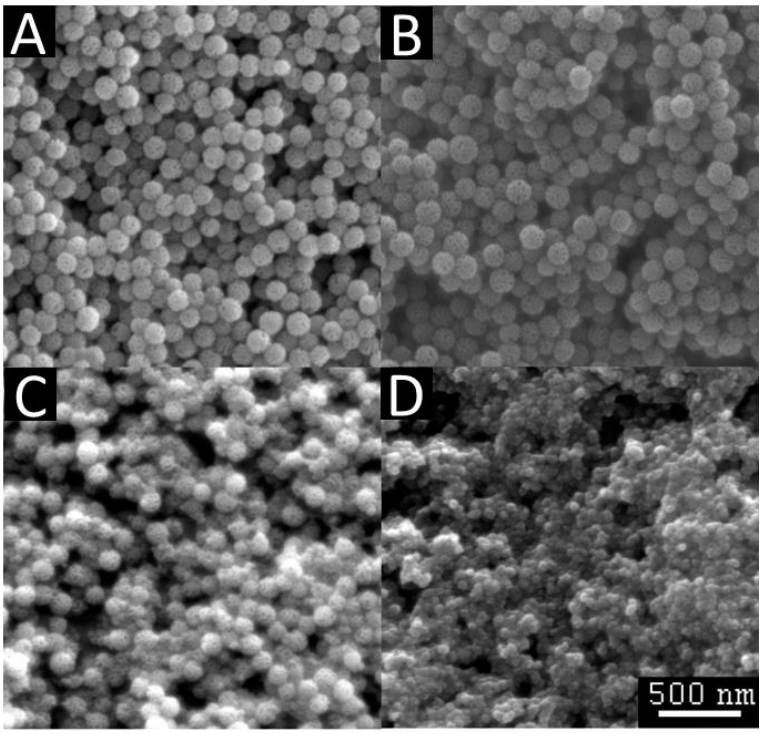

Fig. S6 SEM images of particles synthesized under various catalyst concentrations: (A) TC/2, (B) TC/4, (C) TC/8 and (D) TN.

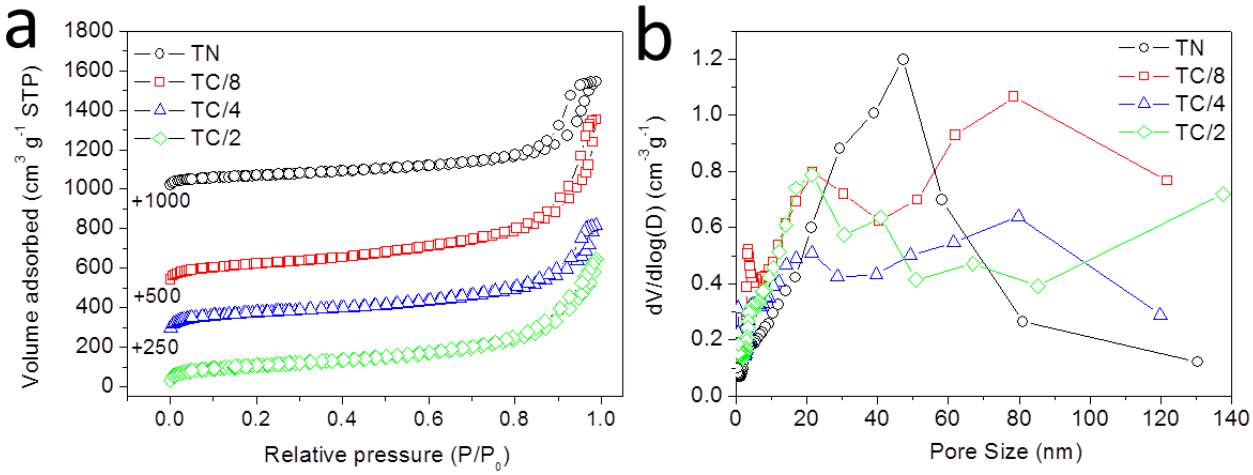

Fig. S7 Nitrogen adsorption-desorption isotherms (a) and respective pore size distribution curves (b) of particles synthesized under different TEA/TEOS ratio.

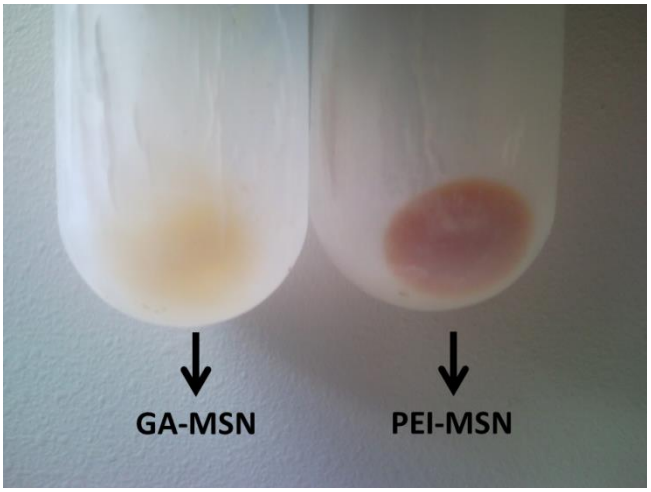

Fig. S8 Color changes of silica nanoparticles from white to yellow and brown after glutaraldehyde and PEI conjugation.

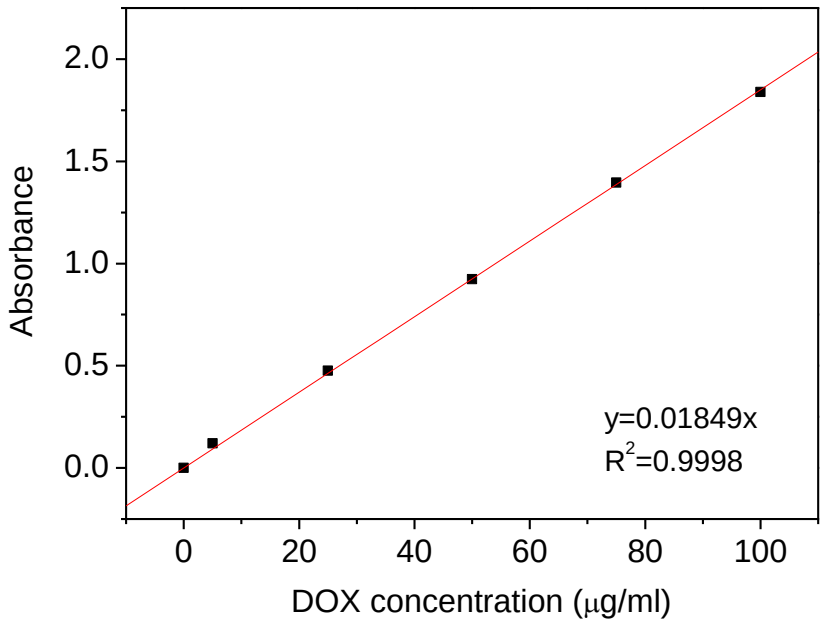

Fig. S9 Calibration curve of doxorubicin in water by absorbance measurements at 480 nm.

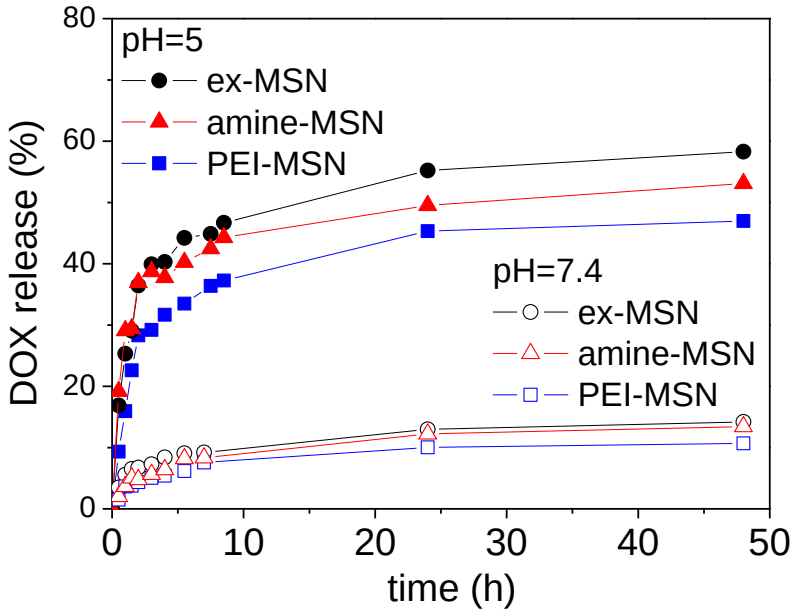

Fig. S10 Release profiles of DOX loaded silica nanoparticles at pH 7.4 and pH 5.0 at 37 °C.

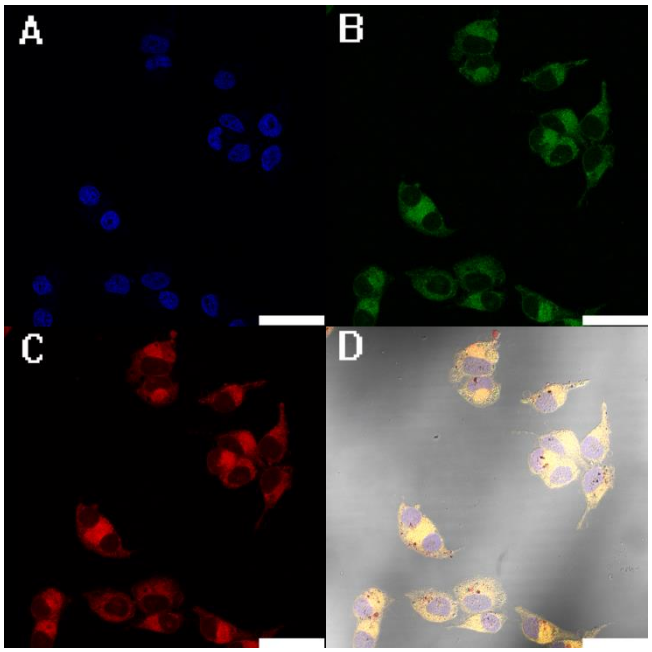

Fig. S11 CLSM images of Hela cells after incubation with 50 μg/ml DOX loaded PEI-MSN for 8 h. Image (D) is the merge picture of blue channel from Hoechst (A), green channel from PEI-silica (B), red channel from DOX (C) and the differential interference contrast (DIC) channel. Scale bars are 50 μm.

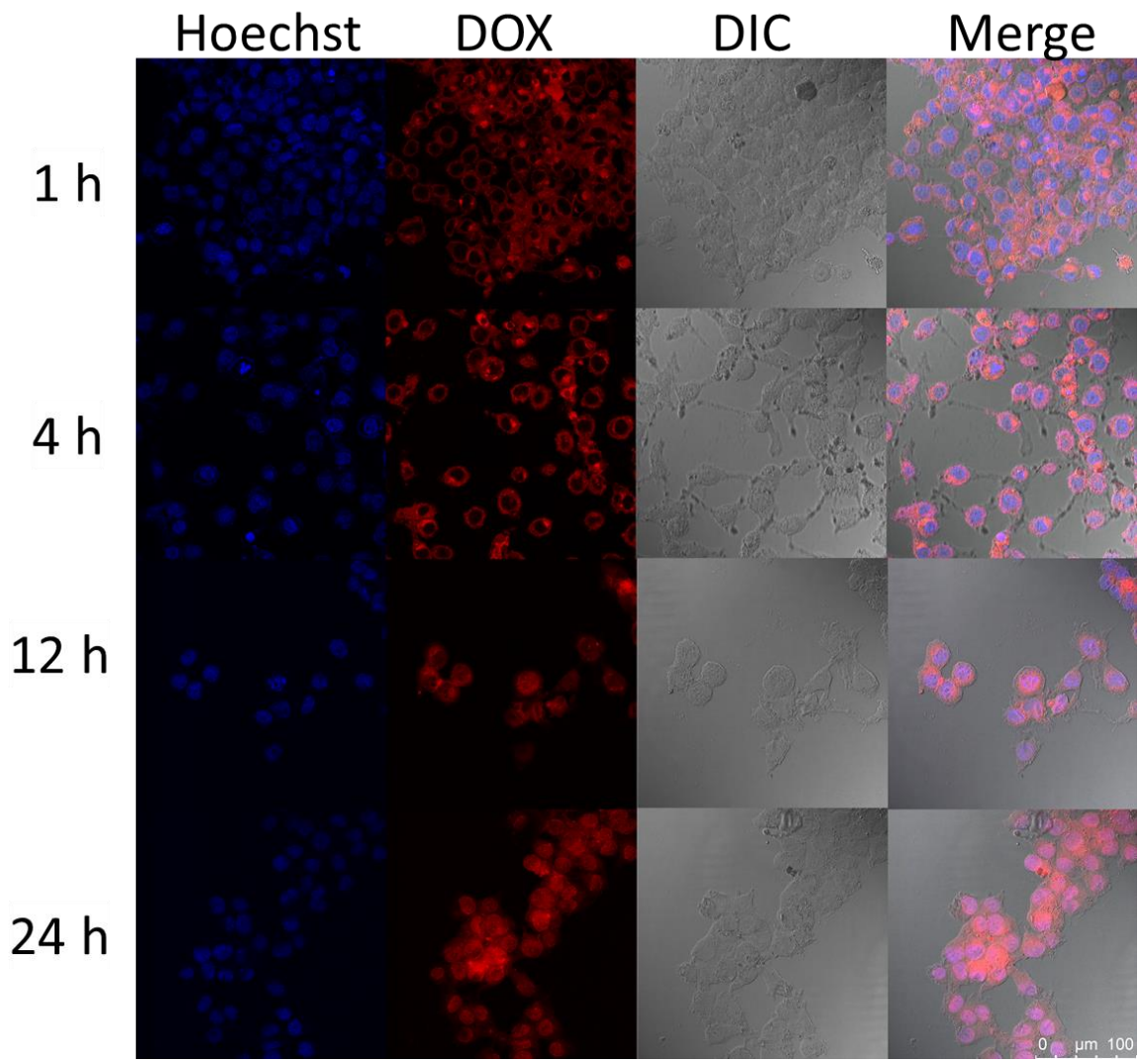

Fig. S12 CLSM images of Hela cells after incubation with DOX loaded PEI-MSN for different time periods (1 h, 4 h, 12 h and 24 h). The equivalent DOX concentration is 1 μg/ml.

Chapter 4 Cancer-Cell-Specific Nuclear Targeted Drug Delivery by Dual Ligand Modified Mesoporous Silica Nanoparticles

4.1 Introduction, Significance and Commentary

Nuclear-targeted anticancer drug delivery by mesoporous silica nanoparticles has emerged as a novel strategy for enhancing anti-cancer efficacy and overcoming drug resistance. However, almost all the previous nuclear-targeted mesoporous silica nanocarriers were using Trans-Activator of Transcription (TAT) peptide as the nuclear-targeting ligand, which could lead to unselective cellular uptake by healthy cells and severe side toxicity. Although several improved designs were proposed for TAT modified MSNs recently, they still had several disadvantages such as complex fabrication process and lack of versatility as cancer cell-specific nuclear-targeted delivery systems.

In this work, in order to circumvent the inherent limitation of TAT modified MSNs, a novel and simple dual-ligands strategy is developed for MSNs towards cancer cell-specific nuclear-targeted drug delivery. The dual-ligands modified MSNs are not only able to induce higher inhibition efficacy on cancer cells through active nucleus accumulation, but also reduce toxic side effects on non-cancer cells though receptor-mediated selective cellular uptake. The highlights and novelty of this work include:

1. Dexamethasone as the nuclear targeting ligand.

Dexamethasone was covalently conjugated to MSNs (~40 nm in size) for the first time by a mild reaction. The nuclear targeting function of dexamethasone was verified on MSNs and resulted in significantly enhanced cancer cell inhibition when the anticancer drug doxorubicin was loaded.

2. Cancer cell and nuclear dual-targeting on one carrier.

By combing co-condensation and post-grafting, both a cell targeting ligand (folic acid) and a nuclear targeting ligand (dexamethasone) were conjugated to the same MSN carrier. The two targeting ligands can work collaboratively without interference, and a cell-nucleus sequential targeting can be achieved with the dual-modified MSNs.

4.2 Cancer-Cell-Specific Nuclear-Targeted Drug Delivery by Dual-Ligand-Modified Mesoporous Silica Nanoparticles

This section is included in the thesis as it appears as a paper published by L. Xiong, X. Du, F. Kleitz and S. Z. Qiao. Cancer-Cell-Specific Nuclear-Targeted Drug Delivery by Dual-Ligand-Modified Mesoporous Silica Nanoparticles, *Small*, **2015**, 11, 5919.

Statement of Authorship

Title of Paper	Cancer-Cell-Specific Nuclear-Targeted Drug Delivery by Dual-Ligand-Modified Mesoporous Silica Nanoparticles
Publication Status	☑ Published ☐ Accepted for Publication ☐ Submitted for Publication ☐ Unpublished and Unsubmitted work written in manuscript style
Publication Details	First published: 1 October 2015 DOI: 10.1002/smll.201501056

Principal Author

Name of Principal Author (Candidate)	Lin Xiong (First Author)		
Contribution to the Paper	Research plan, material synthesis, material characterization, material performance assessment, manuscript drafting		
Overall percentage (%)	80 %		
Certification:	This paper reports on original research I conducted during the period of my Higher Degree by Research candidature and is not subject to any obligations or contractual agreements with a third party that would constrain its inclusion in this thesis. I am the primary author of this paper.		
Signature		Date	2016/11/22

Co-Author Contributions

By signing the Statement of Authorship, each author certifies that:

i. the candidate's stated contribution to the publication is accurate (as detailed above);
ii. permission is granted for the candidate in include the publication in the thesis; and
iii. the sum of all co-author contributions is equal to 100% less the candidate's stated contribution.

Name of Co-Author	Dr. Xin Du		
Contribution to the Paper	Assistance with research plan		
Signature		Date	16-Nov-2016

Name of Co-Author	Prof Freddy Kleitz		
Contribution to the Paper	Assistance with manuscript revision		
Signature		Date	19-Nov-2016

Name of Co-Author	Prof Shi Zhang Qiao (Corresponding Author)		
Contribution to the Paper	Design of the project, organization of the research and supervision, manuscript revision		
Signature		Date	28/4/2016

Please cut and paste additional co-author panels here as required.

Cancer-Cell-Specific Nuclear-Targeted Drug Delivery by Dual-Ligand-Modified Mesoporous Silica Nanoparticles

*Lin Xiong, Xin Du, Freddy Kleitz, and Shi Zhang Qiao**

In the war against cancer, chemotherapy is presently the most common treatment. However, its efficiency is hampered by severe toxic side effects and the emergence of drug resistance. To overcome the limitation of traditional chemotherapy, the concept of nanoparticle-mediated drug delivery has attracted a lot of research interests in the recent years. Among various nanosize constructs, mesoporous silica nanoparticles (MSNs) with good biocompatibility, well-developed mesoporosity, and versatile surface functionalization show great potential for reducing toxic side effects of chemotherapeutic drugs and enhancing anticancer efficacy.[1–3] To minimize side effects of highly toxic anticancer drugs, two general categories of approaches are usually adopted for MSN-based drug carriers. One is to install various smart "gates" on the MSNs so that the drugs can only be released under a specific stimulus, e.g., pH, enzyme, light, or temperature. The other one is to take advantage of the targeting capability of the nanocarriers to deliver the drugs selectively into cancer cells. For example, MSNs with sizes between 30 and 200 nm can accumulate passively in tumor parts through the enhanced permeability and retention effect of leaky tumor vasculature. Besides, various biologic targeting moieties (antibodies, peptides, aptamers, and small molecules) can be conjugated to the external surface of MSNs to achieve active targeting.[4]

In the meantime, different strategies for enhancing anticancer efficacy and overcoming drug resistance have been developed for MSN-based delivery systems, including codelivery of multiple drugs, increasing drug payload using hollow structures, and nuclear-targeted drug delivery.[3] Among these strategies, nuclear-targeted drug delivery is of particular interest because the nuclei of tumor cells are not only the core of cell transcription function but also the exact place where many chemotherapeutic drugs, such as doxorubicin (DOX), play their anticancer role. The first example of nuclear-targeted delivery using MSNs was realized through transactivator of transcription (TAT) peptide modification,[5] and this strategy was subsequently proven to be also effective against multidrug resistant cancer cells.[6] Although the anticancer efficiency was improved significantly by nuclear-targeted MSNs in these initial studies, a serious limitation of TAT-modified nuclear-targeted carriers is that they could translocate quickly into almost any living cells,[7] which means normal cells will also be penetrated easily if the powerful function of TAT is not carefully controlled. Therefore, a key challenge is to achieve cancer cell targeting and nucleus targeting simultaneously. Very recently, several dual targeting MSN carriers have been proposed subject to further modification on the TAT system.[8–10] In these reports, the TAT targeting ligand is temporarily "masked" before cellular uptake of the carrier and then reexposed after carrier internalization. Nevertheless, these carriers are still not perfect. In several of the designs, the cellular uptake of drug carriers is still nonselective, even if nucleus accumulation is activated selectively in the intracellular environment of cancer cells.[3,10] In some other designs, the switch *on–off* of nucleus targeting depends on the presence of some specific enzyme, or a complex peptide modification is involved.[9,10] Therefore, it is still challenging to construct a simple and versatile cancer-cell-specific nuclear-targeted delivery system (CCNTDS) based on MSNs.

Compared with MSNs, gold nanoparticles were explored much earlier concerning their interaction with cell nucleus. In early studies, both peptide targeting cell nucleus and peptide targeting cell membrane receptors were conjugated to the gold nanoparticles, which resulted in successful translocation of the nanoparticles into the nucleus of a specific cell line.[11,12] These reports suggested that dual argeting ligand modification could be an effective approach to cell-specific nuclear-targeted delivery. However, surprisingly, this strategy was seldom adapted to MSNs despite their unique advantages of biocompatibility and nanoporous structure.[13]

In the present study, a novel kind of MSNs modified with dual ligands, i.e., folic acid (FA) and dexamethasone (DEX), is proposed as efficient CCNTDS according to the methodology illustrated in **Scheme 1**. While the tumor cell targeting capability of MSNs modified with folic acid has been well documented,[14,15] the conjugation of dexamethasone to the MSNs as a nuclear targeting ligand and its collaborative function with the other targeting ligand, to the best of our knowledge, have not been explored. Dexamethasone is a potent glucocorticoid which binds to the glucocorticoid receptor (GR), a nuclear receptor expressed in almost every cell, after its entry

L. Xiong, Dr. X. Du, Prof. S. Z. Qiao
School of Chemical Engineering
The University of Adelaide
Adelaide, SA 5005, Australia
E-mail: s.qiao@adelaide.edu.au
Prof. F. Kleitz
Department of Chemistry and Centre de
Recherche sur les Matériaux Avancés (CERMA)
Université Laval
Quebec City, QC G1V 0A6, Canada

DOI: 10.1002/smll.201501056

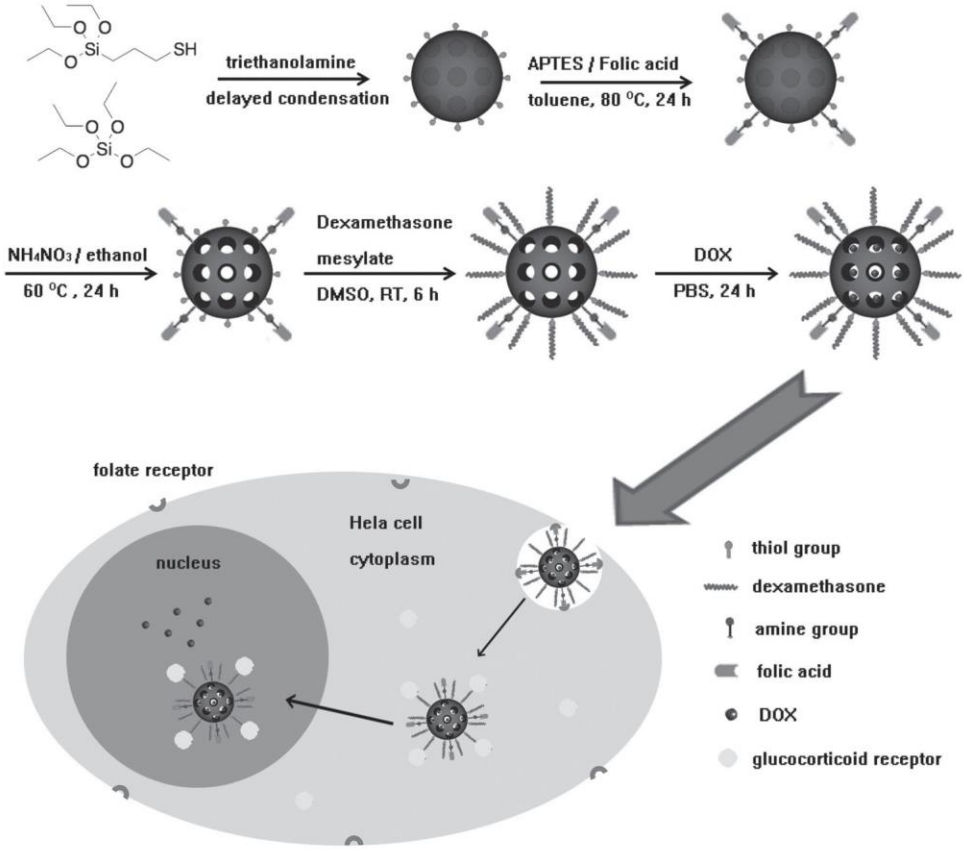

Scheme 1. Construction of mesoporous silica nanoparticle-based cancer-cell-specific nuclear-targeted drug carriers and the proposed delivery process of DOX into Hela cells.

into cytoplasm.[16] The formed DEX-GR complex is then actively transported from the cytoplasm into the nucleus.[17] Meanwhile, DEX is capable of inducing nuclear pore dilation up to 60 nm during the translocation process.[18] In gene transfection research, DEX has previously been conjugated to various nonviral gene carriers, such as polyethylenimine, polyamidoamine, and solid lipids, to enhance nuclear transport of the gene complex.[19–23] More importantly, neither our experiment nor previous literature has observed any significant effect of DEX upon cellular uptake,[24] which could thus be modulated separately by a cell targeting ligand in order to facilitate selective cancer cell uptake. Given the above considerations, we first fabricated MSNs modified with both folic acid and dexamethasone then examined cellular uptake and intracellular location of these nanoparticles. Finally, these MSNs were loaded with doxorubicin and their potential of application as drug delivery carriers was evaluated.

The synthesis and designation of samples are detailed in Scheme 1 and Scheme S1 (see the Supporting Information for details). According to previous reports, the size of MSNs should be smaller than 50 nm for successful nuclear transport directed by nuclear localization signals (NLSs).[5,25] Therefore, the size and morphology of the obtained MSNs were first verified by transmission electron microscopy (TEM), as shown in **Figure 1**a,b. The unmodified sample pMSN consists of nanoparticles ≈40 nm in size and possesses an irregular mesoporous structure. For the FA and DEX dual-modified sample FA-MSN-DEX, the size of nanoparticles is almost the same as the unmodified ones, but a reduction in porosity can be identified from the difference in the contrast in the TEM images, which was further confirmed by nitrogen sorption analysis. As shown in Figure 1c,d and **Table 1**, both the pore volume and specific surface area of the modified nanoparticles decrease with increasing steps of functionalization. From the pore size distribution curves, the pore sizes of unmodified pMSN and thiol-modified MSN-SH material are 2.6 and 2 nm, respectively. The smaller pore size of MSN-SH compared to pMSN is in line with previous reports using a similar cocondensation method.[26] Compared with MSN-SH, the pore sizes of FA-MSN-SH and FA-MSN-DEX are almost unchanged, which suggests that the subsequent functionalization mainly occurs on the external surface of the nanoparticles.[27] The correct location of targeting moieties such as FA and DEX on the external surface is crucial for their normal function in physiological environment. Nevertheless, there is still some degree of pore blockage leading to a reduced pore volume

Table 1. Structure parameters of mesoporous silica nanoparticles derived from nitrogen physisorption.

Sample	Surface area [$m^2 g^{-1}$]	Pore volume [$cm^3 g^{-1}$]	Pore size [nm]
pMSN	609	0.46	2.6
MSN-SH	573	0.41	2.0
FA-MSN-SH	421	0.33	2.0
FA-MSN-DEX	352	0.25	2.0

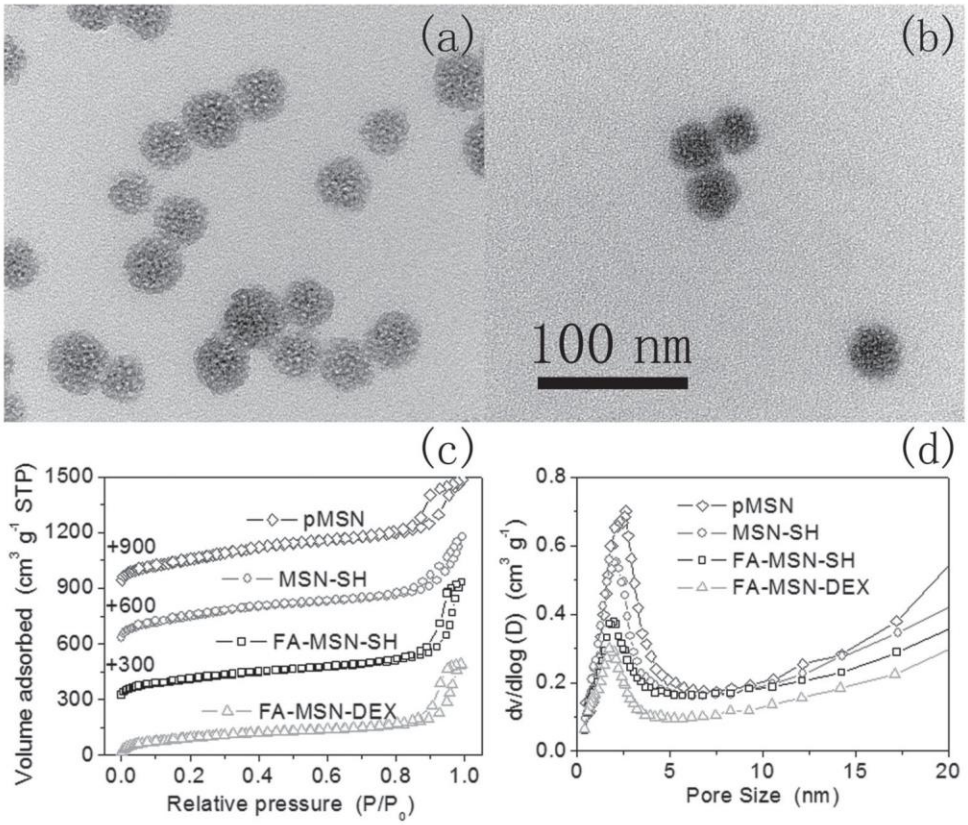

Figure 1. TEM images of a) pMSN and b) FA-MSN-DEX. Nitrogen adsorption–desorption isotherms measured at –196 °C c) and the corresponding pore size distributions d) of the different mesoporous silica nanoparticles.

and lower specific surface area, which is common for postsynthetic functionalization of mesoporous silica.[28] The particle sizes of MSNs are also determined from dynamic light scattering (DLS) as shown in **Table 2** and Figure S1 (Supporting Information). The average particle sizes measured by DLS are generally larger than those observed from TEM, which is attributed to hydration layers around the particle surface in aqueous solution.[29] The larger DLS sizes of FA-MSN-SH and FA-MSN-DEX than MSN-SH suggest the presence of FA and DEX groups on the external particle surfaces. From the zeta potential measurement shown in Table 2 and Figure S2 (Supporting Information), both pMSN and MSN-SH appear highly negatively charged owing to the deprotonation of —OH and —SH groups.[30] After conjugation with FA, the particle zeta potential value changes from negative to positive,[31] which could be attributed to the protonation of amine groups in FA. Further reaction with dexamethasone methylate only slightly affects the surface charge.[32]

Table 2. Hydrodynamic particle diameters and zeta potentials of mesoporous silica nanoparticles dispersed in de-ionized water.

Sample	Zeta potential [mV]	Average particle size [nm]	Polydispersity index
pMSN	–39.2	54	0.048
MSN-SH	–48.5	54	0.076
FA-MSN-SH	+28.6	76	0.085
FA-MSN-DEX	+24.0	82	0.070

The successful surface functionalization was further confirmed by various spectroscopy characterizations. In **Figure 2**a, the thiol group of MSN-SH shows a distinctive Raman peak ≈2580 cm^{-1}, which is absent for pMSN.[33] Moreover, other peaks corresponding to Si—C at 1305 cm^{-1} and C—S at 653 cm^{-1} can also be observed for MSN-SH.[33] After surfactant extraction from the as-prepared sample, a significant reduction of intensity of the bands occurs between 2800 and 3000 cm^{-1}, which corresponds to C—H bonds of surfactant template. The residue C—H signal may be mainly due to the mercaptopropyl groups. The presence of sulfur in MSN-SH is also reflected by energy-dispersive X-ray spectroscopy results in Figure S3 (Supporting Information). In UV–vis spectra shown in Figure 2b, while pMSN does not show any absorption peaks in the wavelength range from 280 to 800 nm, FA-MSN-SH shows a strong absorption peak at 287 nm and a broad shoulder at 380 nm, which are assigned to the π–π^* transition in carboxylate groups and n–π^* transition in enone rings, respectively.[34] The Fourier transform infrared (FTIR) spectra of all the three samples presented in Figure 2c show typical peaks of silica at 789 and 1040 cm^{-1}, corresponding to symmetric and asymmetric Si—O vibrations, respectively.[14] The FA-MSN-SH shows broad absorption bands ≈1510 and 1610 cm^{-1}, which are assigned to amines and phenyl rings after FA conjugation, respectively.[35] After DEX conjugation, absorption peaks at 1666 and 1730 cm^{-1} become pronounced, which correspond to vibrations of conjugated and unconjugated C—O bonds in DEX groups, respectively.[36] Moreover, proper DEX

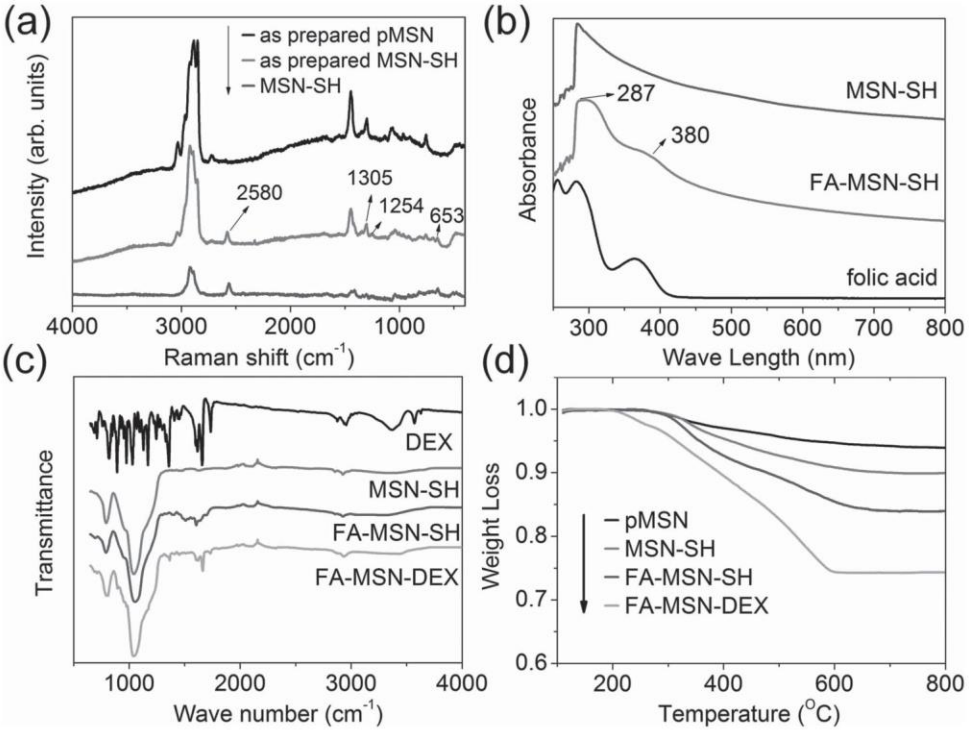

Figure 2. Raman, UV–vis absorption, FTIR spectra, and thermogravimetric curves of different mesoporous silica nanoparticles.

conjugation through reaction with mercaptopropyl group was also corroborated by the solid state ^{13}C NMR results (Figure S4, Supporting Information). Finally, thermogravimetric analysis of MSNs is shown in Figure 2d. As expected, the weight loss observed between 110 and 800 °C increases following more functionalization steps being carried out. Assuming the solid residue after calcination at 800 °C is pure silica, the quantities of grafted FA and DEX groups on FA-MSN-DEX are estimated to be 0.17 and 0.43 mmol g^{-1}, respectively (see the Supporting Information for calculation).

For drug delivery application, the prerequisite for a drug carrier is minimal cytotoxicity to avoid adverse side effects. Thus, the cellular toxicity of FA-MSN-DEX was first evaluated by 3-[4,5-dimethylthialzol-2-yl]-2,5-diphenyltetrazolium bromide (MTT) assay on both cancerous Hela and noncancerous HEK293 cells. In order to elucidate the role of different targeting ligands, unmodified pMSN and only folic acid-modified FA-MSN samples were also evaluated as control samples in the subsequent biological tests. As evident from the MTT results shown in Figure S5 (Supporting Information), all of the three kinds of MSNs show good biocompatibility toward the two different cell lines below a particle concentration of 100 μg mL^{-1}, with cell viability above 80% even after 48 h incubation. This could be explained from the fact that: (1) mesoporous silica nanoparticles have been documented to be biocompatible.[5] (2) Folate is an essential vitamin required by virtually all cells and dexamethasone itself has been approved as antiinflammatory drug.[37,38] Therefore, these results suggest FA-MSN-DEX could be used as a safe drug carrier.

Next, the cellular uptake of fluorescein isothiocyanate (FITC) labeled MSNs was checked by confocal laser scanning microscopy (CLSM) and flow cytometry. As shown in **Figure 3** and Figure S6 (Supporting Information), all the three kinds of MSNs were internalized by Hela cells after 24 h of incubation. Furthermore, compared with pMSN, a significantly higher fluorescence can be observed inside the cells

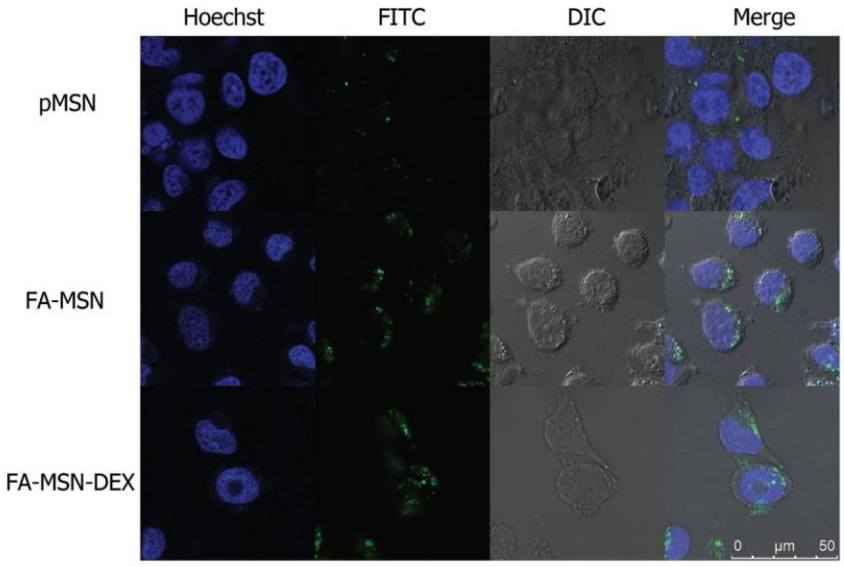

Figure 3. CLSM images of Hela cells after 24 h of incubation with 50 μg mL^{-1} FITC-labeled mesoporous silica nanoparticles.

NANO MICRO small

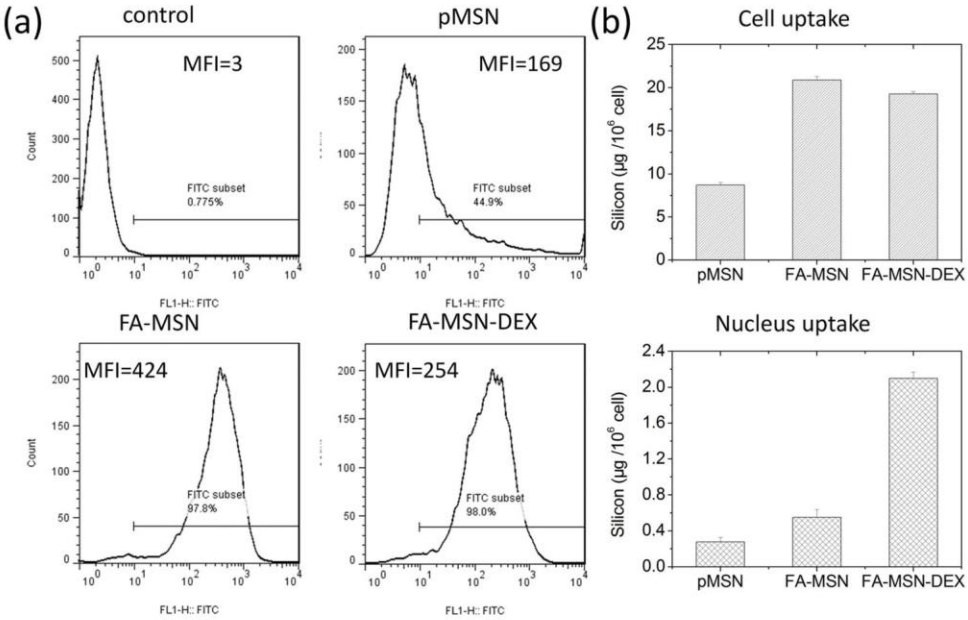

Figure 4. Flow cytometry a) and ICP-MS b) analysis of the uptake by Hela cells after 24 h of incubation with 50 μg mL^{-1} mesoporous silica nanoparticles. The histograms in (a) show distributions of events on the green (FL1) channel. MFI: mean fluorescent intensity.

incubated with FA-MSN and FA-MSN-DEX. This trend is also confirmed by flow cytometry measurement, as shown by the fluorescence histograms (**Figure 4**a). Compared with the control sample without nanoparticle treatment, the percentage of Hela cells with positive FITC signals are about 45%, 98%, and 98% for the samples treated with pMSN, FA-MSN, and FA-MSN-DEX, respectively. To verify the mechanism of the enhanced cellular uptake of FA-MSN and FA-MSN-DEX, folate receptor negative HEK293 cells were also treated with the three kinds of MSNs. As shown in Figure S7a (Supporting Information), this time the differences between MSNs in terms of cellular uptake are much smaller with HEK293. These results suggest that the enhanced cellular uptake of FA-MSN and FA-MSN-DEX over pMSN by the Hela cells should be mainly attributed to folate receptor-mediated endocytosis.[39] Meanwhile, cellular uptakes of FA-MSN and FA-MSN-DEX are close to each other with both Hela and HEK293. This indicates the DEX functionalization has only a small influence on the cellular uptake of MSNs, which is further corroborated by directly comparing the uptake of MSN-SH by Hela cells before and after conjugation with DEX. As shown by flow cytometry measurement (Figure S7b, Supporting Information) and confocal images (Figure S8, Supporting Information), both MSN-SH and its only DEX modified counterpart, MSN-DEX, show very low cellular uptake on Hela cells. This feature makes DEX a quite different nuclear targeting ligand from the TAT peptide, which enhances cellular uptake significantly but unselectively.[40] More interestingly, as evidenced from Figure 3, the FA-MSN-DEX particles can be observed in the blue nuclear region in some of the Hela cells. The Z-stack scans in Figure S9 (Supporting Information) confirm that some FA-MSN-DEX particles have entered the nucleus rather than remaining on the nucleus surface. In contrast, pMSN and FA-MSN particles are only observed in the cytoplasm region of the Hela cells.

The cellular and nuclear uptake of silicon element (from the MSN structure) was quantified by inductively coupled plasma mass spectrometry (ICP-MS) (Figure S10, Supporting Information). As demonstrated in Figure 4b, silicon uptakes of cells treated by FA-MSN and FA-MSN-DEX are 2.4 and 2.2 times higher than that by pMSN, and the silicon quantity in the nuclei of cells treated by FA-MSN-DEX is nearly four times that by FA-MSN. These results suggest that for FA-MSN-DEX nanoparticles not only the FA group can function normally as an endocytosis promoter toward the cancer cells overexpressing folate receptor but also the DEX groups can facilitate transport from cytoplasm to nucleus, in line with what was reported previously in the case of several polymeric delivery systems.[19–21]

In vitro loading and release of DOX with the different MSNs were monitored by UV–vis adsorption (Figure S11, Supporting Information). The DOX loading capability of pMSN, FA-MSN, and FA-MSN-DEX are about 20, 12, and 10 wt%, respectively. The reduced DOX loading capability of the modified samples compared to pMSN could be related to their reduced pore volume and lower surface area. Nevertheless, the loading capability of FA-MSN-DEX is still higher than that of several recently reported silica-based delivery systems[41,42] and an optimal balance between effective targeting and high drug loading may be achieved by further tuning the quantity of the functional groups.[43] In vitro release tests show that the three kinds of MSNs display similarly sustained and pH-dependent release profiles with faster drug release at pH 5.0 than at pH 7.4, which could be attributed to the increased solubility of DOX at lower pH (Figure S12, Supporting Information).[44] Besides, the surface-modified samples show lower DOX release rate compared to pMSN, which suggests the functional groups on the external surface may also affect the outward diffusion of DOX.

www.MaterialsViews.com

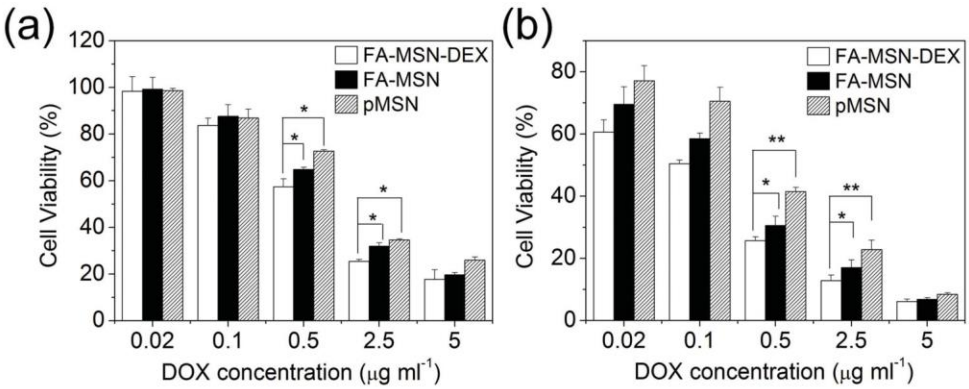

Figure 5. Viability of Hela cells after a) 24 h a) and b) 48 h of incubation with different DOX-loaded mesoporous silica nanoparticles. $^{*}P < 0.05$; $^{**}P < 0.01$.

The anticancer efficacy of DOX-loaded MSNs was evaluated by MTT assay with the Hela cell line. As evidenced by **Figure 5**, DOX-loaded FA-MSN-DEX shows higher cytotoxicity than the other two carriers under equivalent DOX dosage. As the incubation time increases from 24 to 48 h, the advantage of FA-MSN-DEX for the cancer cell inhibition becomes more significant. The calculated IC50 (half maximal inhibitory concentration) at 48 h for FA-MSN-DEX, FA-MSN, and pMSN are 0.78, 1.14, and 1.58 μg mL^{-1}, respectively. Considering that the FA-MSN-DEX does not show faster release rate than the other carriers, as seen in Figure S12 (Supporting Information), the higher anticancer efficacy of FA-MSN-DEX should be related to its enhanced cellular uptake and nuclear targeting capability. To verify this hypothesis, Hela cells treated with different DOX-loaded carriers were subjected to CLSM observations. As shown in **Figure 6** and Figure S13 (Supporting Information), after 12 h incubation, all the three types of MSN carriers were internalized in significant quantities, which are reflected by the strong red fluorescence of DOX in the cytoplasm. However, with a closer look, notable differences between these samples can be identified. In cells that were treated with pMSN, there is little red fluorescence in the blue nuclear region stained by Hoechst dye. In contrast, in cells treated by FA-MSN, a gradual diffusion of DOX from the periphery to the centre of cell nuclei is identifiable. This diffusion is also an indication of the release of DOX from the carrier because FA-MSN is not able to enter the cell nuclei (Figure 3). Although FA-MSN shows a slower release profile than pMSN in vitro as shown in Figure S12 (Supporting Information), the nuclear accumulation of DOX in cells treated by FA-MSN seems higher than that by pMSN in the cellular environment, which could be attributed to the enhanced cellular uptake of FA-MSN by the cancer cells. In cells treated by FA-MSN-DEX, several scattered red spots are present in the nuclear region, which can be assigned to DOX-loaded nanoparticles that have entered the nuclei. For this sample, the red fluorescence of DOX in

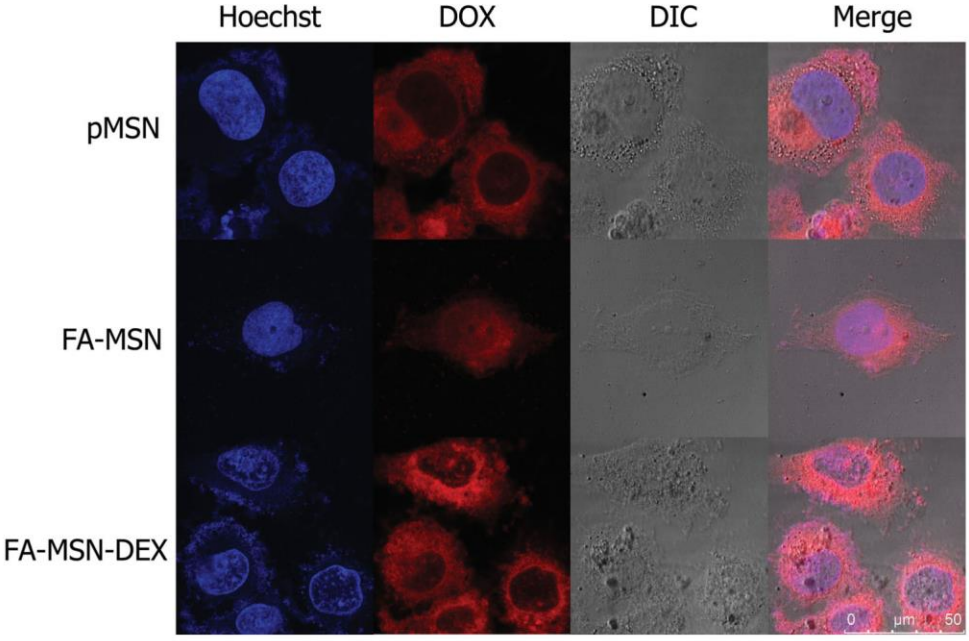

Figure 6. CLSM images of Hela cells after 12 h of incubation with DOX loaded mesoporous silica nanoparticles. The equivalent DOX concentration in all the three samples was 5 μg mL^{-1}.

the nuclear region is not as extensive as in the cells treated with FA-MSN. However, this should not be simply assigned to lower DOX accumulation in the nucleus of cells that were treated by FA-MSN-DEX because the fluorescence of DOX will be quenched dramatically after its intercalation into the DNA.[45] Quite the contrary, the morphology of the nuclei suggests the highest inhibition effectiveness of DOX delivered by FA-MSN-DEX. While the nuclei of cells treated with DOX-loaded pMSN and FA-MSN still show almost intact morphology after 12 h of incubation, nuclear fragmentation, and condensation, characterized by the disintegrated blue region, became identifiable in the cells treated with FA-MSN-DEX.[46] Therefore, the results of Figure 5 can be explained by the fact that DOX released from the intranuclear FA-MSN-DEX nanoparticles can intercalate into DNA of cancer cells more readily and thus induce much higher cytotoxicity. These results confirm that the dual targeting ligand modification of MSNs can indeed also significantly improve the delivery efficiency of DOX.

To summarize, a cell targeting ligand, folic acid, and a nucleus targeting ligand, dexamethasone, were easily conjugated to 40 nm mesoporous silica nanoparticles. The resulting dual-modified MSNs are able to not only enhance the inhibition efficacy of DOX on Hela cells through active nucleus accumulation but also reduce toxic side effects on noncancer cells through receptor-mediated selective cellular uptake. Therefore, it is proven that the two targeting moieties can operate collaboratively to achieve a cell-nucleus sequential targeting using MSNs. In contrast to previous research efforts focusing on TAT, the use of dexamethasone as an alternative intracellular nucleus targeting ligand and its cofunction with another cell targeting ligand on MSNs were first explored in this contribution. Further work is still needed to optimize the ratio between the two targeting ligands and to investigate the combination of dexamethasone with other cell targeting ligands, such as hyaluronic acid or transferrin. Consequently, a more simple and versatile cell-specific nucleus-targeted drug delivery strategy can be anticipated in the near future.

Supporting Information

Supporting Information is available from the Wiley Online Library or from the author.

Acknowledgements

This work was financially supported by the Australian Research Council (ARC) through the Discovery Project program (DP130104459 and DP140104062). F.K. acknowledges financial support from the Natural Sciences and Engineering Research Council of Canada (NSERC).

[1] M. Vallet-Regi, A. Rámila, R. P. del Real, J. Pérez-Pariente, *Chem. Mater.* **2001**, *13*, 308.
[2] M. Vallet-Regí, F. Balas, D. Arcos, *Angew. Chem. Int. Ed.* **2007**, *46*, 7548.
[3] Q. He, J. L. Shi, *Adv. Mater.* **2014**, *26*, 391.
[4] C. Argyo, V. Weiss, C. Brauchle, T. Bein, *Chem. Mater.* **2014**, *26*, 435.
[5] L. Pan, Q. He, J. Liu, Y. Chen, M. Ma, L. Zhang, J. L. Shi, *J. Am. Chem. Soc.* **2012**, *134*, 5722.
[6] L. Pan, J. Liu, Q. He, L. Wang, J. L. Shi, *Biomaterials* **2013**, *34*, 2719.
[7] E. Jin, B. Zhang, X. Sun, Z. Zhou, X. Ma, Q. Sun, J. Tang, Y. Shen, E. Van Kirk, W. J. Murdoch, M. Radosz, *J. Am. Chem. Soc.* **2013**, *135*, 933.
[8] Z. H. Li, K. Dong, S. Huang, E. G. Ju, Z. Liu, M. L. Yin, J. S. Ren, X. G. Qu, *Adv. Funct. Mater.* **2014**, *24*, 3612.
[9] Z. Y. Li, Y. Liu, J. J. Hu, Q. Xu, L. H. Liu, H. Z. Jia, W. H. Chen, Q. Lei, L. Rong, X. Z. Zhang, *ACS Appl. Mater. Interfaces* **2014**, *6*, 14568.
[10] J. Li, F. Liu, Q. Shao, Y. Min, M. Costa, E. K. Yeow, B. Xing, *Adv. Healthcare Mater.* **2014**, *3*, 1230.
[11] A. G. Tkachenko, H. Xie, D. Coleman, W. Glomm, J. Ryan, M. F. Anderson, S. Franzen, D. L. Feldheim, *J. Am. Chem. Soc.* **2003**, *125*, 4700.
[12] B. Kang, M. A. Mackey, M. A. El-Sayed, *J. Am. Chem. Soc.* **2010**, *132*, 1517.
[13] L. Pan, J. Liu, Q. He, J. L. Shi, *Adv. Mater.* **2014**, *26*, 6742.
[14] H. X. Wu, G. Liu, S. J. Zhang, J. L. Shi, L. X. Zhang, Y. Chen, F. Chen, H. R. Chen, *J. Mater. Chem.* **2011**, *21*, 3037.
[15] F. Porta, G. E. M. Lamers, J. Morrhayim, A. Chatzopoulou, M. Schaaf, H. den Dulk, C. Backendorf, J. I. Zink, A. Kros, *Adv. Healthcare Mater.* **2013**, *2*, 281.
[16] C. Anacker, P. A. Zunszain, L. A. Carvalho, C. M. Pariante, *Psychoneuroendocrinology* **2011**, *36*, 415.
[17] J. Yao, Y. Fan, Y. Li, L. Huang, *J. Drug Targeting* **2013**, *21*, 926.
[18] V. Shahin, L. Albermann, H. Schillers, L. Kastrup, C. Schafer, Y. Ludwig, C. Stock, H. Oberleithner, *J. Cell. Physiol.* **2005**, *202*, 591.
[19] J. Choi, K. Ko, J. Park, Y. Kim, S. Kim, M. Lee, *Int. J. Pharm.* **2006**, *320*, 171.
[20] Y. Mi Bae, H. Choi, S. Lee, S. Ho Kang, Y. Tae Kim, K. Nam, J. Sang Park, M. Lee, J. Sig Choi, *Bioconjugate Chem.* **2007**, *18*, 2029.
[21] Z. Chen, L. Zhang, Y. He, Y. Li, *ACS Appl. Mater. Interfaces* **2014**, *6*, 14196.
[22] F. Kong, W. Wang, F. Zhou, L. Ge, X. Liu, *Int. J. Nanomed.* **2012**, *7*, 2513.
[23] W. Wang, F. Zhou, L. Ge, X. Liu, F. Kong, *Pharm. Biol.* **2014**, *52*, 1039.
[24] P. Ballard, *Monogr. Endocrinol.* **1978**, *12*, 25.
[25] N. Pante, *Mol. Biol. Cell* **2002**, *13*, 425.
[26] J. Kobler, K. Moller, T. Bein, *ACS Nano* **2008**, *2*, 791.
[27] B. Chang, D. Chen, Y. Wang, Y. Chen, Y. Jiao, X. Sha, W. Yang, *Chem. Mater.* **2013**, *25*, 574.
[28] D. Bruhwiler, *Nanoscale* **2010**, *2*, 887.
[29] F. Lu, S.-H. Wu, Y. Hung, C.-Y. Mou, *Small* **2009**, *5*, 1408.
[30] S. Sadasivan, D. Khushalani, S. Mann, *J. Mater. Chem.* **2003**, *13*, 1023.
[31] I. Slowing, B. G. Trewyn, V. S. Y. Lin, *J. Am. Chem. Soc.* **2006**, *128*, 14792.
[32] N. Lodhi, N. K. Mehra, N. K. Jain, *J. Drug Targeting* **2013**, *21*, 67.
[33] K. Moller, J. Kobler, T. Bein, *J. Mater. Chem.* **2007**, *17*, 624.
[34] J.-M. Oh, S.-J. Choi, G.-E. Lee, S.-H. Han, J.-H. Choy, *Adv. Funct. Mater.* **2009**, *19*, 1617.
[35] P. Huang, L. Bao, C. Zhang, J. Lin, T. Luo, D. Yang, M. He, Z. Li, G. Gao, B. Gao, S. Fu, D. Cui, *Biomaterials* **2011**, *32*, 9796.
[36] D. G. Watson, *Pharmaceutical Analysis: A Textbook for Pharmacy Students and Pharmaceutical Chemists*, Churchill Livingstone, Edinburgh, UK, **1999**, p. 107.
[37] C. P. Leamon, P. S. Low, *Proc. Natl. Acad. Sci. USA* **1991**, *88*, 5572.
[38] N. J. S. London, A. Chiang, J. A. Haller, *Adv. Ther.* **2011**, *28*, 351.

[39] J. M. Rosenholm, A. Meinander, E. Peuhu, R. Niemi, J. E. Eriksson, C. Sahlgren, M. Lindén, *ACS Nano* **2009**, *3*, 197.
[40] V. P. Torchilin, *Adv. Drug Delivery Rev.* **2008**, *60*, 548.
[41] Z. Chen, Z. Li, Y. Lin, M. Yin, J. Ren, X. Qu, *Chem. Eur. J.* **2013**, *19*, 1778.
[42] Q. Zhang, X. L. Wang, P. Z. Li, K. T. Nguyen, X. J. Wang, Z. Luo, H. C. Zhang, N. S. Tan, Y. L. Zhao, *Adv. Funct. Mater.* **2014**, *24*, 2450.
[43] M. Bouchoucha, R. C.-Gaudreault, M. A. Fortin, F. Kleitz, *Adv. Funct. Mater.* **2014**, *24*, 5911.
[44] Y. Gao, Y. Chen, X. Ji, X. He, Q. Yin, Z. Zhang, J. L. Shi, Y. Li, *ACS Nano* **2011**, *5*, 9788.
[45] P. Mohan, N. Rapoport, *Mol. Pharm.* **2010**, *7*, 1959.
[46] C. Wang, P. Lv, W. Wei, S. Tao, T. Hu, J. Yang, C. Meng, *Nanotechnology* **2011**, *22*, 415101.

Received: April 16, 2015
Revised: July 29, 2015
Published online: October 1, 2015

4.3 Supplementary Information

This section is included in the thesis as supplementary information to section 4.2. It includes additional information which is not put in the main text of the published paper, but as electronic supplementary information freely accessible online.

Cancer Cell Specific Nuclear-Targeted Drug Delivery by Dual Ligands-Modified Mesoporous Silica Nanoparticles

*Lin Xiong, Xin Du, Freddy Kleitz, Shi Zhang Qiao**

Experiment Section

Materials

Tetraethyl orthosilicate (TEOS), γ -mercapto-propyl trimethoxysilane (MPTES), (3-Aminopropyl)-triethoxysilane (APTES), triethanolamine, triethylamine, cetyl trimethylammonium bromide (CTAB), folic acid (FA), toluene, ethanol, dimethylsulfoxide (DMSO), N-ethyl-N'(3-dimethylaminopropyl)carbodiimide hydrochloride (EDC), fluorescein isothiocyanate (FITC), 3-[4,5-dimethylthialzol-2-yl]-2,5-diphenyltetrazolium bromide (MTT), trypsin (0.25%) were purchased from Sigma Aldrich. Dexamethasone-21-mesylate was purchased from Steraloids Inc. (Newport, RI). Doxorubicin hydrochloride (DOX) was purchased from Bejing Huafeng United Technology Co., Ltd. Dulbecco's Modified Eagle's Medium (DMEM), fetal bovine serum (FBS), and phosphate buffered saline (PBS) were purchased from Gibco-BRL (Grand Island, USA). All chemicals were used as received without further purification. Water used in all experiments was purified

using a Milli-Q Plus 185 water purification system (Millipore, Bedford, MA) with a resistivity higher than 18 MΩ cm.

Synthesis and functionalization of MSNs

The procedure for nanoparticle synthesis and functionalization is presented in Scheme 1 and Scheme S1. At first, unmodified plain MSNs (pMSN) and thiol-modified MSNs (MSN-SH) were synthesized separately according to a slightly modified reported method.[1] For pMSN, 3 mL of TEOS was added quickly into 25 ml of aqueous solution containing 0.4 g of CTAB under vigorous stirring and 87 mg of triethanolamine. The mixture was allowed to react for 2 h at 80 °C followed by centrifugation at 16000 rpm for 10 min to precipitate the nanoparticles. For MSN-SH, the procedure was almost the same as above except that a 200 µL mixture of TEOS and MPTES (volume ratio 1:1) was added 1 h after the reaction began. The CTAB containing-precipitate was washed with DI water three times and dried in vacuum oven for further treatment. For FITC labelling, 10 mg of FITC was mixed with 50 µL of APTES in 5 ml of ethanol for 24 h under dark condition to form a stock FITC-APTES solution. The synthesis procedure of FITC-labelled MSNs was almost the same as the unlabelled counterparts except that 100 µL of FITC-APTES stock solution was added with TEOS during the reaction.

Next, pMSN or MSN-SH was conjugated to folic acid (FA) to obtain FA-MSN or FA-MSN-SH by a post-grafting method.[2] Briefly, 44 mg of folic acid was dissolved in 5 mL of anhydrous DMSO containing 100 mg of EDC and stirred for 2 h under dark environment. Then 30 µL of APTES was added to the activated FA solution and stirred for another 4 h. After that, the mixture was added directly to 20 mL of toluene containing 500 mg of pMSN or MSN-SH obtained in the previous step. The mixture was allowed to react at 80 °C for 24 h followed by centrifugation. The precipitate was washed by toluene and ethanol sequentially. The CTAB in the product was removed at this time by extraction in 100 ml 2 wt % NH_4NO_3/ethanol solution for two times.

Finally, folic acid and dexamethasone dual modified MSNs (FA-MSN-DEX) were prepared through a highly selective reaction between α-Keto mesylates and thiol groups.[3] Briefly, 10 mg of dexamethasone methylate and 20 mg of surfactant-extracted FA-MSN-SH was dispersed in 10 mL anhydrous DMSO. Then 5 μL of triethylamine was added and the mixture was stirred at room temperature for 6 h followed by centrifugation. The precipitate was washed sequentially with DMSO and DI water for several times and dried in vacuum oven for further use.

DOX loading and release

For DOX loading, 5 mg of MSN, FA-MSN or FA-MSN-DEX were mixed with 5 ml of DOX solution in PBS (0.5 mg mL^{-1}) and stirred for 24 h under dark environment. Then, the nanoparticles were collected by centrifugation at 16000 rpm for 10 min. The precipitate was washed gently with PBS for three times and dried at 60 °C. To evaluate the DOX loading efficiency, the supernatant and all the washing liquid fractions were collected, and the residual DOX content was determined using a standard curve by UV-vis adsorption at 480 nm. The release profile of DOX from MSNs was investigated at 37 °C in two different release media: (a) acetate buffer, pH 5.0; and (b) PBS, pH 7.4, using a dialysis bag diffusion technique. The DOX-loaded particles (5 mg) were suspended in 5 mL release media in the dialysis membrane bag (MWCO ¼ 16K) and the bag was immersed in 15 mL release media and shaken at a speed of 100 rpm at 37 °C. The amount of DOX released at different time intervals was determined by UV-vis measurement at 480 nm.

Cell culture and cell viability

HeLa or HEK293 cells were grown in DMEM culture medium supplemented with 10% (v/v) FBS in a humidified 5% CO_2 atmosphere at 37 °C. For all experiments, cells were harvested by using 0.25% trypsin and resuspended in fresh medium before plating. The viability of cells in the presence of MSNs was investigated using MTT assay. HeLa or HEK293 cells were seeded into 96-well plates at a density of 1×10^4 per well in 100 μL of media and grown for 24 h. Then, the growth medium was replaced with 100 μL of cell culture medium containing different concentrations of nanoparticles

with or without DOX loading. After incubation for 24 h, the medium was removed. Then 100 µL fresh medium and 10 µL MTT (5.0 mg mL^{-1} in PBS) were added to each well and the cells were further incubated for 4 h. After that, the growth medium was removed and 150 µL of DMSO was added to each well to ensure complete solubilisation of formazan crystals. Finally, the absorbance was determined using a micro-plate reader (Biotek, USA) at the wavelength of 570 nm. The viability of untreated cells was assumed to be 100%.

Cellular uptake by confocal laser scanning microscopy (CLSM)

To check cellular uptake and subcellular localization of MSNs, HeLa cells were seeded at a concentration of 2×10^5 cells/well in a 6-well plate with one piece of cover glass at the bottom of each well and cultured for 24 h. FITC-labelled MSNs were then added to the incubation medium at a concentration of 50 µg mL^{-1}. After 24 h, the medium was removed. The cells were washed twice with PBS and fixed with 4 wt % formaldehyde. The cell nucleus was stained with Hoechst 33258 (1 µg mL^{-1}) for 15 min at room temperature. After the staining, the cells were softly washed again with PBS to remove excessive Hoechst dye. At last, 2 mL of PBS was added and the cover glass was visualized under a confocal laser scanning microscope (Leica Confocal 1P/FCS). Optical sections were averaged 4 times to reduce noise. Images were processed using Leica confocal software.

Cellular uptake by flow cytometry

HeLa or HEK293 cells were seeded at 1×10^5 in 12 well plates. After 24 h attachment, the cells were treated with FITC-labelled pMSN, FA-MSN or FA-MSN-DEX dispersed in culture medium (50 µg mL^{-1}) for 24 h. Then, the cells were washed with PBS twice to remove the extracellular particles and trypsinized. After centrifugation and washing with PBS, the cells were resuspended in PBS containing trypan blue (200 µg mL^{-1}). The fluorescence of endocytosed particles was detected by a FACSCalibur flow cytometer (Becton Dickinson) in FITC-A channel. The cellular uptake was calculated by the percentage of fluorescence positive cells using the untreated cells as negative

control. 2×10^4 cells were analysed at a rate of 200-600 cells per second. CellQuest software was used for data analysis.

Cell and nuclear uptake by ICP-MS

Hela cells were seeded at 1×10^6 cells in T25 flasks. After 24 h attachment, the cells were treated with pMSN, FA-MSN or FA-MSN-DEX dispersed in culture medium (50 μg mL^{-1}) for 24 h. Then, the cells were washed with PBS twice and trypsinized. After centrifugation, the cell pellet was washed twice with PBS. The cell nuclei were separated from the cell cytosol following a reported procedure.[4] The cells were suspended in a nuclei extraction buffer (100 mM NaCl solution with 1 mM EDTA, 1% Triton X-100, and 10 mM Tris buffer) at a concentration of 10^6 cells mL^{-1} for 10 min at 4 °C. The suspension was then centrifuged and the cell nuclei were collected as the resulting precipitate. Then 3 mL cell lysis solution (0.5% Triton X-100, 1 M NaOH) was added to disrupt the cell nuclei with ultrasound. The mass of pMSN, FA-MSN or FA-MSN-DEX in the nuclei was determined by measuring the silicon concentration with inductively coupled plasma mass spectrometry (ICP-MS). The cellular uptake of pMSN, FA-MSN or FA-MSN-DEX was quantified as described above without the step of nuclei separation.

Characterization

Scanning electron microscopy (SEM) observation was carried out on a FEI Quanta 450 FEG environmental emission scanning electron microscope with energy dispersive X-ray (EDX) accessory. Specimens were coated with platinum before SEM observation. For transmission electron microscopy (TEM) observation, the powder samples were dispersed in ethanol by sonication for 20 min, and deposited onto carbon-coated copper grids. TEM observation was carried out on a FEI Tecnai G2 Spirit transmission electron microscope at an acceleration voltage of 120 kV. UV-vis absorption spectra were recorded on a UV-2600 spectrophotometer (Shimadzu Corporation). Fourier transform infrared (FTIR) spectra were recorded on a Thermo Scientific NICOLET 6700 FTIR spectrometer at room temperature. Thermogravimetric analysis (TGA) was performed on a S60/51920 TGA/DSC thermogravimetric analyzer

(Setaram Instrumentation), using an oxidant atmosphere (oxygen, 30 mL min^{-1}) with a heating ramp of 10 ˚C min^{-1}. Nitrogen adsorption-desorption measurement was carried out at -196 ˚C using a TriStar II surface area and porosity analyzer from Micromeritics. Prior to the measurement, the samples were degassed at 120 ˚C for 12 h. Brunauer-Emmett-Teller (BET) specific surface area was calculated using adsorption data at a relative pressure range of P/P_0 range of 0.05-0.30. Pore size distribution was derived from adsorption branch of the isotherm using the Barrett-Joyner-Halenda (BJH) method. Pore volume was determined from the amount of N_2 adsorbed at the single point of P/P_0=0.99. The hydrodynamic size and zeta-potential of nanoparticles in aqueous dispersions were measured on a Malvern Zetasizer Nano ZS (Malvern Inst. Ltd., U.K.) operating at a wavelength of 633 nm, where scattered light was collected at a fixed angle of 173°. Concentrations of silicon were determined with an Agilent 7500cs ICP-MS using a standard curve. Solid state ^{13}C cross-polarization magic-angle spinning nuclear magnetic resonance (^{13}C CP/MAS NMR) measurement was performed on a Bruker Avance III 400 MHz spectrometer equipped with a 4 mm solid state probe.

Statistical analysis

Quantitative data were reported as mean ± standard deviation (SD) of at least three independent experiments. The statistical analyses were performed using a two sample, two tailed Student's t-test, with a p-value less than 0.05 considered being statistically significant.

Supplementary Figures and Calculation

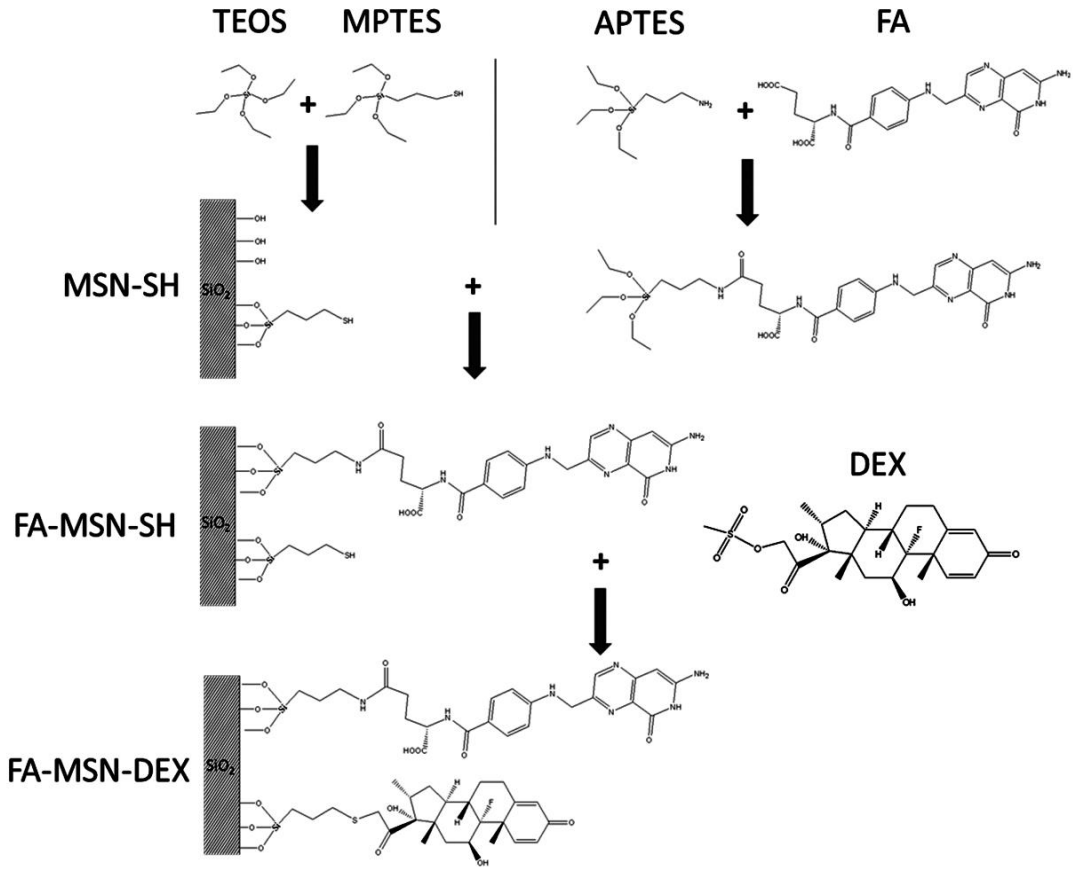

Scheme S1. Surface reactions of mesoporous silica nanoparticles during the functionalization steps.

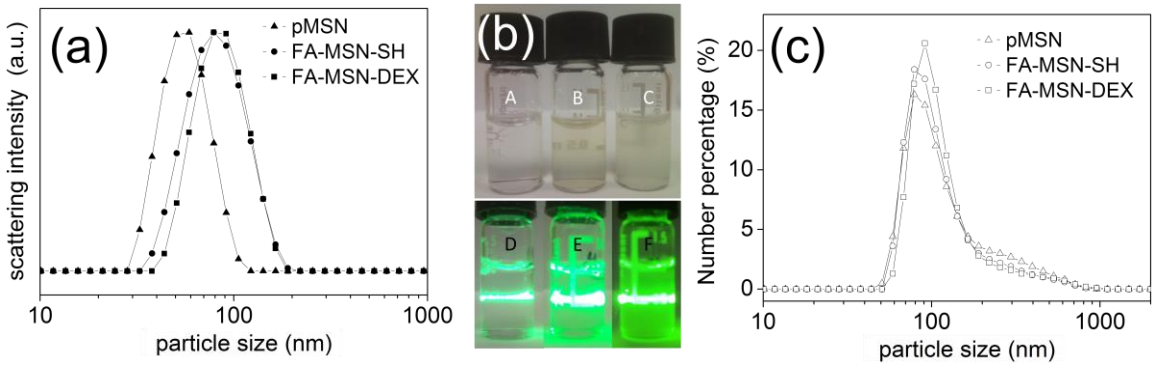

Figure S1. Hydrodynamic particle size distributions in water (a), digital photos and Tyndall effects (b) of (A, D) pMSN, (B, E) FA-MSN-SH, (C, F) FA-MSN-DEX in water, hydrodynamic particle size distributions in DMEM supplemented with 10% FBS (c).

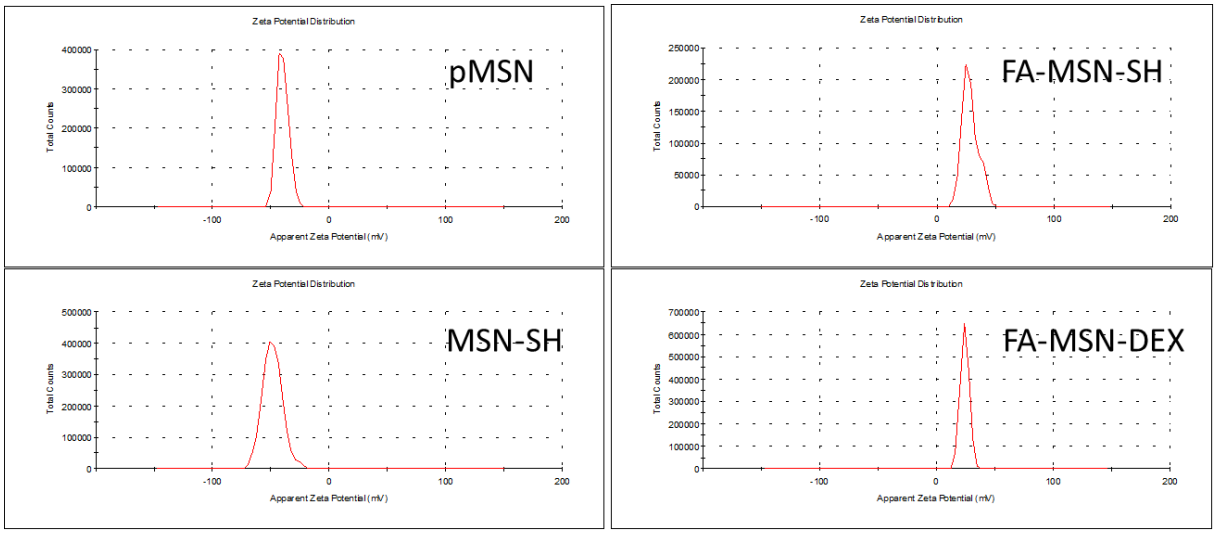

Figure S2. Zeta potential distributions of mesoporous silica nanoparticles in DI water.

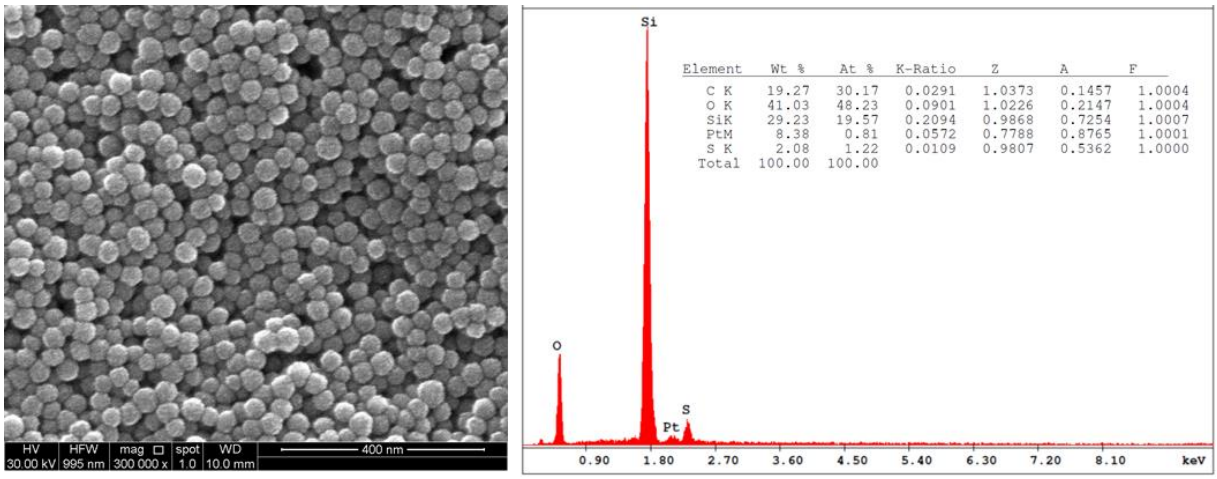

Figure S3. SEM (left) and Energy-dispersive X-ray spectrum (right) of MSN-SH.

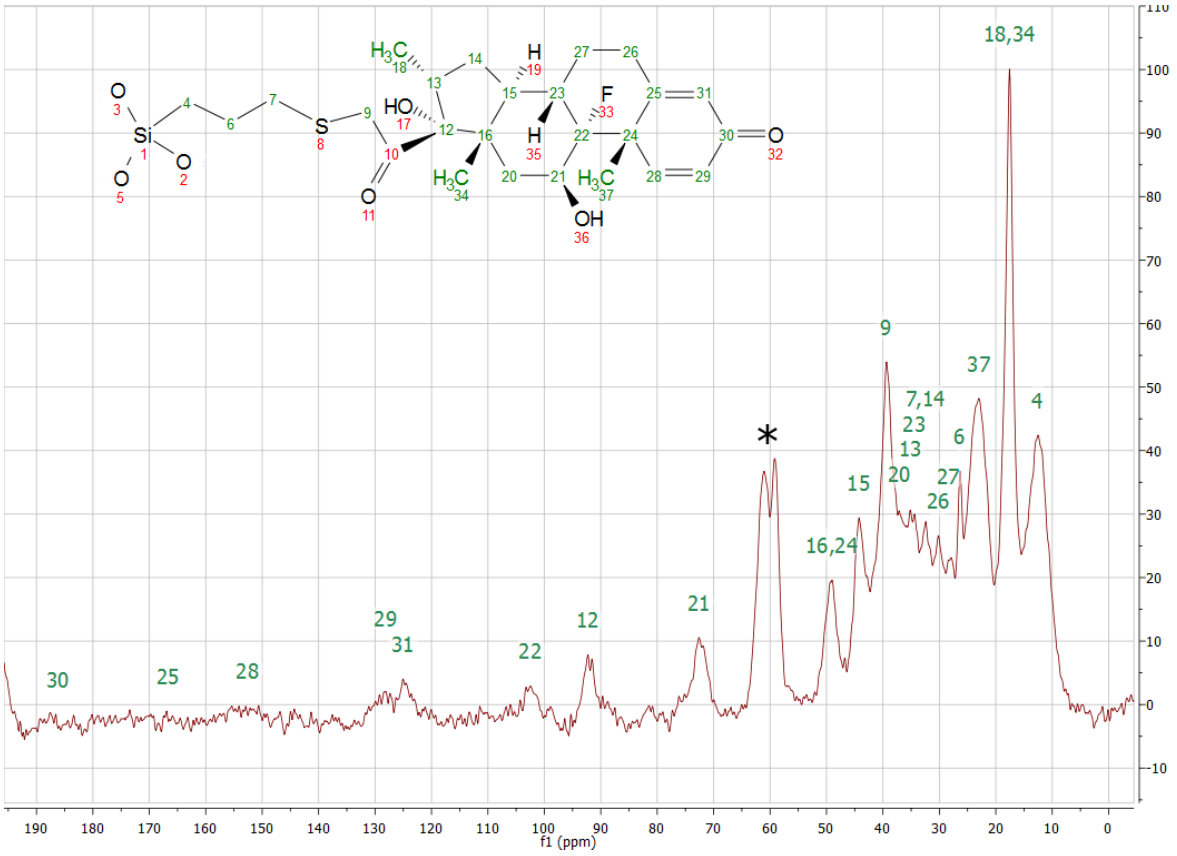

Figure S4. Solid state ^{13}C CP/NMR of MSN-DEX obtained by reaction of MSN-SH with dexamethasone methylate. Note: for the clarity of spectrum interpretation, this sample is prepared without the folic acid modification step. The peaks around 60 ppm denoted with * are assigned to the carbon atoms of residue ethoxy groups, which originated from incomplete silane hydrolysis and/or the ethanol extraction process.[5-6]

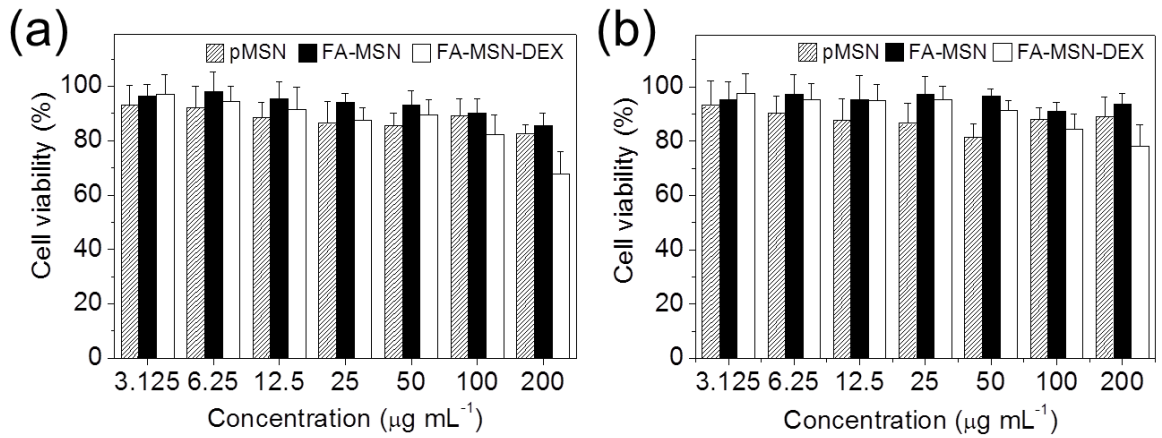

Figure S5. Viability of Hela (a) and HEK293 (b) cells after 48 h of incubation with different mesoporous silica nanoparticles without drug loading.

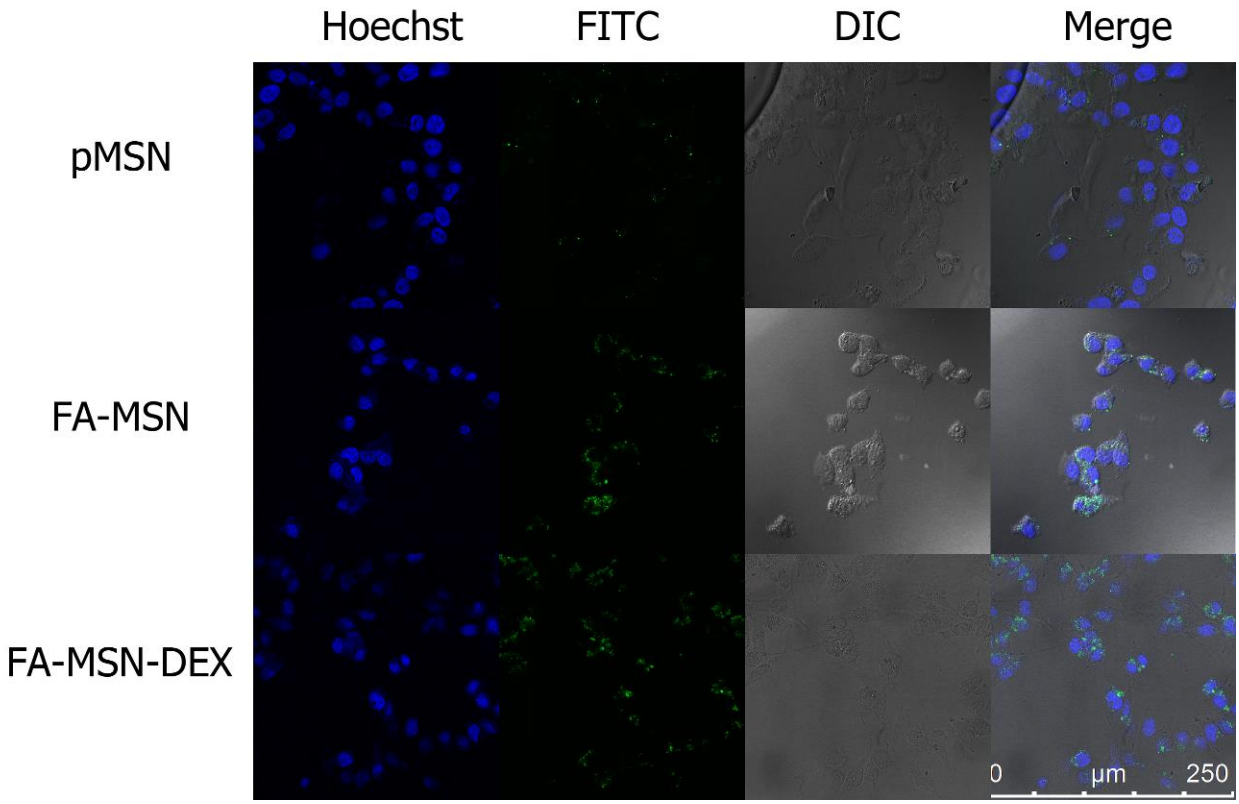

Figure S6. Low magnification CLSM images of Hela cells after 24 h of incubation with 50 μg ml^{-1} FITC-labelled mesoporous silica nanoparticles.

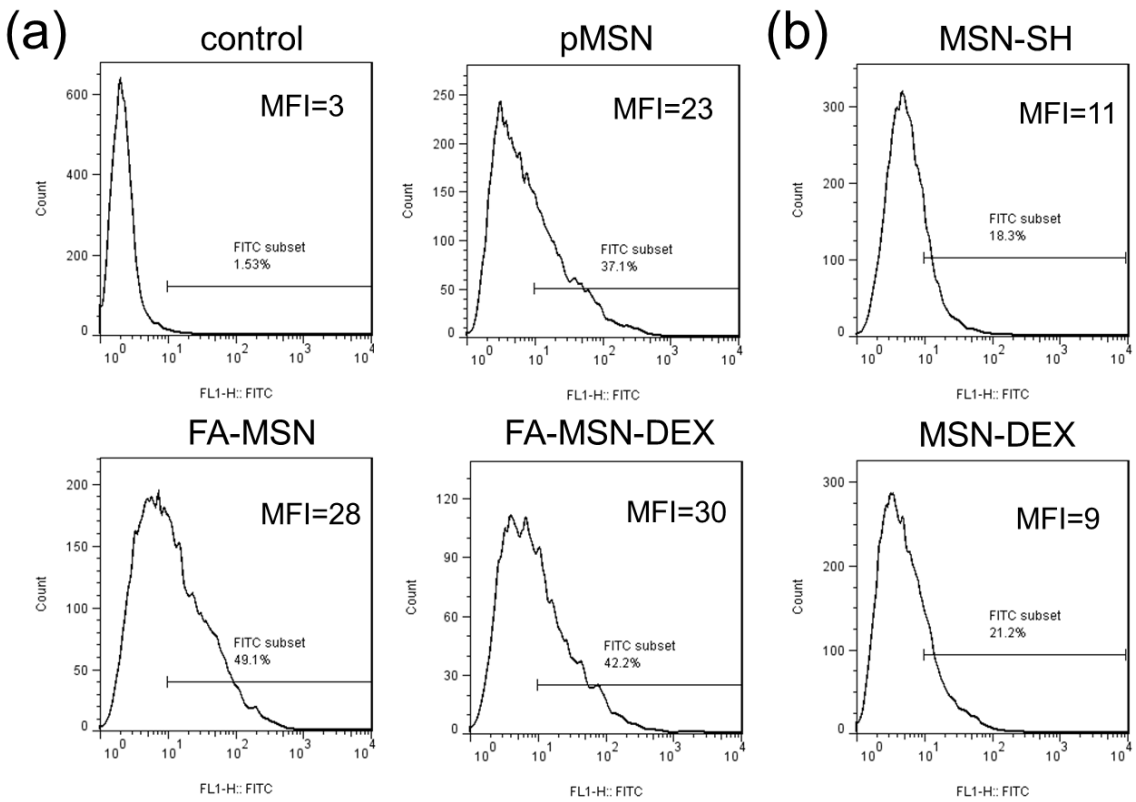

Figure S7. Flow cytometry analysis of the uptake of FITC-labelled (a) MSNs with HEK293 cells and (b) MSN-SH before and after DEX conjugation by Hela cells after 24 h of incubation. The histograms show distribution of events on the green (FL1) channel. MFI: mean fluorescent intensity.

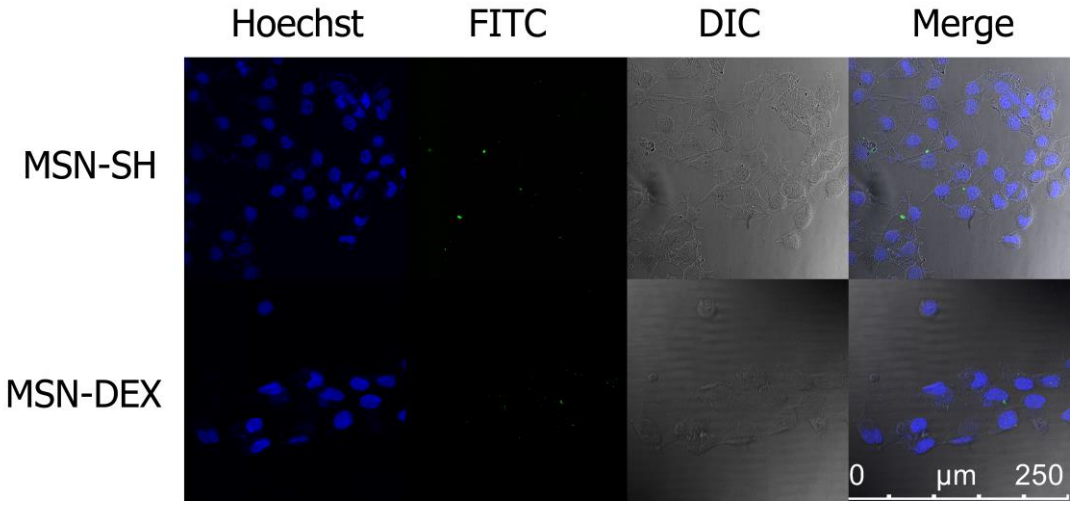

Figure S8. CLSM images of Hela cells after 24 h of incubation with 50 μg ml^{-1} FITC-labelled MSN-SH (only thiol modified) and MSN-DEX (only DEX modified). Note that although MSN-DEX can be observed in some nuclear region, the overall cellular uptakes for both MSN-SH and MSN-DEX are very limited.

Figure S9. Z-stack images of one Hela cell after 24 h of incubation with 50 µg ml^{-1} FITC labelled FA-MSN-DEX.

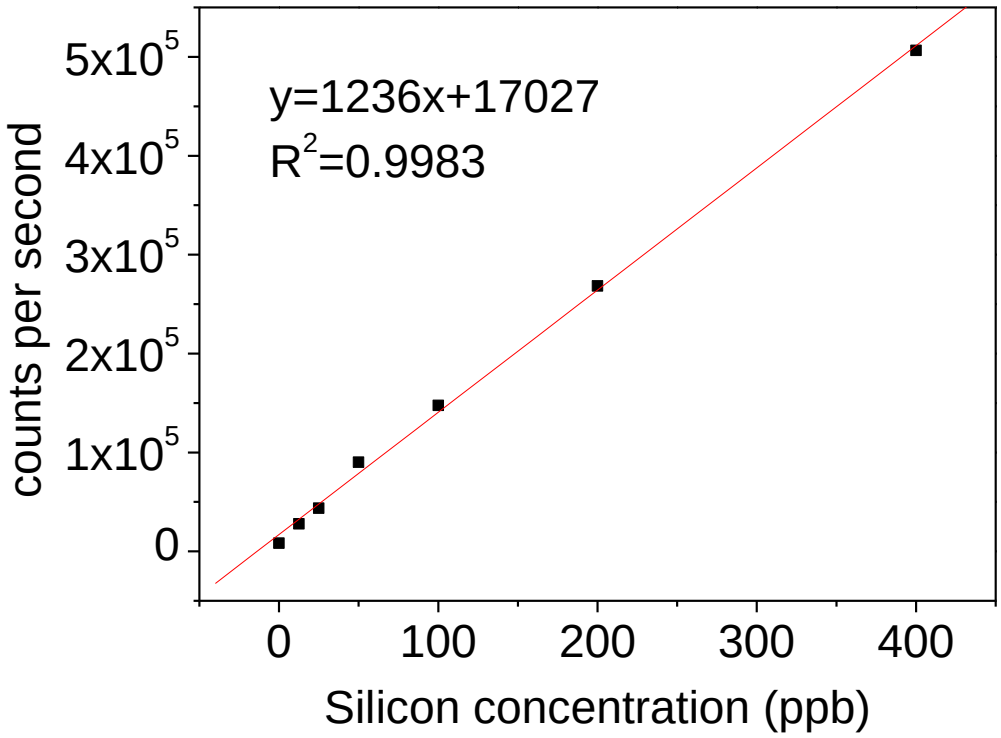

Figure S10. Standard calibration curve of silicon concentration measured by ICP-MS.

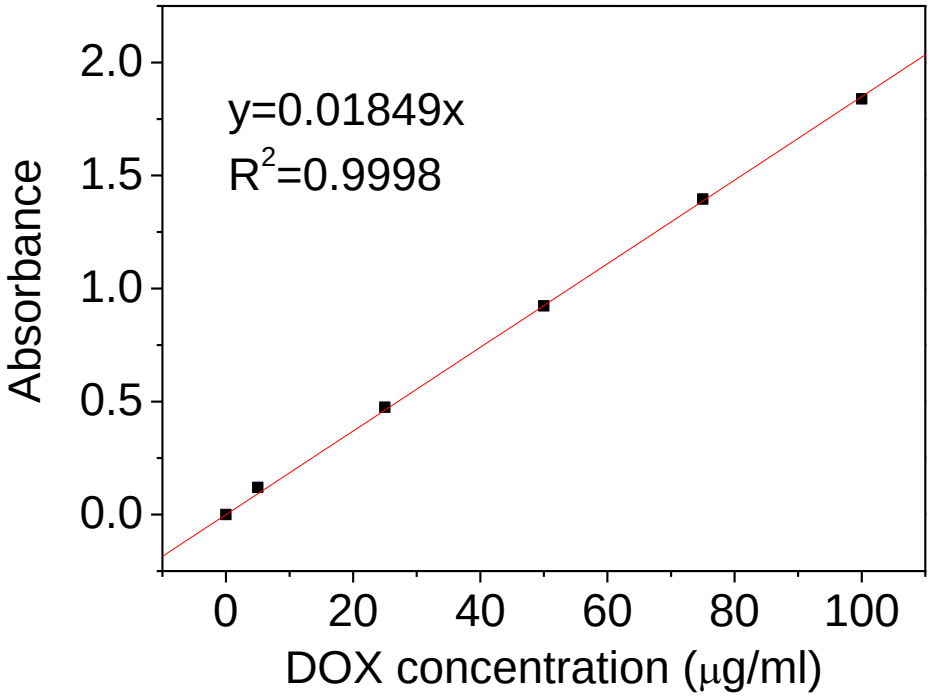

Figure S11. Standard calibration curve of DOX in aqueous solution.

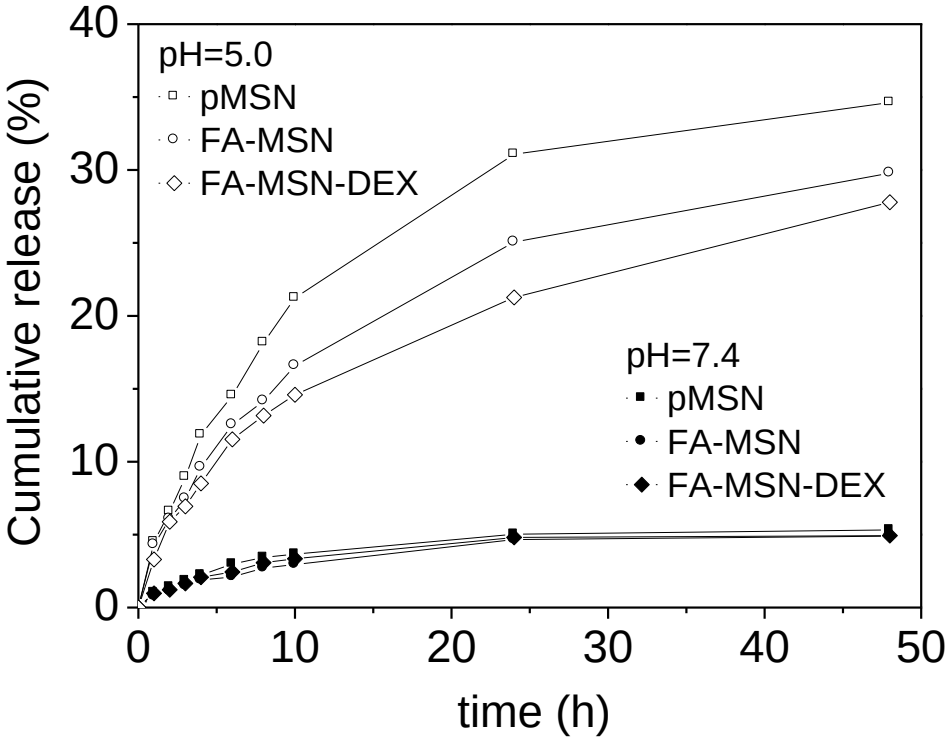

Figure S12. DOX release profiles from mesoporous silica nanoparticles under different pH values.

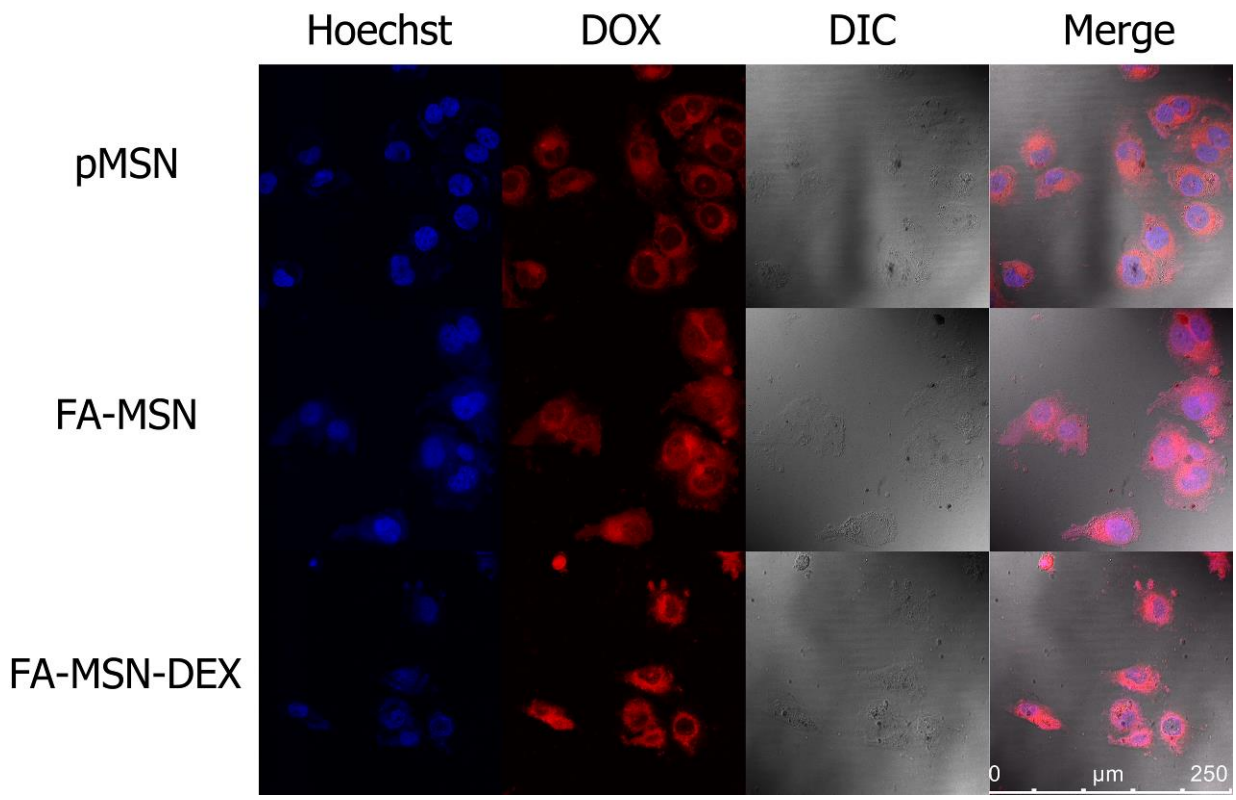

Figure S13. Low magnification CLSM images of Hela cells after 12 h of incubation with DOX-loaded mesoporous silica nanoparticles. The equivalent DOX concentration in all the three samples was 5 μg ml^{-1}.

Quantification of grafted functional groups

The weight loss of pMSN, MSN-SH, FA-MSN-SH and FA-MSN-DEX are 6%, 10%, 16% and 26% from TGA, respectively. Assuming the solid residue after calcination at 800 ˚C is pure silica, the burned-off contents (including organic functional groups and dehydrated hydroxyl groups) per gram of SiO_2 are 64 mg, 110 mg, 190 mg and 350 mg for the four samples. Because the functionalization was carried out step by step, the grafted quantity can be estimated from the differences between the burned-off contents.

The difference between pMSN and MSN-SH is due to mercapto-propyl group ($-CH_2CH_2CH_2SH$, 75 g mol^{-1}), thus the thiol group quantity per gram of SiO_2 can be determined as

(110 mg -64 mg)/ 75 g mol^{-1}= 0.61 mmol g^{-1};

The difference between MSN-SH and FA-MSN-SH is due to FA-APTES conjugate, ($C_{19}H_{18}N_7O_5$-$NHCH_2CH_2$, 481 g mol^{-1}), thus the FA quantity per gram of SiO_2 can be determined as

(190 mg -110 mg)/ 481 g mol^{-1}= 0.17 mmol g^{-1};

The difference between FA-MSN-DEX and FA-MSN-SH is due to DEX ($C_{22}H_{28}FO_4$, 375 g mol^{-1}), thus the DEX quantity per gram of SiO_2 can be determined as

(350 mg -190 mg)/ 375 g mol^{-1}= 0.43 mmol g^{-1}.

References

[1] K. Zhang, L.-L. Xu, J.-G. Jiang, N. Calin, K.-F. Lam, S.-J. Zhang, H.-H. Wu, G.-D. Wu, B. Albela, L. Bonneviot, P. Wu, *J. Am. Chem. Soc.* **2013,** *135*, 2427.

[2] I. Slowing, B. G. Trewyn, V. S. Y. Lin, *J. Am. Chem. Soc.* **2006,** *128*, 14792.

[3] S. S. Simons, M. Pons, D. F. Johnson, *J. Org. Chem.* **1980,** *45*, 3084.

[4] L. Pan, Q. He, J. Liu, Y. Chen, M. Ma, L. Zhang, J. L. Shi, *J. Am. Chem. Soc.* **2012,** *134*, 5722.

[5] J. Kecht, T. Bein, *Microporous Mesoporous Mater.* **2008,** *116*, 123.

[6] S. B. Hartono, S. Z. Qiao, J. Liu, K. Jack, B. P. Ladewig, Z. P. Hao, G. Q. M. Lu, *J. Phys. Chem. C* **2010,** *114*, 8353.

Chapter 5 Magnetic Core-Shell Silica Nanoparticles with Large Radial Mesopores for siRNA Delivery

5.1 Introduction, Significance and Commentary

Gene therapy through small interfering RNA (siRNA) is a promising technology to treat cancer and other diseases. The successful RNA interference therapy strongly relies on the development of efficient gene delivery systems. In this contribution, a novel type of magnetic core–shell mesoporous silica nanoparticles was developed for siRNA delivery. The capability of this nano-carrier to load, protect and deliver anti-cancer siRNA into the cancer cells was demonstrated in vitro. The highlights and novelty of this work include:

1. Magnetic core-shell silica nanoparticles with large radial mesopores

A novel type of super-paramagnetic core-shell mesoporous silica nanoparticles with large radial mesopores was fabricated for the first time. These nanoparticles exhibit small particle size of 150 nm, large open mesopores of 12 nm, large surface area of 411 $m^2 g^{-1}$, high pore volume of 1.13 $cm^3 g^{-1}$ and magnetization of 25 emu g^{-1} simultaneously. The small particle size, high siRNA loading capability and strong response under external magnetic fields make these nanoparticles a very suitable carrier for intracellular delivery of siRNA.

2. Tannic acid/Al^{3+} coating serves as an acid-liable pore capping

Acid-liable Tannic acid/Al^{3+} complex was formed as a coating layer onto the siRNA-loaded magnetic core-shell mesoporous silica nanoparticles to cap the radial mesopores. The tannic acid/Al^{3+} layer can further protect siRNA against enzyme degradation under neutral extracellular condition and decompose in the mild acidic intracellular environment for on-demand release of siRNA.

3. Magnetic field enhanced delivery

The cellular uptake of the siRNA-loaded nano-carrier was compared both with and without the presence of an external magnetic field. Under the external magnetic

field, the cellular uptake was significantly increased (up to 40% in 6 h) which led to enhanced inhibition efficacy on human osteosarcoma cancer cell line.

5.2 Magnetic Core-Shell Silica Nanoparticles with Large Radial Mesopores for siRNA Delivery

This section is included in the thesis as it appears as a paper published by L. Xiong, J. Bi, Y. Tang and S. Z. Qiao. Magnetic Core-Shell Silica Nanoparticles with Large Radial Mesopores for siRNA Delivery, *Small*, **2016**, 12, 4735.

Statement of Authorship

Title of Paper	Magnetic Core–Shell Silica Nanoparticles with Large Radial Mesopores for siRNA Delivery
Publication Status	☑ Published ☐ Accepted for Publication ☐ Submitted for Publication ☐ Unpublished and Unsubmitted work written in manuscript style
Publication Details	First published: 19 May 2016 DOI: 10.1002/smll.201600531

Principal Author

Name of Principal Author (Candidate)	Lin Xiong (First Author)		
Contribution to the Paper	Research plan, material synthesis, material characterization, material performance assessment, manuscript drafting		
Overall percentage (%)	80 %		
Certification:	This paper reports on original research I conducted during the period of my Higher Degree by Research candidature and is not subject to any obligations or contractual agreements with a third party that would constrain its inclusion in this thesis. I am the primary author of this paper.		
Signature		Date	2016/11/22

Co-Author Contributions

By signing the Statement of Authorship, each author certifies that:

i. the candidate's stated contribution to the publication is accurate (as detailed above);
ii. permission is granted for the candidate in include the publication in the thesis; and
iii. the sum of all co-author contributions is equal to 100% less the candidate's stated contribution.

Name of Co-Author	A/Prof Jingxiu Bi		
Contribution to the Paper	Assistance with research organization and manuscript revision		
Signature		Date	24/11/2016

Name of Co-Author	Dr. Youhong Tang		
Contribution to the Paper	Assistance with material characterization		
Signature		Date	18-Nov-2016

Name of Co-Author	Prof Shi Zhang Qiao (Corresponding Author)		
Contribution to the Paper	Design of the project, organization of the research and supervision, manuscript revision		
Signature		Date	24/11/2016

Please cut and paste additional co-author panels here as required.

Materials Views
www.MaterialsViews.com

NANO MICRO small

Magnetic Nanoparticles

Magnetic Core–Shell Silica Nanoparticles with Large Radial Mesopores for siRNA Delivery

*Lin Xiong, Jingxu Bi, Youhong Tang, and Shi-Zhang Qiao**

***A** novel type of magnetic core–shell silica nanoparticles is developed for small interfering RNA (siRNA) delivery. These nanoparticles are fabricated by coating super-paramagnetic magnetite nanocrystal clusters with radial large-pore mesoporous silica. The amine functionalized nanoparticles have small particle sizes around 150 nm, large radial mesopores of 12 nm, large surface area of 411 m^2 g^{-1}, high pore volume of 1.13 cm^3 g^{-1} and magnetization of 25 emu g^{-1}. Thus, these nanoparticles possess both high loading capacity of siRNA (2 wt%) and strong magnetic response under an external magnetic field. An acid-liable coating composed of tannic acid can further protect the siRNA loaded in these nanoparticles. The coating also increases the dispersion stability of the siRNA-loaded carrier and can serve as a pH-responsive releasing switch. Using the magnetic silica nanoparticles with tannic acid coating as carriers, functional siRNA has been successfully delivered into the cytoplasm of human osteosarcoma cancer cells in vitro. The delivery is significantly enhanced with the aid of the external magnetic field.*

1. Introduction

Gene therapy through small interfering RNA (siRNA) has emerged as a promising technology to treat cancer and other diseases by halting the production of target proteins.[1] However, the naked siRNA is susceptible to enzyme degradation, thus not able to survive in biological fluids for a long time. Moreover, the high negative charge and large molecular weight (≈13 KDa) of the naked siRNA limit its penetration through the cell membrane. Thus, the successful RNA interference therapy strongly relies on the development of efficient gene delivery systems.

L. Xiong, Prof. J. Bi, Prof. S.-Z. Qiao
School of Chemical Engineering
The University of Adelaide
SA 5005, Australia
E-mail: s.qiao@adelaide.edu.au
Dr. Y. Tang
Centre for Nano Scale Science and Technology
School of Computer Science, Engineering and Mathematics
Flinders University
Adelaide, SA 5042, Australia

DOI: 10.1002/smll.201600531

In the past decade, mesoporous silica nanoparticles (MSNs) have emerged as a promising vehicle for siRNA delivery due to its high biocompatibility, unique porous structure and variety of functionalization.[2–9] Compared with traditional MSNs with typical pore sizes ranging from 2 to 5 nm, large-pore MSNs (6–50 nm in mesopore size) are more favorable to encapsulate siRNA into their porous structure. Moreover, they can also effectively shield the negative charge of siRNA and protect against enzyme degradation.[5,10] Meanwhile, the combination of magnetic property with MSNs can endow the resulting composite with multifunctionality including magnetic targeting, hyperthermia therapy, and magnetic resonance imaging.[11,12] Furthermore, it has been proven by several research groups that the nucleic acid delivery can be significantly enhanced with the aid of magnetic fields by using magnetic delivery vectors. A specialized term "magnetofection" has been coined for this kind of transfection method.[13,14]

Although intensive efforts have already been made toward the development of magnetic large-pore MSNs, several critical limitations still exist for their usage in siRNA delivery.In previous reports, the particle sizes are usually too large (>200 nm) for effective cellular uptake and cannot evade rapid clearance from circulation.[15–23] Moreover, the composite materials often suffer from low saturation

magnetization (<20 emu g^{-1}) due to a low fraction of magnetic component loading,[18,24–26] or the porosity is significantly compromised by high magnetic loading inside the pore structure.[27] Furthermore, although various types of stimuli-responsive switches have been designed on traditional MSNs for controlled release of small molecule drugs, similar function is seldom realized on large-pore MSNs for release of siRNA and the realization usually needs complex multistep preparation processes.[28–30] Therefore, it is still a great challenge to construct a magnetic large-pore MSN, especially magnetic radial large-pore MSN, for siRNA delivery which has small particle size, large open pores, high pore volume, high saturation magnetization, and controlled-release function at the same time.

In this study, a novel type of magnetic radial large-pore MSN with core–shell structure is fabricated and proposed as a siRNA delivery platform (**Scheme 1**). The superior features of this system are illustrated from four aspects: (1) it consists of nearly uniform core–shell nanoparticles with particle size below 200 nm and negligible aggregation; (2) super-paramagnetic magnetite nanocrystal clusters were incorporated as the cores to ensure a strong response for magnetic-guided delivery without sacrificing the aqueous dispersity; (3) dendrimer-like silica shells provide both large pore volume and entry pore size for high siRNA loading capacity; (4) an acid-liable surface coating composed of tannic acid acts simultaneously as pore capping for effective protection of siRNA and a pH-responsive switch for on-demand intracellular release of siRNA. As a proof-of-concept application, the capability of this nanocomposite carrier to load, protect and deliver anticancer siRNA into the cytoplasm of KHOS cancer cells was demonstrated in vitro.

2. Results and Discussion

2.1. Material Synthesis and Characterization

As shown in Scheme 1, the magnetic nanocrystal clusters (MNC) were first synthesized by a hydrothermal method. Their morphology was observed by scanning electron microscopy (SEM) and transmission electron microscopy (TEM) (**Figure 1**a,b,d). The MNC consist of nearly monodispersed spherical nanoparticles with particle sizes around 100 nm (Figure S1a, Supporting Information). Both high magnification SEM (Figure 1b) and TEM (Figure 1d) images demonstrate that each nanoparticle is composed of many smaller nanocrystals around 10 nm. The energy dispersive X-ray (EDX) spectrum (Figure 1c) confirms the composition of MNC is iron oxide and the fast Fourier transform (FFT) image (Figure 1e) suggests the crystal phase is magnetite.[31] The crystal phase of MNC is further confirmed by Raman spectrum (Figure 1f) and X-ray diffraction (XRD) (**Figure 2**c). The Raman spectrum of MNC exhibits the characteristic band of magnetite at 668 cm^{-1} assigned to the A_{1g} transition.[31] After controlled oxidation in air at 400 °C for 3 h, the product shows typical Raman spectrum of a-Fe_2O_3.[32] In XRD pattern (Figure 2c), all detected diffraction peaks can be indexed to the spinel structure of magnetite (Fe_3O_4, JCPDS no. 19–0629). The average crystallite size of MNC was calculated to be 12 ± 1 nm by the Debye–Scherrer formula based on the (311) reflection. This domain size is in agreement with the TEM and SEM observation and is below the critical domain size of super-paramagnetic magnetite, which is generally considered to be around 20–30 nm at room temperature.[33]

In the next step, the MNC nanoparticles were coated with a dendrimer-like mesoporous silica layer by an oil/water two phase reaction method. Figure 2a,b,d,e shows SEM and TEM images of the product obtained, which is MNC coated by large-pore mesoporous silica (denoted as MNC@LPMS). These particles show clear core–shell structure with dendrimer-like radial mesopore channels in the shell, relatively uniform particle sizes around 150 nm (Figure S1b, Supporting Information) and negligible interparticle aggregation. The successful coating of

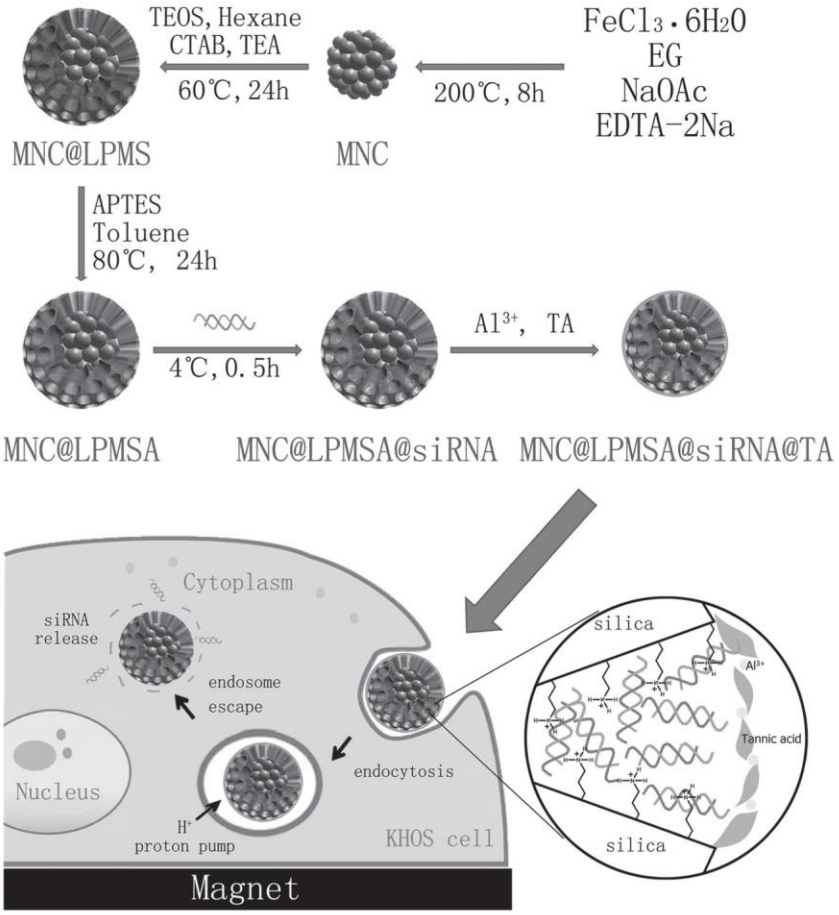

Scheme 1. Fabrication of siRNA carrier based on magnetic large-pore mesoporous silica nanoparticle for magnetofection.

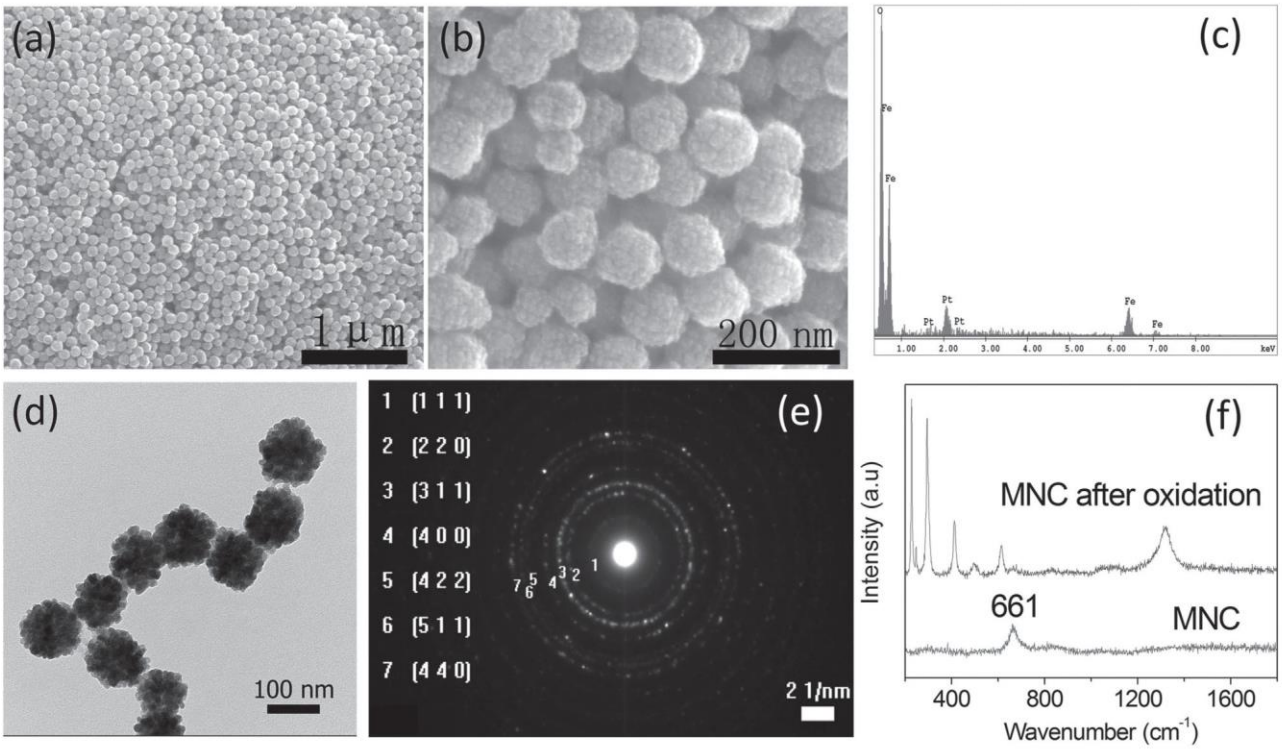

Figure 1. a,b) SEM images, c) EDX spectrum, d) TEM image, e) fast Fourier transform image, and f) Raman spectrum of MNC.

the large-pore mesoporous silica shell is corroborated with nitrogen physical sorption (**Figure 3** and **Table 1**). Before silica coating, the MNC shows a surface area of 54 m^2 g^{-1} and a pore volume of 0.27 cm^3 g^{-1} due to texture porosity. After coating, the MNC@LPMS shows a significantly increased surface area of 456 m^2 g^{-1} and a pore volume of 1.44 cm^3 g^{-1}. Meanwhile, a peak centered at 12 nm can be identified in the pore size distribution curve, which agrees well with TEM and SEM images. In the XRD pattern of MNC@LPMS (Figure 2c), a broad peak at 20°–26° appears in addition

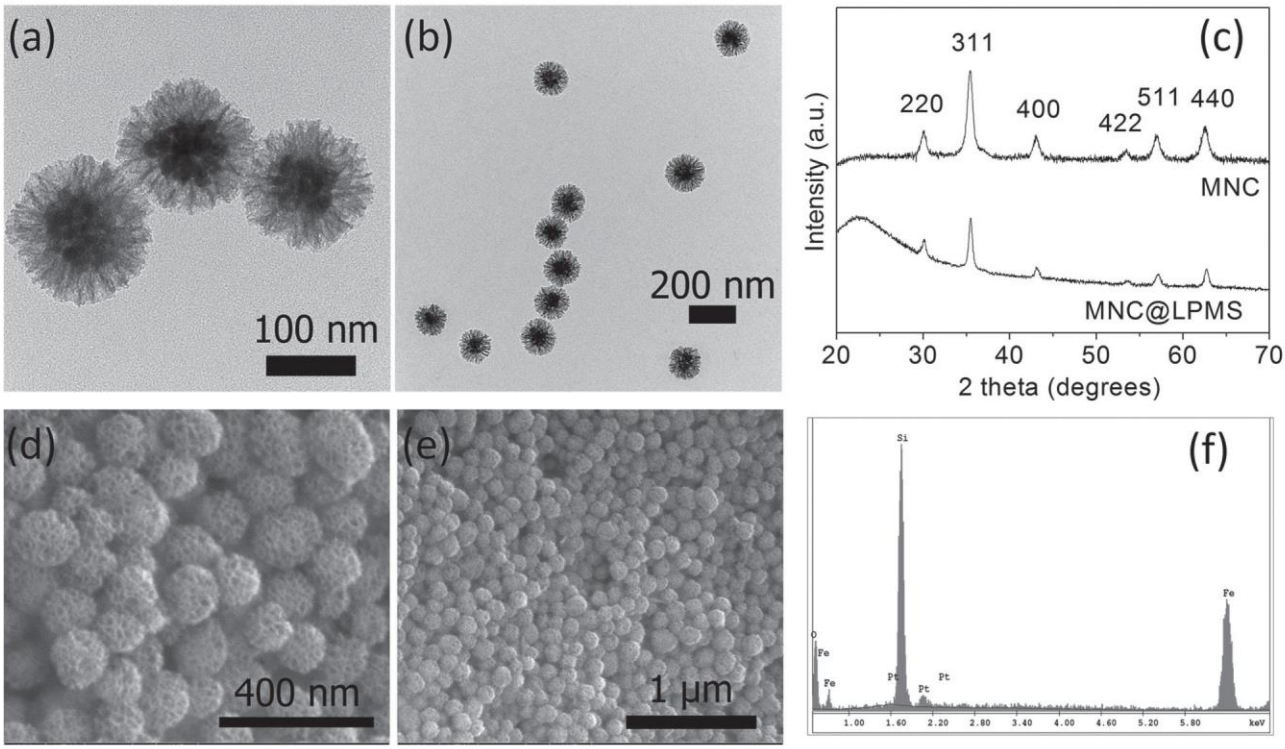

Figure 2. a,b) TEM images, c) XRD diffraction patterns, d,e) SEM images, and f) EDX spectrum of MNC@LPMS.

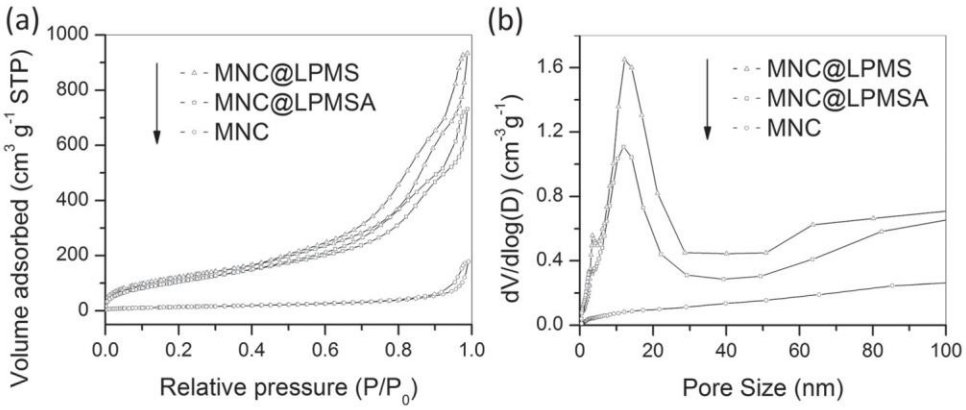

Figure 3. a) Nitrogen adsorption-desorption isotherms measured at –196 °C and b) the corresponding pore size distributions of MNC, MNC@LPMS, and MNC@LPMSA.

to the peaks of MNC and is characteristic of amorphous silica.[18] The presence of silicon and iron in MNC@LPMS is also validated by EDX spectrum (Figure 2f). As for magnetic property (**Figure 4**), the saturation magnetization drops from 69 emu g $^{-1}$ for MNC to 30 emu g $^{-1}$ for MNC@LPMS due to the weight fraction of silica in the composite particles and a surface coating related effect.[34] Nevertheless, the saturation magnetization value of MNC@LPMS is much higher than several Fe_3O_4/SiO_2 nanocomposites reported previously,[18,27] which ensures a strong magnetic response under external magnetic fields. Furthermore, no hysteresis is observed in low fields for both MNC and MNC@LPMS, indicating the super-paramagnetic property of these nanoparticles. The good dispersity and magnetic response of these nanoparticles in aqueous suspension are demonstrated by digital images and light scattering measurements (Figure S2, Supporting Information).In addition, it is noteworthy that acid etching of MNC@LPMS can result in hollow silica nanoparticles with radial mesoporous shell (Figure S3, Supporting Information). These nanoparticles could also be interesting for bioapplications due to their large radial mesopores and inner cavity.

For the loading of negatively charged nucleic acid, it is usually necessary to modify negatively charged primary silica surface to positive charge. Previously, various positively charged moieties including amino silane, polyethyleneimine (PEI), and poly(L-lysine) (PLL), have been studied for this purpose.[6,28,35,36] In this work, the surfactant-extracted MNC@LPMS (Figure S4, Supporting Information) was simply functionalized with (3-Aminopropyl)-triethoxysilane (APTES) by a conventional post-grafting method. The successful functionalization was confirmed by Fourier transform infrared (FTIR) spectra (Figure S5, Supporting Information) and zeta potential measurements (**Table 2**). The amine functionalized product (denoted as MNC@LPMSA) shows amine peak around 1540 cm^{-1} in FTIR spectrum and a positive surface zeta potential of 21 mV in neutral water. Herein, in comparison with PEI or PLL functionalization, the amino silane strategy has more advantages in addition to the easiness of synthesis: (1) the small amino-propyl groups grafted to the mesopore wall lead to a minimal loss in pore volume and surface area. As shown in Figure 3 and Table 1, there is only moderate/slight reduction in pore volume and surface area, and there is almost no change in pores size after APTES functionalization. On the contrary, functionalization with large cationic polymers may easily lead to severe pore volume reduction or even pore-blockage.[28] As it has been suggested that siRNA is adsorbed on functionalized mesoporous silica by both monolayer and multilayer mechanisms,[37] a high residual surface area and pore volume would be beneficial to siRNA adsorption. (2) The saturation magnetization is also only slightly compromised from 30 emu g^{-1} for MNC@LPMS to 25 emu g^{-1} for MNC@LPMSA due to minimal addition of organic fraction. (3) In contrast to cationic polymers with toxicity concerns, the amino silane modification is highly biocompatible.[38]

Table 1. Structure parameters of nanoparticles derived from nitrogen sorption.

Sample	Surface area [m^2 g^{-1}]	Pore volume [cm^3 g^{-1}]	Pore size [nm]
MNC	54	0.27	–
MNC@LPMS	456	1.44	12.2
MNC@LPMSA	411	1.13	12.0

2.2. Loading Capacity and Protection of siRNA

The siRNA loading capacity was evaluated by both agarose gel electrophoresis and zeta potential measurements (**Figure 5**a,b). As MNC@LPMSA to siRNA weight ratio increased from 5 to 200, the migration of siRNA on the gel was gradually retarded and eventually completely stopped at the weight ratios of carrier/siRNA above 50, which suggests a loading capacity around 2 wt%. Notably, despite the large MNC fraction in the composite, the loading capacity of MNC@LPMSA is still comparable with several previous reports which used mesoporous silica nanoparticles as siRNA carriers.[5,7,37] This could be attributed to the accessible radial mesopore up to 12 nm in the silica shell. To further illustrate the effect of mesopore structure, nanoparticles with similar core–shell structure, particle size and surface functionalization but 2 nm mesopores (Figure S6, Supporting Information)

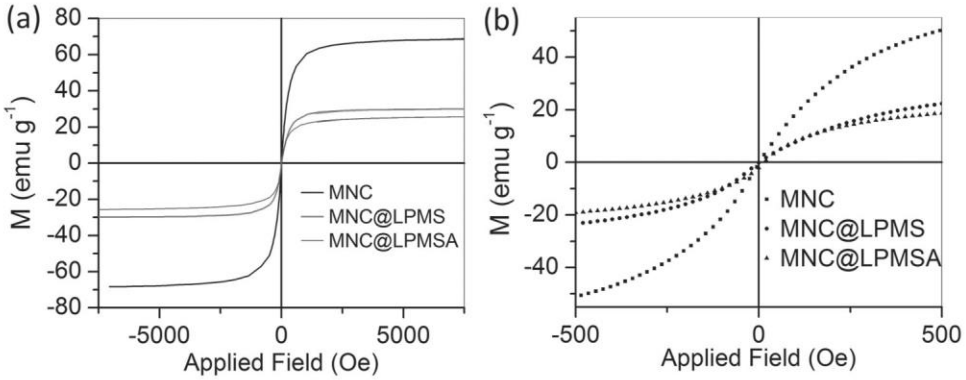

Figure 4. Field-dependent magnetization of MNC, MNC@LPMS, and MNC@LPMSA at 25 °C.

were prepared and evaluated for siRNA loading. These nanocomposites (denoted as MNC@MSA) are obtained by coating the MNC with ordinary mesoporous silica shell and being functionalized with APTES.As expected, the MNC@MSA can stop siRNA migration only at weight ratios of carrier/siRNA beyond 200, which suggests a much lower loading capacity than MNC@LPMSA. The good siRNA loading capacity of MNC@LPMSA was further confirmed by zeta potential measurements. The zeta potential of the siRNA-loaded nanoparticles (denoted as MNC@LPMSA@siRNA) shifts from negative to positive as the weight ratio of carrier/siRNA increases, and reaches zero at a weight ratio between 30 and 50. This is in agreement with the electrophoresis result. Thus, the loading ratio of MNC@LPMSA to siRNA was fixed at 50 (2 wt% payload) to achieve complete loading of siRNA with minimal carrier usage for all subsequent experiments.

Another challenge in siRNA delivery is the degradation of the therapeutic gene by endonucleases in physiological fluids. Thus, the siRNA protection capability was evaluated by treating the carrier/siRNA complex with ribonuclease A extracted from bovine pancreas (RNase). As shown in the gel pattern (Figure 5c), while naked siRNA is completely degraded by 5 mU RNase treatment, the band of nanocomposite-loaded siRNA is still identifiable when treated by 10 mU RNase. However, the intensity of siRNA band was severely reduced compared to the control without RNase treatment. This indicates that the MNC@LPMSA carrier is able to protect siRNA to some extent but the protection capability still needs to be improved. We assume the degradation process of siRNA may follow the following pathways: (1) Part of siRNA was absorbed and located on the external particle surface, as indicated by the lower surface potential of MNC@LPMSA@siRNA compared with MNC@LPMSA (Table 2). These siRNA could be easily degraded when it contacted with RNase. (2) The siRNA absorbed in the pores would be gradually released out with increasing incubation time and then degraded by RNase.[5,37] (3) As the size of RNase is about 2.2 nm × 2.8 nm × 3.8 nm and close to that of siRNA (6 nm long × 3 nm diameter),[37,39] the RNase can diffuse into the large radial mesopore of carriers and degrade the siRNA located inside the pores.

Table 2. Hydrodynamic diameters and zeta potentials of nanoparticles dispersed in water.

Sample	Zeta potential [mV]	Average particle size [nm]	Polydispersity index
MNC	−44.2	107	0.039
MNC@LPMS	−35.2	180	0.048
MNC@LPMSA	21.0	209	0.115
MNC@LPMSA@siRNA	5.4	912	0.288
MNC@LPMSA@siRNA@TA	−53.1	291	0.086

To block these possible degradation pathways and further improve the protection capability of the carrier, a recently developed acid-liable coating was applied to the MNC@LPMSA@siRNA based on the pH-dependent complexation between tannic acid (TA), a polyphenolic ligand, and metal ions.[40] By simply mixing solutions containing Al^{3+} ions and TA with the siRNA loaded nanoparticles, and adjusting the reaction pH, the surface coating is formed in minutes. In contrast to previous carrier coating strategies using lipid bilayer or cationic polymers,[4,8,30,41] this TA coating has been featured by high biocompatibility, availability to various substrates, facile one-step preparation and pH-dependent decomposition.[40,42,43] In this study, the successful coating of TA onto the nanoparticles is first confirmed by FTIR, X-ray photoelectron spectroscopy (XPS), thermogravimetric analysis (Figure S7, Supporting Information). The TA coated sample shows additional C–H adsorption peaks in 1300–1500 cm^{-1} range of FTIR spectrum. In XPS spectra, the increased carbon/silicon atom ratio (Table S1, Supporting Information) and the presence of Al peak also indicates the coating by TA/Al^{3+} complex. Based on weight loss in thermogravimetric analysis, the TA coating is estimated to be about 3 wt% of the total nanocomposite. In TEM images (Figure S8, Supporting Information), compared with MNC@LPMSA, MNC@LPMSA@siRNA@TA shows reduced pore/channel and core/shell contrast due to the cargo loading and TA coating.

Next, the pH-dependent decomposition of TA/Al^{3+} coating in physiological relevant pH range was verified. As determined by UV–vis absorption (Figure S9a–c, Supporting Information), the detachment of TA from nanoparticles at pH 5 is significantly faster than that at pH 7 due to the pH-dependent assembly of TA/Al^{3+} (Figure S9d, Supporting Information).[40] The release of siRNA from the TA coated carrier/siRNA complex (denoted as

www.MaterialsViews.com

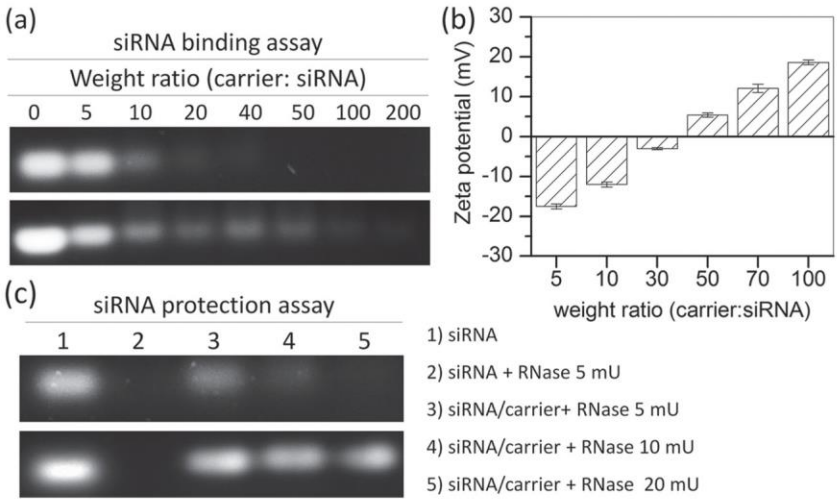

Figure 5. a) Agarose gel retardation assay of carrier/siRNA complex at various weight ratios of carrier/siRNA. The carriers are MNC@LPMSA (top) and MNC@MSA (bottom). b) Zeta potentials of MNC@LPMSA@siRNA complex at various weight ratios of carrier/siRNA in water. c) Protection of siRNA against RNase digestion. The carrier/siRNA complex is MNC@LPMSA@siRNA (top) and MNC@LPMSA@siRNA@TA (bottom).

MNC@LPMSA@siRNA@TA) also follows a pH-dependent behavior (Figure S10, Supporting Information). After 24 h of incubation at pH 7 and pH 5, the residual siRNA in the carriers is 44% and 19%, respectively. Thus, the TA coating can serve as a pH-responsive switch during siRNA delivery.

Finally, the siRNA protection performance of TA-coated carriers is evaluated. As shown in Figure 5c, the siRNA is well protected in MNC@LPMSA@siRNA@TA even with 20 mU RNase whereby it is almost completely degraded in MNC@LPMSA@siRNA. This enhanced protection could be explained by the retardation effect of TA coating on the diffusion of siRNA/RNase molecules through the coating layer. Besides, the TA coating may contribute two additional benefits for siRNA delivery application: (1) it improves the colloid stability of the carrier/siRNA complex as indicated from the hydrodynamic size distributions (Figure S11, Supporting Information) by shifting its zeta potential in water from 5.4 to –53.1 mV (Table 2). The colloid stability can be even kept in serum-containing cell culture medium for 24 h; (2) the disassembly of TA/Al^{3+} coating is a proton-consuming reaction, which could facilitate the intracellular endosome escape process through the "proton sponge" mechanism.[44]

2.3. Biocompatibility and Cellular Delivery of siRNA

The cellular delivery of fluorescein isothiocyanate (FITC)-labeled siRNA by MNC@LPMSA with TA coating (denoted as MNC@LPMSA-TA) was analyzed by confocal microscopy and flow cytometry on the human osteosarcoma KHOS cell line. As shown in confocal images (**Figure 6**), siRNA fluorescence is negligible in the KHOS cells in the absence of nanoparticles due to the poor cellular uptake of naked siRNA.[6] In contrast, siRNA fluorescence can be clearly observed in the cytoplasm region of cells treated with MNC@LPMSA@siRNA@TA, indicating the effective siRNA uptake mediated through the nanocarrier. Furthermore, the highest siRNA uptake was achieved when the cells were incubated under a magnetic field at the same time. This could be attributed to magnetic field guided accumulation of nanocarriers toward the cell surface.[13] To quantify the effect of magnetic field on siRNA cellular uptake, flow cytometry analysis was conducted (Figure S12, Supporting Information) and the results show the percentage of siRNA signal-positive cells is nearly 40% higher with magnetic field treatment than that without magnetic field treatment (38% vs 27%) after 6 h of incubation. Therefore it is concluded that the magnetic response of the nanocarrier can promote cellular entry of siRNA with the aid of an external magnetic field. Another critical barrier in the siRNA delivery process is endosome escape and efficient delivery vectors must initiate effective endosomal escape before the degradation of their packaged siRNA in lysosome.[41] Thus, the subcellular location of carrier/siRNA complex relative to endosome was examined by confocal microscopy (Figure S13, Supporting Information). After 12 h incubation, the siRNA signal is not overlapped with the endosome signal in most of the region observed, indicating the successful endosome escape of siRNA after cellular uptake. Meanwhile, in only a few cells (Figure S13b, Supporting Information), the partial overlap of two signals confirms that the cellular uptake of carrier/siRNA complex is through an endocytosis pathway.

The cellular biocompatibility and siRNA delivery function of MNC@LPMSA-TA was evaluated by 3-(4,5-dimethylthiazol-2-yl)-2,5-diphenyltetrazolium bromide (MTT) assays. To illustrate the cytotoxicity of TA coating, equivalent amount of poly(acrylic acid) (PAA) (2 wt%) is used as a nontoxic model payload of siRNA. As shown in **Figure 7**a, both the MNC@

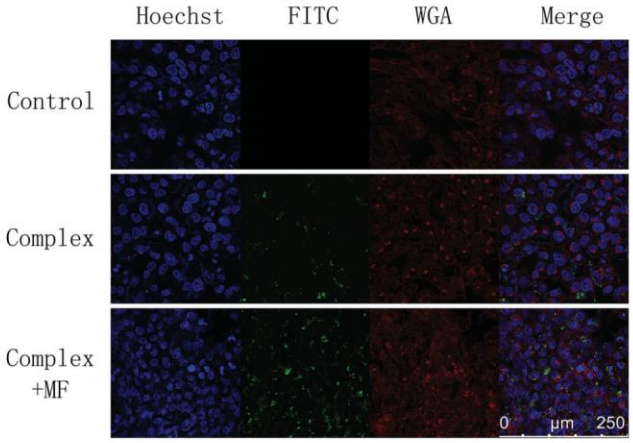

Figure 6. CLSM images of KHOS cells after 6 h of incubation with 20 μg mL^{-1} MNC@LPMSA@siRNA@TA complex with and without magnetic field (MF). Cells incubated with naked siRNA were used as control. The cell nucleus (blue) was labeled with Hoechst 33258; the siRNA (green) was labeled with FITC; the plasma membrane (red) was labeled with Alexa Fluor 594-WGA.

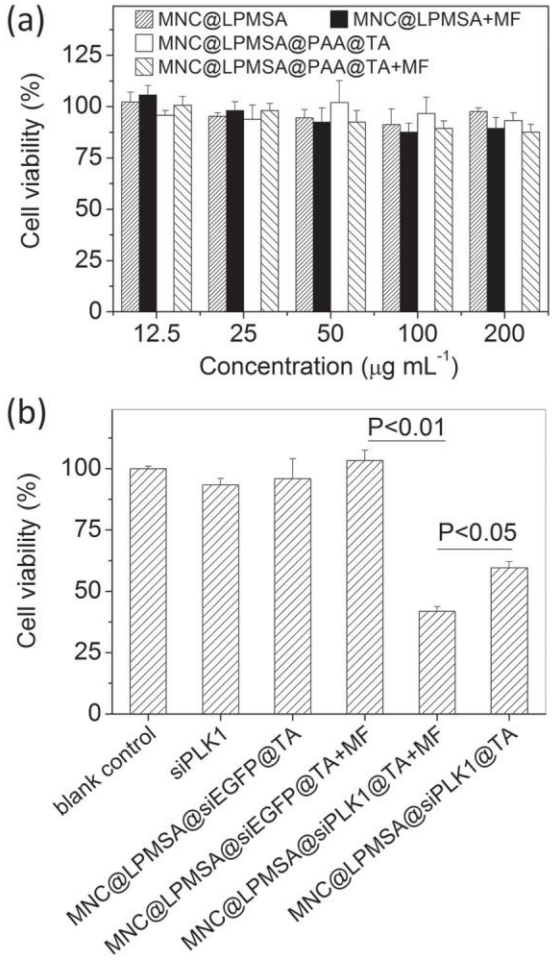

Figure 7. a) Cytotoxicity of MNC@LPMSA and MNC@LPMSA@PAA@TA against KHOS cells with or without magnetic field (MF) after 48 h. b) Biological function analysis of MNC@LPMSA-TA delivery systems by delivering functional siRNA against oncogenes PLK1 (siPLK1) in osteosarcoma cell line KHOS. The siRNA against enhanced green fluorescent protein (siEGFP) was used as a negative control. The siRNA concentrations are fixed at 1 μg mL^{-1}. The *P* values are from Student's *t* test.

LPMSA nanoparticles and MNC@LPMSA@PAA@TA nanocomposite show negligible toxicity toward KHOS cells under the concentration of 200 μg mL^{-1}. In addition, the presence of a magnetic field does not affect the cell viability significantly in this concentration range. The good biocompatibility of the MNC@LPMSA-TA is within the expectation as both the silica and magnetite nanoparticles have been extensively investigated for intracellular delivery applications.[12,33] Furthermore, the tannic acid is a natural polyphenol widely distributed in various plant tissues and generally recognized as safe by the U.S. Food and Drug Administration.[42,45] To demonstrate functional siRNA delivery by the MNC@LPMSA-TA system, the siRNA against polo-like kinase 1 (siPLK1) was chosen as the functional payload because the PLK1 gene is highly expressed in KHOS cells. Meanwhile, the siRNA against enhanced green fluorescent protein (siEGFP) was used as a negative control as the EGFP gene is absent in KHOS cells. As shown in Figure 7b, the delivery of siPLK1 through MNC@LPMSA-TA led to a reduced cell viability of 60% compared to the untreated cells while the delivery of siEGFP by the same carrier caused little change. This suggests reduction effect is due to the interference function of siPLK1 which suggests the successful delivery of siPLK1 into the cytoplasm. On the other hand, when a magnetic field is present, the cell viability after treatment with MNC@LPMSA@siPLK1@TA is further reduced to 42%. Because the magnetic field itself has negligible effect on cell viability as shown in the cytotoxicity assay, the increased inhibition effect should be due to the enhanced uptake of the carrier/siPLK1 complex under a magnetic field.

3. Conclusion

In summary, a novel type of magnetic core–shell silica nanoparticles with 150 nm particle size and 12 nm radial large mesopores was fabricated for the first time. Compared with silica/magnetite composites reported previously, these amine functionalized nanoparticles exhibit large surface area of 411 m^2 g^{-1}, high pore volume of 1.13 cm^3 g^{-1} and magnetization of 25 emu g^{-1} simultaneously after amine functionalization.As a result, these nanoparticles exhibit both high siRNA loading capacity of 2 wt% and strong response under external magnetic fields. The protection of siRNA by these nanoparticles can be further improved by an acid-liable tannic acid coating. The coating can also improve the dispersion stability of the siRNA-loaded carrier and serve as a pH-responsive releasing switch. Using this nanocomposite carrier, functional siRNA was successfully delivered into the cytoplasm of KHOS cancer cells in vitro. The delivery was significantly enhanced with the aid of an external magnetic field. These results suggest the above magnetic silica nanoparticles with tannic acid coating could be a very promising platform for siRNA therapeutic applications. Future work can be anticipated by exploring the multifunctionality of these nanoparticles such as magnetic resonance imaging and/or further functionalization such as pegylation toward in vivo application.

Supporting Information

Supporting Information is available from the Wiley Online Library or from the author.

Acknowledgements

This work was financially supported by the Australian Research Council (ARC) through the Discovery Project program (DP130104459 and DP140104062).

[1] M. E. Davis, J. E. Zuckerman, C. H. Choi, D. Seligson, A. Tolcher, C. A. Alabi, Y. Yen, J. D. Heidel, A. Ribas, *Nature* **2010**, *464*, 1067.
[2] C. Hom, J. Lu, M. Liong, H. Luo, Z. Li, J. I. Zink, F. Tamanoi, *Small* **2010**, *6*, 1185.
[3] M.-H. Kim, H.-K. Na, Y.-K. Kim, S.-R. Ryoo, H. S. Cho, K. E. Lee, H. Jeon, R. Ryoo, D.-H. Min, *ACS Nano* **2011**, *5*, 3568.

[4] C. E. Ashley, E. C. Carnes, K. E. Epler, D. P. Padilla, G. K. Phillips, R. E. Castillo, D. C. Wilkinson, B. S. Wilkinson, C. A. Burgard, R. M. Kalinich, J. L. Townson, B. Chackerian, C. L. Willman, D. S. Peabody, W. Wharton, C. J. Brinker, *ACS Nano* **2012**, *6*, 2174.
[5] N. Hee-Kyung, K. Mi-Hee, P. Kihyun, R. Soo-Ryoon, L. Kyung Eun, J. Hyesung, R. Ryong, H. Changbong, M. Dal-Hee, *Small* **2012**, *8*, 1752.
[6] S. B. Hartono, W. Gu, F. Kleitz, J. Liu, L. He, A. P. Middelberg, C. Yu, G. Q. Lu, S.-Z. Qiao, *ACS Nano* **2012**, *6*, 2104.
[7] D. Lin, Q. Cheng, Q. Jiang, Y. Huang, Z. Yang, S. Han, Y. Zhao, S. Guo, Z. Liang, A. Dong, *Nanoscale* **2013**, *5*, 4291.
[8] K. Moller, K. Muller, H. Engelke, C. Brauchle, E. Wagner, T. Bein, *Nanoscale* **2016**, *8*, 4007.
[9] M. Wu, Q. Meng, Y. Chen, L. Zhang, M. Li, X. Cai, Y. Li, P. Yu, L. Zhang, J. L. Shi, *Adv. Mater.* **2016**, *28*, 1963.
[10] N. Z. Knezevic, J. O. Durand, *Nanoscale* **2015**, *7*, 2199.
[11] R. Otero-Lorenzo, A. B. Davila-Ibanez, M. Comesana-Hermo, M. A. Correa-Duarte, V. Salgueirino, *J. Mater. Chem. B* **2014**, *2*, 2645.
[12] Y. Wang, H. C. Gu, *Adv. Mater.* **2015**, *27*, 576.
[13] F. Scherer, M. Anton, U. Schillinger, J. Henke, C. Bergemann, A. Kruger, B. Gansbacher, C. Plank, *Gene Ther.* **2002**, *9*, 102.
[14] C. Plank, O. Zelphati, O. Mykhaylyk, *Adv. Drug Delivery Rev.* **2011**, *63*, 1300.
[15] S. Gai, P. Yang, P. a. Ma, D. Wang, C. Li, X. Li, N. Niu, J. Lin, *J. Mater. Chem.* **2011**, *21*, 19422.
[16] J. M. Rosenholm, J. Zhang, W. Sun, H. C. Gu, *Microporous Mesoporous Mater.* **2011**, *145*, 14.
[17] J. M. Rosenholm, C. Sahlgren, M. Linden, *Curr. Drug Targets* **2011**, *12*, 1166.
[18] J. Liu, B. Wang, S. B. Hartono, T. Liu, P. Kantharidis, A. P. Middelberg, G. Q. Lu, L. He, S.-Z. Qiao, *Biomaterials* **2012**, *33*, 970.
[19] K. J. Yu, X. B. Zhang, H. W. Tong, X. Y. Yan, S. M. Liu, *Mater. Lett.* **2013**, *106*, 151.
[20] J. Yang, F. Zhang, W. Li, D. Gu, D. Shen, J. Fan, W. X. Zhang, D. Y. Zhao, *Chem. Commun.* **2014**, *50*, 713.
[21] Z. Sun, Q. Yue, Y. Liu, J. Wei, B. Li, S. Kaliaguine, Y. Deng, Z. Wu, D. Y. Zhao, *J. Mater. Chem. A* **2014**, *2*, 18322.
[22] D. Niu, Z. Liu, Y. Li, X. Luo, J. Zhang, J. Gong, J. L. Shi, *Adv. Mater.* **2014**, *26*, 4947.
[23] Q. Yue, J. Li, W. Luo, Y. Zhang, A. A. Elzatahry, X. Wang, C. Wang, W. Li, X. Cheng, A. Alghamdi, A. M. Abdullah, Y. H. Deng, D. Y. Zhao, *J. Am. Chem. Soc.* **2015**, *137*, 13282.
[24] T. Atabaev, J. H. Lee, J. J. Lee, D. W. Han, Y. H. Hwang, H. K. Kim, N. H. Hong, *Nanotechnology* **2013**, *24*, 345603.
[25] C. L. Tao, Y. F. Zhu, X. L. Li, N. Hanagata, *RSC Adv.* **2014**, *4*, 45823.
[26] C. Tao, Y. Zhu, *Dalton Trans.* **2014**, *43*, 15482.
[27] S. B. Hartono, M. Yu, W. Gu, J. Yang, E. Strounina, X. Wang, S.-Z. Qiao, C. Z. Yu, *Nanotechnology* **2014**, *25*, 055701.
[28] X. Du, B. Shi, J. Liang, J. Bi, S. Dai, S.-Z. Qiao, *Adv. Mater.* **2013**, *25*, 5981.
[29] J. Zhang, M. Niemela, J. Westermarck, J. M. Rosenholm, *Dalton Trans.* **2014**, *43*, 4115.
[30] S. B. Hartono, N. T. Phuoc, M. H. Yu, Z. F. Jia, M. J. Monteiro, S.-Z. Qiao, C. Z. Yu, *J. Mater. Chem. B* **2014**, *2*, 718.
[31] T. J. Daou, G. Pourroy, S. Begin-Colin, J. M. Greneche, C. Ulhaq-Bouillet, P. Legare, P. Bernhardt, C. Leuvrey, G. Rogez, *Chem. Mater.* **2006**, *18*, 4399.
[32] H. Deng, X. Li, Q. Peng, X. Wang, J. Chen, Y. D. Li, *Angew. Chem. Int. Ed.* **2005**, *44*, 2782.
[33] M. Lin, H. Huang, Z. Liu, Y. Liu, J. Ge, Y. P. Fang, *Langmuir* **2013**, *29*, 15433.
[34] J. Ge, Y. Hu, M. Biasini, W. P. Beyermann, Y. D. Yin, *Angew. Chem. Int. Ed.* **2007**, *46*, 4342.
[35] F. Gao, P. Botella, A. Corma, J. Blesa, L. Dong, *J. Phys. Chem. B* **2009**, *113*, 1796.
[36] Y. F. Zhu, W. J. Meng, H. Gao, N. Hanagata, *J. Phys. Chem. C* **2011**, *115*, 13630.
[37] J. L. Steinbacher, C. C. Landry, *Langmuir* **2014**, *30*, 4396.
[38] M. A. Malvindi, V. De Matteis, A. Galeone, V. Brunetti, G. C. Anyfantis, A. Athanassiou, R. Cingolani, P. P. Pompa, *PLoS One* **2014**, *9*, e85835.
[39] J. Zhang, S. Karmakar, M. Yu, N. Mitter, J. Zou, C. Z. Yu, *Small* **2014**, *10*, 5068.
[40] Y. Ping, J. Guo, H. Ejima, X. Chen, J. J. Richardson, H. Sun, F. Caruso, *Small* **2015**, *11*, 2032.
[41] M. Wang, X. Li, Y. Ma, H. C. Gu, *Int. J. Pharm.* **2013**, *448*, 51.
[42] H. Ejima, J. J. Richardson, K. Liang, J. P. Best, M. P. van Koeverden, G. K. Such, J. Cui, F. Caruso, *Science* **2013**, *341*, 154.
[43] J. Guo, Y. Ping, H. Ejima, K. Alt, M. Meissner, J. J. Richardson, Y. Yan, K. Peter, D. von Elverfeldt, C. E. Hagemeyer, F. Caruso, *Angew. Chem. Int. Ed.* **2014**, *53*, 5546.
[44] I. Slowing, B. G. Trewyn, V. S. Lin, *J. Am. Chem. Soc.* **2006**, *128*, 14792.
[45] T. S. Sileika, D. G. Barrett, R. Zhang, K. H. Lau, P. B. Messersmith, *Angew. Chem. Int. Ed.* **2013**, *52*, 10766.

Received: February 17, 2016
Revised: April 10, 2016
Published online: May 19, 2016

5.3 Supplementary Information

This section is included in the thesis as supplementary information to section 5.2. It includes additional information which is not put in the main text of the published paper, but as electronic supplementary information freely accessible online.

Magnetic Core-Shell Silica Nanoparticles with Large Radial Mesopores for siRNA Delivery

*Lin Xiong, Jingxu Bi, Youhong Tang and Shi-Zhang Qiao**

L. Xiong, Prof. J. Bi, Prof. S. Z. Qiao
School of Chemical Engineering, The University of Adelaide, SA 5005, Australia
E-mail: s.qiao@adelaide.edu.au

Dr. Y. Tang
Centre for Nano Scale Science and Technology
School of Computer Science, Engineering, and Mathematics,
Flinders University, Adelaide, SA 5042, Australia

I. Experiment Section

Materials

Tetraethyl orthosilicate (TEOS), (3-Aminopropyl)-triethoxysilane (APTES), triethanolamine (TEA), cetyltrimethylammonium bromide (CTAB), Iron(III) chloride hexahydrate ($FeCl_3 \cdot 6H_2O$), ethylene glycol (EG), sodium acetate anhydrous (NaAc), tannic acid (TA), aluminium(III) chloride, 3-(N-morpholino)propanesulfonic acid (MOPS), hexane, ethanol, methylsulfoxide (DMSO), 2-(N-morpholino)ethanesulfonic acid (MES), ammonium nitrate, sodium dodecyl sulfate (SDS), poly(acrylic acid) (PAA, M.W.=800), 3-[4,5-dimethylthialzol-2-yl]-2,5-diphenyltetrazolium bromide (MTT), KHOS (human osteogenic sarcoma) cell lines, siRNA targeting polo-like-kinase 1

(siPLK1), siRNA targeting enhanced green fluorescent protein (siEGFP), and ribonuclease A from bovine pancreas (RNase) were purchased from Sigma Aldrich. Fluorescein isothiocyanate (FITC)-conjugated siRNA was purchased from Santa Cruz Biotechnology. Ethylenediaminetetraacetic acid disodium salt (EDTA-2Na) was purchased from Ajax Finechem, Australia. Dulbecco's Modified Eagle's Medium (DMEM), fetal bovine serum (FBS), and phosphate buffered saline (PBS), Tris Acetate-EDTA (TAE) buffers, and agarose were purchased from Gibco-BRL (Grand Island, U.S.A.). Plasma membrane and nuclear labelling kit were purchased from Life science, Australia. LysoTracker Red was purchased from Beyotime Biotechnology Company, China. Water used in all experiments was purified using a Milli-Q Plus 185 water purification system (Millipore, Bedford, MA) with a resistivity higher than 18 MΩ cm.

Super-paramagnetic magnetite nanocrystal clusters

Super-paramagnetic magnetite nanocrystal clusters (MNC) were synthesized according to a previous report.[1] Typically, 0.68 g of $FeCl_3 \cdot 6H_2O$, 0.6 g of NaAc, and 0.034 g of EDTA-2Na were dissolved in 20 mL of ethylene glycol. After sonication treatment in a water bath (Branson B5510-DTH) for 2 h, the dark yellow mixture was transferred to a Teflon-lined stainless-steel autoclave and heated at 200 °C for 8 h. After that, the black precipitate was rinsed with water and ethanol three times each and then dried at 50 °C in a vacuum oven.

Magnetic nanocrystal clusters coated with large pore mesoporous silica

Magnetic nanocrystal clusters coated with large pore mesoporous silica (MNC@LPMS) are synthesized through a modified two phase reaction method.[2, 3] The reaction was carried out in a three-neck reaction flask equipped with nitrogen flow and reflux condenser. Briefly, 20 mg of MNC was first dispersed in 20 ml of H_2O with the aid of ultrasound. Then, the dispersion was added dropwise to 20 mL aqueous solution containing 0.4 g of CTAB and 100 mg of TEA under vigorous stirring. The mixture was further sonicated (Branson B5510-DTH) for 20 minutes and mechanical stirred for 1 hour. Afterwards, 50 µL of TEOS dissolved in 20 ml hexane

was added slowly. The system was allowed to react at 60 ˚C for 24 h in an oil bath. Afterwards, a brown solid product was collected by centrifugation and subject to surfactant extraction in 100 ml of ethanol containing 2 wt % ammonium nitrate for two cycles. To obtain amine functionalized product (MNC@LPMSA), 50 mg of surfactant-free MNC@LPMS was dispersed in 20 ml of toluene. Then, 100 µL of APTES was added and the mixture was refluxed at 80 °C for 24 h under nitrogen flow. Finally, MNC@LPMSA was obtained after centrifugation and washing repeatedly with toluene and ethanol. For comparison, magnetic nanocrystal clusters were also coated by silica shell with ordinary 2-3 nm mesoporous pore. The synthesis of these nanoparticles, denoted as MNC@MS, were the same as that for MNC@LPMS except that TEOS was added directly without hexane and the quantity was adjusted to 100 µL. The MNC@MS was functionalized with APTES in the same way as MNC@LPMSA to obtain MNC@MSA.

Loading capacity and protection of siRNA

The siRNA loading and protection by MNC@LPMSA was evaluated by agarose gel electrophoresis. In the loading capacity assay, MNC@LPMSA and siRNA (0.2 µg) were mixed at different weight ratios from 5:1 to 200:1 (MNC@LPMSA to siRNA). After brief vortex, the mixture was incubated for 0.5 h at 4 °C to allow the formation of carrier/siRNA complex (MNC@LPMSA@siRNA). Then the complex was subjected to electrophoresis on an agarose gel (0.8% w/v) for 1 h at 60 V in TAE buffer. The resulting migration patterns were recorded under UV irradiation (G-BOX, SYNGENE). In the protection assay, 0.2 µg of siRNA that had been loaded into MNC@LPMSA with or without tannic acid coating was incubated with varied amounts of RNase at 37 °C for 0.5 h. Then, 5 µL of sodium dodecyl sulfate (2 mg ml^{-1}) was added to denature RNase A and stop the enzymatic reaction at 60 °C for 5 min. To further break the TA coating and displace the siRNA, 5 µL of poly(acrylic acid) (2 mg ml^{-1}) was added and incubated for 10 min. The samples were subsequently analysed by agarose gel electrophoresis to determine the extent of siRNA degradation.

Tannic acid coating and siRNA release

According to the loading capacity of MNC@LPMSA determined by gel electrophoresis, the final siRNA delivery system was obtained by coating the siRNA-loaded MNC@LPMSA with an acid-degradable tannic acid shell.[4, 5] First, 10 μL of siRNA (2 μg) was mixed with 10 μL of MNC@LPMSA (10 mg ml^{-1}) in an Eppendorf tube and incubated for 30 min at 4 °C to form MNC@LPMSA@siRNA complex. Then, 2.5 μL of $AlCl_3$ (2.4 mM) and 2.5 μL of tannic acid (TA, 2.4 mM) solution were added and mixed thoroughly. After 1 minute, 25 μL of MOPS buffer (20 mM, pH=7) was added and the suspension was centrifuged to remove excess reactant. The resulting complex MNC@LPMSA@siRNA@TA was further washed with water twice and used for subsequent in vitro experiment.

To study the degradation of the tannic acid layer, 10 mg of TA coated nanoparticles was incubated with 1 ml of either MOPS (pH=7) or MES (pH=5) buffer at 37 °C for desired periods. Then, the suspension was centrifuged. The supernatant liquid was diluted properly and adjusted to pH=2 with 1 M chloric acid to completely dissociate the TA/Al^{3+} complex. Then the TA concentration was determined using a calibration curve with a Uv-vis spectrometer (UV-2600, Shimadzu Corporation) at the wavelength of 275 nm. Note, due to the UV adsorption of siRNA near the wavelength, 2 wt% PAA was used as the model payload in this coating degradation experiment. The siRNA release was monitored by analyzing the residual siRNA in the solid carrier. The MNC@LPMSA@siRNA@TA complex (20 μg) was incubated in 1 ml of either MOPS (pH=7) or MES (pH=5) buffer at 37 °C for desired periods. Then, the suspension was centrifuged. The residual siRNA in the precipitate was replaced by poly(acrylic acid) and quantified by gel electrophoresis using GeneTools 4.03 software.

Cell culture and cell viability

Human osteosarcoma cell line KHOS were purchased from ATCC (American Type Culture Collection) and grown in DMEM culture medium supplemented with 10% (v/v) fetal bovine serum (FBS) in a humidified 5% CO_2 atmosphere at 37 °C. For all experiments, cells were harvested by using 0.25% trypsin and resuspended in fresh

medium before plating. The viability of cells was investigated using MTT assay. KHOS cells were seeded into 96-well plates at a density of 1×10^4 per well in 100 µL of media and grown for 24 h. Then, the growth medium was replaced with 100 µL of cell culture medium containing nanoparticles with or without siRNA loading. After incubation for 48 h, the medium was replaced by 100 µL of fresh medium and 10 µL of MTT (5.0 mg mL^{-1} in PBS) were added to each well. The cells were further incubated for 4 h. After that, the growth medium was removed and 150 µL of DMSO was added to each well to dissolve formazan crystals. Finally, the absorbance was determined using a micro-plate reader (Biotek, USA) at the wavelength of 595 nm. The viability of cells without nanoparticle treatment was assumed to be 100%.

Cellular uptake by flow cytometry

Quantification of cellular uptake was performed by flow cytometry analysis. KHOS cells were seeded in a 6-well plate (1×10^5 cells/well) and incubated for 24 h. Then, the cells were incubated with carrier/siRNA complex dispersed in culture medium (20 µg mL^{-1}). To investigate the influence of magnetic field on the cellular uptake, another 6-well plate seeded with the same conditions was put on a neodymium–iron–boron (Nd–Fe–B) permanent magnet brick. After desired incubation time, the cells were washed twice with PBS and trypsinized. After centrifugation, the cells were resuspended in PBS containing trypan blue (200 µg mL^{-1}). The fluorescence of endocytosed carrier/siRNA complex was detected by a FACSCalibur flow cytometer (Becton Dickinson) in FL1-H channel. The cellular uptake was calculated by the percentage of fluorescence-positive cells using the mock cells without siRNA treatment as negative control. For each sample, 1×10^4 cells were analysed at a rate of 200-400 cells per second. CellQuest 6.0 software was used for data analysis.

Cellular uptake and subcellular location by confocal laser scanning microscopy (CLSM)

The cellular uptake and subcellular location of carrier/siRNA complex were also observed with confocal laser scanning microscopy. KHOS cells were seeded in 6-well

plates (1×10^5 cells/well) with one piece of cover glass at the bottom of each well and cultured for 24 h. Then, the growth medium was changed to fresh medium containing nanoparticles (20 μg mL^{-1}) loaded with FITC-labelled siRNA. After 6 h, the cells were washed twice with PBS and fixed with 4 wt % formaldehyde. The cell nucleus and plasma membrane were stained with Hoechst 33258 and Alexa Fluor® 594 Wheat Germ Agglutinin (WGA), respectively. After the staining, the cells were softly washed twice with PBS to remove excessive dye and incubated in PBS before imaging. To investigate the effect of magnetic field on cellular uptake, another 6-well plate was put on the magnet brick with the other steps being the same as above. To investigate the endosome escape of gene carriers, samples with endosome and lysosome staining were also prepared. For these samples, LysoTracker Red was added to the culture medium 1 h before the fixation of cells following the supplier's protocol. The cover glasses were visualized under a confocal laser scanning microscope (Leica Confocal 1P/FCS). Optical sections were averaged 4 times to reduce noise. Images were processed using Leica confocal software.

Material characterization

Transmission electron microscopy (TEM) images were taken with FEI Tecnai G2 operated at 120 kV. The samples were prepared by dispersing the powder in ethanol and then dropped on carbon film supported by a Cu grid and air dried. Scanning electron microscopy (SEM) observation was carried out on a FEI Quanta 450 FEG environmental emission scanning electron microscope with energy dispersive X-ray (EDX) accessory. The samples were prepared by adding powder onto carbon tape and coated with platinum before SEM observation. The hydrodynamic size and zeta-potential of nanoparticles in aqueous dispersions were measured on a Malvern Zetasizer Nano ZS operated at a wavelength of 633 nm, where scattered light was collected at a fixed angle of 173°. X-ray diffraction (XRD) analysis was carried out on Rigaku Miniflex 600 with the Cu Kα line at 40 kV and 15 mA. Raman spectra were collected with HORIBA LabRAM HR Evolution with 633 nm laser. Fourier transform infrared (FTIR) spectra were recorded on a Thermo Scientific NICOLET 6700 FTIR

spectrometer with a Diamond ATR (attenuated total reflection) crystal. For each spectrum, 64 scans were collected at a resolution of 4 cm^{-1} over the range 650-4000 cm^{-1}. UV-vis absorption spectra were recorded on a UV-2600 spectrophotometer (Shimadzu Corporation). Thermogravimetric analysis (TGA) was performed on a Mettler Toledo Thermogravimetric Analyser, using an air atmosphere (60 mL min^{-1}) with a heating ramp of 20 ˚C min^{-1}. X-ray photoelectron spectroscopy (XPS) measurements were performed on an Axis Ultra (Kratos Analytical, UK) XPS spectrometer equipped with an Al Kα source (1486.6 eV). Nitrogen adsorption-desorption measurement was carried out at -196 ˚C using a TriStar II surface area and porosity analyser from Micromeritics. Prior to the measurement, the samples were degassed at 120 ˚C for 12 h. Brunauer-Emmett-Teller (BET) specific surface area was calculated using adsorption data at a relative pressure P/P_0 range of 0.05-0.30. Pore size distribution was derived from adsorption branch of the isotherm using the Barrett-Joyner-Halenda (BJH) method. Pore volume was determined from the amount of N_2 adsorbed at the single point of P/P_0=0.99. Magnetic properties were measured by Quantum Design 9 T Physical Properties Measurement System (PPMS 9T) equipped with AC Measurement System (ACMS).

Statistical analysis

Quantitative data were reported as mean ± standard deviation (SD) of at least three independent experiments. The statistical analyses were performed using a two sample, two tailed Student's t-test, with a *P*-value less than 0.05 considered being statistically significant.

References

[1] M. Lin, H. Huang, Z. Liu, Y. Liu, J. Ge, Y. P. Fang, *Langmuir* **2013,** *29*, 15433.

[2] D. Shen, J. Yang, X. Li, L. Zhou, R. Zhang, W. Li, L. Chen, R. Wang, F. Zhang, D. Y. Zhao, *Nano Lett.* **2014,** *14*, 923.

[3] Q. Yue, J. Li, W. Luo, Y. Zhang, A. A. Elzatahry, X. Wang, C. Wang, W. Li, X. Cheng, A. Alghamdi, A. M. Abdullah, Y. H. Deng, D. Y. Zhao, *J. Am. Chem. Soc.* **2015,** *137*, 13282.

[4] J. Guo, Y. Ping, H. Ejima, K. Alt, M. Meissner, J. J. Richardson, Y. Yan, K. Peter, D. von Elverfeldt, C. E. Hagemeyer, F. Caruso, *Angew. Chem. Int. Ed.* **2014,** *53*, 5546.

[5] Y. Ping, J. Guo, H. Ejima, X. Chen, J. J. Richardson, H. Sun, F. Caruso, *Small* **2015,** *11*, 2032.

II. Supplementary Figures and Tables

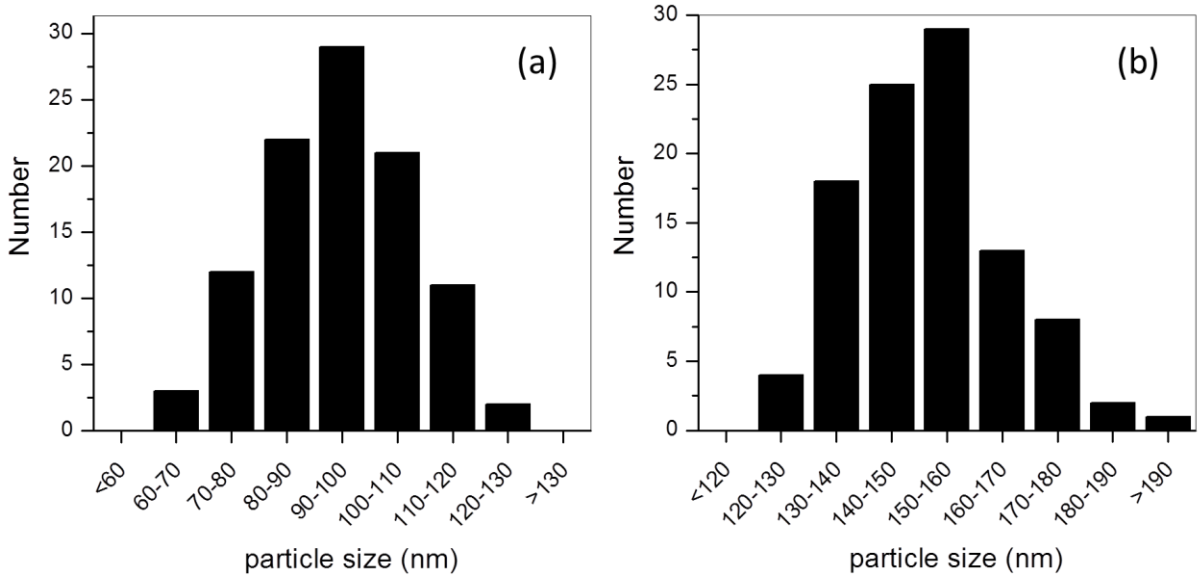

Figure S1. Particle size distributions of (a) MNC and (b) MNC@LPMS from scanning electron microscopy images by analysing 100 nanoparticles.

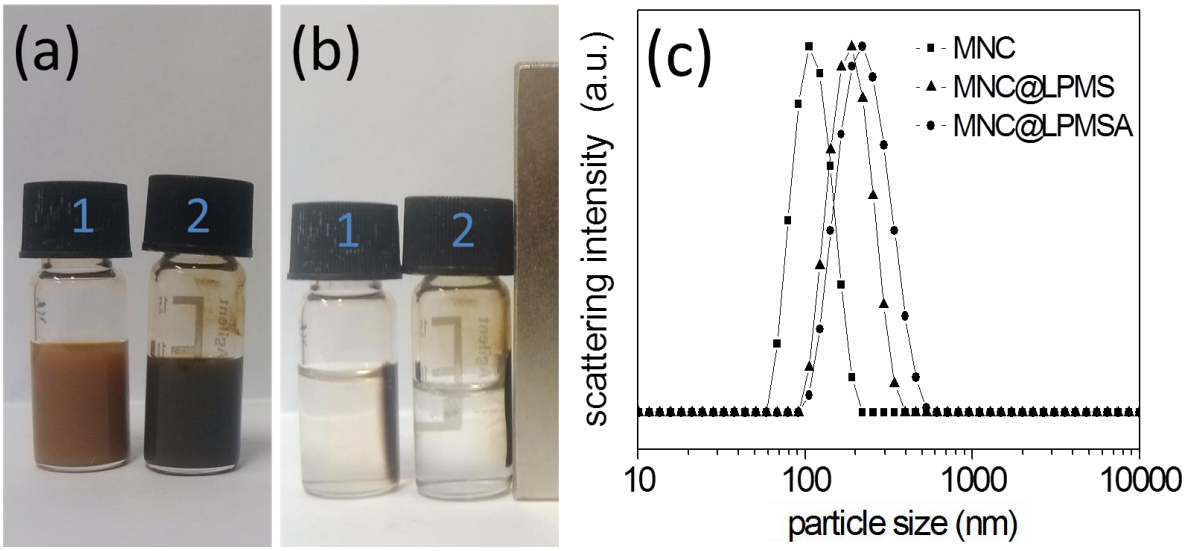

Figure S2. (a) Digital images of MNC@LPMS (1) and MNC (2) dispersed in water and (b) after 30 s under an external magnetic field. (c) Hydrodynamic particle size distributions of nanoparticles in water.

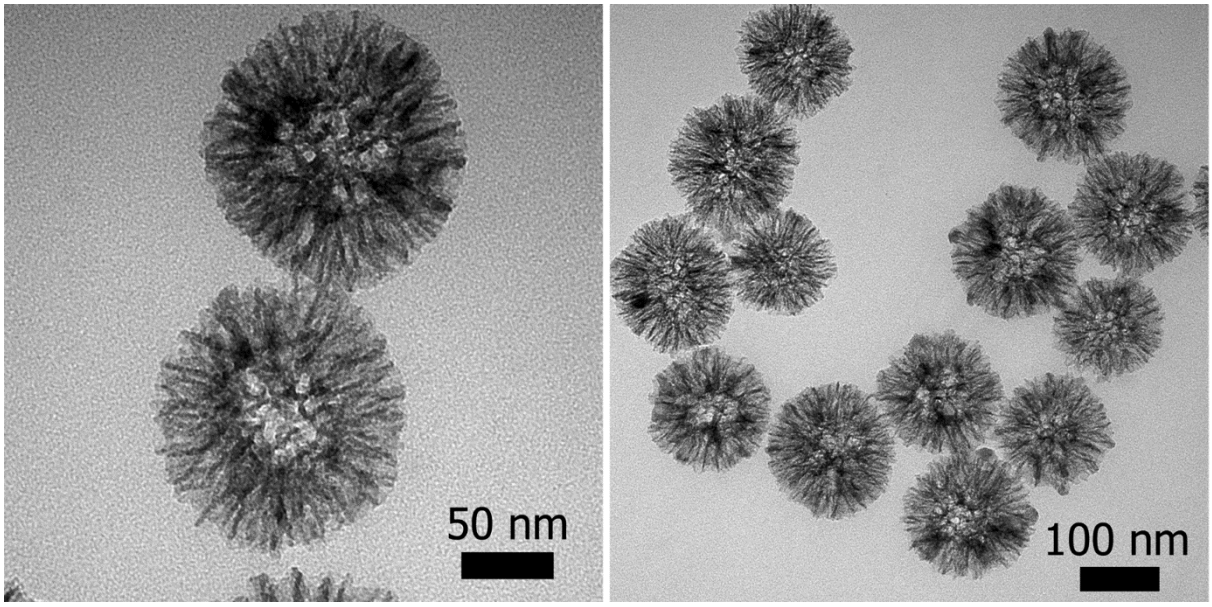

Figure S3. TEM images of hollow silica nanospheres with radial mesopores after etching MNC@LPMS with concentrated chloric acid**.**

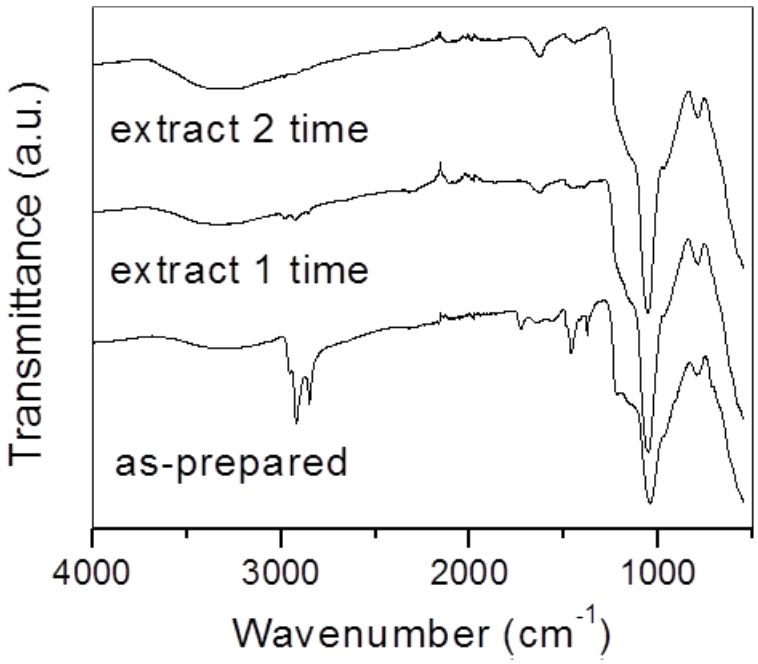

Figure S4. FTIR spectra of as prepared MNC@LPMS and after surfactant extraction with NH_4NO_3 for two times. The disappearance of C-H band in 2800-3000 cm^{-1} range indicates the removal of CTAB.

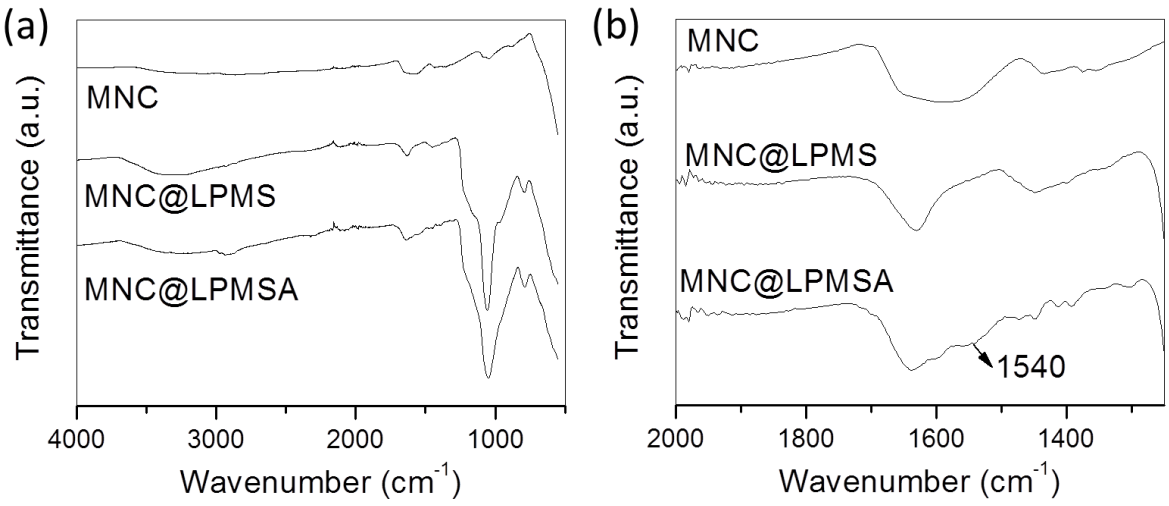

Figure S5. FTIR spectra of MNC, MNC@LPMS and MNC@LPMSA. Spectra (b) is an enlarged part of spectra (a). For MNC@LPMS and MNC@LPMSA, the typical Si-O peaks at 800 cm^{-1} and 1040 cm^{-1} confirms silica coating. The peaks around 1630 cm^{-1} are due to water absorbed. The shoulder around 1540 cm^{-1} for MNC@LPMSA is assigned to amine group. The broad peak around 1600 cm^{-1} for MNC is due to absorbed organic species during the hydrothermal synthesis.

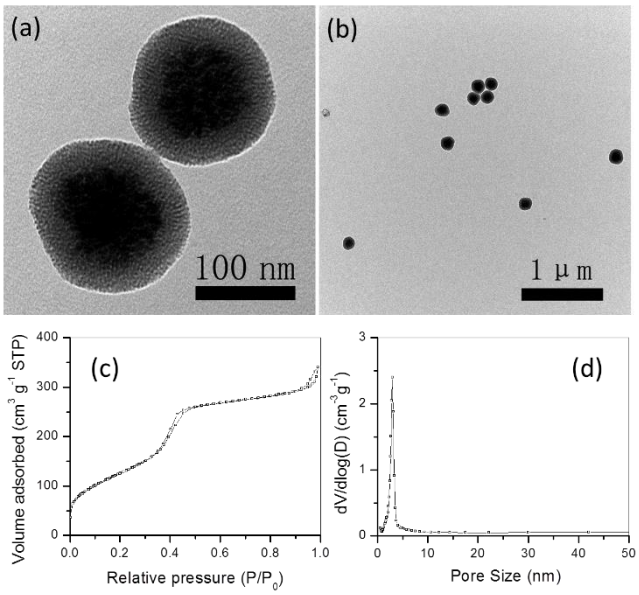

Figure S6. (a, b) TEM images, (c) nitrogen adsorption-desorption isotherms measured at -196 °C and (d) the corresponding pore size distributions of MNC@MSA.

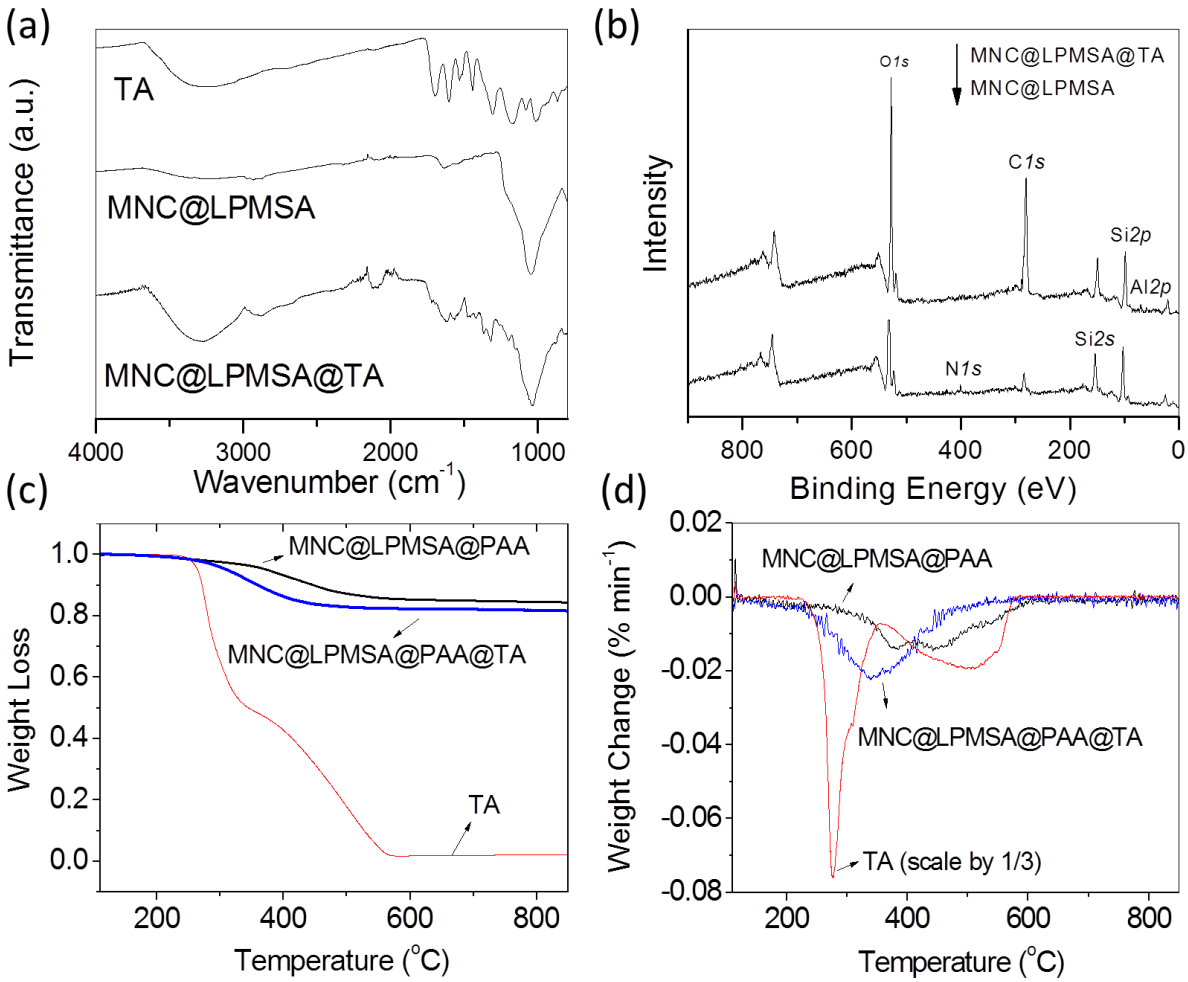

Figure S7. (a) FTIR, (b) XPS spectra, (c) thermogravimetric (TG) and (d) derivative thermogravimetric (DTG) curves of MNC@LPMSA nanoparticles before and after tannic acid coating. For spectra clarity and cost reasons, the spectra (a, b) were recorded without cargo loading and the samples in (c, d) were loaded with 2 wt% PAA as model payload.

In thermal analysis, the uncoated sample show major weight loss above 350 ˚C with two very broad DTG peaks around 380 ˚C and 450 ˚C. After tannic acid coating, the onset temperature for major weight loss is shifted lower to 280 ˚C and a more prominent DTG peak appears at 340 ˚C. The lower onset temperature for coated sample is consistent with the TG/DTG curves of tannic acid, which show a significant weight loss around 280 ˚C.

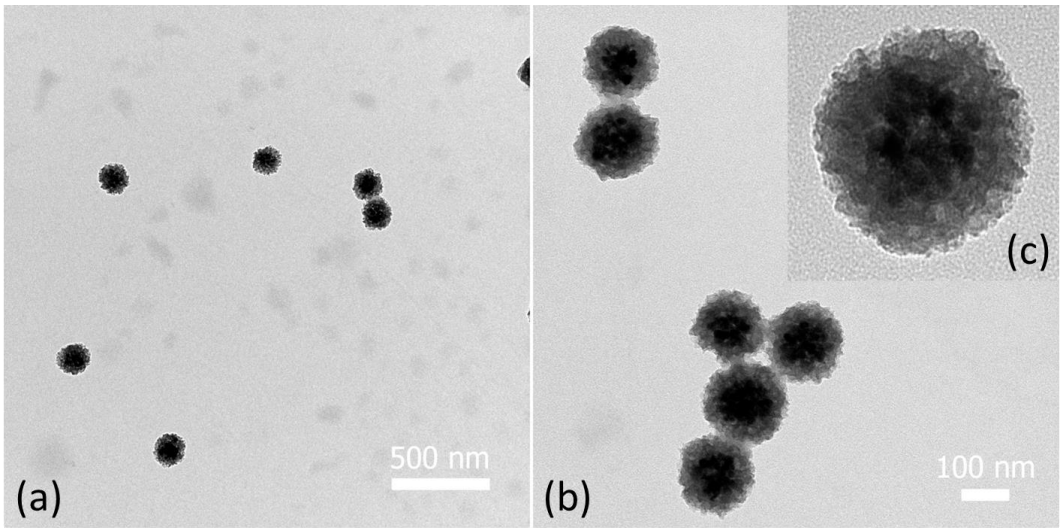

Figure S8. TEM images of MNC@LPMSA@siRNA@TA at different magnifications.

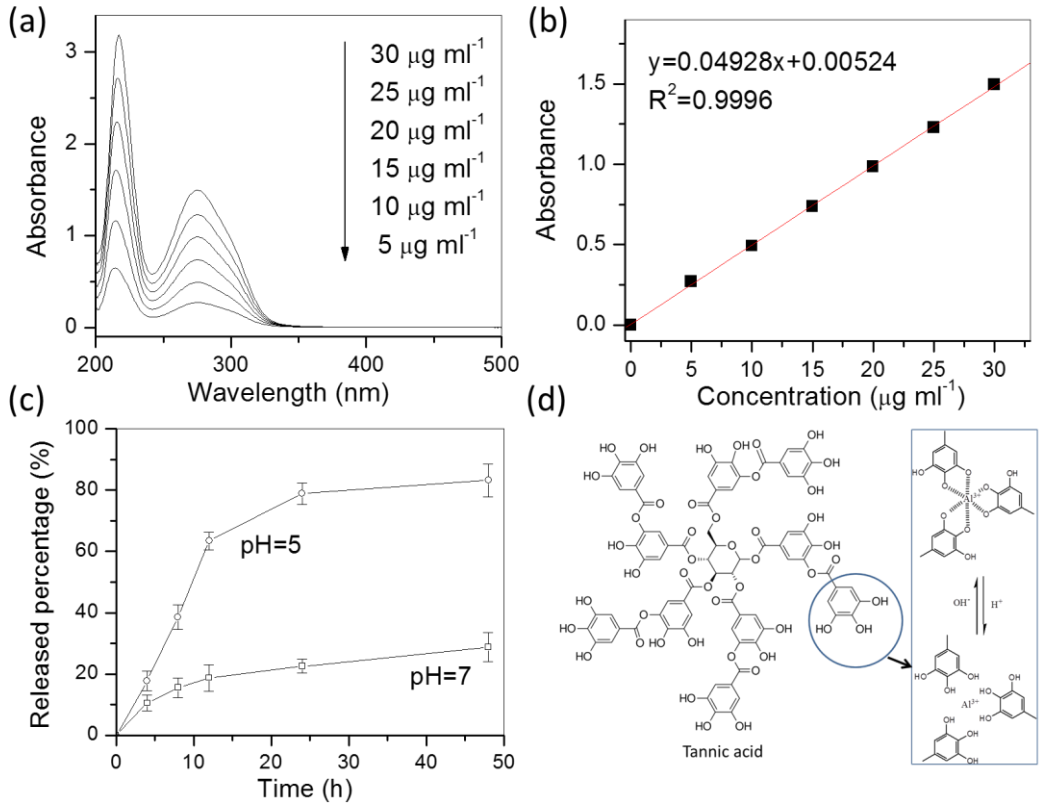

Figure S9. (a) UV-vis spectra and (b) calibration curve of TA. (c) pH-dependent disassembly of TA from nanoparticles. (d) the molecule structure of TA and the scheme of its pH-dependent assembly with Al^{3+} ion.

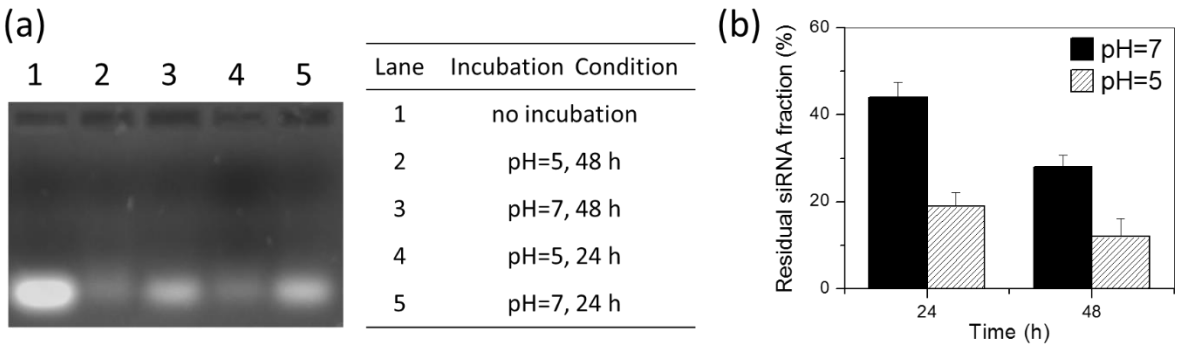

Figure S10. (a) MNC@LPMSA@siRNA@TA was incubated at different pH buffers for 24 h and 48 h. The residual siRNA was analysed by gel electrophoresis. (b) Residual siRNA fraction quantified by GeneTools.

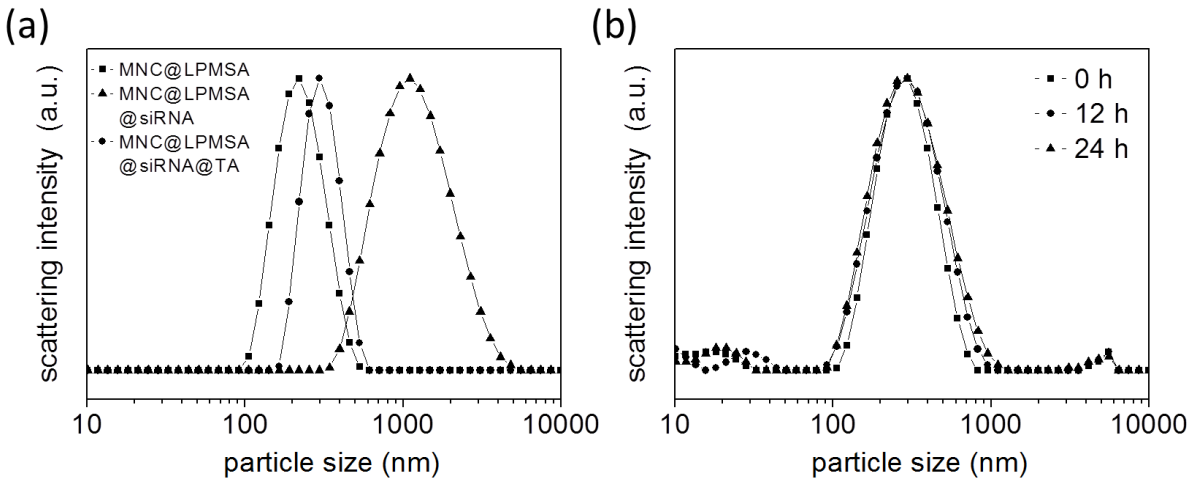

Figure S11. Hydrodynamic particle size distributions of (a) siRNA loaded nanoparticles in water and (b) MNC@LPMSA@siRNA@TA in in cell culture medium (DMEM) containing 10 % serum (FBS) for different periods. The small peaks below 100 nm and above 5000 nm in (b) are due to proteins and impurities in serum, respectively.

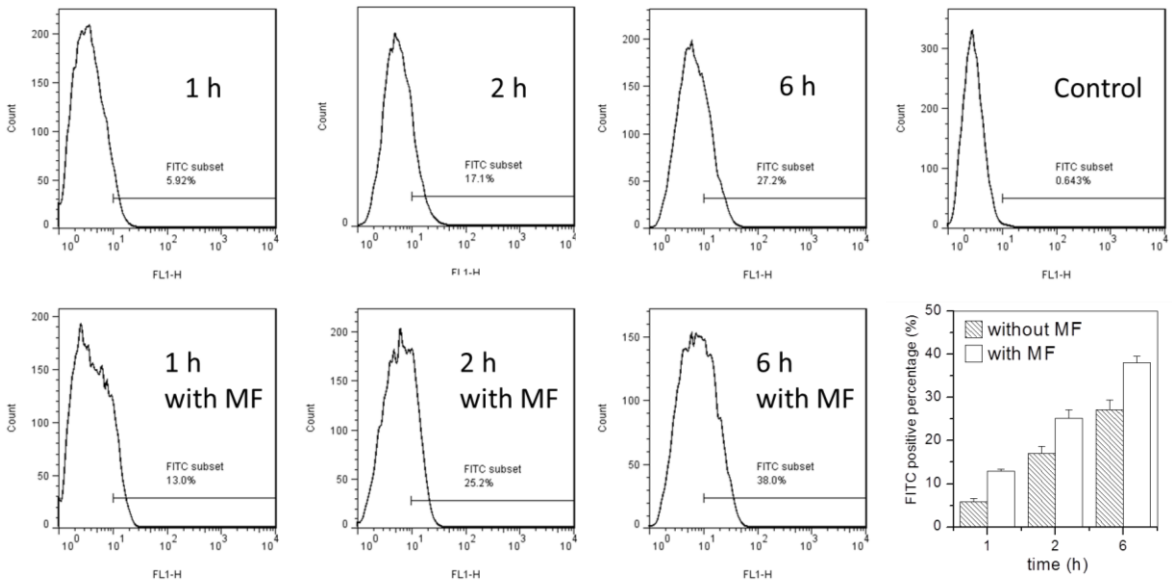

Figure S12. Flow cytometry analysis of KHOS cells incubated in culture medium containing 20 μg ml^{-1} MNC@LPMSA@siRNA@TA after different time periods with or without magnetic field (MF). The cells incubated in blank culture medium were used as the control. The histograms show distribution of events on the FITC (FL1) channel.

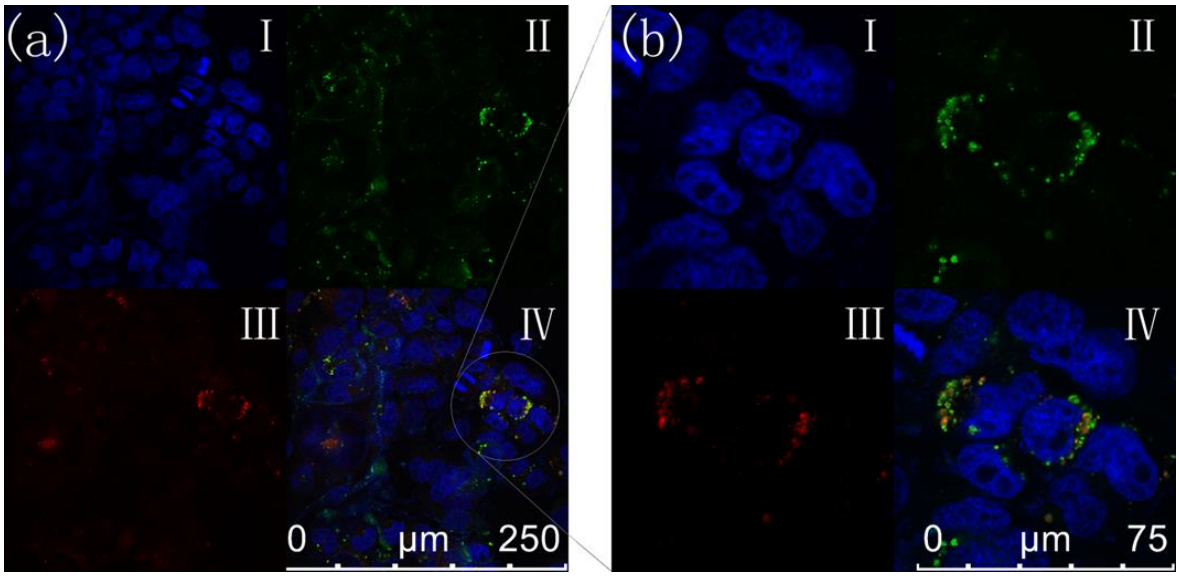

Figure S13. CLSM images of KHOS cells after 12 h of incubation with 20 μg ml^{-1} MNC@LPMSA@siRNA@TA complex under a magnetic field. (Ⅰ) cell nucleus (blue) labelled with Hoechst 33258; (Ⅱ) siRNA (green) was labelled with FITC; (Ⅲ) endosome (red) labelled with LysoTracker Red; (Ⅳ) overlay image of (Ⅰ), (Ⅱ) and (Ⅲ). Panel (b) is the high magnification image of the circle part in panel (a). The location overlap of siRNA signal and endosome signal is indicated by orange colour.

Table S1. Elemental composition (atom %) derived from X-ray photoelectron spectroscopy

Sample	O	C	Si
MNC@LPMSA	57.88	13.35	28.77
MNC@LPMSA@TA	50.78	35.23	13.99

Chapter 6 Mesoporous Organosilica Nano-bowl with High DNA Loading Capacity – a Potential Gene Delivery Carrier

6.1 Introduction, Significance and Commentary

Gene therapy is one of the most promising therapeutic strategies for treating various diseases. The successful gene therapy strongly relies on the development of efficient delivery carrier. Mesoporous silica based nanocomposites, as one type of non-viral delivery system, have unique advantages in terms of biocompatibility and preparation cost. However, the loading capacity of silica based nanocomposites is usually limited by the fact that large gene molecules, especially double-stranded DNA, can hardly enter into the mesopores of traditional mesoporous silica nanoparticles.

In this work, we report for the first time the synthesis of mesoporous organosilica nanoparticles with novel bowl-like morphology. Their application potential as a high-loading gene delivery carrier is demonstrated by DNA transfection in vitro. The highlights and novelty of this work include:

1. Mesoporous organosilica nanoparticles with novel bowl-like morphology.

Bowl-like mesoporous organosilica nanoparticles were prepared for the first time by a simple “hard templating followed by hydrothermal etching” method. These non-aggregated nano-bowls show uniform particle sizes around 180 nm and open cavities of about 140 nm in the centre, which is especially suitable for accommodating very large guest species. The synthesis procedure is characterized step-by-step and a clear synthesis mechanism is given.

2. Nano-bowls with high DNA loading and delivery capacity.

After amine functionalization, these mesoporous organosilica nano-bowls show significantly higher loading capability for plasmid DNA than traditional (hollow, dendric, MCM41 type) silica-based nanoparticles thanks to their large accessible

center cavity. Furthermore, after co-loading with an endosomolytic reagent in the mesopores, enhanced transfection efficiency comparable to polymer standard was achieved for in vitro plasmid DNA transfection.

6.2 Mesoporous Organosilica Nano-bowl with High DNA Loading Capacity – a Potential Gene Delivery Carrier

This section is included in the thesis as it appears as a paper published by L. Xiong and S.-Z. Qiao. A Mesoporous Organosilica Nano-bowl with High DNA Loading Capacity – a Potential Gene Delivery Carrier, *Nanoscale*, **2016**, 8, 17446.

Statement of Authorship

Title of Paper	A mesoporous organosilica nano-bowl with high DNA loading capacity – a potential gene delivery carrier
Publication Status	☑ Published ☐ Accepted for Publication ☐ Submitted for Publication ☐ Unpublished and Unsubmitted w ork w ritten in manuscript style
Publication Details	First published online 20 Sep 2016 DOI: 10.1039/C6NR06777H

Principal Author

Name of Principal Author (Candidate)	Lin Xiong (First Author)		
Contribution to the Paper	Research plan, material synthesis, material characterization, material performance assessment, manuscript drafting		
Overall percentage (%)	80 %		
Certification:	This paper reports on original research I conducted during the period of my Higher Degree by Research candidature and is not subject to any obligations or contractual agreements with a third party that would constrain its inclusion in this thesis. I am the primary author of this paper.		
Signature		Date	2016/11/22

Co-Author Contributions

By signing the Statement of Authorship, each author certifies that:

i. the candidate's stated contribution to the publication is accurate (as detailed above);

ii. permission is granted for the candidate in include the publication in the thesis; and

iii. the sum of all co-author contributions is equal to 100% less the candidate's stated contribution.

Name of Co-Author	Prof Shi Zhang Qiao (Corresponding Author)		
Contribution to the Paper	Design of the project, organization of the research and supervision, manuscript revision		
Signature		Date	24/11/2016

Please cut and paste additional co-author panels here as required.

Nanoscale

COMMUNICATION

View Article Online
View Journal | View Issue

Cite this: *Nanoscale*, 2016, **8**, 17446

Received 26th August 2016,
Accepted 19th September 2016

DOI: 10.1039/c6nr06777h

www.rsc.org/nanoscale

A mesoporous organosilica nano-bowl with high DNA loading capacity – a potential gene delivery carrier†

Lin Xiong and Shi-Zhang Qiao*

Mesoporous organosilica nanoparticles with a novel bowl-like morphology were synthesized. These nano-bowls possess uniform particle sizes around 180 nm and open cavities around 140 nm, which lead to higher loading capability for plasmid DNA than traditional silica-based nanoparticles. *In vitro* DNA transfection using these nano-bowls is demonstrated.

Introduction

Gene therapy is one of the most promising therapeutic strategies for treating various diseases (such as cancer, heart disease and neurologic disorders) by delivering foreign nucleic acids (DNA, RNA, and oligonucleotides) into living cells.[1,2] However, negatively charged naked nucleic acids cannot cross cellular membranes with the same charge type by passive diffusion and are rapidly degraded by serum nuclease. Therefore, successful gene therapy strongly relies on the development of efficient delivery carriers. The current delivery systems are divided into two major categories: viral and non-viral systems. Although viral carriers generally exhibit higher efficiency than non-viral ones, they also increase potential risks such as excessive immune response and mutagenesis. On the other hand, non-viral systems including lipids, polymers, peptides and inorganic nanoparticles have drawn great research attention in recent years due to the ease of preparation and reduced safety concern.[3,4] Among various non-viral carriers, silica based composite nanoparticles have unique advantages such as well-defined morphology, size, versatile surface functionalization and good biocompatibility.[5–7] In previous research, the efforts on developing silica-based gene delivery carriers focused on two general aspects: surface chemistry and particle structure. For surface chemistry, because the primary silica surface is negatively charged under biologically relevant conditions, the loading of nucleic acids is usually carried out on the silica surface modified by various species such as metal ions,[8] amine silane,[4] cationic polymers,[9,10] and peptides.[11] For particle structure, the silica based gene carriers have evolved from solid spheres to mesoporous nanoparticles, and hierarchical structures like hollow or dendritic particles.[9,12–17] It has been proven that porous silica with large mesopore sizes (>10 nm) are more favourable for loading nucleic acids than those with small pores (<5 nm).[8,13–15,17] Apart from the carrier, it is noteworthy that the loading behaviour is also dependent on the specific type of nucleic acids due to the significant differences between various genetic materials.[18,19] For small interfering RNA (siRNA), the molecular weight is about 13 kDa and the size is about 6 nm in length × 3 nm in diameter. Thus, siRNA can reasonably be loaded into the pore channels of large pore mesoporous silica materials.[20] However, for double-stranded DNA, the molecular weight can be several hundred times greater than that of siRNA and the size can be of hundred nanometers in the extended conformation.[13,18,21] Furthermore, considering that the optimal particle size for efficient cellular uptake is usually below 200 nm, the DNA molecules are generally too large to be fully incorporated into the mesoporous particles.[22] Thus, a specific nanostructure different from the traditional mesoporous silica nanoparticles needs to be developed for DNA delivery carriers.

In this work, mesoporous organosilica nanoparticles with a novel bowl-like morphology and sub-200 nm size were synthesized by a simple method using Stöber silica as the template followed by hydrothermal etching. These nano-bowls show high loading capacity for plasmid DNA and great potential for DNA delivery applications.

School of Chemical Engineering, The University of Adelaide, SA 5005, Australia. E-mail: s.qiao@adelaide.edu.au; Fax: +61 8 8303 4373; Tel: +61 8 8313 6443

†Electronic supplementary information (ESI) available: Experimental section and additional TEM and SEM images, confocal and fluorescence images, and gel-retardation images. See DOI: 10.1039/c6nr06777h

Results and discussion

Mesoporous organosilica nano-bowls were synthesized in three steps (Fig. 1): (1) silica nanospheres (SS) were first prepared by

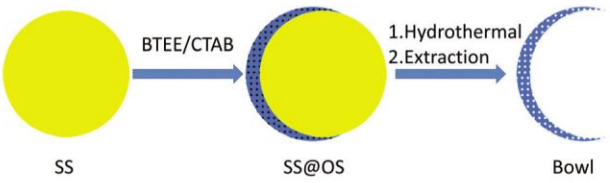

Fig. 1 Synthesis scheme of mesoporous organosilica nano-bowls.

the Stöber method. (2) After hydrolysis and condensation of bis(triethoxysilyl)ethane (BTEE) in the presence of cetyltrimethylammonium bromide (CTAB), an asymmetric organosilica coating was formed on the SS particles to produce core–shell particles (SS@OS). (3) After hydrothermal treatment of SS@OS, mesoporous organosilica nano-bowls (Bowl) were obtained.

From the scanning electron microscopy (SEM) and transmission electron microscopy (TEM) images (Fig. S1, ESI†), it can be seen that the SS sample is composed of uniform silica spheres with particle sizes around 160 nm. After coating with BTEE organosilica, the SS@OS sample shows increased particle size around 210 nm. The size increase can also be observed from the hydrodynamic diameters (Fig. S2 and Table S1, ESI†). More importantly, from the TEM contrast image of SS@OS, the SS core is not located at the centre but at one side of the SS@OS particle. This is due to the anisotropic growth of the BTEE/CTAB mesostructure on the silica surface.[23,24] From the SEM and TEM images of Bowl (Fig. 2a–c), the nanoparticles show a morphology characterized by a thin hemisphere shell. The formation of nano-bowls is due to the etching of the SS core under the hydrothermal conditions.[25,26] The particle sizes or "bowl diameters" are about 180 nm and smaller than that of SS@OS. The reason is that the further condensation of the organosilica framework during the hydrothermal treatment leads to the shrinkage of the particle size. The shell or "bowl wall" is only about 20 nm in thickness and thus results in an open cavity with a diameter of 140 nm in the centre, which is especially suitable for accommodating very large guest species. Nitrogen sorption results (Fig. 2d and Table S2, ESI†) show that the Bowl shell is mesoporous with a pore size of 2.5 nm. The bowl-like morphology is retained after repeated sonication and centrifugation cycles, suggesting that these nanoparticles possess enough mechanic stability for delivery application even with a thin shell and a large cavity.

Regarding the synthesis of nano-bowls, three factors should be strictly controlled. The first is the quantity ratio between BTEE and SS. Keeping other parameters fixed, irregular and hollow particles were produced with 10 μL or 50 μL BTEE, respectively (Fig. S3a and b, ESI†). In other words, a suitable coating thickness of BTEE is essential for obtaining the nano-bowls after hydrothermal etching. The second is the addition rate of BTEE during the coating step. It is found that a very slow BTEE addition rate does not lead to an asymmetric core–shell but Janus type particles (Fig. S3c, ESI†), in which the BTEE/CTAB mesostructure mainly grows on one side of the SS particles. The third is the etching method for removing the SS core. We have also tried other etching reagents like Na_2CO_3. However, only donut-type particles were obtained (Fig. S3d, ESI†). Thus, hydrothermal treatment is essential to etch away the SS core while maintaining the bowl-like morphology. These nano-bowls were subsequently post-grafted with (3-aminopropyl)triethoxysilane (APTES) to construct a gene carrier. The amine functionalized sample (A-Bowl) retains the bowl-like morphology (Fig. S4, ESI†) but shows a decreased specific surface area and a pore size of 2.1 nm (Fig. 2d and Table S2†). The A-Bowl particles show a positive zeta potential of 15 mV in deionized water, which is in contrast to the Bowl sample with a −20 mV zeta potential.

The incorporation of the organosilica framework and surface functionalization on the nano-bowls are further verified by Fourier transform infrared (FTIR) spectra, Raman spectra and thermogravimetric analysis. As shown in the FTIR spectra (Fig. 3a and S5a, ESI†), the as-prepared core–shell SS@OS particles show prominent asymmetric and symmetric Si–O–Si stretching vibrations around 1020 and 770 cm^{-1}, respectively. The Si–OH stretching band is observed at 915 cm^{-1}.[27] The peaks at 1410 and 1270 cm^{-1} are attributed to the C–H deformation of the CH_2 group in organosilica.[28–31] The peak at 694 cm^{-1} is due to the Si–C bond.[31] CTAB in the as-prepared SS@OS is evidenced by the C–H deformation peak around 1470 cm^{-1} and the surfactant also contributes to the C–H stretching modes at 2932 and 2852 cm^{-1}.[32] The adsorption band around 1640 cm^{-1} is assigned to the absorbed water molecules.[33] After the hydrothermal treatment of SS@OS and subsequent surfactant extraction, all the peaks assigned to organosilane are well preserved in the obtained Bowl sample. This is due to the hydrothermal stability of the organosilica layer which contains bridged ethane groups in the framework.[25,28,34] The band around 1470 cm^{-1} assigned to CTAB dis-

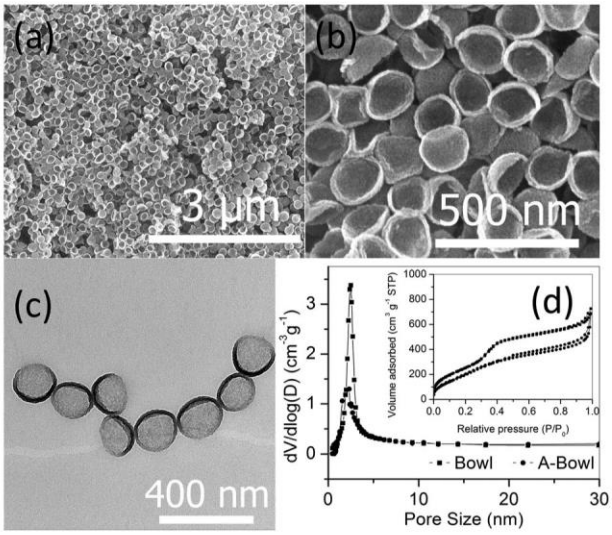

Fig. 2 (a, b) SEM and (c) TEM images of mesoporous organosilica nano-bowls. (d) Nitrogen sorption isotherms (inserted) and the corresponding pore size distributions of nano-bowls.

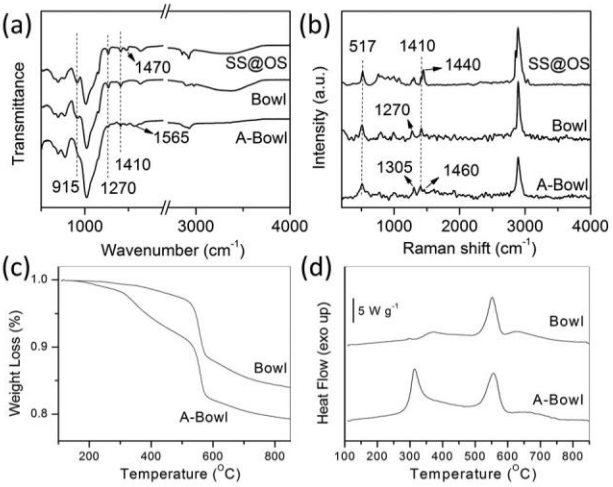

Fig. 3 (a) FTIR spectra, (b) Raman spectra, (c) thermogravimetric and (d) differential scanning calorimetry curves of mesoporous organosilica nano-bowls.

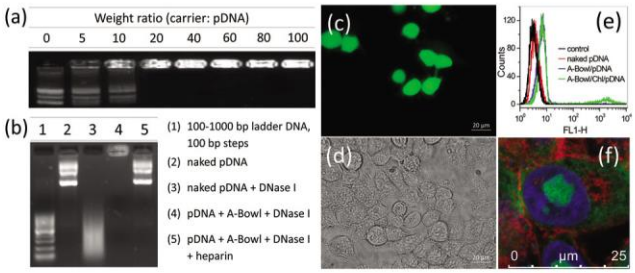

Fig. 4 (a) Gel retardation assay of A-Bowl/pDNA complex at different carrier/pDNA weight ratios. (b) Protection of pDNA against DNase I by A-Bowl. (c) Fluorescent and (d) bright field images of HEK293 cells transfected with A-Bowl containing 4% chloroquine. (e) Flow cytometry analysis of GFP expression levels with different transfection reagents. (f) Confocal image of YOYO-1-labeled pDNA (green) delivered by A-Bowl in HEK293 cells. The cell nucleus (blue) and plasma membrane (red) were labelled by Hoechst and Alexa Fluor 594, respectively.

appears in the Bowl sample, suggesting the complete removal of the surfactant. For the functionalized A-Bowl sample, the aminopropyl group leads to the N–H bending peak at 1565 cm^{-1} and the C–H band around 1480 cm^{-1}.[35] The results from Raman spectra are consistent with the FTIR spectra (Fig. 3b and S5b, ESI†). All three samples show Raman peaks at 517 cm^{-1} and 1410 cm^{-1}, which are attributed to the Si–C and C–H bonds in organosilica, respectively.[32] In the spectrum of SS@OS, the presence of CTAB is indicated by the C–H bending and stretching mode at 1440 cm^{-1} and 2850 cm^{-1}. Both peaks are not observed for the Bowl sample. For the A-Bowl sample, the CH_2–Si mode at 1305 cm^{-1} and the C–H mode at 1460 cm^{-1} confirm the grafting of the aminopropyl group.[36] In the thermogravimetric curve (Fig. 3c), the Bowl sample shows a steep weight loss of about 10% between 500 and 600 °C. This is assigned to the removal of the bridged ethane group.[30] This weight loss is also accompanied by an exothermic peak at 552 °C in the heat flow curve (Fig. 3d). For the A-Bowl sample, the presence of the aminopropyl group is manifested by the increased weight loss from 110 °C to 500 °C and the additional exothermic peak at 314 °C in the heat flow curve.

The gene binding capability of A-Bowl was evaluated by gel electrophoresis. As shown in Fig. 4a, the mobility of pEGFP-N1 plasmid DNA (pDNA, 4.7 kb) is gradually reduced with increasing weight ratios of carrier/pDNA. When the weight ratio of carrier/pDNA is above 20, no migration pattern is observed and the pDNA is fully retained in the sample. Although it is common to modify silica nanoparticles with cationic polymers (such as polyethyleneimine) to achieve even higher gene binding capacity,[10,15,37] only amino silane functionalization is carried out in this study for comparison between different particle structures.[13,14] For this purpose, other types of silica nanoparticles with MCM41-type, dendritic and hollow morphologies were prepared and functionalized by the same procedure as A-Bowl (Fig. S6 and S7, ESI†). These nanostructures are all in the size range of 100–200 nm and extensively studied as drug/gene delivery carriers. As shown by gel retardation assays (Fig. S8, ESI†), the migration of pDNA can only be stopped above the weight ratios of 40, 60, 200 and 400 for A-Hollow, A-Dendritic, A-MCM41 and A-SS, respectively (see the ESI† for sample denotations). This suggests that the loading capacity of different nanoparticles follows the order: A-Bowl > A-Hollow > A-Dendritic > A-MCM41 > A-SS. Although the loading capacity is known to be affected by several correlated factors including particle size,[21,38] surface chemistry[39] and pore structure,[25] in this case, the unique morphology of A-Bowl plays a critical role in maintaining its highest DNA loading capacity considering the similarity of these particles in size and surface chemistry (Table S2, ESI†). As illustrated in the proposed scheme (Fig. S9, ESI†), because the pDNA molecules are too large to enter into 2 nm mesopores,[13] only the external surfaces of A-Hollow, A-Dendritic, A-MCM41 and A-SS can contribute to the adsorption capacity. Thus, the capacity sequence of A-Hollow > A-MCM41 > A-SS is explained by the decreasing inner porosity of this sequence. For the A-Dendritic with a radial pore structure, although the large pore-openings near the particle surface allow for pDNA entering, the pDNA molecules are more likely to be partially inside the pores due to the large size of pDNA. As a result, A-Dendritic shows a higher capacity than A-MCM41, but still lower than A-Hollow. On the other hand, because pDNA can hardly penetrate the shell of A-Hollow, the inner cavity of A-Hollow cannot contribute to pDNA loading. In contrast, the bowl particle can be considered as the product of breaking the hollow one into two halves. Thus, the 140 nm cavity in the center of A-Bowl becomes accessible to pDNA and explains the higher capacity of A-Bowl than A-Hollow. The effect of the bowl cavity on pDNA loading is supported by TEM images of A-Bowl before and after pDNA loading (Fig. S10, ESI†). From the TEM image, there is indeed polymeric species located in the bowl cavity after pDNA loading. The gene protection capability of A-Bowl was examined against an endonuclease, deoxyribo-

nuclease I (DNase I). While the naked pDNA is cleaved by DNase I into DNA fragments less than 1 kb, the pDNA loaded by A-Bowl is well preserved and can be released intactly after replacement with heparin (Fig. 4b). This protection of pDNA by A-Bowl against enzymatic digestion is consistent with previous reports on silica nanoparticles and attributed to the conformation change of absorbed pDNA molecules.[4,12]

The cellular biocompatibility and uptake was evaluated by 3-(4,5-dimethylthiazol-2-yl)-2,5-diphenyltetrazolium bromide (MTT) assay and confocal microscopy, respectively. The A-Bowl shows very good biocompatibility up to 200 μg ml^{-1} and can be efficiently taken up by human embryonic kidney 293 (HEK293) cells (Fig. S11, ESI†). Therefore, the A-Bowl is further tested for pDNA transfection on HEK293 cells *in vitro*. While the naked pDNA does not produce any fluorescence signal, the pDNA delivered with A-Bowl does induce green fluorescent protein (GFP) expression in HEK293 cells, although the transfection efficiency is low at about 5% (Fig. S12, ESI†). It has been well established that the three main cellular barriers for DNA delivery are cellular uptake, endosome escape and nuclear entry.[1] As the cellular uptake of A-Bowl is confirmed, we tried to improve the transfection efficiency by promoting the endosome escape of A-Bowl. Thus, the A-Bowl preloaded with 4 wt% chloroquine (Chl) was used as the pDNA carrier. Chl is an endosomolytic reagent and is often used to enhance gene transfection of non-viral vectors by facilitating endosome escape.[40–42] It is noteworthy that the preloading of 4 wt% Chl does not significantly affect the pDNA binding capability and biocompatibility of A-Bowl from our experiments. A possible explanation is that the small molecules of Chl are mainly absorbed by the 2 nm mesopores in the bowl shell, which contribute little to the pDNA loading. As shown in microscopy images (Fig. 4c, d and S12, ESI†) and flow cytometry analysis (Fig. 4e), the co-delivery of pDNA and Chl by A-Bowl leads to a significantly improved transfection efficiency of 16%. The successful delivery of labelled pDNA into the nucleus of HEK293 cell is also directly observed in the confocal image (Fig. 4f). Under the same conditions, the polyethyleneimine (PEI, 25 kDa) polymer, which is regarded as the gold standard for non-viral gene carriers,[43] results in a transfection efficiency of 21%. Although these amine functionalized organosilica nano-bowls show slightly lower transfection efficiency than the polymer carrier, they possess unique advantages in terms of biocompatibility and preparation cost. In addition, there is still much room for further improvement based on these nano-bowls, such as conjugation with other DNA binding moieties and/or cell-penetrating peptides. Therefore, these novel nano-bowls have demonstrated great potential for the delivery of large gene molecules.

Conclusions

In conclusion, novel bowl-like mesoporous organosilica nanoparticles were synthesized by a simple "hard templating followed by hydrothermal etching" method. These nano-bowls show uniform particle sizes around 180 nm and open cavities of about 140 nm in the centre. After amine functionalization, these nano-bowls show a much higher loading capacity for plasmid DNA than common MCM41-type, dendritic and hollow nanoparticles. By using these nano-bowls as plasmid DNA carriers, HEK293 cells were successfully transfected *in vitro*. These results suggest that these nano-bowls have great application potential for the delivery of large gene molecules.

Acknowledgements

We would like to acknowledge the financial support from the Australian Research Council (ARC) through the Discovery Project program (DP130104459, DP140104062 and DP160104866).

References

1 M. A. Mintzer and E. E. Simanek, *Chem. Rev.*, 2009, **109**, 259.
2 V. Sokolova and M. Epple, *Angew. Chem., Int. Ed.*, 2008, **47**, 1382.
3 C. Kneuer, M. Sameti, U. Bakowsky, T. Schiestel, H. Schirra, H. Schmidt and C.-M. Lehr, *Bioconjugate Chem.*, 2000, **11**, 926.
4 D. J. Bharali, I. Klejbor, E. K. Stachowiak, P. Dutta, I. Roy, N. Kaur, E. J. Bergey, P. N. Prasad and M. K. Stachowiak, *Proc. Natl. Acad. Sci. U. S. A.*, 2005, **102**, 11539.
5 D. Luo and W. M. Saltzman, *Gene Ther.*, 2005, **13**, 585.
6 I. Slowing, J. Viveroescoto, C. Wu and V. Lin, *Adv. Drug Delivery Rev.*, 2008, **60**, 1278.
7 C. Hom, J. Lu and F. Tamanoi, *J. Mater. Chem.*, 2009, **19**, 6308.
8 S. M. Solberg and C. C. Landry, *J. Phys. Chem. B*, 2006, **110**, 15261.
9 D. R. Radu, C.-Y. Lai, K. Jeftinija, E. W. Rowe, S. Jeftinija and V. S. Y. Lin, *J. Am. Chem. Soc.*, 2004, **126**, 13216.
10 T. Xia, M. Kovochich, M. Liong, H. Meng, S. Kabehie, S. George, J. I. Zink and A. E. Nel, *ACS Nano*, 2009, **3**, 3273.
11 D. Brevet, O. Hocine, A. Delalande, L. Raehm, C. Charnay, P. Midoux, J.-O. Durand and C. Pichon, *Int. J. Pharm.*, 2014, **471**, 197.
12 X.-x. He, K. Wang, W. Tan, B. Liu, X. Lin, C. He, D. Li, S. Huang and J. Li, *J. Am. Chem. Soc.*, 2003, **125**, 7168.
13 F. Gao, P. Botella, A. Corma, J. Blesa and L. Dong, *J. Phys. Chem. B*, 2009, **113**, 1796.
14 M.-H. Kim, H.-K. Na, Y.-K. Kim, S.-R. Ryoo, H. S. Cho, K. E. Lee, H. Jeon, R. Ryoo and D.-H. Min, *ACS Nano*, 2011, **5**, 3568.
15 X. Du, B. Shi, J. Liang, J. Bi, S. Dai and S. Z. Qiao, *Adv. Mater.*, 2013, **25**, 5981.

16 Y. Fatieiev, J. G. Croissant, S. Alsaiari, B. A. Moosa, D. H. Anjum and N. M. Khashab, *ACS Appl. Mater. Interfaces*, 2015, **7**, 24993.
17 K. Zhu, M. Wu, H. Lai, C. Guo, J. Li, Y. Wang, Y. Chen, C. Wang and J. L. Shi, *Biomaterials*, 2016, **74**, 188.
18 A. Schroeder, C. G. Levins, C. Cortez, R. Langer and D. G. Anderson, *J. Intern. Med.*, 2010, **267**, 9.
19 Y. Niu, A. Popat, M. Yu, S. Karmakar, W. Gu and C. Z. Yu, *Ther. Delivery*, 2012, **3**, 1217.
20 J. L. Steinbacher and C. C. Landry, *Langmuir*, 2014, **30**, 4396.
21 M. Yu, Y. Niu, J. Zhang, H. Zhang, Y. Yang, E. Taran, S. Jambhrunkar, W. Gu, P. Thorn and C. Z. Yu, *Nano Res.*, 2015, **9**, 291.
22 J. Rejman, V. Oberle, I. S. Zuhorn and D. Hoekstra, *Biochem. J.*, 2004, **377**, 159.
23 X. Li, L. Zhou, Y. Wei, A. M. El-Toni, F. Zhang and D. Y. Zhao, *J. Am. Chem. Soc.*, 2014, **136**, 15086.
24 X. Li, L. Zhou, Y. Wei, A. M. El-Toni, F. Zhang and D. Y. Zhao, *J. Am. Chem. Soc.*, 2015, **137**, 5903.
25 M. Wu, Y. Chen, L. Zhang, X. Li, X. Cai, Y. Du, L. Zhang and J. L. Shi, *J. Mater. Chem. B*, 2015, **3**, 766.
26 Q. Yu, P. Wang, S. Hu, J. Hui, J. Zhuang and X. Wang, *Langmuir*, 2011, **27**, 7185.
27 M. A. Wahab, I. Kim and C.-S. Ha, *J. Solid State Chem.*, 2004, **177**, 3439.
28 X. Yuan, H. I. Lee, J. W. Kim, J. E. Yie and J. M. Kim, *Chem. Lett.*, 2003, **32**, 650.
29 Y. Yang, J. Liu, X. Li, X. Liu and Q. H. Yang, *Chem. Mater.*, 2011, **23**, 3676.
30 H. Zou, R. Wang, X. Li, X. Wang, S. Zeng, S. Ding, L. Li, Z. Zhang and S. L. Qiu, *J. Mater. Chem. A*, 2014, **2**, 12403.
31 M. A. Wahab, I. Kim and C.-S. Ha, *Microporous Mesoporous Mater.*, 2004, **69**, 19.
32 V. Rebbin, M. Jakubowski, S. Pötz and M. Fröba, *Microporous Mesoporous Mater.*, 2004, **72**, 99.
33 L. Zhang, J. Liu, J. Yang, Q. Yang and C. Li, *Microporous Mesoporous Mater.*, 2008, **109**, 172.
34 J. Liu, Q. H. Yang, M. P. Kapoor, N. Setoyama, S. Inagaki, J. Yang and L. Zhang, *J. Phys. Chem. B*, 2005, **109**, 12250.
35 J. Kim, J. Cho, P. M. Seidler, N. E. Kurland and V. K. Yadavalli, *Langmuir*, 2010, **26**, 2599.
36 K. Moller, J. Kobler and T. Bein, *J. Mater. Chem.*, 2007, **17**, 624.
37 M. Wu, Q. Meng, Y. Chen, L. Zhang, M. Li, X. Cai, Y. Li, P. Yu, L. Zhang and J. L. Shi, *Adv. Mater.*, 2016, **28**, 1963.
38 J. Liu, A. Stace-Naughton and C. J. Brinker, *Chem. Commun.*, 2009, 5100.
39 Z. Csőgör, M. Nacken, M. Sameti, C. M. Lehr and H. Schmidt, *Mater. Sci. Eng., C*, 2003, **23**, 93.
40 S. R. Bhattarai, E. Muthuswamy, A. Wani, M. Brichacek, A. L. Castañeda, S. L. Brock and D. Oupicky, *Pharm. Res.*, 2010, **27**, 2556.
41 M. Wang, X. Li, Y. Ma and H. C. Gu, *Int. J. Pharm.*, 2013, **448**, 51.
42 S. B. Hartono, N. T. Phuoc, M. H. Yu, Z. F. Jia, M. J. Monteiro, S. Z. Qiao and C. Z. Yu, *J. Mater. Chem. B*, 2014, **2**, 718.
43 D. Schaffert and E. Wagner, *Gene Ther.*, 2008, **15**, 1131.

6.3 Supplementary Information

This section is included in the thesis as supplementary information to section 6.2. It includes additional information which is not put in the main text of the published paper, but as electronic supplementary information freely accessible online.

A Mesoporous Organosilica Nano-bowl with High DNA Loading Capacity - a Potential Gene Delivery Carrier

Lin Xiong and Shi-Zhang Qiao*

School of Chemical Engineering, The University of Adelaide, SA 5005, Australia.

* Address correspondence to: s.qiao@adelaide.edu.au

Experimental Section

Materials

Tetraethyl orthosilicate (TEOS), (3-Aminopropyl)-triethoxysilane (APTES), 1, 2-Bis(triethoxysilyl)ethane (BTEE), cetyltrimethylammonium bromide (CTAB), ammonia solution (25 wt %), cetyltrimethylammonium tosylate (CTAT), triethanolamine (TEA), ammonium nitrate, toluene, ethanol, fluorescein isothiocyanate (FITC), 3-[4,5-dimethylthialzol-2-yl]-2,5-diphenyltetrazolium bromide (MTT), sodium hydroxide, ethylenediaminetetraacetic acid (EDTA),

Tris(hydroxymethyl)aminomethane (Tris), methylsulfoxide (DMSO), polyethylenimine (PEI, 25 kDa) and deoxyribonuclease I (DNase I) were purchased from Sigma Aldrich. Dulbecco's Modified Eagle's Medium (DMEM), fetal bovine serum (FBS), and phosphate buffered saline (PBS), trypsin, Tris Acetate-EDTA (TAE) buffers, and agarose were purchased from Gibco-BRL (Grand Island, U.S.A.). Gel Red (10000x in water) was purchased from Biotium, Australia. Gel loading dye blue (6x) was purchased from Biolab, Australia. Water used in all experiments was purified using a Milli-Q Plus 185 water purification system (Millipore, Bedford, MA) with a resistivity higher than 18 MΩ cm.

Synthesis of silica nanospheres

Silica nanospheres (denoted as SS) with sizes around 160 nm were prepared by the Stöber method. Briefly, ethanol (20 mL), H_2O (1 mL), and ammonia solution (25 wt %, 1 mL) were combined at 40 °C under stirring. Then, TEOS (1 mL) was added and stirred for another 8 h at 40 °C.

Synthesis of mesoporous organosilica nano-bowls

The SS was then coated with an organosilica layer to obtain core-shell particle (denoted as SS@OS). The above Stöber reaction mixture (2 mL) was added to a solution containing water (75 mL), ethanol (5 mL), CTAB (150 mg) and ammonia (25 wt %, 1 mL). After stirring at room temperature for 0.5 h, a total of BTEE (30 µL) dissolved in ethanol (3 ml) was added in 3 times at 10 min intervals. After reaction for another 24 h, the SS@OS product was collected by centrifugation and washed with ethanol and water for several times.

Mesoporous organosilica nano-bowl (denoted as Bowl) was obtained after removing the core part of the SS@OS by a hydrothermal-etching method.[1] The washed SS@OS was redispersed in a solution containing water (20 mL), Na_2SO_4 (80 mg) by sonication. Then, the dispersion was adjust to pH 3 with H_2SO_4 (0.1 M) and stirred at room temperature for 24 h. Afterwards, the mixture was transferred into a sealed autoclave and heated at 180 °C for 10 h. The etched particles were centrifuged and washed with water for several times.

Synthesis of hollow mesoporous organosilica nanoparticles

Hollow mesoporous organosilica nanoparticles (denoted as Hollow) were prepared according to the literature with slight modification.[2] The above Stöber silica solution was further mixed with H_2O (20 mL), CTAB (150 mg) and ammonia solution (0.5 mL).Then, BTEE (0.5 mL) was added and the mixture was allowed to react for 6 h at 30 °C. The particles were collected by centrifugation and redispersed into Na_2CO_3 aqueous solution (0.6 M). After stirring at 80 °C for 1 h, the hollow particles were centrifuged and washed with water for several times.

Synthesis of MCM-41 type nanoparticles

MCM-41 type mesoporous silica nanoparticles (denoted as MCM41) were prepared according to the literature.[3] Sodium hydroxide aqueous solution (2 M, 0.7 mL) was added to water (96 mL) containing CTAB (0.2 g) at 80 °C. Then, TEOS (1 mL) was added under vigorous stirring. The mixture was allowed to react for 2 h at 80 °C and then centrifuged to get the precipitate. The white precipitate was washed with water for several times.

Synthesis of dendric mesoporous silica nanoparticles

Dendric type mesoporous silica nanoparticles (denoted as Dendric) were prepared according to the literature.[4] CTAT (0.48 g) and TEA (87 mg) was dissolved in water (25 mL) at 80 °C. Then, TEOS (4.9 mL) was added under vigorous stirring. The mixture was allowed to react for 2 h at 80 °C and then centrifuged to get the precipitate. The white precipitate was washed with water for several times.

Surfactant removal, amine functionalization and fluorescence labeling

The surfactant in the above as-prepared product was removed by extraction for two cycles. In each cycle, the as-prepared powder (50 mg) was refluxed in ethanol solution (10 mL) containing ammonium nitrate (2 wt %) for 6 h. For amine functionalization, the extracted powders were refluxed in toluene (20 mL) containing APTES (50 μL) at 90 °C for 12 h followed by washing sequentially with toluene and ethanol. The amine functionalized products are denoted with a prefix A for each type of particles. For example, A-Bowl stands for amine functionalized organosilica

nano-bowls. For fluorescence labelling, A-Bowl (10 mg) were stirred in ethanol solution of FITC (5 mL, 10 μg mL^{-1}) in dark for 24 h at room temperature. The labelled nanoparticles were collected by centrifugation and washed with ethanol repeatedly until the supernatants were colourless.

Cell culture

Human embryonic kidney 293 (HEK293) cells were purchased from American Type Culture Collection and grown in DMEM culture medium supplemented with 10% (v/v) FBS in a humidified 5% CO_2 atmosphere at 37 °C. For all experiments, cells were harvested by using 0.25% trypsin and resuspended in fresh medium before plating.

Cytotoxicity assay

HEK293 cells were seeded into 96-well plates at a density of 1×10^4 per well in culture medium (100 μL) and grown for 24 h. Then, the medium was replaced by ones containing varied concentrations of nanoparticles. After 24 h incubation, the medium was replaced by fresh medium and 10 μL of MTT (5.0 mg mL^{-1} in PBS) was added to each well. After further incubation for 4 h, the medium was removed and 150 μL of DMSO was added to each well to dissolve formazan crystals. Finally, the absorbance was determined using a micro-plate reader (Biotek, USA) at the wavelength of 595 nm. The viability of cells without nanoparticle treatment was assumed to be 100%. Data were expressed as mean ± standard deviation (SD) of at least three independent experiments.

Plasmid DNA preparation

The pEGFP-N1 plasmid DNA (pDNA, 4.7kb) expressing the enhanced green fluorescent protein (EGFP) was prepared in Escherichia coli DH5α strain and extracted using a QIAGEN Plasmid Midi kit (QIAGEN, Hilden, Germany) according to the manufacturer's protocol. The integrity and purity of the prepared pDNA was analyzed using 0.8% agarose gel electrophoresis and the pDNA concentration was determined using a nanophotometer (P300, Implen GmbH). For microscopy imaging experiment, the pDNA was further labelled by fluorescent dye (YOYO-1) at a molar ratio of 1 molecular dye to 100 nucleic acid base pairs.

Gel retardation assay

The binding capability of nanoparticles for pDNA was evaluated by agarose gel electrophoresis. Samples were prepared by mixing nanoparticles and pDNA (0.2 μg) at different weight ratios and incubated for 30 min at room temperature. After the addition of gel loading dye blue, the samples were electrophoresed through a 0.8% agarose gel containing gel red in TAE buffer solution at 60 V for 60-90 min. The resulting pDNA migration patterns were recorded under UV irradiation (G-BOX, SYNGENE). To evaluate the DNA protection capability, the nanoparticles and pDNA were mixed at a weight ratio of 20 and incubated for 30 min at room temperature. Then, 2.5 U of DNase I (0.5 U μL^{-1}) in 10mM Tris-HCl, 2.5 mM $MgCl_2$, 0.5 mM $CaCl_2$ solution (pH 7.6) was added and the mixture was further incubated at 37 °C for 30 min. The DNase I was inactivated by adding 500 mM EDTA (2 μL). The pDNA was then released from the complex by treatment with heparin (10 mg mL^{-1}) for 30 min. Naked pDNA was also treated in the same procedure as the control.

In vitro transfection

HEK293 cells were seeded into a 24-well plate with coverslips at the density of 2×10^4 cells per well in culture medium (400 μL) 24 h before transfection. Prior to transfection, nanoparticle/pDNA complexes were freshly prepared by mixing pDNA (0.4 μg) and A-Bowl (8 μg) in water (20 μL).The mixture was incubated for 30 min at room temperature and then diluted with 400 μL DMEM media. The cells were incubated with this particle/pDNA suspension for 4 h and then the medium was replaced by DMEM containing 10% FBS. After 48 h, the transfection results was observed using a fluorescence microscope (Zeiss Axio Vert. A1) equipped with a 488 nm laser and the transfection efficiency was evaluated using a flow cytometry (Becton Dickinson) in FL1-H channel. For co-delivery of pDNA and cholorquine, A-Bowl (2 mg) was first incubated with cholorquine aqueous solution (200 μg mL^{-1}, 1 mL) for 24 h, then the suspension was centrifuged and the precipitate was washed with water twice. The amount of loaded cholorquine was determined by the UV–vis absorption of super liquid at the wavelength of 329 nm before and after

incubation.[5] Then, the cholorquine-loaded A-Bowl was mixed with pDNA following the process described above and used for subsequent transfection. For transfection mediated by PEI, pDNA (0.4 μg) in 50 μL DMEM was mixed with PEI (2 μg) in 50 μL DMEM. After incubation for 30 min at room temperature, the mixture was diluted with 300 μL DMEM and used for subsequent transfection. The delivery of pDNA and its subcellular location were also observed using a Leica SP5 confocal laser scanning microscope. HEK293 cells were fixed with 4 wt % formaldehyde at 16 h after transfection with the particle/YOYO-1-labelled pDNA complex. The cell nucleus and plasma membrane were stained with Hoechst 33258 (1 μg mL^{-1}) and Alexa Fluor 594 Wheat Germ Agglutinin (WGA, 5 μg mL^{-1}) for 15 min at room temperature, respectively. After the staining, the cells were softly washed twice with PBS to remove excessive dye and incubated in PBS before imaging.

Material characterization

Transmission electron microscopy (TEM) images were taken with FEI Tecnai G2 operated at 120 kV. The samples were prepared by dispersing the powder in ethanol and then dropped on carbon film supported by a Cu grid and air dried. Scanning electron microscopy (SEM) observation was carried out on a FEI Quanta 450 FEG environmental emission scanning electron microscope. The samples were prepared by adding powder onto carbon tape and coated with platinum before SEM observation. The hydrodynamic size and zeta-potential of nanoparticles in aqueous dispersions were measured on a Malvern Zetasizer Nano ZS operated at a wavelength of 633 nm, where scattered light was collected at a fixed angle of 173°. Raman spectra were collected with HORIBA LabRAM HR Evolution with 633 nm laser. Fourier transform infrared (FTIR) spectra were recorded on a Thermo Scientific NICOLET 6700 FTIR spectrometer with a Diamond ATR (attenuated total reflection) crystal. For each spectrum, 64 scans were collected at a resolution of 4 cm^{-1} over the range 400-4000 cm^{-1}. UV-vis absorption spectra were recorded on a UV-2600 spectrophotometer (Shimadzu Corporation). Thermogravimetric analysis (TGA) and differential scanning calorimetry (DSC) was performed on a Mettler Toledo

Thermogravimetric Analyser, using an air atmosphere (60 mL min^{-1}) with a heating ramp of 20 ˚C min^{-1}. Nitrogen sorption measurement was carried out at -196 ˚C using a TriStar II surface area and porosity analyser (Micromeritics). Prior to the measurement, the samples were degassed at 120 ˚C for 12 h.

References

[1] Q. Yu, P. Wang, S. Hu, J. Hui, J. Zhuang, X. Wang, *Langmuir* **2011,** *27*, 7185.

[2] Y. Chen, P. Xu, H. Chen, Y. Li, W. Bu, Z. Shu, Y. Li, J. Zhang, L. Zhang, L. Pan, X. Cui, Z. Hua, J. Wang, L. Zhang, J. L. Shi, *Adv. Mater.* **2013,** *25*, 3100.

[3] I. Slowing, B. G. Trewyn, V. S. Lin, *J. Am. Chem. Soc.* **2006,** *128*, 14792.

[4] L. Xiong, X. Du, B. Y. Shi, J. X. Bi, F. Kleitz, S. Z. Qiao, *J. Mater. Chem. B* **2015,** *3*, 1712.

[5] S. B. Hartono, N. T. Phuoc, M. H. Yu, Z. F. Jia, M. J. Monteiro, S. Z. Qiao, C. Z. Yu, *J. Mater. Chem. B* **2014,** *2*, 718.

Supporting Data

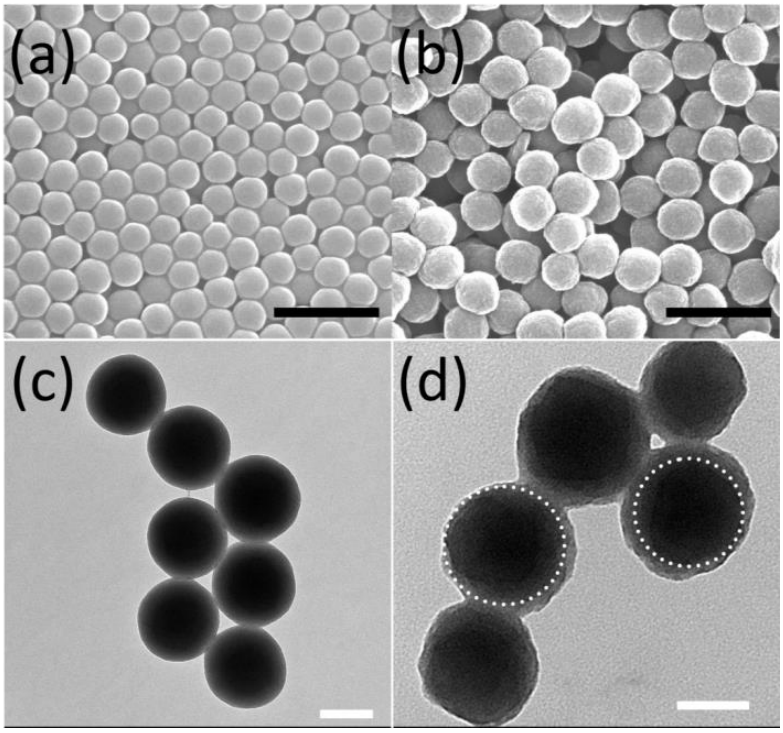

Fig. S1 SEM (a, b) and TEM (c, d) images of SS (a, c) and SS@OS (b, d). The positions of two SS cores in SS@OS (d) are circled with dotted-line to illustrate the asymmetric coating of organosilica layer. The scale bars in (a, b) and (c, d) are 500 nm and 100 nm, respectively.

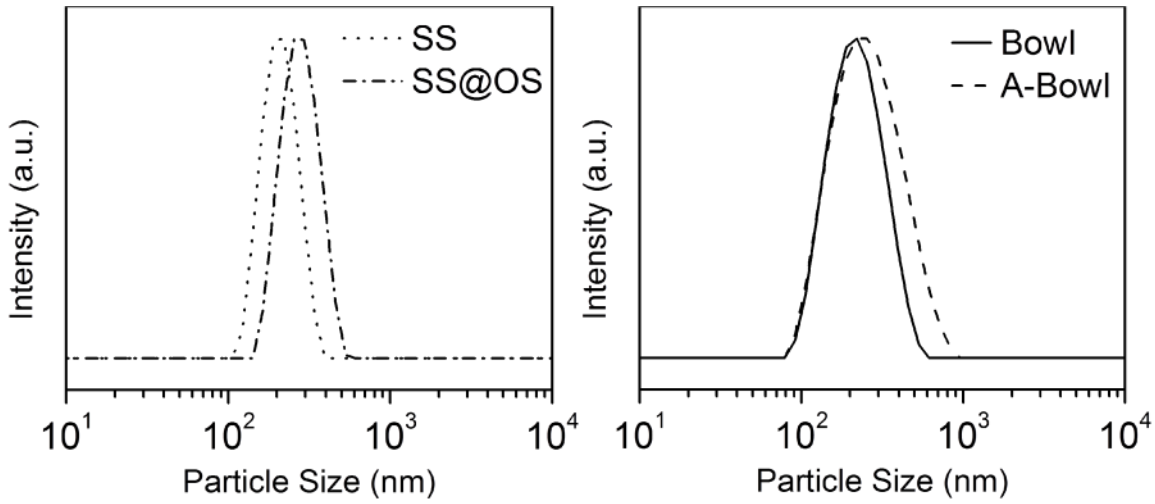

Fig. S2 Hydrodynamic size distributions of nanoparticles dispersed in water.

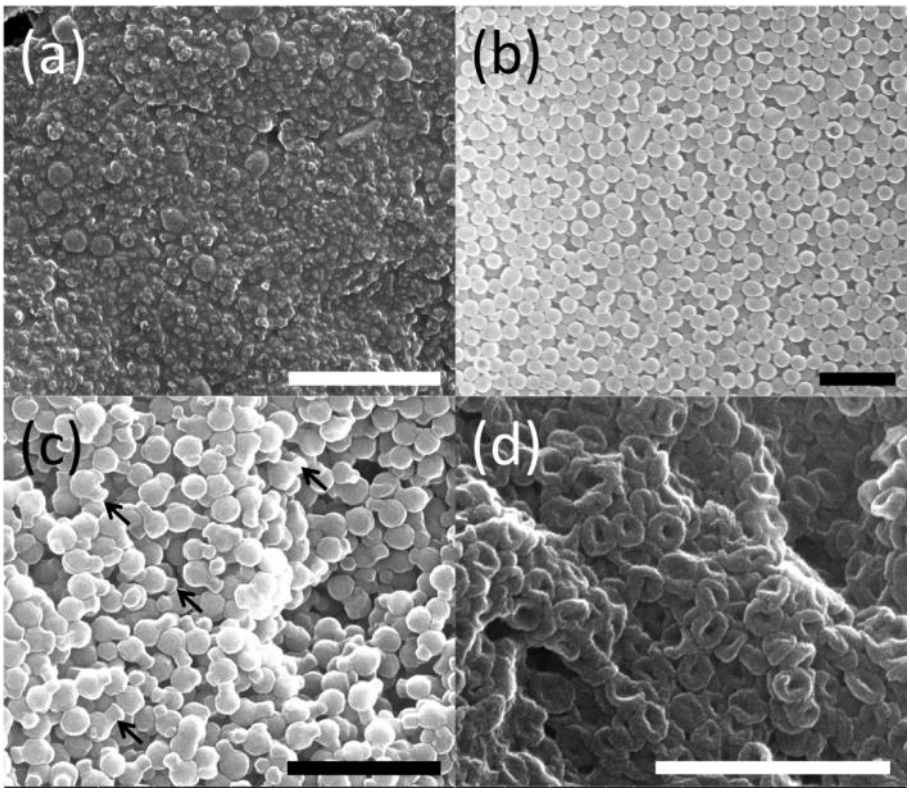

Fig. S3 SEM images of products after hydrothermal treatment when the BTEE addition is (a) 10 µL and (b) 50 µL. SEM images of products when (c) 30 µL BTEE is added over a period of 6 h, the Janus part is indicated with black arrow, (d) SS@OS is etched with 0.6 M Na_2CO_3 at 60 °C for 6 h.

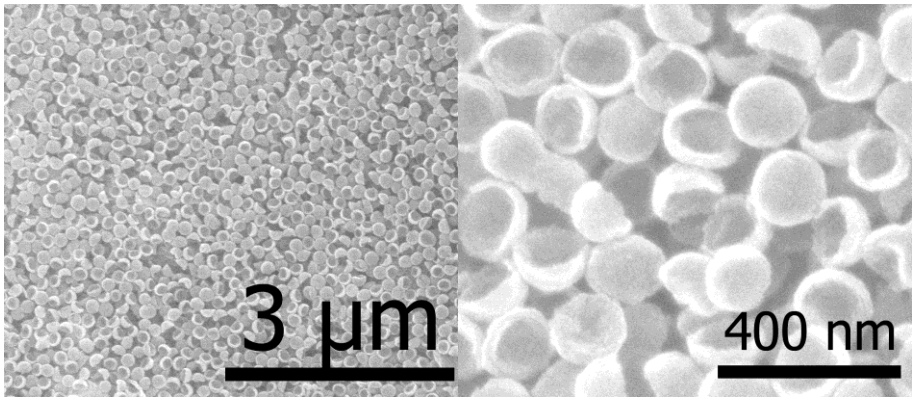

Fig. S4 SEM images of amine functionalized mesoporous organosilica nano-bowls.

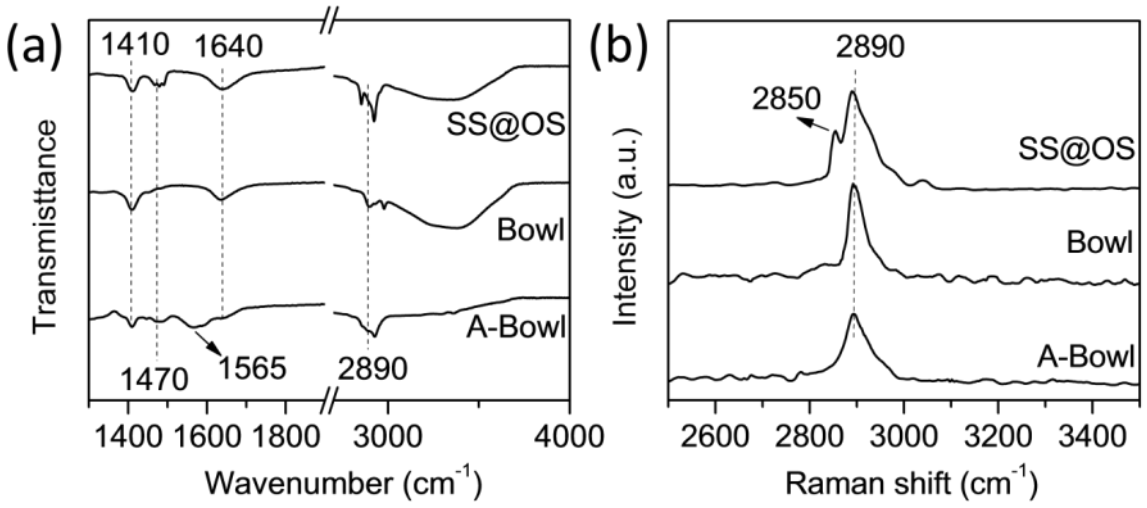

Fig. S5 Enlarged (a) FTIR and (b) Raman spectra of mesoporous organosilica nano-bowls.

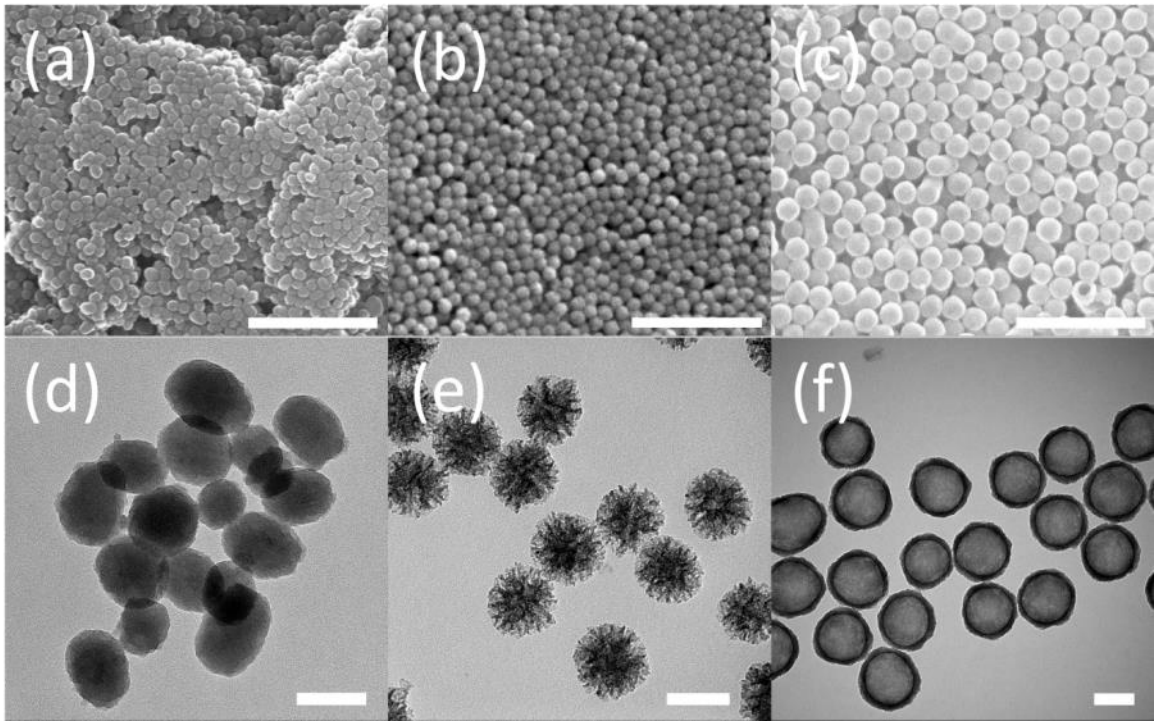

Fig. S6 SEM (a, b, c) and TEM (d, e, f) images of A-MCM41 (a, d), A-Dendric (b, e) and A-hollow (c, f). The scale bars in (a, b, c) and (d, e, f) are 1 μm and 100 nm, respectively.

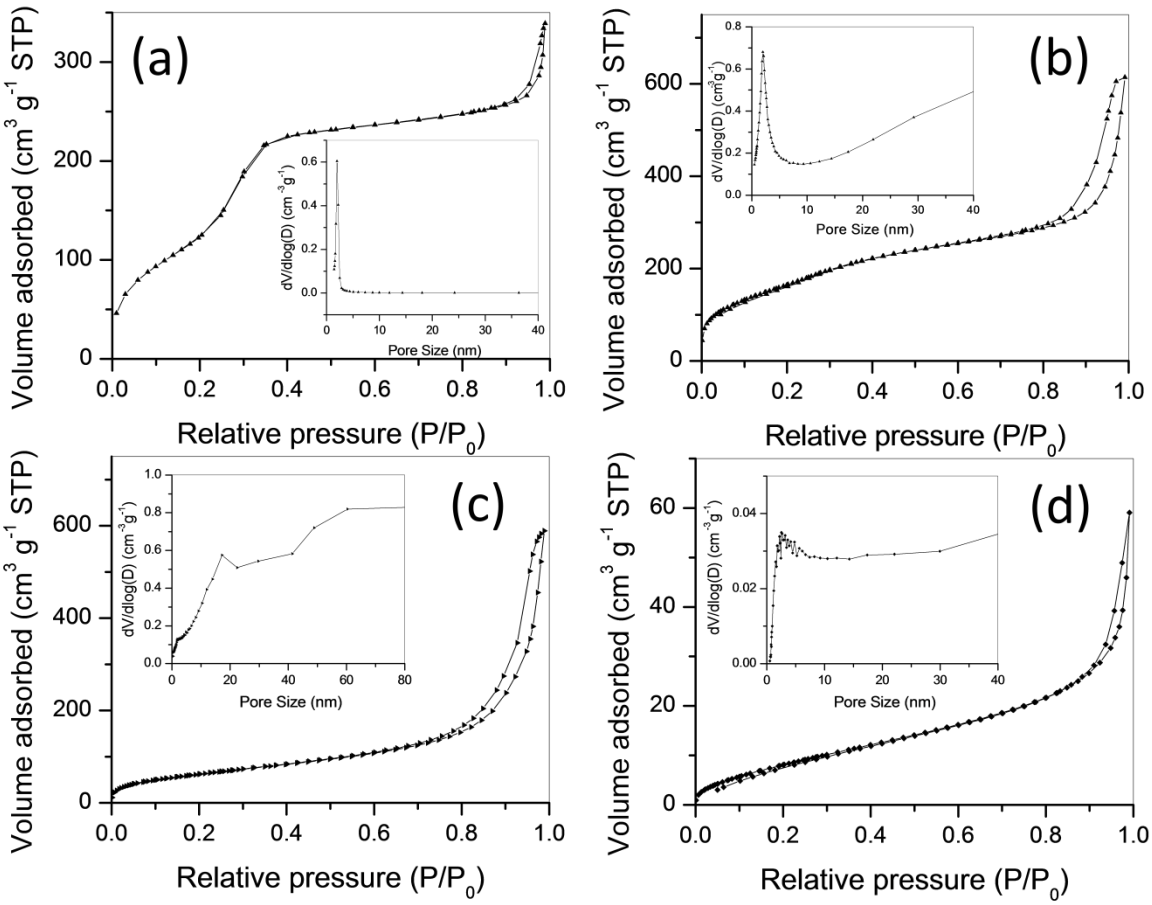

Fig. S7 Nitrogen sorption and pore size distribution (insert) curves of (a) A-MCM41, (b) A-Hollow, (c) A-Dendric and (d) A-SS.

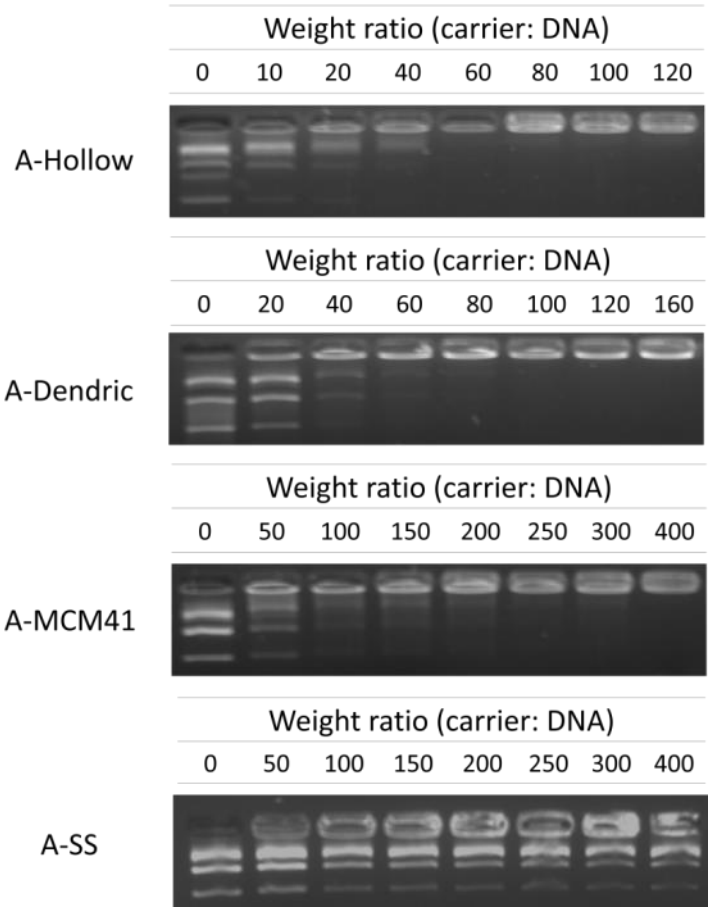

Fig. S8 Gel retardation assays of nanoparticles/pDNA complex at different carrier/pDNA weight ratios.

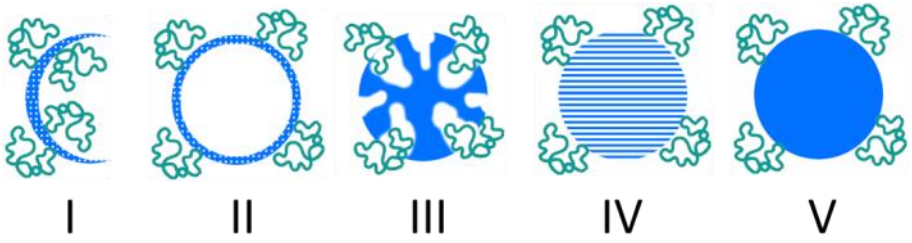

Fig. S9. Proposed loading status of plasmid DNA on various amine functionalized silica-based nanoparticles: (Ⅰ) A-Bowl, (Ⅱ) A-Hollow, (Ⅲ) A-Dendric, (Ⅳ) A-MCM41, (V) A-SS.

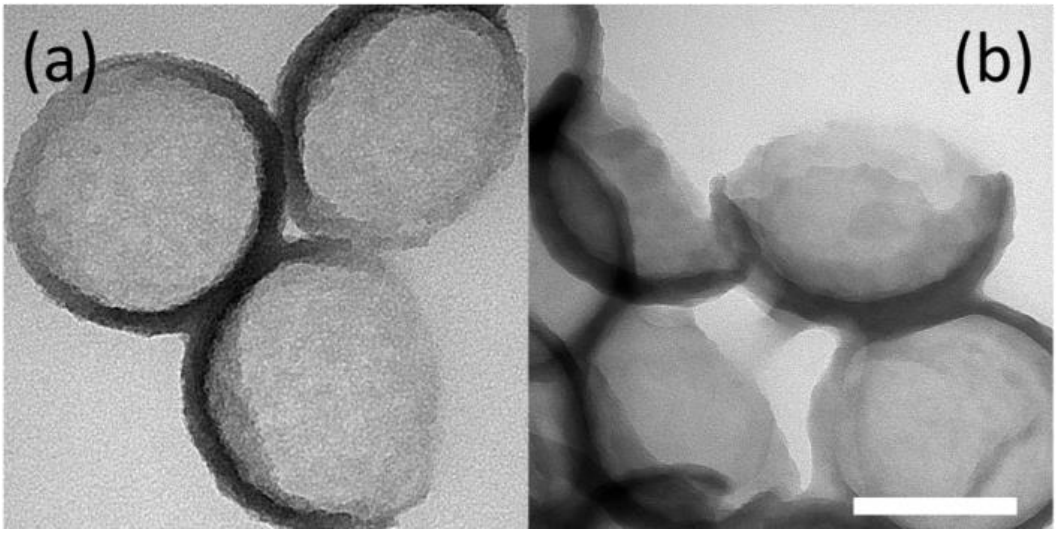

Fig. S10 TEM images of A-Bow (a) before and (b) after loading of pDNA. The scale bar is 100 nm.

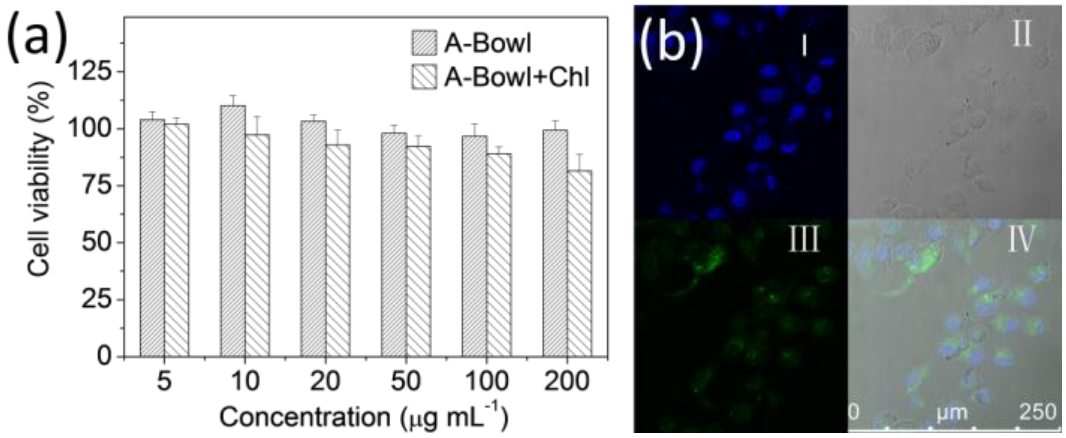

Fig. S11. (a) Viability of HEK293 cells after 24 h incubation with A-Bowl or A-Bowl containing 4 % chloroquine. (b) Confocal images of HEK293 cells after 4 h incubation with 20 μg ml^{-1} A-Bowl. (Ⅰ) cell nucleus (blue) labelled with Hoechst 33258; (Ⅱ) differential interference contrast image; (Ⅲ) A-Bowl particles (green) labeled with FITC; (Ⅳ) overlay image of (Ⅰ), (Ⅱ) and (Ⅲ).

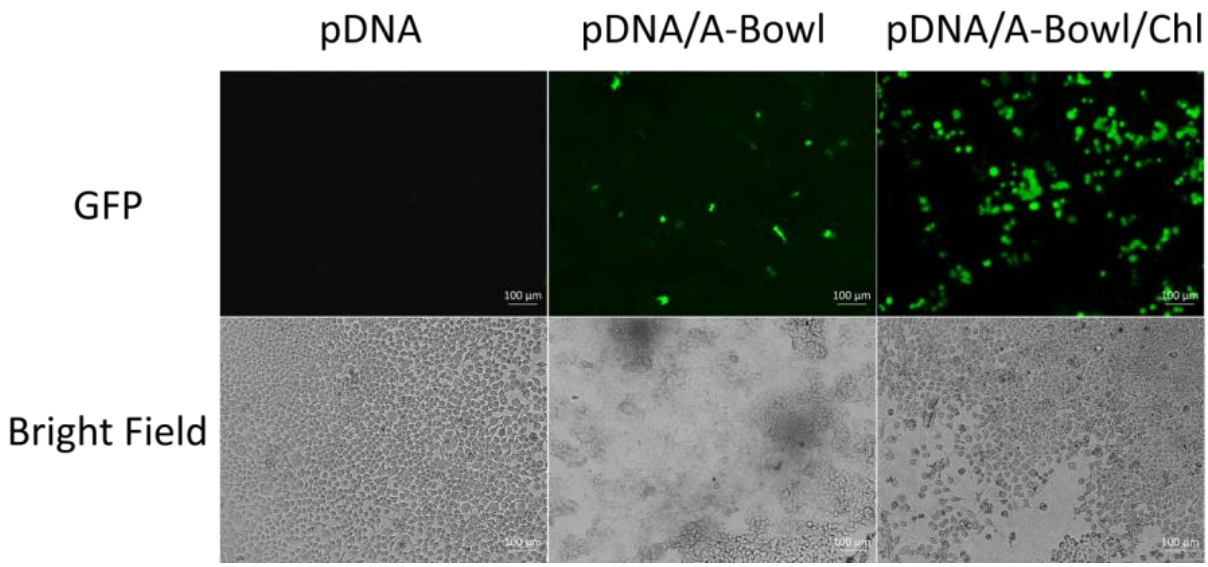

Fig. S12. Fluorescent and bright field images of HEK293 cells transfected with different transfection reagents.

Table S1. Hydrodynamic diameters of nanoparticles dispersed in water.

Sample	Average Particle Size (nm)	Polydispersity Index
SS	196	0.036
SS@OS	268	0.042
Bowl	207	0.178
A-Bowl	240	0.218

Table S2. Structure parameters of nanoparticles.

Sample	Surface Area[a] ($m^2 g^{-1}$)	Pore Volume[b] ($cm^3 g^{-1}$)	Pore Size[c] (nm)	Surface Amine[d] (mmol g^{-1})
Bowl	985	1.08	2.5	-
A-Bowl	876	0.97	2.1	0.81
A-MCM41	754	0.59	2.0	1.69
A-Dendric	234	0.91	17.2	1.24
A-Hollow	852	0.95	2.0	0.93
A-SS	31	0.09	-	0.11

a) Brunauer-Emmett-Teller (BET) specific surface area was calculated using N_2 adsorption data at a relative pressure P/P_0 range of 0.05-0.30. b) Pore size distribution was derived from adsorption branch of the isotherm using the Barrett-Joyner-Halenda (BJH) method. c) Pore volume was determined from the amount of N_2 adsorbed at the single point of P/P_0=0.99. d) Surface amine group was calculated from the difference of weight loss in thermogravimetry between modified and unmodified samples.

Chapter 7 Conclusion and Perspective

7.1 Conclusion

The researches in this thesis are aimed at developing a serial of novel mesoporous silica nanocomposites with favorable structure and surface functionalization for drug and gene delivery. Based on these studies, the following results have been obtained:

(1) We firstly studied the controllable synthesis of stellate mesoporous silica nanoparticles with radial pore morphology. For the delivery application, a precise control over the particle size and the pore structure of the material is highly desirable, because these properties affect the bio-distribution, cellular uptake, drug release profile, and loading capacity of the nanocarrier. Therefore, we conducted systematic study to elucidate the effects of synthesis conditions (including reaction temperature and time, and reagent ratio) on the final particle product. It was found that the formation of stellate particles is a two-phase process and the reaction kinetics plays an important role in determining the structure parameters. The particle size of the material could be tailored continuously ranging from 50 to 140 nm and the pore size from 2 to 20 nm. After further functionalization with low molecular weight poly(ethyleneimine), these nanocomposites demonstrated good capability for intracellular delivery of the anticancer drug doxorubicin.

(2) Then, we developed a cancer cell-specific nuclear-targeted delivery system based on mesoporous silica nanoparticles. To minimize the side effects of highly toxic anticancer drugs, it is necessary to deliver the drugs selectively into cancer cells. Meanwhile, for many anticancer drugs, the cell nucleus is the sub-cellular organelle where they exert their anticancer effect. Therefore, we modified the 40 nm mesoporous silica nanoparticles with two biologic targeting moieties, folic acid and dexamethasone, to selectively deliver anticancer drugs in to the nucleus of cancer cells. The results suggest this strategy can not only enhance the inhibition efficacy of doxorubicin on cancerous Hela cells through active nucleus accumulation but also

reduce toxic side effects on normal cells though receptor-mediated selective cellular uptake.

(3) Next, we developed magnetic core–shell silica nanoparticles with large radial mesopores for small interfering RNA (siRNA) delivery. Delivery of siRNA is an emerging technology to treat various diseases by halting the production of target proteins. As the naked siRNA molecule is susceptible to enzyme degradation and cannot cross the cell membrane, we prepared 150 nm magnetic core–shell silica nanoparticles with large radial mesopores to load the siRNA inside the mesopores. These nanoparticles possess both high loading capacity of siRNA and strong magnetic response under an external magnetic field. Furthermore, an acid-liable coating composed of tannic acid was applied to further protect the loaded siRNA. The coating also increased the dispersion stability of the siRNA-loaded carrier and served as a pH-responsive releasing switch. Using these nanocarriers, enhanced delivery of functional siRNA into human osteosarcoma cancer cells was achieved with the aid of the external magnetic field.

(4) Finally, we prepared bowl-like mesoporous organosilica nanoparticles for plasmid DNA delivery. Due to the much larger size of plasmid DNA than siRNA, a specific nanostructure distinct from traditional mesoporous silica nanoparticles needs to be developed for DNA delivery. Therefore, we fabricated 180 nm organosilica nanoparticles with a novel bowl-like structure, which can load DNA molecules in the central bowl cavity. Under the same amine functionalization, these nano-bowls showed significantly higher loading capacity for plasmid DNA than traditional (hollow, dendric, MCM41 type) silica-based nanocarriers thanks to their large accessible center cavity. Furthermore, after co-loading with an endosomolytic reagent in the mesopores, enhanced transfection efficiency comparable to the polymer standard was achieved for in vitro plasmid DNA transfection.

In summary, these findings have demonstrated the design and fabrication of several novel silica nanocomposties for drug and gene delivery, and may pave a way of the further development of silica-based delivery system.

7.2 Perspective

Based on the work presented in this thesis, we propose that future studies can be carried out in the following directions:

1) Synthesis of stellate mesoporous organosilica nanoparticles. In chapter 3, tunable synthesis of stellate mesoporous silica nanoparticles with radial pore morphology was demonstrated using a weak base triethanolamine as the catalyst in a two phase reaction system. It would be interesting to investigate whether similar reaction conditions can be applied to the controllable synthesis of stellate mesoporous organosilica nanoparticles. Due to the versatile organic groups incorporated in their silica framework, stellate mesoporous organosilica silica nanoparticles may exhibit some unique properties for drug delivery and other applications.

2) Bioactive molecules modified mesoporous silica nanoparticles. In chapter 4, cancer cell-specific nuclear-targeted delivery was achieved by mesoporous silica nanoparticles modified simultaneously with two bioactive small molecules. This illustrates the importance of combining biologically active components with relatively inert mesoporous silica structure for efficient drug delivery. With the convergence of nanotechnology and molecular biology, we anticipate that more bioactive molecules such as aptamers and antibodies will be exploited in mesoporous silica nanocomposite delivery systems.

3) Multifunctional large-pore core-shell mesoporous silica nanoparticles. In chapter 5, core–shell silica nanoparticles with large radial mesopores were prepared for magnetically-targeted siRNA delivery. Due to the intrinsic multifunctionality of the magnetite core, these core-shell nanoparticles could be further explored for magnetic resonance imaging (MRI) or hypothermia therapy. Furthermore, using similar synthesis method, the magnetic core component could be replaced with other functional materials like gold or carbon nanospheres. Thus, other types of multifunctional large-pore core-shell mesoporous silica nanoparticles could be developed.

4) Functional bowl-like nanoparticles. In chapter 6, we prepared bowl-like mesoporous organosilica nanoparticles for DNA delivery. However, only simple amine functionalization was carried out for comparison purpose. We anticipate more complex nanostructure could be constructed based on these nano-bowls through elaborate functionalization. For example, a bowl cover may be fabricated to seal the cargo loaded in the bowl cavity. In another possible and interesting aspect, these organosilica nano-bowls could be transformed into carbon nano-bowls through thermal carbonization and used in delivery and catalysis applications.

5) In vivo delivery evaluation. In this project, the silica nanocomposites are only evaluated for drug and gene delivery in vitro. For the ultimate goal of clinical translation, systematic in vivo evaluations are essential. Because many additional biological barriers such as blood compatibility, reticuloendothelial system and kidney filtration exist in the body environment, the delivery results of these silica nanocomposites in vivo can be significantly different from that in vitro. Therefore, more material engineering may be needed for these silica nanocomposites based on the results of in vivo evaluation.

Appendix: Publications during Ph.D

Journal Papers

[1] **L. Xiong**, S. Z. Qiao. A mesoporous organosilica nano-bowl with high DNA loading capacity – a potential gene delivery carrier, *Nanoscale,* **2016**, 8, 17446.

[2] **L. Xiong**, X. Du, B. Shi, J. Bi, F. Kleitz, S. Z. Qiao. Tunable stellate mesoporous silica nanoparticles for intracellular drug delivery, *J. Mater. Chem. B,* **2015**, 3, 1712.

[3] **L. Xiong**, X. Du, F. Kleitz, S. Z. Qiao. Cancer-Cell-Specific Nuclear-Targeted Drug Delivery by Dual-Ligand-Modified Mesoporous Silica Nanoparticles, *Small,* **2015**, 11, 5919.

[4] **L. Xiong**, J. Bi, Y. Tang, S. Z. Qiao. Magnetic Core-Shell Silica Nanoparticles with Large Radial Mesopores for siRNA Delivery, *Small,* **2016**, 12, 4735.

[5] D. Mahony, A. S. Cavallaro, K. T. Mody, **L. Xiong**, T. J. Mahony, S. Z. Qiao, N. Mitter. In vivo delivery of bovine viral diahorrea virus, E2 protein using hollow mesoporous silica nanoparticles, *Nanoscale,* **2014**, 6, 6617.

[6] X. Du, **L. Xiong**, S. Dai, S. Z. Qiao. γ-PGA-Coated Mesoporous Silica Nanoparticles with Covalently Attached Prodrugs for Enhanced Cellular Uptake and Intracellular GSH-Responsive Release, *Adv. Healthcare Mater.,* **2015**, 4, 771.

[7] X. Du, **L. Xiong**, S. Dai, F. Kleitz, S. Z. Qiao. Intracellular Microenvironment-Responsive Dendrimer-Like Mesoporous Nanohybrids for Traceable, Effective, and Safe Gene Delivery, *Adv. Funct. Mater.,* **2014**, 24, 7627.

[8] X. Du, X. Li, **L. Xiong**, X. Zhang, F. Kleitz, S. Z. Qiao. Mesoporous silica nanoparticles with organo-bridged silsesquioxane framework as innovative platforms for bioimaging and therapeutic agent delivery, *Biomaterials,* **2016**, 91, 90

Conference Papers

[9] **L. Xiong**, X. Du, S. Z. Qiao. Influence of Synthesis Temperature on the Porosity of Mesoporous Silica Nanoparticles, *International Conference on Nanoscience and Nanotechnology,* **2014**, Abstract Collection.